TECHNICKÁ UNIVERZITA V LIBERCI
FAKULTA TEXTILNÍ

NANOKOMPOZITNÍ MATERIÁLY

HABILITAČNÍ PRÁCE

Souhrn uveřejněných vědeckých a
odborných prací doplněný komentářem

Ing. Bc. Eva Košťáková, Ph.D.

Prosinec 2012

Obsah

1. SOUHRN UVEŘEJNĚNÝCH VĚDECKÝCH A ODBORNÝCH PRACÍ 3

1.1 Publikace v recenzovaných časopisech 3

1.2 Publikace v ostatních časopisech 3

1.3 Příspěvek ve sborníku mezinárodní konference 3

1.4 Příspěvek ve sborníku domácí konference 6

1.5 Realizované technické dílo, patenty 6

1.6 Monografie a skripta 7

1.7 Reakce na publikace v databázi Web of Knowledge 7

2. KOMENTÁŘ K PUBLIKACÍM 13

2.1 Úvod 13

2.2 Nanokompozitní materiály s integrovanými uhlíkovými nanočásticemi 14

2.3 Kompozitní a nanokompozitní materiály jako scaffoldy pro tkáňové inženýrství 27

2.4 Prohlášení 29

2.5 Použitá literatura 29

3. SEZNAM PŘÍLOH 31

1. SOUHRN UVEŘEJNĚNÝCH VĚDECKÝCH A ODBORNÝCH PRACÍ

1.1 Publikace v recenzovaných časopisech

[1]. Lukáš D. Chaloupek J., Kostakova E., Pan N., Martinkova, I.: Morphological transitions of capillary rise in a bundle of two and three solid parallel cylinders, Physica A, 371 (2006) 226-248, IF=1,373(11)

[2]. M. Rampichova, E. Filova, L. Kolacna E. Kostakova, L. Ocheretna, D. Lukas, A. Lytvynets, E. Amler: Improved biological properties of non-woven PGA/PVA scaffolds for artificial cartilage, FEBS Journal, Vol 273, Suppl 1, June 2006, p. 269, IF = 3,790 (11)

[3]. Kolacna, L., Bakesová, J., Varga, F., Kostakova, E., Planka, L., Necas, A., Lukas, D., Amler, E., Pelouch, V.: Biochemical and biophysical aspects of collagen nanostructure in the extracellular matrix, Physiol. Res.; 56 (Suppl. 1) Biophysics in Mecial Research, pg.51-60. (2007), IF = 1,555 (11)

[4]. Filova E, Rampichova M, Handl M, Lytvynets A, Halouzka R, Usvald D, Hlucilova J, Prochazka R, Dezortova M, Rolencova E, Kostakova E, Trc T, Stastny E, Kolacna L, Hajek M, Motlik J, Amler E. Composite hyaluronate-type I collagen-fibrin scaffold in the therapy of osteochondral defects in miniature pigs, Physiol. Res.; 56 (Suppl. 1): pg.5-16 (2007), IF =1.555 (11)

[5]. Kostakova, E., Meszaros, L., Gregr,J.: Composite nanofibers produced by modified electrospinning method; Material Letters, Vol.63, pg.2419-2422 (2009), IF = 2,307 (11)

[6]. Rampichová M, Košťáková E, Filová E, Prosecká E, Ocheretná L, Lytvynets A, Lukáš D, Amler E. Non-woven PGA/PVA Fibrous Mesh as an Appropriate Scaffold for Chondrocyte Proliferation; Physiol. Res.; Vol.59, Issue 5; pg.773-781 (2010), ISSN: 0862-8408, IF =1.555 (11)

[7]. D. Lukas, N. Pan, A. Sarkar, M. Weng, J. Chaloupek, E. Kostakova, L. Ocheretna, P. Mikes, M. Pociute, E. Amler, Auto-model based computer simulation of Plateau–Rayleigh instability of mixtures of immiscible liquids, Physica A (2010),doi:10.1016/j.physa.2010.01.046, IF=1,373 (11)

[8]. Filova, E., Burdikova, Z., Rampichova, M., Bianchini, P., Čapek, M., Košťáková, E., Amler, E., Kubínová, L.: Analysis and three-dimensional visualization of collagen in artificial scaffolds using non-linear microscopy techniques; Journal of Biomedical Optics; Vol.15, No.6; (2010), IF =3,157 (11)

[9]. Rampichova, M., Martinova, L., Kostakova, E., Filova,E. et al: A simple drug anchoring microfiber scaffold for chondrocyte seeding and proliferation, JOURNAL OF MATERIALS SCIENCE-MATERIALS IN MEDICINE, Volume: 23 Issue: 2 Pages: 555-563 DOI: 10.1007/s10856-011-4518-x Published: FEB 2012, ISSN: 0957-4530, IF=2,316 (11)

[10]. Kostakova, E., Gregr, J., Meszaros, L., Chotebor, M., Nagy, Z., K., Pokorny, P., Lukas, D.: Laboratory synthesis of carbon nanostructured materials using natural gas, Materials Letters, 79 (2012) 35–38, 2012, IF=2,307 (11)

1.2 Publikace v ostatních časopisech

[11]. Gombos, Z., Nagy, V., Kostakova, E., Vas, L.,M.: Absorbency behaviour of vertically positioned nonwoven glass fiber mats in case of two different resin viscosities, Macromolecular symposia, Vol. 239, pg.227-231, 2006

[12]. Molnar, K., Kostakova, E., Meszaros, L.: Electrospinning of PVA/carbon nanotube composite nanofibers: the effect of processing parameters, Material Science Forum, Vol. 589 (2008) pp 221-226

[13]. Kostakova, E., Chotebor, M., Gregr, J., Meszarosz, J., Nagy, Z.,K: Unconventional substrates for CVD production of carbon nanostructures, World Journal of Engineering, World Journal of Engineering, , Vol. 7, Supplement 1, p. 48, 2010, ISSN 1708-5284

1.3 Příspěvek ve sborníku mezinárodní konference

[14]. Košťáková, E.,Grégr, J.: Dynamics of liquid's penetration into textile systems from carbon fibres, Strutex, Liberec 2000

[15]. Košťáková, E., Grégr, J.: Dynamics of penetration of liquids into fibre systems TEXSCI`2000, Liberec 2000
[16]. Grégr, J., Košťáková, E.: 3D Visualisation of Molecular Structure of Fiber Polymers, conference Strutex, Liberec 2001
[17]. Košťáková, E.: Liquid Penetration through the Ledger Point (The Simulation Using the Issing Model – The Monte Carlo Method), conference XXII. Reinforced Plastics, Balatonfüred 2002
[18]. Nagy, V., Košťáková, E.,Vas, L.: Investigation of Porosity in Polyester Staple Yarns, TEXSCI 2003, Liberec 2003
[19]. Košťáková,E.: Spontaneous Penetration of Liquid Droplets into Nonwovens, TEXSCI 2003, Liberec 2003
[20]. Jirsák,O., Lukáš,D., Martinová, L.,Chaloupek, J.,Růžičková, J., Košťáková, E., Hrůza, J.:Production and Properties of Polymeric Nanofibers, Nano`03, Brno 2003
[21]. Košťáková,E., Pociute,M.,Lukas,D.:The Radial Capillary, Strutex 03, Liberec 2003
[22]. Lukáš,D., Košťáková ,E.,Torres,S.: Relationship Between Surface Tension and Electrical Field Intensity for Electrospinning, Strutex 03, Liberec 20031
[23]. Košťáková, E.: Nanofibers as Reinforcement in Composites, Reinforced Plastics 2004, International BALATON conference, Hungary, 2004
[24]. Jirsák,O., Bharanitharan, R., Růžičková,J., Košťáková, E., Hrůza,J.: Nanofibers and Its Application, HPTEX 2004, Coimbatore – 6, India, 2004
[25]. Košťáková, E.: Spherical Drop's Penetration into Needle-Punched Nonwovens, 4th Autex World Textile Conference, Roubaix – France, 2004, ISBN 2-9522440-0-6
[26]. Košťáková, E.: Computer Simulation of Drop's Penetration into the Fibrous Materials, 2nd International Textile, Clothing & Design Conference – Magic World of Textiles, Dubrovník – Croatia, 2004, ISBN 953-7105-05-9
[27]. Lukáš, D., Košťáková, E., Torres, S.: Relationship Between Surface Tension and Electric Field Intensity for Electrospinning, 2004 International Textile Congress, Terrassa - Spain, 2004, ISBN 84-608-0188-8
[28]. Košťáková, E., Poláchová, J., Krsek, J.: Electrospun Nanofiber Nonwoven Web as a Reinforcement for Composite Materials, Strutex 04, Liberec – Czech Republic, 2004, ISBN 80-7083-891-4
[29]. Lukáš, D., Košťáková, E., Chaloupek, J., Očeretna, L., Pociute, M.: Instability of Liquid Jets, Strutex 04, Liberec – Czech Republic, 2004, ISBN 80-7083-891-4
[30]. Košťáková, E., Grégr, J., Müllerová, J., Štefaňáková, L., Šišková, A.: Carbonization of Electrospun Polyvinylalcohol Nanofibers, 5th World Textile Conference, AUTEX, Portorož, Slovenia 2005, ISBN 86-435-0709-1
[31]. Ocheretna, L., Košťáková, E.: Ultrasound in Textile Technology – Modeling and Experiments, Forum Acusticum Budapest 2005 Proceedings, Hungary, ISBN:963 8241 68 3
[32]. Gombos, Z., Nagy, V., Košťáková, E., Vas, L.,M.: Resin Absorbency of Glass Fiber Mats, 5thInternational Conference IN-TECH-ED 2005, Budapest, 7-9 September 2005
[33]. Gombos, Z., Nagy, V., Koštáková, E., Vas, L.,M.: Vertical Resin Absorption in Glass Fiber Nonwoven Mats, PAT 2005, Budapest, Sept. 13-16th;
[34]. Košťáková, E., Grégr, J., Müllerová, J.:Manufacturing of Carbon Nanofiber Web from Electrospun Nanofiber Precursors, Chemické listy S, 3rd Meeting on Chemistry and Life, Brno 2005, ISSN 0009-2770
[35]. Košťáková E. Chaloupek J. Lukáš D.: Mysteries in fibre mass wetting. In: Incontinence: The engineering challenge, UCL, London, Registered number:206882, 2005
[36]. E. Filová, M. Rampichová, E. Košťáková, A. Špániková, M. Martinová, L. Ocheretná, D. Lukáš, A. Lytvynets, F. Jelínek, M. Handl, E. Amler. ARTIFICIAL SCAFFOLDS IN CARTILAGE REGENERATION, 82. Fyziologické dny, 7.-9.2. 2006, Praha, Phys Res. 2006; 55(4): 19P
[37]. M. Rampichová, E. Filová, E. Košťáková, M. Martinová, L. Ocheretná, D. Lukáš, A. Lytvynets, E. Amler. NON-WOVEN PGA/PVA SCAFFOLDS IN TISSUE ENGINEERING OF CARTILAGE, 82. Fyziologické dny, 7.-9.2. 2006, Praha, Phys Res. 2006; 55(4): 39P
[38]. E. Amler, M. Rampichová, E. Filová, L. Koláčná, E. Košťáková, M. Martinová, L. Ocheretná, A. Lytvynets, D. Lukáš. NANOFIBRES IN CARTILAGE ENGINEERING, 82. Fyziologické dny, 7.-9.2. 2006, Praha, Phys Res. 2006; 55(4): 13P

[39]. Grégr J., Košťáková E.,Slavík M.: Carbon fibers: micro- and nano-fibers, 13th Int. Conf. Structure and Structural Mechanics of Textiles, STRUTEX 2006, Liberec Nov. 2006, Proceedings pg. 543-8, ISBN 80-7372-135-X
[40]. Goyal A Sarkar A Plíva Z Košťáková E and Lukáš D.: "Designed electric circuits used as collector for electrospinning", In: 13th STRUTEX, November 2006.
[41]. Košťáková, E.: Electrospun PVA-derived carbon nanofibers, Proceedings of Advanced Materials and Technologies – International Summer Conference – School, Palanga, Lithuania (2006).
[42]. Goyal A Sarkar A Plíva Z Košťáková E and Lukáš D.: "Designed electric circuits used as collector for electrospinning", In: 13th STRUTEX, Liberec, November 2006.
[43]. Mészáros, L., Košťáková, E., Pokorný, P., Romhány, G.: Nanotubes' separation by means of ultrasound for nanocomposite materials' production, 13th International conference STRUTEX 2006, Liberec Nov. 2006, pg-353-358, ISBN 80-7372-135-X
[44]. Kostakova, E., Lukas, D., Martinova, L., Novak, O., Filova, E., Rampichova, M., Amler, E.: Textiles as Scaffolds for Tissue Engineering, Czech-Polish Workshop on Composites as Biomaterials, Czech Carbon and Composite Materials Society, Institute of Rock Structure and Mechanics, 2007
[45]. Kostakova, E., Kosturikova, M., Pokorny, P., Lukas, D.: Electrospun nanofibrous threads for medicine, 6th International Conference TexSci 2007, Book of Abstracts, 2007, ISBN 978-80-7376-207-4
[46]. Grégr, J., Hanuš, J., Charvát, B., Kostakova, E.: Carbon nonwovens, 6th International Conference TexSci 2007, Book of Abstracts, 2007, ISBN 978-80-7376-207-4
[47]. Kostakova, E., Gregr, J.: Nanofibers derived from electrospun precursors, Proceedings of international conference Autex 2007, Finland, ISBN 978-952-15-1794-5 RIV
[48]. Košťáková, E., Mészáros, L., Molnár, K-, Gombos, Z.: Electrospinning of PVA / carbon nanotubes composite nanofibers: the effects of processing parameters, VI. hungarian Materials Science Conference 14-16 october, 2007, Siófok, Hungary RIV
[49]. Košťáková, E., Ivánková, L., Lukáš, D., Filová, E., Rampichová, M., Amler, E.: Wet laid nonwovens as scaffold for tissue engineering of knee cartilage, 14th International Conference STRUTEX, November 2007, ISBN 978-80-7372-271-5
[50]. Filová E., Rampichová, M., Martinová, L., Kostakova E., Lukas, D., Lytvynets, A., Amler, E., Nanofibers from pHEMA and PVA/CHitosan in tissue Engineering, 4thInternational Workshop on Nanosciences and Nanotechnologies, 16-18 July, 2007, Thessaloniki, Greece
[51]. Filová E., Rampichová, M., Kostakova E., Lukas, D., Lytvynets, A., Amler, E.: Composite nonwoven scaffolds containing PGA, PVA and chitosan improve pH stability and cell proliferation. ICRS 2007, 29 September-2 October 2007, Warsaw, Poland, Book of abstracts, p 193
[52]. Kostakova, E., Meszaros, L., Gregr, J.: Composite nanofibers – Polyvinylalcohol electrospun nanofibers containing carbon nanotubes, international conference AUTEX 2008, Book of Abstracts, Biella, Italy 2008, ISBN978-88-89280-49-2
[53]. Molnar, K., Kostakova, E., Vas, L., M.: Preparation of composites reinforced with "in situ" electrospun fibers, 14th European conference on composite materials, Budapest, Hungary 2010, Paper ID:116-ECCM14, ISBN: 978-963-313-008-7
[54]. Kostakova, E., Chotěbor, M, Gregr, J, Pokorny, P., Meszaros, L., Nagy, Z.: Unconventional substrates for CVD production of carbon nanostructures, Textile Science 2010, Liberec, Czech Republic, pg.109-113, ISBN: 978-80-7372-635-5
[55]. Charvát, R., Kostakova, E., Lukas, D.: Computer simulation and modeling of Liquid droplets deposition on nanofibers, 7th international conference – TexSci 2010, Liberec, Czech Republic, pg.103-108 ISBN:978-80-7372-635-5
[56]. Kostakova, E., Gregr, J., Pokorny, P., Meszaros, L., Chotebor, M.: Carbon nanostructures produced by CCVD method, NanoOstrava, Ostrava 2011
[57]. Kostakova, E., Zemanova, E., Klouda, K.: Fullerene C60 and its Derivatives as nanocomposites in Polymer Nanofibres; conference proceedings NANOCON 2011, Brno 2011 ISBN 978-80-87294-23-9
[58]. Kostakova, E., Gregr, J., Jansta, R., Meszaros, L.: Synthesis of Carbon Nanoparticles on Wires, 18th International Conference Strutex, December 2011, ISBN 978-80-7372-786-4, pg.301-306
[59]. Kostakova, E., Gregr, J., Nagy, Z.,K.: Growth of Carbon Nanotubes Directly on Metal Wires by Thermal CVD, Book of Proceedings of 12th World Textile conference AUTEX, 13-15th June 2012, Zadar, Croatia, 2012, ISBN 978-953710548-8

1.4 Příspěvek ve sborníku domácí konference

[60]. Pociute, M., Chaloupek, J., Košťáková, E., Očeretna, L., Lukáš, D.: Systém projektování textilních struktur – Tři vývojové etapy, Závěrečná zpráva Výzkumného centra TEXTIL, Technická univerzita v Liberci, Liberec – Česká republika, 2004

[61]. Košťáková, E., Grégr, J., Očeretna, L.: Nanovlákna a možnosti jejich uplatnění v kompozitních materiálech, XXIII. Vyztužené plasty, Karlovy Vary, Czech Republic, 2005

[62]. Grégr J., Košťáková E., Kovačič V., Grabmüllerová J.: Méně známé formy uhlíku, mezinárodní seminář „Soudobé trendy v chemickém vzdělávání“, PdF UHK, 14. září 2006

[63]. Kostakova, E.: Textilie pro medicínu, přednáška v rámci výstav y Hospimedica, Brno 18.10.2007, sborník – Textile pro zdravotnictví: funkčnost a životnost – klíče k trhu, str.41-55, ISBN978-80-7372-263-0

[64]. Filová, E., Rampichová, M., Kostakova, E., Lukas, D., Varga, F., Lytvynets, A., Amler, E.: Gelatine scaffolds support cartilaginous matrix formation. XXX.Dny lékařské biofyziky, 30.5.-1.6.2007, Jindřichův Hradec, Sborník abstraktů str.18

[65]. Rampichová, M., Filová, E., Martinová, L., Kostakova, E., Lukas, D., Lytvynets A., Amler, E.,: Nanovlákna z pHEMA a PVA/CHitosanu jako scaffoldy pro artificiální chrupavku, Vědecká conference 2.lékařksé fakulty UK, 25.-26.4.2007

[66]. Jakubová R., Rampichová M. , Filová E., Košťáková E., Brezovianová D., Míčková A., Prosecká E., Plencner M., Lukáš D., Amler E. : Polykaprolakton ako vhodný materiál pre kultiváciu mezenchymálnych kmeňových buniek a chondrocytov, XXXI. Dny lékařské biofyziky (28.-30.5. Malá Morávka, Česka republika)

[67]. Grégr, J, Košťáková, E., Chotěbor, M., Pokorný, P.: Uhlíková vlákna - uhlíkové nanotrubice, POLYMER COMPOSITES 2010, sborník přednášek z mezinárodní konference, poř. Západočeská univerzita v Plzni, 27.-28.4.2010, edit. B. Foller, J. Orlt, str. 100-104, ISBN 978-80-7043-872-5

1.5 Realizované technické dílo, patenty

[68]. Užitný vzor. Číslo dokumentu: 19818 – Dutá nanovlákna obohacená liposomy. Úřad průmyslového vlastnictví. Zapsáno: 7. 7. 2009; Datum zveřejnění zápisu: 15.07.2009; Přihlášeno: 17. 4. 2009., Přihlašovatel:Student Science, s.r.o., Nanopharma a.s., Ústav experimentální medicíny AV ČR, v.v.i., Technická univerzita v Liberci, Původce: Amler, E. - Míčková, A. - Jakubová, R. - Plencner, M. - Prosecká, E. - Filová, E. - Rampichová, M. - Pokorný, I. - Lukáš, D. - Košťáková, E. - Pokorný P.

[69]. Užitný vzor. Číslo dokumentu: 20291 – Kolagen/fibrinová síť s nanovlákny z polykaprolaktonu. Úřad průmyslového vlastnictví. Zapsáno: 30.11.2009; Přihlášeno: 17.4.2009., Přihlašovatel: Student Science, s.r.o., Nanopharma a.s., Ústav experimentální medicíny AV ČR, v.v.i., Technická univerzita v Liberci., Původce: Amler, E. - Míčková, A. - Jakubová, R. - Plencner, M. - Prosecká, E. - Filová, E. - Rampichová, M. - Pokorný, I.- Lukáš, D.- Martinová, L.- Košťáková, E.- Pokorný P

[70]. Užitný vzor. Číslo dokumentu: 20292 – Síťka z polykaprolaktonu nebo z polyglykolové kyseliny nebo ze směsi kyseliny polymléčné a polyglykolové s nanovlákny. Úřad průmyslového vlastnictví. Zapsáno: 30.11.2009; Přihlášeno: 17.4.2009., Přihlašovatel: Student Science, s.r.o., Nanopharma a.s., Ústav experimentální medicíny AV ČR, v.v.i., Technická univerzita v Liberci., Původce: Amler, E. - Míčková, A. - Jakubová, R. - Plencner, M. - Prosecká, E. - Filová, E. - Rampichová, M. - Pokorný, I. - Lukáš, D. - Martinová, L. - Košťáková, E. - Pokorný P.

[71]. Užitný vzor. Číslo dokumentu: 20293 –Nanovlákenná síťka s nanovlákny s dotovanými liposomy.Úřad průmyslového vlastnictví. Zapsáno: 30.11.2009; Přihlášeno: 17.4.2009. Přihlašovatel: Student Science, s.r.o., Nanopharma a.s., Ústav experimentální medicíny AV ČR, v.v.i., Technická univerzita v Liberci., Původce: Amler, E. - Míčková, A. - Jakubová, R.- Plencner, M -Prosecká, E.- Filová, E. - Rampichová, M.- Pokorný, I.- Lukáš, D. - Martinová, L.- Košťáková, E.- Pokorný P

[72]. Užitný vzor. Číslo dokumentu: 20346 – Síťka obohacená nanovlákny z polykaprolaktonu nebo ze směsi kyseliny polymléčné a polyglykolové či polyvinylchloridu s adherovanými liposomy. Úřad průmyslového vlastnictví. Zapsáno: 9.12.2009; Přihlášeno: 17.4.2009., Přihlašovatel: Student Science, s.r.o., Nanopharma a.s., Ústav experimentální medicíny AV ČR, v.v.i., Technická univerzita v Liberci., Původce: Amler, E. - Míčková, A. - Jakubová, R. - Plencner,

M. - Prosecká, E. - Filová, E. - Rampichová, M. - Pokorný, I. - Lukáš, D. - Martinová, L. - Košťáková, E. - Pokorný P.

[73]. Užitný vzor. číslo přihlášky: 2007-19250 Pokorný, P., Košťáková, E., Lukáš, D.: Zařízení pro výrobu nanovláken elektrostatickým zvlákňováním, číslo zápisu: 18094, , datum zápisu: 11.12.2007, majitel: Technická univerzita v Liberci

1.6 Monografie a skripta

[74]. Lukas D. Kostakova E. and Sakar A.: "Computer simulation of moisture transport in fibrous materials", Thermal and moisture transport in fibrous materials, edited by N. Pan, P. Gibson, Woodhead Publishing Limited, Cambridge, pp. 469-541. ISBN-13: 978-1-84569-057-1.

[75]. Lukáš, D., Vodseďálková, K., Chaloupek, J., Mikeš, P., Komárek, M., Košťáková, E., Raab, M., Sarkar, A.: Fyzika Polymerů, skripta TUL, Liberec 2008, ISBN 978-80-7372-312-5

[76]. Lukáš, D., Martinová, L., Amler, E., Čapek, L, Košťáková, E., Novák, O., Vodseďálková, K.: Lékařské textilie, Technická univerzita v Liberci, tiskárna VŠP, Liberec 2009, ISBN 978-80-7372-475-7 (Kostakova E.: Scaffoldy pro tkáňové inženýrství chrupavky, kapitola 6, str.129-158)

1.7 Reakce na publikace v databázi Web of Knowledge

V tomto odstavci je uveden přehled článků, které citovaly práce Evy Košťákové zařazené do databáze Web of Knowledge ke dni 31.10.2012.

Record 1 of 51
Title: Matrix Crosslinking Forces Tumor Progression by Enhancing Integrin Signaling **Author(s):** Levental, KR (Levental, Kandice R.); Yu, HM (Yu, Hongmei); Kass, L (Kass, Laura); Lakins, JN (Lakins, Johnathon N.); Egeblad, M (Egeblad, Mikala); Erler, JT (Erler, Janine T.); Fong, SFT (Fong, Sheri F. T.); Csiszar, K (Csiszar, Katalin); Giaccia, A (Giaccia, Amato); Weninger, W (Weninger, Wolfgang); Yamauchi, M (Yamauchi, Mitsuo); Gasser, DL (Gasser, David L.); Weaver, VM (Weaver, Valerie M.)
Source: CELL **Volume:** 139 **Issue:** 5 **Pages:** 891-906 **DOI:** 10.1016/j.cell.2009.10.027 **Published:** NOV 25 2009 **Accession Number:** WOS:000272169400014 **ISSN:** 0092-8674

Record 2 of 51
Title: Electrospinning of collagen/biopolymers for regenerative medicine and cardiovascular tissue engineering **Author(s):** Sell, SA (Sell, Scott A.); McClure, MJ (McClure, Michael J.); Garg, K (Garg, Koyal); Wolfe, PS (Wolfe, Patricia S.); Bowlin, GL (Bowlin, Gary L.)**Source:** ADVANCED DRUG DELIVERY REVIEWS **Volume:** 61 **Issue:** 12 **Pages:** 1007-1019 **DOI:** 10.1016/j.addr.2009.07.012 **Published:** OCT 5 2009 **Accession Number:** WOS:000271395700003 **ISSN:** 0169-409X

Record 3 of 51
Title: Nanotechnology for nanomedicine and delivery of drugs **Author(s):** Venugopal, J (Venugopal, J.); Prabhakaran, MP (Prabhakaran, Molamma P.); Low, S (Low, Sharon); Choon, AT (Choon, Aw Tar); Zhang, YZ (Zhang, Y. Z.); Deepika, G Deepika, G.); Ramakrishna, S (Ramakrishna, S.)**Source:** CURRENT PHARMACEUTICAL DESIGN **Volume:** 14 **Issue:** 22 **Pages:** 2184-2200 **DOI:** 10.2174/138161208785740180 **Published:** AUG 2008 **Accession Number:** WOS:000259448000006 **ISSN:** 1381-6128

Record 4 of 51
Title: Higher-Order Assembly of Collagen Peptides into Nano- and Microscale Materials **Author(s):** Przybyla, DE (Przybyla, David E.); Chmielewski, J (Chmielewski, Jean)**Source:** BIOCHEMISTRY **Volume:** 49 **Issue:** 21 **Pages:** 4411-4419 **DOI:** 10.1021/bi902129p **Published:** JUN 1 2010 **Accession Number:** WOS:000277912100001 **ISSN:** 0006-2960

Record 5 of 51
Title: Cartilage and Bone Extracellular Matrix **Author(s):** Gentili, C (Gentili, Chiara); Cancedda, R (Cancedda, Ranieri) **Source:** CURRENT PHARMACEUTICAL DESIGN **Volume:** 15 **Issue:** 12 **Pages:** 1334-1348 **Published:** APR 2009 **Accession Number:** WOS:000265789700006 **ISSN:** 1381-6128

Record 6 of 51
Title: Production of Bioactive, Post-Translationally Modified, Heterotrimeric, Human Recombinant Type-I Collagen in Transgenic Tobacco **Author(s):** Stein, H (Stein, Hanan); Wilensky, M (Wilensky, Michal); Tsafrir, Y (Tsafrir, Yehuda); Rosenthal, M (Rosenthal, Michal); Amir, R (Amir, Rachel); Avraham, T (Avraham, Tal); Ofir, K (Ofir, Keren); Dgany, O (Dgany, Or); Yayon, A (Yayon, Avner); Shoseyov, O (Shoseyov, Oded)**Source:** BIOMACROMOLECULES **Volume:** 10 **Issue:** 9 **Pages:** 2640-2645 **DOI:** 10.1021/bm900571b **Published:** SEP 2009 **Accession Number:** WOS:000269671200032 **ISSN:** 1525-7797

Record 7 of 51
Title: Electrospun water soluble polymer mat for ultrafast release of Donepezil HCl **Author(s):** Nagy, ZK (Nagy, Zs. K.); Nyul, K (Nyul, K.); Wagner, I (Wagner, I.); Molnar, K (Molnar, K.); Marosi, G (Marosi, Gy.)**Source:** EXPRESS POLYMER LETTERS **Volume:** 4 **Issue:** 12 **Pages:** 763-772 **DOI:** 10.3144/expresspolymlett.2010.92 **Published:** DEC 2010 **Accession Number:** WOS:000284150400004 **ISSN:** 1788-618X

Record 8 of 51
Title: Biochemical and biomechanical gradients for directed bone marrow stromal cell differentiation toward tendon and bone **Author(s):** Sharma, RI (Sharma, Ram I.); Snedeker, JG (Snedeker, Jess G.)**Source:** BIOMATERIALS **Volume:** 31 **Issue:** 30 **Pages:** 7695-7704 **DOI:** 10.1016/j.biomaterials.2010.06.046 **Published:** OCT 2010 **Accession Number:** WOS:000281498600011 **ISSN:** 0142-9612

Record 9 of 51
Title: An In Vitro Assessment of a Cell-Containing Collagenous Extracellular Matrix-like Scaffold for Bone Tissue Engineering **Author(s):** Pedraza, CE (Pedraza, Claudio E.); Marelli, B (Marelli, Benedetto); Chicatun, F (Chicatun, Florencia); McKee, MD (McKee, Marc D.); Nazhat, SN (Nazhat, Showan N.)**Source:** TISSUE ENGINEERING PART A **Volume:** 16 **Issue:** 3 **Pages:** 781-793 **DOI:** 10.1089/ten.tea.2009.0351 **Published:** MAR 2010 **Accession Number:** WOS:000275041500003 **ISSN:** 1937-3341

Record 10 of 51
Title: Technological advances in electrospinning of nanofibers **Author(s):** Teo, WE (Teo, Wee-Eong); Inai, R (Inai, Ryuji); Ramakrishna, S (Ramakrishna, Seeram)**Source:** SCIENCE AND TECHNOLOGY OF ADVANCED MATERIALS **Volume:** 12 **Issue:** 1 **Article Number:** 013002 **DOI:** 10.1088/1468-6996/12/1/013002 **Published:** FEB 2011 **Accession Number:** WOS:000287449000002 **ISSN:** 1468-6996

Record 11 of 51
Title: Autologous chondrocyte implantation in the knee using fibrin
Author(s): Kim, MK (Kim, Myung Ku); Choi, SW (Choi, Sung Wook); Kim, SR (Kim, Sang Rim); Oh, IS (Oh, In Suk); Won, MH (Won, Man Hee)**Source:** KNEE SURGERY SPORTS TRAUMATOLOGY ARTHROSCOPY **Volume:** 18 **Issue:** 4 **Pages:** 528-534 **DOI:** 10.1007/s00167-009-0905-y **Published:** APR 2010 **Accession Number:** WOS:000275657900014 **ISSN:** 0942-2056

Record 12 of 51
Title: In situ force mapping of mammary gland transformation **Author(s):** Lopez, JI (Lopez, Jose I.); Kang, I (Kang, Inkyung); You, WK (You, Weon-Kyoo); McDonald, DM (McDonald, Donald M.); Weaver, VM (Weaver, Valerie M.)**Source:** INTEGRATIVE BIOLOGY **Volume:** 3 **Issue:** 9 **Pages:** 910-921 **DOI:** 10.1039/c1ib00043h **Published:** 2011 **Accession Number:** WOS:000294448600004 **ISSN:** 1757-9694

Record 13 of 51
Title: Fibrin/Hyaluronic Acid Composite Hydrogels as Appropriate Scaffolds for In Vivo Artificial Cartilage Implantation **Author(s):** Rampichova, M (Rampichova, Michala); Filova, E (Filova, Eva); Varga, F (Varga, Ferdinand); Lytvynets, A (Lytvynets, Andriy); Prosecka, E (Prosecka, Eva); Kolacna, L (Kolacna, Lucie); Motlik, J (Motlik, Jan); Necas, A (Necas, Alois); Vajner, L (Vajner, Ludek); Uhlik, J (Uhlik, Jiri); Amler, E (Amler, Evzen)**Source:** ASAIO JOURNAL **Volume:** 56 **Issue:** 6 **Pages:** 563-568 **DOI:** 10.1097/MAT.0b013e3181fcbe24 **Published:** NOV-DEC 2010 **Accession Number:** WOS:000283719600014 **ISSN:** 1058-2916

Record 14 of 51
Title: Intratumoral Drug Delivery with Nanoparticulate Carriers **Author(s):** Holback, H (Holback, Hillary); Yeo, Y (Yeo, Yoon) **Source:** PHARMACEUTICAL RESEARCH **Volume:** 28 **Issue:** 8 **Pages:** 1819-1830 **DOI:** 10.1007/s11095-010-0360-y **Published:** AUG 2011 **Accession Number:** WOS:000292518800003 **ISSN:** 0724-8741

Record 15 of 51
Title: Regeneration of full-thickness abdominal wall defects in rats using collagen scaffolds loaded with collagen-binding basic fibroblast growth factor **Author(s):** Shi, CY (Shi, Chunying); Chen, W (Chen, Wei); Zhao, YN (Zhao, Yannan); Chen, B (Chen, Bing); Xiao, ZF (Xiao, Zhifeng); Wei, ZL (Wei, Zhenliang); Hou, XL (Hou, Xianglin); Tang, J (Tang, Jinglong); Wang, ZX (Wang, Zhaoxu); Dai, JW (Dai, Jianwu)**Source:** BIOMATERIALS **Volume:** 32 **Issue:** 3 **Pages:** 753-759 **DOI:** 10.1016/j.biomaterials.2010.09.038 **Published:** JAN 2011 **Accession Number:** WOS:000285322600010 **ISSN:** 0142-9612

Record 16 of 51
Title: Use of Allogenic Stem Cells for the Prevention of Bone Bridge Formation in Miniature Pigs **Author(s):** Planka, L (Planka, L.); Necas, A (Necas, A.); Srnec, R (Srnec, R.); Rauser, P (Rauser, P.); Stary, D (Stary, D.); Jancar, J (Jancar, J.); Amler, E (Amler, E.); Filova, E (Filova, E.); Hlucilova, J (Hlucilova, J.); Kren, L (Kren, L.); Gal, P (Gal, P.)**Source:** PHYSIOLOGICAL RESEARCH **Volume:** 58 **Issue:** 6 **Pages:** 885-893 **Published:** 2009 **Accession Number:** WOS:000273296600013 **ISSN:** 0862-8408

Record 17 of 51
Title: Tissue Engineering for Damaged Surface and Lining Epithelia: Stem Cells, Current Clinical Applications, and Available Engineered Tissues **Author(s):** Guerra, L (Guerra, Liliana); Dellambra, E (Dellambra, Elena); Panacchia, L (Panacchia, Laura); Paionni, E (Paionni, Emanuel)**Source:** TISSUE ENGINEERING PART B-REVIEWS **Volume:** 15 **Issue:** 2 **Pages:** 91-112 **DOI:** 10.1089/ten.teb.2008.0418 **Published:** JUN 2009 **Accession Number:** WOS:000266574000001 **ISSN:** 1937-3368

Record 18 of 51
Title: Capillary rise between cylinders **Author(s):** Liu, T (Liu, T.); Choi, KF (Choi, K. F.); Li, Y (Li, Y.)**Source:** JOURNAL OF PHYSICS D-APPLIED PHYSICS **Volume:** 40 **Issue:** 16 **Pages:** 5006-5012 **DOI:** 10.1088/0022-3727/40/16/038 **Published:** AUG 21 2007 **Accession Number:** WOS:000248783200039 ResearcherID Numbers:**ISSN:** 0022-3727

Record 19 of 51
Title: Electrospun nanofiber-based regeneration of cartilage enhanced by mesenchymal stem cells **Author(s):** Shafiee, A (Shafiee, Abbas); Soleimani, M (Soleimani, Masoud); Chamheidari, GA (Chamheidari, Gholamreza Abedi); Seyedjafari, E (Seyedjafari, Ehsan); Dodel, M (Dodel, Masumeh); Atashi, A (Atashi, Amir); Gheisari, Y (Gheisari, Yousof)**Source:** JOURNAL OF BIOMEDICAL MATERIALS RESEARCH PART A **Volume:** 99A **Issue:** 3 **Pages:** 467-478 **DOI:** 10.1002/jbm.a.33206 **Published:** DEC 2011 **Accession Number:** WOS:000296608900015 **ISSN:** 1549-3296

Record 20 of 51
Title: Electrospinning jets and nanofibrous structures **Author(s):** Garg, K (Garg, Koyal); Bowlin, GL (Bowlin, Gary L.) **Source:** BIOMICROFLUIDICS **Volume:** 5 **Issue:** 1 **Article Number:** 013403 **DOI:** 10.1063/1.3567097 **Published:** MAR 2011 **Accession Number:** WOS:000289148400006 **ISSN:** 1932-1058

Record 21 of 51
Title: Nano-approaches in cartilage repair **Author(s):** Giannoni, P (Giannoni, Paolo); Narcisi, R (Narcisi, Roberto) **Source:** JOURNAL OF APPLIED BIOMATERIALS & BIOMECHANICS **Volume:** 7 **Issue:** 1 **Pages:** 1-12 **Published:** JAN-APR 2009 **Accession Number:** WOS:000269103400001 **ISSN:** 1722-6899

Record 22 of 51
Title: Comparison of electrospun and extruded soluplus (R)-based solid dosage forms of improved dissolution **Author(s):** Nagy, ZK (Nagy, Zsombor K.); Balogh, A (Balogh, Attila); Vajna, B (Vajna, Balazs); Farkas, A (Farkas, Attila); Patyi, G (Patyi, Gergo); Kramarics, A (Kramarics, Aron); Marosi, G (Marosi, Gyoergy)**Source:** JOURNAL OF PHARMACEUTICAL SCIENCES **Volume:** 101 **Issue:** 1 **Pages:** 322-332 **DOI:** 10.1002/jps.22731 **Published:** JAN 2012 **Accession Number:** WOS:000298018000031 **ISSN:** 0022-3549

Record 23 of 51
Title: Current strategies for osteochondral regeneration: from stem cells to pre-clinical approaches **Author(s):** Rodrigues, MT (Rodrigues, Marcia T.); Gomes, ME (Gomes, Manuela E.); Reis, RL (Reis, Rui L.)**Source:** CURRENT OPINION IN BIOTECHNOLOGY **Volume:** 22 **Issue:** 5 **Pages:** 726-733 **DOI:** 10.1016/j.copbio.2011.04.006 **Published:** OCT 2011 **Accession Number:** WOS:000296114600018 **ISSN:** 0958-1669

Record 24 of 51
Title: Comparison of the Resistance to Bending Forces of the 4.5 LCP Plate-rod Construct and of 4.5 LCP Alone Applied to Segmental Femoral Defects in Miniature Pigs **Author(s):** Urbanova, L (Urbanova, Lucie); Srnec, R (Srnec, Robert); Proks, P (Proks, Pavel); Stehlik, L (Stehlik, Ladislav); Florian, Z (Florian, Zdenek); Navrat, T (Navrat, Tomas); Necas, A (Necas, Alois) **Source:** ACTA VETERINARIA BRNO **Volume:** 79 **Issue:** 4 **Pages:** 613-U118 **DOI:** 10.2754/avb201079040613 **Published:** DEC 2010 **Accession Number:** WOS:000287418300014 **ISSN:** 0001-7213

Record 25 of 51
Title: Breakdown of cell-collagen networks through collagen remodeling **Author(s):** Iordan, A (Iordan, Andreea); Duperray, A (Duperray, Alain); Gerard, A (Gerard, Anais); Grichine, A (Grichine, Alexei); Verdier, C (Verdier, Claude)**Source:** BIORHEOLOGY **Volume:** 47 **Issue:** 5-6 **Pages:** 277-295 **DOI:** 10.3233/BIR-2010-0575 **Published:** 2010 **Accession Number:** WOS:000288321700002 **ISSN:** 0006-355X

Record 26 of 51
Title: Free surface electrospinning from a wire electrode **Author(s):** Forward, KM (Forward, Keith M.); Rutledge, GC (Rutledge, Gregory C.)**Source:** CHEMICAL ENGINEERING JOURNAL **Volume:** 183 **Pages:** 492-503 **DOI:** 10.1016/j.cej.2011.12.045 **Published:** FEB 15 2012 **Accession Number:** WOS:000301274100059 **ISSN:** 1385-8947

Record 27 of 51
Title: Design Parameters for a Robust Superhydrophobic Electrospun Nonwoven Mat **Author(s):** Rawal, A (Rawal, Amit)

Source: LANGMUIR **Volume:** 28 **Issue:** 6 **Pages:** 3285-3289 **DOI:** 10.1021/la204535s **Published:** FEB 14 2012 **Accession Number:** WOS:000300138500029 **ISSN:** 0743-7463

Record 28 of 51
Title: A Myocardial Patch Made of Collagen Membranes Loaded with Collagen-Binding Human Vascular Endothelial Growth Factor Accelerates Healing of the Injured Rabbit Heart **Author(s):** Gao, J (Gao, Jian); Liu, JZ (Liu, Jianzhou); Gao, Y (Gao, Yuan); Wang, C (Wang, Chao); Zhao, YN (Zhao, Yannan); Chen, B (Chen, Bing); Xiao, ZF (Xiao, Zhifeng); Miao, Q (Miao, Qi); Dai, JW (Dai, Jianwu)**Source:** TISSUE ENGINEERING PART A **Volume:** 17 **Issue:** 21-22 **Pages:** 2739-2747 **DOI:** 10.1089/ten.tea.2011.0105 **Published:** NOV 2011 **Accession Number:** WOS:000296619500015 **ISSN:** 1937-3341

Record 29 of 51
Title: Immobilization of thrombocytes on PCL nanofibres enhances chondrocyte proliferation in vitro **Author(s):** Jakubova, R (Jakubova, R.); Mickova, A (Mickova, A.); Buzgo, M (Buzgo, M.); Rampichova, M (Rampichova, M.); Prosecka, E (Prosecka, E.); Tvrdik, D (Tvrdik, D.); Amler, E (Amler, E.)**Source:** CELL PROLIFERATION **Volume:** 44 **Issue:** 2 **Pages:** 183-191 **DOI:** 10.1111/j.1365-2184.2011.00737.x **Published:** APR 2011 **Accession Number:** WOS:000288455000009 **ISSN:** 0960-7722

Record 30 of 51
Title: Imbibition and Evaporation of Water Droplets on Paper and Solid Substrates **Author(s):** Oko, A (Oko, A.); Swerin, A (Swerin, A.); Claesson, PM (Claesson, P. M.)**Source:** JOURNAL OF IMAGING SCIENCE AND TECHNOLOGY **Volume:** 55 **Issue:** 1 **Article Number:** 010201 **DOI:** 10.2352/J.ImagingSci.Technol.2011.55.1.010201 **Published:** JAN-FEB 2011 **Accession Number:** WOS:000287563500002 **ISSN:** 1062-3701

Record 31 of 51
Title: Mathematical Modelling of Crack Fractography after Implant Failure of Titanium 4.5 LCP Used for Flexible Bridging Osteosynthesis in a Miniature Pig **Author(s):** Necas, A (Necas, Alois); Urbanova, L (Urbanova, Lucie); Furst, T (Fuerst, Tomas); Zencak, P (Zencak, Pavel); Tucek, P (Tucek, Pavel)**Source:** ACTA VETERINARIA BRNO **Volume:** 79 **Issue:** 4 **Pages:** 621-U127 **DOI:** 10.2754/avb201079040621 **Published:** DEC 2010 **Accession Number:** WOS:000287418300015 **ISSN:** 0001-7213

Record 32 of 51
Title: Targeting the Tumor Proteasome as a Mechanism to Control the Synthesis and Bioactivity of Matrix Macromolecules **Author(s):** Skandalis, SS (Skandalis, S. S.); Aletras, AJ (Aletras, A. J.); Gialeli, C (Gialeli, C.); Theocharis, AD (Theocharis, A. D.); Afratis, N (Afratis, N.); Tzanakakis, GN (Tzanakakis, G. N.); Karamanos, NK (Karamanos, N. K.)**Source:** CURRENT MOLECULAR MEDICINE **Volume:** 12 **Issue:** 8 **Pages:** 1068-1082 **Published:** SEP 2012 **Accession Number:** WOS:000307950000015 **ISSN:** 1566-5240

Record 33 of 51
Title: The cartilage matrix molecule components produced by human foetal cartilage rudiment cells within scaffolds and the role of exogenous growth factors **Author(s):** Chuang, CY (Chuang, Christine Y.); Shahin, K (Shahin, Kifah); Lord, MS (Lord, Megan S.); Melrose, J (Melrose, James); Doran, PM (Doran, Pauline M.); Whitelock, JM (Whitelock, John M.)**Source:** BIOMATERIALS **Volume:** 33 **Issue:** 16 **Pages:** 4078-4088 **DOI:** 10.1016/j.biomaterials.2012.02.032 **Published:** JUN 2012 **Accession Number:** WOS:000303096300007 **ISSN:** 0142-9612

Record 34 of 51
Title: Preparation and Characterization of New Nano-Composite Scaffolds Loaded With Vascular Stents **Author(s):** Xu, HZ (Xu, Hongzhen); Su, JS (Su, Jiansheng); Sun, J (Sun, Jun); Ren, TB (Ren, Tianbin)**Source:** INTERNATIONAL JOURNAL OF MOLECULAR SCIENCES **Volume:** 13 **Issue:** 3 **Pages:** 3366-3381 **DOI:** 10.3390/ijms13033366 **Published:** MAR 2012 **Accession Number:** WOS:000302174500048 **ISSN:** 1661-6596

Record 35 of 51
Title: Paracrine Interactions between Mesenchymal Stem Cells Affect Substrate Driven Differentiation toward Tendon and Bone Phenotypes **Author(s):** Sharma, RI (Sharma, Ram I.); Snedeker, JG (Snedeker, Jess G.)**Source:** PLOS ONE **Volume:** 7 **Issue:** 2 **Article Number:** e31504 **DOI:** 10.1371/journal.pone.0031504 **Published:** FEB 15 2012 **Accession Number:** WOS:000302741300073 **ISSN:** 1932-6203

Record 36 of 51
Title: Can liquid supercooling and glassy-like structure be invoked to interpret collective cell behaviour in the human body? **Author(s):** Knapp-Mohammady, M (Knapp-Mohammady, Michaela); March, NH (March, Norman H.)**Source:** PHYSICS AND CHEMISTRY OF LIQUIDS **Volume:** 50 **Issue:** 2 **Pages:** 137-151 **DOI:** 10.1080/00319104.2011.609959 **Published:** 2012 **Accession Number:** WOS:000304271100001 **ISSN:** 0031-9104

Record 37 of 51

Title: Fiber Generators in Needleless Electrospinning **Author(s):** Niu, HT (Niu, Haitao); Lin, T (Lin, Tong) **Source:** JOURNAL OF NANOMATERIALS **Article Number:** 725950 **DOI:** 10.1155/2012/725950 **Published:** 2012 **Accession Number:** WOS:000305025800001 **ISSN:** 1687-4110

Record 38 of 51
Title: Nanotechnology and mesenchymal stem cells with chondrocytes in prevention of partial growth plate arrest in pigs **Author(s):** Planka, L (Planka, Ladislav); Srnec, R (Srnec, Robert); Rauser, P (Rauser, Petr); Stary, D (Stary, David); Filova, E (Filova, Eva); Jancar, J (Jancar, Josef); Juhasova, J (Juhasova, Jana); Kren, L (Kren, Leos); Necas, A (Necas, Alois); Gal, P (Gal, Petr)**Source:** BIOMEDICAL PAPERS-OLOMOUC **Volume:** 156 **Issue:** 2 **Pages:** 128-134 **DOI:** 0.5507/bp.2012.041 **Published:** 2012 **Accession Number:** WOS:000306401700007 **ISSN:** 1213-8118

Record 39 of 51
Title: Ordered Collagen Membranes: Production and Characterization **Author(s):** Ruderman, G (Ruderman, G.); Mogilner, IG (Mogilner, I. G.); Tolosa, EJ (Tolosa, E. J.); Massa, N (Massa, N.); Garavaglia, M (Garavaglia, M.); Grigera, JR (Grigera, J. R.)
Source: JOURNAL OF BIOMATERIALS SCIENCE-POLYMER EDITION **Volume:** 23 **Issue:** 6 **Pages:** 823-832 **DOI:** 10.1163/092050611X560942 **Published:** 2012 **Accession Number:** WOS:000300651300006 **ISSN:** 0920-5063

Record 40 of 51
Title: A high frequency ultrasound aided study of kinetics of drug delivery in tumor models **Author(s):** Torosean, S (Torosean, Sason); Flynn, B (Flynn, Brendan); Samkoe, KS (Samkoe, Kimberley S.); Gunn, J (Gunn, Jason); Axelsson, J (Axelsson, Johan); Doyle, M (Doyle, Marvin); Pogue, BW (Pogue, Brian W.)**Editor(s):** Bosch JG; Doyley MM **Source:** MEDICAL IMAGING 2012: ULTRASONIC IMAGING, TOMOGRAPHY, AND THERAPY **Book Series:** Proceedings of SPIE **Volume:** 8320 **Article Number:** 83200Y **DOI:** 10.1117/12.911954 **Published:** 2012 **Accession Number:** WOS:000304871800033 **Conference Title:** Conference on Medical Imaging - Ultrasonic Imaging, Tomography, and Therapy **Conference Date:** FEB 05-06, 2012 **Conference Location:** San Diego, CA **Conference Sponsors:** SPIE, Agilent Technol, Diamond SA, DQE Instruments, Inc, eMagin, Isuzu Glass Co Ltd, Medtron, Inc, Ocean Thin Films, Inc**ISSN:** 0277-786X
ISBN: 978-0-8194-8969-2

Record 41 of 51
Title: Treatment of a Bone Bridge by Transplantation of Mesenchymal Stem Cells and Chondrocytes in a Composite Scaffold in Pigs. Experimental Study **Author(s):** Planka, L (Planka, L.); Necas, A (Necas, A.); Crha, M (Crha, M.); Proks, P (Proks, P.); Vojtova, L (Vojtova, L.); Gal, P (Gal, P.)**Source:** ACTA CHIRURGIAE ORTHOPAEDICAE ET TRAUMATOLOGIAE CECHOSLOVACA **Volume:** 78 **Issue:** 6 **Pages:** 528-536 **Published:** DEC 2011 **Accession Number:** WOS:000298771400007
Vojtova, Lucy **ISSN:** 0001-5415

Record 42 of 51
Title: ELECTROSPUN NANOFIBERS FOR TOPICAL DRUG DELIVERY **Author(s):** Wagner, I (Wagner, I.); Pataki, H (Pataki, H.); Balogh, A (Balogh, A.); Nagy, ZK (Nagy, Zs. K.); Harasztos, AH (Harasztos, A. H.); Suhajda, A (Suhajda, A.); Marosi, G (Marosi, Gy.)**Source:** EUROPEAN JOURNAL OF PHARMACEUTICAL SCIENCES **Volume:** 44 **Pages:** 148-149 **Supplement:** 1 **Published:** SEP 24 2011 **Accession Number:** WOS:000295543600133 **Conference Title:** 4th BBBB-Bled International Conference on Pharmaceutical Sciences - New Trends in Drug Discovery, Delivery Systems and Laboratory Diagnostics **Conference Date:** SEP 29-OCT 01, 2011 **Conference Location:** Bled, SLOVENIA **ISSN:** 0928-0987

Record 43 of 51
Title: Bioengineered vascular grafts: improving vascular tissue engineering through scaffold design **Author(s):** McClure, MJ (McClure, M. J.); Wolfe, PS (Wolfe, P. S.); Rodriguez, IA (Rodriguez, I. A.); Bowlin, GL (Bowlin, G. L.)**Source:** JOURNAL OF DRUG DELIVERY SCIENCE AND TECHNOLOGY **Volume:** 21 **Issue:** 3 **Pages:** 211-227 **Published:** MAY-JUN 2011 **Accession Number:** WOS:000292120600001 **ISSN:** 1773-2247

Record 44 of 51
Title: FULLERENE C60 AND ITS DERIVATIVES AS NANOCOMPOSITES IN POLYMER NANOFIBRES **Author(s):** Kostakova, E (Kostakova, Eva); Zemanova, E (Zemanova, Eva); Klouda, K (Klouda, Karel)**Book Group Author(s):** TANGER Ltd **Source:** NANOCON 2011 **Pages:** 470-474 **Published:** 2011 **Accession Number:** WOS:000306686700075 **Conference Title:** 3rd International Conference on NANOCON **Conference Date:** SEP 21-23, 2011 **Conference Location:** Brno, CZECH REPUBLIC **Conference Sponsors:** Tanger, Reg Ctr Adv Technol & Mat, CSNMT **ISBN:** 978-80-87294-27-7

Record 45 of 51
Title: HISTOCHEMICAL AND IMMUNOHISTOCHEMICAL STUDIES ON THE TESTES OF THE BACTRIAN CAMEL (Camelus bactrianus) **Author(s):** Xu, ZH (Xu, Zhihao); Luo, YW (Luo, Yiwei); Yang, C (Yang, Chun); Wang, JL (Wang, JianLin) **Source:** JOURNAL OF CAMEL PRACTICE AND RESEARCH **Volume:** 17 **Issue:** 1 **Pages:** 117-122 **Published:** JUN 2010 **Accession Number:** WOS:000282861900026 **ISSN:** 0971-6777

Record 46 of 51
Title: Ties That Bind: Evaluation of Collagen I and alpha-Chitin **Author(s):** Omokanwaye, T (Omokanwaye, Tiffany); Wilson, O (Wilson, Otto, Jr.)**Editor(s):** Herold KE; Bentley WE; Vossoughi J**Source:** 26TH SOUTHERN BIOMEDICAL ENGINEERING CONFERENCE: SBEC 2010 **Book Series:** IFMBE Proceedings **Volume:** 32 **Pages:** 183-187 **Published:** 2010 **Accession Number:** WOS:000307744700047 **Conference Title:** 26th Southern Biomedical Engineering Conference, SBEC 2010 **Conference Date:** APR 30-MAY 02, 2010 **Conference Location:** College Park, MD **Conference Sponsors:** Natl Sci Fdn, Biomedical Engn Soc, Natl Canc Inst**Conference Host:** Univ Maryland
ISSN: 1680-0737 **ISBN:** 978-3-642-14997-9

Record 47 of 51
Title: Extraction and Characterization of a Soluble Chicken Bone Collagen **Author(s):** Omokanwaye, T (Omokanwaye, Tiffany); Wilson, O (Wilson, Otto, Jr.); Iravani, H (Iravani, Hoda); Kariyawasam, P (Kariyawasam, Pramodh) **Editor(s):** Herold KE; Bentley WE; Vossoughi J**Source:** 26TH SOUTHERN BIOMEDICAL ENGINEERING CONFERENCE: SBEC 2010 **Book Series:** IFMBE Proceedings **Volume:** 32 **Pages:** 520-523 **Published:** 2010 **Accession Number:** WOS:000307744700133 **Conference Title:** 26th Southern Biomedical Engineering Conference, SBEC 2010 **Conference Date:** APR 30-MAY 02, 2010 **Conference Location:** College Park, MD **Conference Sponsors:** Natl Sci Fdn, Biomedical Engn Soc, Natl Canc Inst**Conference Host:** Univ Maryland **ISSN:** 1680-0737 **ISBN:** 978-3-642-14997-9

Record 48 of 51
Title: Fiber Reinforced Electrospun-matrix Composites **Author(s):** Yang, RH (Yang, Rui-Hua); Gao, WD (Gao, Wei-Dong); Wang, HB (Wang, Hong-Bo)**Source:** INTERNATIONAL JOURNAL OF NONLINEAR SCIENCES AND NUMERICAL SIMULATION **Volume:** 11 **Pages:** 57-59 **Supplement:** S **Published:** 2010 **Accession Number:** WOS:000287558000012 **ISSN:** 1565-1339

Record 49 of 51
Title: Capillary rise between cylinders **Author(s):** Liu, T (Liu, T.); Choi, KF (Choi, K. F.)**Source:** SURFACE AND INTERFACE ANALYSIS **Volume:** 40 **Issue:** 3-4 **Pages:** 368-370 **DOI:** 10.1002/sia.2690 **Published:** MAR-APR 2008 **Accession Number:** WOS:000255486200055 **ISSN:** 0142-2421

Record 50 of 51
Title: International textile and clothing research register **Author(s):** [Anonymous] ([Anonymous]) **Source:** INTERNATIONAL JOURNAL OF CLOTHING SCIENCE AND TECHNOLOGY **Volume:** 20 **Issue:** 6 **Pages:** 6-116 **Published:** 2008 **Accession Number:** WOS:000262296800002 **ISSN:** 0955-6222

Record 51 of 51
Title: International textile clothing research register **Author(s):** [Anonymous] ([Anonymous]) **Source:** INTERNATIONAL JOURNAL OF CLOTHING SCIENCE AND TECHNOLOGY **Volume:** 19 **Issue:** 6 **Pages:** 8-14 **Published:** 2007 **Accession Number:** WOS:000251450000003 **ISSN:** 0955-6222

2. KOMENTÁŘ K PUBLIKACÍM

2.1 Úvod

První kapitola této habilitační práce představuje uveřejněné vědecké a odborné práce, jejichž je autorka hlavním autorem nebo spoluautorem. V příloze jsou potom uvedeny plné texty vybraných publikací uveřejněných zejména v recenzovaných impaktovaných časopisech vztahující se k problematice kompozitních a nanokompozitních materiálů. Publikované práce je možné rozdělit do tří témat:

a) Nanokompozitní materiály s integrovanými uhlíkovými nanočásticemi
b) Kompozitní a nanokompozitní materiály pro tkáňové inženýrství
c) Smáčení vlákenných materiálů a simulace založené na automodelech

První dvě témata týkající se kompozitních materiálů, jejich výroby a testování jsou blíženi uvedena v následující kapitole. Posledně jmenovaná oblast byla tématem disertační práce autorky, a proto nebude v tomto komentáři dále podrobněji popisována.

Nanokompozitní či kompozitní materiály s alespoň jednou vlákennou složkou jsou velmi širokým pojmem. Pod tímto označením si lze představit celou řadu materiálů. V práci budou představovány dvě varianty z této obsáhlé oblasti a to elektrostaticky zvlákněné nanovlákenné materiály s integrovanými uhlíkovými nanočásticemi (uhlíkovými nanotrubicemi a sférickými fullereny) a oblast materiálů jako scaffoldů pro tkáňové inženýrství, zejména kolenní chrupavky, které svou podstatou je také možné zařadit do oblasti kompozitních či nanokompozitních materiálů.

2.2 Nanokompozitní materiály s integrovanými uhlíkovými nanočásticemi

Elektrostatické zvlákňování jako metoda výroby nanovláken i nanovlákna samotná jako výsledky tohoto procesu jsou v posledních letech zkoumána a testována po celém světě. Technologie využívající elektrostatických sil k procesu samoorganizace polymerního roztoku či polymerní taveniny do podoby nanovlákenné vrstvy je obecně velmi známá. V poslední době se začíná prosazovat zejména tak zvaná bezjehlová podoba [77] výše zmíněné metody výroby, i když zařízení na průmyslovou výrobu nanovlákenných materiálů pomocí elektrostatického zvlákňování z volné hladiny bylo patentováno již dříve [78, 79].

Vedle elektrostaticky zvlákňovaných nanovlákenných materiálů jsou dalšími velmi rozšířenými nanovlákennými materiály uhlíkové nanotrubice (někdy označovány jako válcovité fullereny) [80]. Pro jejich výborné mechanické odolnosti, elektrické vodivosti a tepelné odolnosti jsou v současnosti využívány zejména k vyztužování kompozitních materiálů pro různé speciální účely. Spolu s uhlíkovými nanotrubicemi jsou v současnosti diskutovány a studovány další uhlíkové nanomateriály a to sférické fullereny, zejména pak nejstabilnější C60 složený ze šedesáti atomů uhlíku s různými chemickými modifikacemi. Spojením uhlíkových nanomateriálů a elektrostaticky zvlákněných nanovlákenných vrstev vznikají velmi zajímavé kompozitní materiály různých vlastností.

Samotná výroba uhlíkových nanomateriálů je velmi zajímavá a rozmanitá. Existuje mnoho přístupů a mnoho různých postupů s výrazně odlišnými výsledky zejména co se finálních vlastností vyrobených uhlíkových nanomateriálů týče. Výchozí metodou pro výrobu jak uhlíkových nanotrubic, tak sférických fullerenů je metoda elektrického oblouku. Sférické fullereny se dále vyrábí pomocí různých procesů spalování [81]. Uhlíkové nanotrubice se pak nejčastěji vyrábějí metodami využívajícími laser (tzv omývání laserem) nebo metodou katalytického tepelného rozkladu uhlovodíků (CVD - chemical vapor deposition) [80].

Metoda CVD je relativně velmi nenáročnou technologií a pomocí ní je možné vyrábět uhlíkové nanotrubice i v jednoduchých laboratorních podmínkách. Změnou nastavení celého procesu je pak možné vytvářet nejen uhlíkové nanotrubice ale i jiné strukturně velmi zajímavé uhlíkové nanomateriály. Pro tuto technologii je možné jako zdroj uhlíku používat nejen metan, etan, acetylen, etanol, LPG atd. ale lze využít i zemní plyn.

Vedle dostupného zdroje uhlíku je také možné využít netradiční substráty s integrovanými katalyzátory (nejčastěji částice přechodových kovů - Fe, Co, Ni) pro růst uhlíkových nanostruktur a to nerosty (například čediče), kovové plechy či dráty. Pro studie možnosti laboratorní CVD metody výroby uhlíkových nanotrubic na substrátech z nerostů byly po konzultaci s geology vytipovány podložky ze severočeských čedičů. Tyto materiály obsahují velmi jemné částice magnetitu Fe_3O_4 a olivínů $(Fe, Mg)_2SiO_4$, které se mohou stát katalyzátory pro rozklad uhlovodíků.

Syntéza uhlíkových nanočástic probíhala v horizontální trubkové peci s regulátorem teploty a přívodem inertního plynu (dusíku) a zdroje uhlovodíků pro výrobu uhlíkových nanočástic (zemního plynu). Substrát s katalyzátorem, na němž se uhlíkové nanostruktury syntetizují za optimální teploty nad *800°C* byl umístěn do středu pece na speciální křemenné lodičce. Jako plyn dodávající do reaktoru byl využit zemní plyn – obsahující především metan CH_4 (přibližně *98 mol%*) a dále pak malá množství etanu, propanu, iso-butanu, N-butanu, iso-pentanu, N-pentanu atd. Reakce byla odzkoušena v rozsahu teplot *830 – 1120°C*. Při nejvyšších teplotách nad *1100°C* docházelo k natavování podložek a tím k vymizení jejich katalytické aktivity. Podložky z běžných čedičových kamínků pocházely ze Smrčí u Železného Brodu, z Heřmanic u Frýdlantu, Kamenického Šenova a Šluknova. Kamínky byly nařezány diamantovým kotoučem na kousky ve tvaru hranolků cca *5 x 6 x 2 mm* a plochy vyleštěny leštícím kotoučem s hrubostí *500*. Výsledky experimentů byly posuzovány na základě snímků rastrovací elektronové mikroskopie (SEM Vega Tescan, FT, TUL). Byl proveden kontrolní rozbor složení povrchové vrstvy podložek pomocí metody EDS (EDS-SEM, Jeol, JED-2300 analysis station, FS, BME, Budapešť, Maďarsko). Bylo prokázáno, že částice obsahující železo jsou v povrchu horniny a jsou rovnoměrně rozptýleny v povrchu viz obr.1.

Při experimentech byly získány uhlíkové nanočástice různých tvarů a uspořádání (obr.2 a obr.3). Nejjemnější vláknité částice byly studovány Ramanovou spektroskopií (Horiba JOBIN Yvon – LabRam IR s mikroskopem Olympus BX41, FS, BME, Budapešť, Maďarsko) a prokázána existence vícevrstvých uhlíkových nanotrubic – MWNT. Principem této metody je měření laserem excitované energie. Výstupem je pak charakteristické spektrum, které u uhlíkových nanotrubic obsahuje typické dva píky [82]. Tak zvaný G-pík (okolo *1580 cm^{-1}*) je charakteristickým rysem grafitických vrstev. Druhý je pak tak zvaný D-pík (okolo *1350 cm^{-1}*) typický pro vadné

grafitické struktury (různé vady, ale zejména fullerenové konce, případně ohnutí konců trubic apod.).

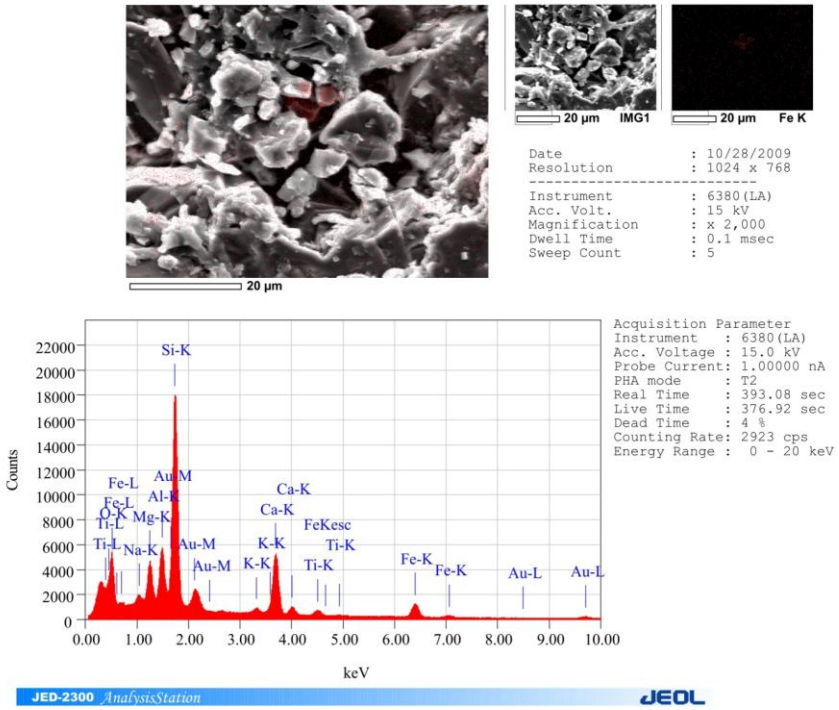

Obr 1. *SEM snímek a graf z analýzy EDS čediče z Heřmanic. Graf i snímek zobrazují přítomnost částic železa v povrchu vzorku. Zlato je ve vzorku nalezeno díky pozlacení vzorku pro dokonalejší zobrazení povrchu pomocí SEM.*

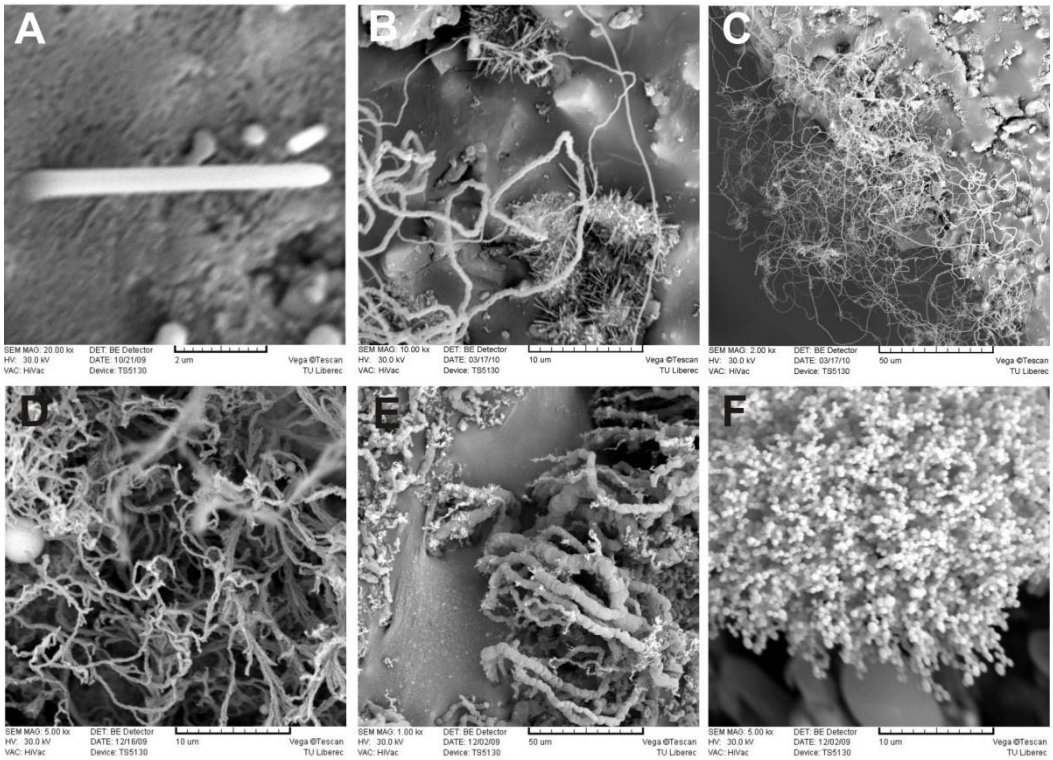

Obr. 2. *SEM snímky uhlíkových nanostruktur syntetizovaných na povrchu heřmanického čediče při různých teplotách: A – 850°C, uzavřené vícestěnné uhlíkové nanotrubice; B a C – 900°C, směs nanotrubic a jiných vláknitých nanostruktur; D – 1000°C, vláknité nanostruktury; E a F – 1120°C, kuličky a jiné uhlíkové struktury.*

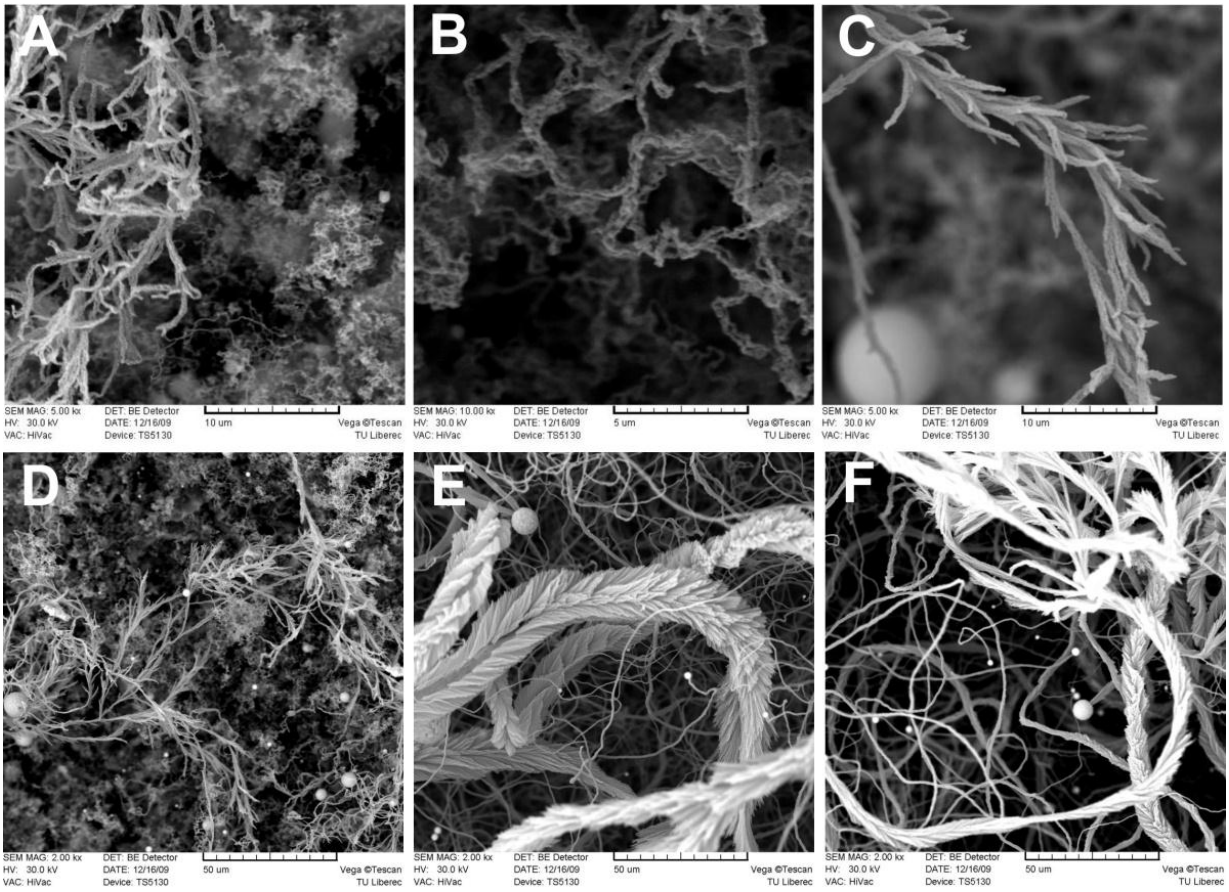

Obr. 3. *SEM snímky dalších uhlíkových nanostruktur syntetizovaných na površích ostatních čedičů pomocí CCVD metody (za podmínek 1000°C; průtok zemního plynu 40ml; doba působení 100min): A a B – substrát z čediče z Kamenického Šenova; C a D – substrát ze Smrčí; E a F – substrát ze Šluknova.*

Vedle nerostů byly použity jako substráty i kovové materiály - plechy a dráty. Postup syntézy uhlíkových nanotrubic na kovových substrátech je v literatuře nejčastěji popisován na oceli [83-86], ale i na kovových slitinách [87-89]. Společnost Kanthal (KNTL Ltd.) laskavě poskytla několik druhů materiálů obsahujících Fe, Co či Ni. Po analýze pomocí SEM-EDS metody byly vybrány Niktrotal 80 (79.15% Ni; 19.5% Cr; 1.35% Si) a Cuprothal 49 (44% Ni; 0.5% Fe; 45,3% Cu; 0,5% Mn, 0,3% Co). Laboratorní zařízení a studované podmínky výroby byly stejné jako při experimentech s nerosty jako substráty pro výrobu uhlíkových nanostruktur. Rastrovací elektronová mikroskopie ukázala různé morfologie vytvořených uhlíkových materiálů v závislosti na změnách parametrů výroby (rychlost toku zemního plynu, reakční teplota, reakční doba, různý substrát či různá úprava substrátu [59]). Byly nalezeny optimální podmínky pro výrobu uhlíkových nanotrubic na těchto kovových substrátech viz obr.4. Dle Ramanovy spektroskopie se jedná o vícestěnné uhlíkové nanotrubice. Vedle uhlíkových nanotrubic byly pozorovány i

různé další velmi zajímavé uhlíkové nanostruktury připomínající například propojené kuličky, stočené lístky nebo ojehlené větvičky.

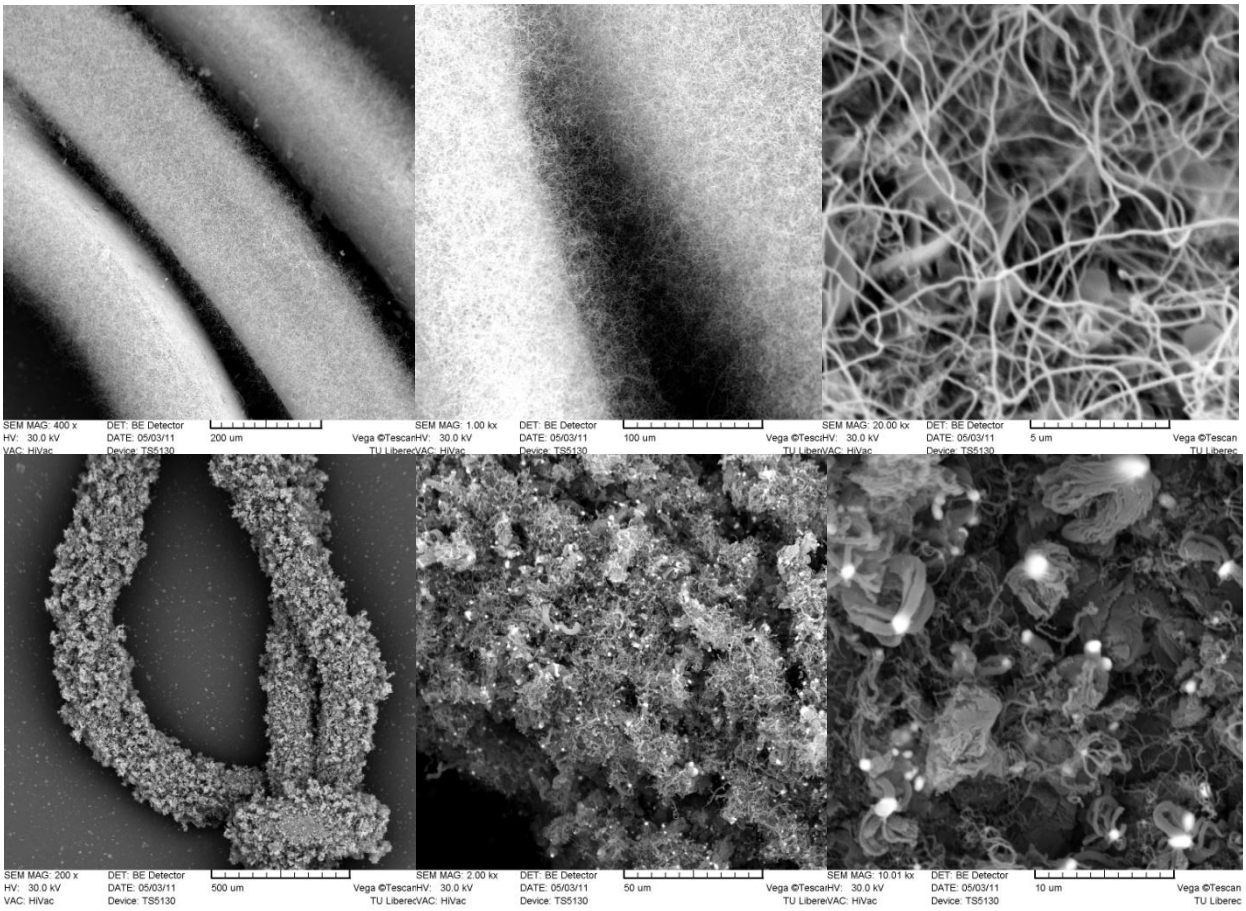

Obr.4: *Příklady výsledků laboratorní CVD syntézy s využitím zemního plynu jako zdroje uhlíku na substrátech z drátů. Nahoře Nikrothal, dole Cuprothal: reakční teplota 840°C, průtok zemního plynu 40ml/min, reakční doba 30 minut. Průměr uhlíkových nanotrubic na Nikrothalu byl 107±13 nm.*

Jak bylo ukázáno výše a v publikacích [10, 13, 54, 56, 58 a 59], výroba uhlíkových nanomateriálů nemusí být vždy podpořena nejmodernějšími technologickými prostředky. Pro výrobu uhlíkových nanomateriálů, a to i uhlíkových vícestěnných nanotrubic, je možné použít velmi jednoduché laboratorní zařízení, zemní plyn a dokonce i netradiční substráty s integrovanými katalyzátory a to čediče či kovové dráty. Takto tedy mohou vzniknout nejen samotné vícestěnné uhlíkové nanotrubice, ale i jiné uhlíkové nanomateriály. Ovšem i celek včetně kovové mřížky může být finální produkt využitelný jako speciální filtr odolávající vysokým teplotám, neboť bylo prokázáno [58, 59], že uhlíkové nanotrubice za určitých podmínek nerostou jen na povrchu drátů, ale přerůstají mezi nimi a vyplňují mezery velmi hustou odolnou sítí (viz obr.5).

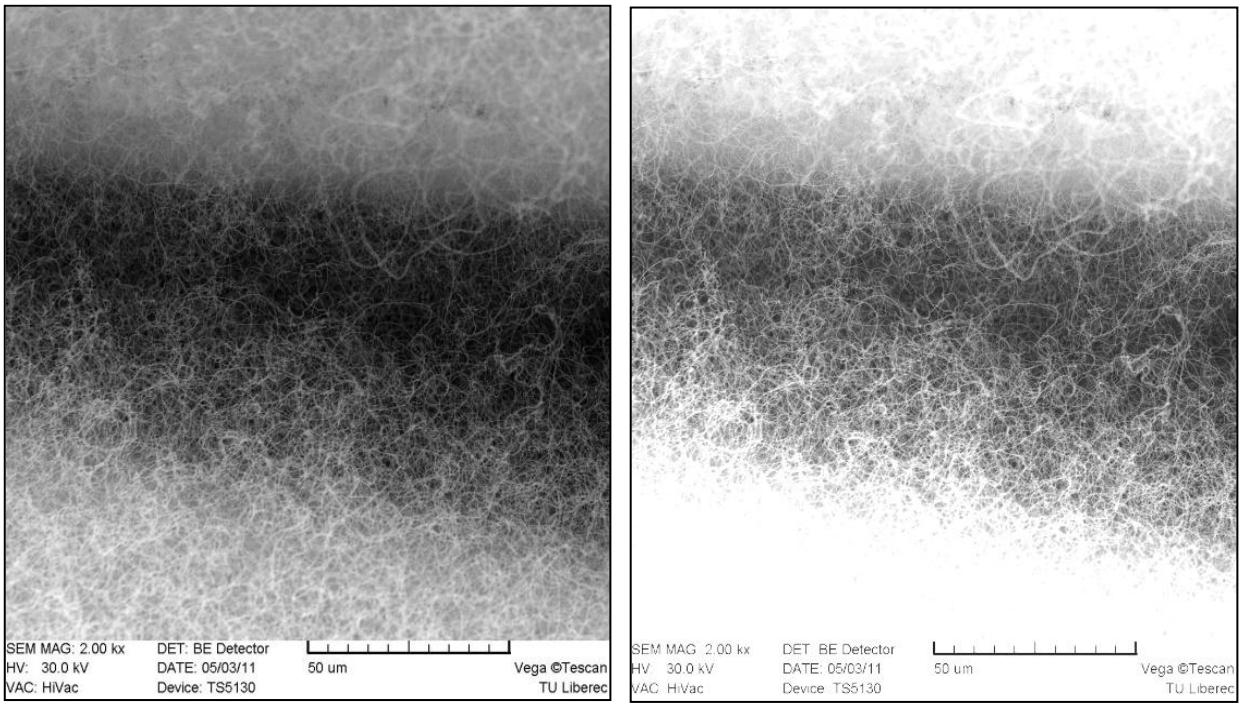

Obr.5: *Příklad přerůstání uhlíkových nanotrubic mezi dráty substrátu. Napravo je tentýž snímek s o 30% zvýšeným jasem a kontrastem pro zvýraznění struktury uhlíkových nanotrubic v mezeře mezi dráty.*

Vlastnosti vzniklých nanostruktur jsou jednoznačně závislé na použitém substrátu včetně jeho úprav [58, 59] a na výši použité teploty. Doba působení, jak se prokázalo, nemá významný vliv na strukturu vzniklých nanočástic (vyjma délky vzniklých materiálů).

Mimo výroby uhlíkových nanotrubic jako jednoho typu uhlíkových nanovláken, je možné vyrábět i uhlíková nanovlákna karbonizací elektrostaticky zvlákněných prekurzorů například nanovláken z polyvinylalkoholu či polyakrylonitrilu [30, 34, 41, 47]. Takto vyráběné materiály (bez napínání v průběhu karbonizace) ovšem nedosahují příliš dobrých mechanických vlastností a jejich využití se objevuje zejména ve filtraci či absorpci toxických materiálů nebo jako nosičů katalyzátorů.

Uhlíkové nanomateriály včetně uhlíkových nanotrubic či sférických fullerenů jsou velmi často součástí kompozitních materiálů. Zajišťují zejména zvýšení tepelné odolnosti, mechanické odolností, elektrickou vodivost a tak dále. Tyto uhlíkové nanomateriály (uhlíkové nanotrubice a sférické fullereny) mohou být součástí i elektrostaticky zvlákněných nanovlákenných vrstev a dodávat jim právě výše zmíněné zlepšení celkových vlastností. Doposud publikované studie se v této problematice věnují zejména jehlovému elektrostatickému nebo jinému

neprůmyslově využívanému procesu zvlákňování nanovláken s integrovanými uhlíkovými nanočásticemi [90-96].

Jak se ukázalo, zejména v průběhu zpracovávání publikací [5, 12, 57], je možné za určitých podmínek "vytáhnout" uhlíkové nanotrubice z polymerního roztoku (disperze) do vznikajících nanovláken při bezjehlovém zvlákňování z téměř volného povrchu kapaliny (polymerního roztoku - disperze), i když neexistuje žádná jistota, že se nanočástice (nanotrubice či fulleren) budou vyskytovat v povrchové vrstvě v průběhu elekrostatického zvlákňování. Zásadní pro bezjehlové zvlákňování takovýchto kompozitních nanovláken je příprava roztoku respektive postup přípravy roztoku a dispergace nanočástic v něm.

Pro studie [5] a [12] byl použit jako nosný polymer polyvinylalkohol, rozpouštědlo destilovaná voda či kombinace destilovaná voda a etanol (4:3), síťovadla pro následnou tepelnou stabilizaci nanovlákenných vrstev vůči působení vody (kyselina fosforečná a glyoxal) a uhlíkové nanotrubice několika typů (vícestěnné uhlíkové nanotrubice bez povrchových modifikací - MWNTs, vícestěnné uhlíkové nanotrubice s povrchovou modifikací hydroxydovou skupinou - MWNTs+OH, jednostěnné uhlíkové nanotrubice s povrchovou modifikací karboxylovou skupinou - SWNTs+COOH). Množství uhlíkových nanotrubic bylo ve všech případech 1hm% z hmotnosti sušiny polyvinylalkoholu v roztoku. Optimální postup přípravy roztoku je popsán dále. Uhlíkové nanotrubice byly nejprve vloženy do rozpouštědla. Následně byly rozdispergovány v rozpouštědle pomocí ultrazvuku. Dále byl přidán polymer a síťovadla. Takto připravená disperze byla míchána za normální teploty na magnetickém míchadle.

Volba různých povrchových modifikací uhlíkových nanotrubic (skupiny COOH a OH) i volba směsi voda/etanol jako rozpouštědla, měla ukázat možnosti vytváření dokonalejších disperzí. Povrchové modifikace karboxylovou i hydroxydovou skupinou umožňují lepší dispergaci uhlíkových nanotrubic v polárních rozpouštědlech, tedy i ve vodě. Etanol měl nejen lépe "přijímat" uhlíkové nanotrubice, ale měl zajistit i snazší elektrostatické zvlákňování výsledného roztoku, díky sníženému povrchovému napětí, oproti roztokům s pouze vodným rozpouštědlem.

Všechny roztoky, až na roztok se základními MWNTs, bylo možné zvláknit pomocí bezjehlového elektrostatického zvlákňování z válečku (Nanospider^{TM}) v dostatečné kvalitě i objemu. Výsledné vrstvy byly velmi homogenní bez většího množství defektů viz obr. 6. Je zřejmé, že vzorek s etanolem vykazuje vlákna

výrazně větších průměrů. To je zřejmě způsobeno nižší elektrickou vodivostí tohoto roztoku. Střední hodnota průměru vláken vyrobených elektrostatickým zvlákňováním je totiž ovlivňován i hodnotou elektrické vodivosti roztoků, jak je popsáno například v [97]. Snížení povrchového napětí, které ma jistě také vliv na výsledky tohoto procesu nebylo tak výrazné.

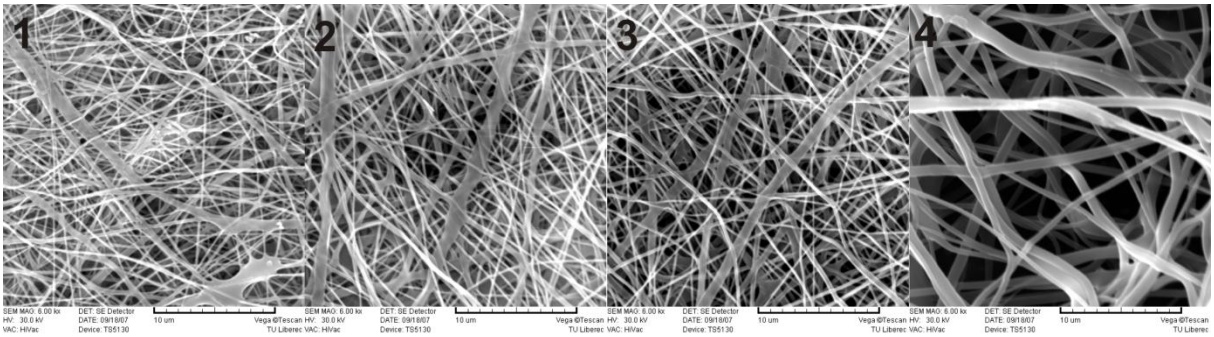

Obr.6: *Snímky z rastrovacího elektronového mikroskopu všech elektrostaticky zvlákněných materiálů: 1- slepý vzorek bez nanotrubic; 2- vzorek s SWNTs+COOH; 3- vzorek s MWNTs+OH; 4 - vzorek s MWNTs+OH s rozpouštědlem voda/etanol.*

Dalším podstatným krokem po výrobě kompozitních nanovláken je prokázání jejich finálního složení a ověření kompozitního složení. K tomu se nejčastěji využívají transmisní elektronové mikroskopy [90, 93, 94] a Ramanova spektroskopie [90, 95]. Potvrzení přítomnosti uhlíkových nanotrubic v elektrostaticky zvlákněných materiálech v popisované studii bylo provedeno pomocí Ramanovy spektroskopie. Uhlíkové nanotrubice se vykazují dvěma charakteristickými píky, jak bylo zmíněno výše. Porovnání spektra uhlíkových nanotrubic, slepého vzorku nanovláken z polyvinylalkoholu a kompozitních nanovláken přineslo jasné důkazy o přítomnosti uhlíkových nanotrubic ve vytvořených nanovlákenných materiálech (viz obr.7). Několikrát opakovaná měření na různých místech vzorků prokázala rovnoměrnost rozložení uhlíkových nanotrubic v objemu nanovláken u vzorků zvlákňovaných z vody. Naopak různost spekter získaných ze vzorků zvlákňovaných ze směsi voda/etanol prokázala [5] sice větší obsah nanotrubic, ale zřejmě spíše ve formě shluků, které mohly do vláken větších průměrů spíše přejít.

Dalším uhlíkovým nanomateriálem nabízejícím se svou současnou "popularitou" ke studiu jsou sférické fullereny. V současné době existuje jen velmi málo prací popisujících zakomponování sférických fullerenů do elektrostaticky zvlákněných nanovláken, například [98, 99]. Téměř vždy se jedná o nestabilnější formu sférických fullerenů tedy C60.

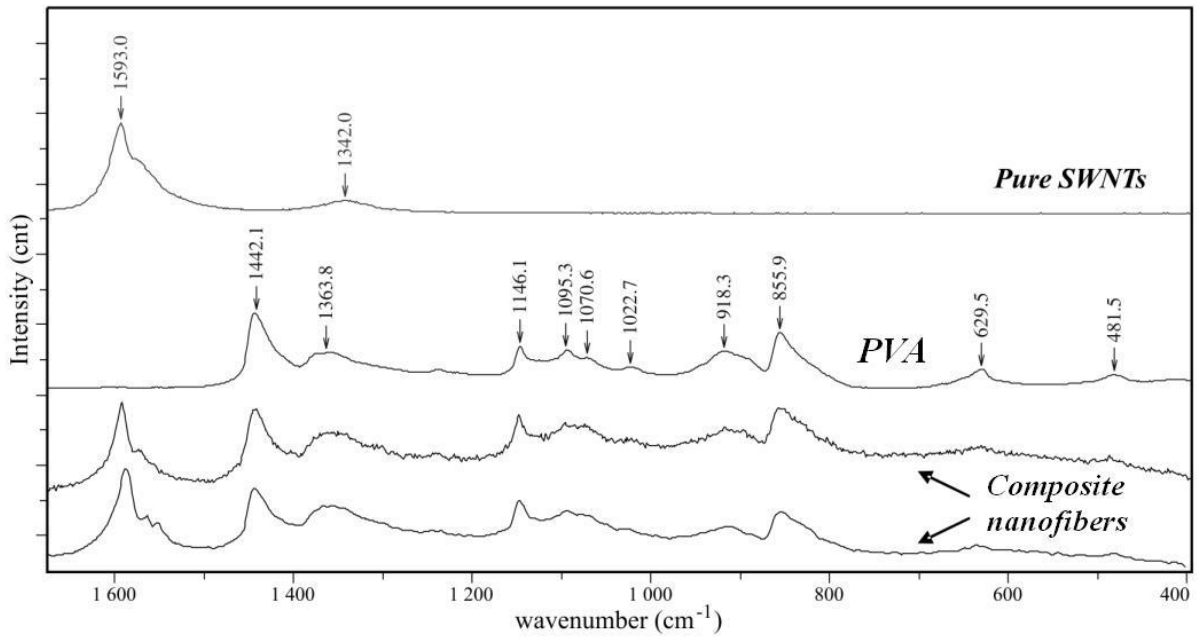

Obr.7: *Příklad porovnání Ramanových spekter pro uhlíkové nanotrubice (SWNTs+COOH), slepý vzorek elektrostaticky zvlákněných nanovláken polyvinylalkoholu po zesíťování a kompozitních zesíťovaných nanovláken.*

Experimenty popisované v [57] jsou věnovány přípravě a studiu elektrostaticky zvlákněných nanovlákenných materiálů s obsahem sférických fullerenů a jejich derivátů. Pro tyto experimenty byl opět zvolen jako základní polymer polyvinylalkohol a také polyuretan. Do těchto základních polymerů byly přidávány různé koncentrace sférických fullerenů C60 a to jak základních tak jejich derivátů (zejména oxiderivátu C60-OH). Různé typy fullerenů byly zvoleny s ohledem na jejich různé povrchové vlastnosti (energie). U C60 je známo, že se jedná o hydrofóbní strukturu, což se projevuje ve výrazné agregaci C60 ve vodě a neochotě vytvářet stabilní disperze s malými částicemi - shluky fullerenů [100]. V literatuře se hovoří o špatné "rozpustnosti" těchto nanočástice ve vodě. Ovšem je možné připravit různé deriváty fullerenu C60. Oxidací C60 je možné získat oxidační produkt tedy oxiderivát [101], jehož "rozpustnost" ve vodě a vodných roztocích je výrazně lepší než u prostého C60. Dochází k jednoznačnému zmenšování klastrů fullerenů a to díky hydrofilním skupinám OH na povrchu fullerenů. Je ovšem nutné zajistit optimální množství OH skupin na povrchu fullerenu. Nejlepším obsazením je 24 ± 2 OH skupin symetricky rozložených kolem koule C60 (tzv. fullerennol). Pokud je OH skupin méně "rozpustnost" ve vodě je horší. Pokud je skupin více, začnou převažovat přitažlivé interakce mezi OH skupinami a hydrofilita se již nezlepšuje. Naopak nastane opětná agregace, kdy se přitahují konce a uzavírají se do skupin. Celý systém se pak opět

jeví jako hydrofobní. Platí, že k hydrofilizaci musí být zachována symetrie molekuly, aby bylo množství OH stejné ve všech směrech.

Pro vytváření kompozitních nanovláken s integrovanými fullereny je opět zřejmé, že pro co nejlepší dispergaci fullerenů v roztoku polymeru je potřeba postupovat podobně jako u dispergace uhlíkových nanotrubic v polymerním roztoku. Fullereny mají tendenci k interakcím mezi sebou a tím k agregaci. Je možné pracovat s vodnými roztoky fullerenů přímo z jejich oxidace, která je prováděna přímo reakci s peroctovou kyselinou [101] nebo odpařit vodu a pracovat s práškovou podobou. Výhodou roztoku je téměř dokonalá dispergace avšak za cenu malé koncentrace fullerenů ve výsledném polymerním roztoku. Použití prášků přináší libovolné možnosti koncentrace, ale nutnost postupovat jako u uhlíkových nanotrubic, tedy vkládat fullereny do rozpouštědla, použít ultrazvuku a následně vmíchat polymer. Ve většině případů byly tedy experimenty prováděny s prášky C60 a C60-OH. Pro vodný roztok PVA byl použit oxiderivát fullerenů, který je k vodě afinní díky OH skupinám a pro roztok PUR v dimethylformamidu byl použit základní fulleren C60 bez povrchových úprav.

Vlastní elektrostatické zvlákňování bylo vždy testování na zařízení pro zvlákňování z tyčky a následně bylo dostatečné množství nanovláken o vysoké plošné hmotnosti vyrobeno pomocí bezjehlového elektrostatického zvlákňování z válečku (Nanospider^{TM}) viz obr 8 a 9.

Výsledné nanovlákenné materiály z PVA byly následně zesíťovány a všechny materiály byly podrobeny dalším analýzám (obrazová analýza, Ramanova spektroskopie a TGA-DTA analýza). Z výsledků měření průměrů vláken jak PUR tak PVA se ukazuje, že se zvyšujícím se procentem zastoupení fullerenů ve vzorku se velmi mírně zvyšuje průměr vláken. Neprokázal se výrazný vliv procenta zastoupení fullerenů ve vláknech na jejich střední hodnotu průměru (viz obr. 8 a 9).

Ramanova spektroskopie prokázala u všech vyrobených vzorků přítomnost fullerenů v nanovláknech, avšak prokázala také zejména u polyuretanových nanovláken nerovnoměrnost rozložení fullerenů ve vláknech (viz obr.10). Opakovaná měření na jednom vzorku v různých místech umožní porovnat jednotlivá spektra (průměr měřícího bodu je u použitého zařízení 1,2 μm jak je popsané v [5].

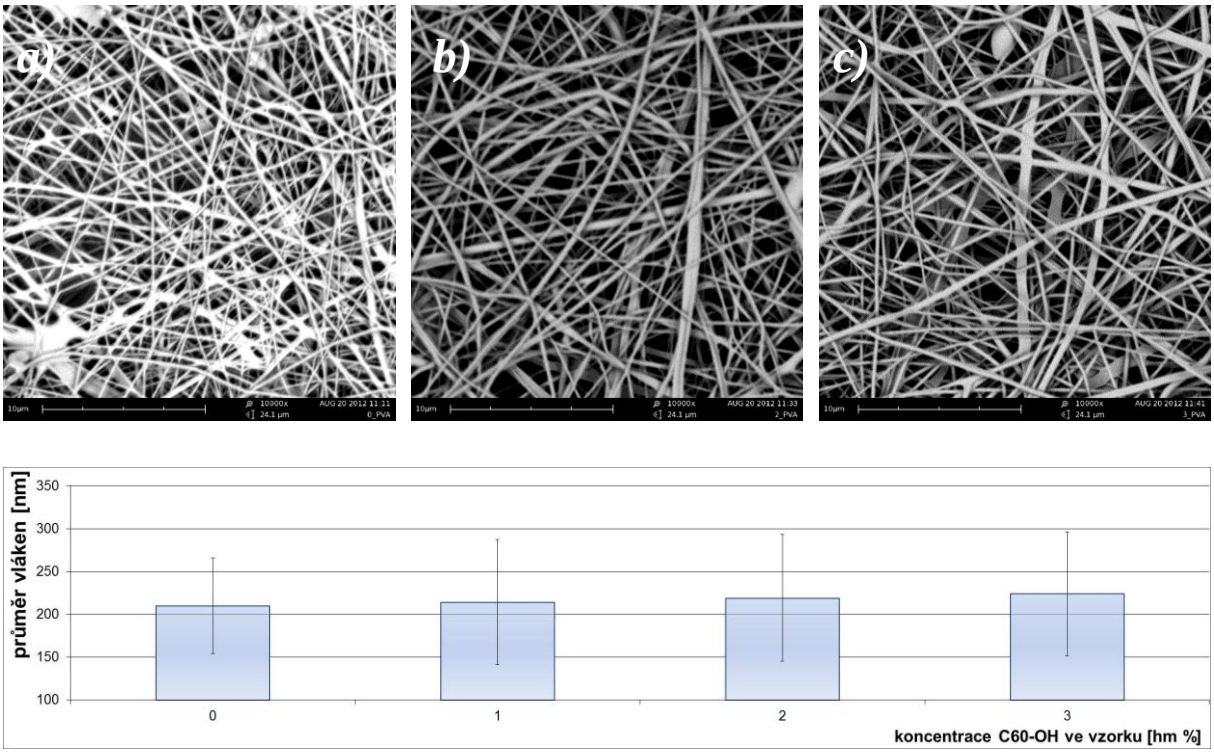

Obr.8: *SEM snímky slepého vzorku PVA (a), vzorku PVA s 2hm% (b) a s 3hm% (c) C60-OH a graf středních hodnot průměrů vláken.*

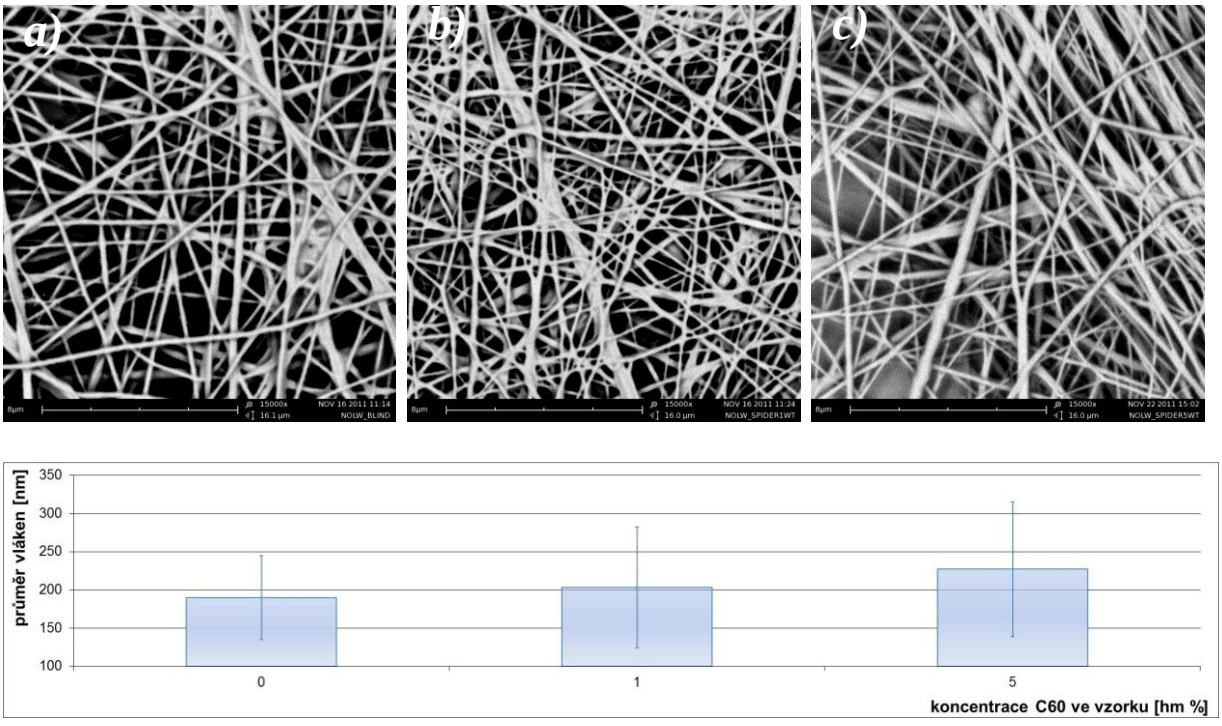

Obr.9: *SEM snímky slepého vzorku PUR (a), vzorku PUR s 1hm% (b) a s 5hm% (c) C60. Graf znázorňuje střední hodnoty průměrů vláken v příslušném vzorku.*

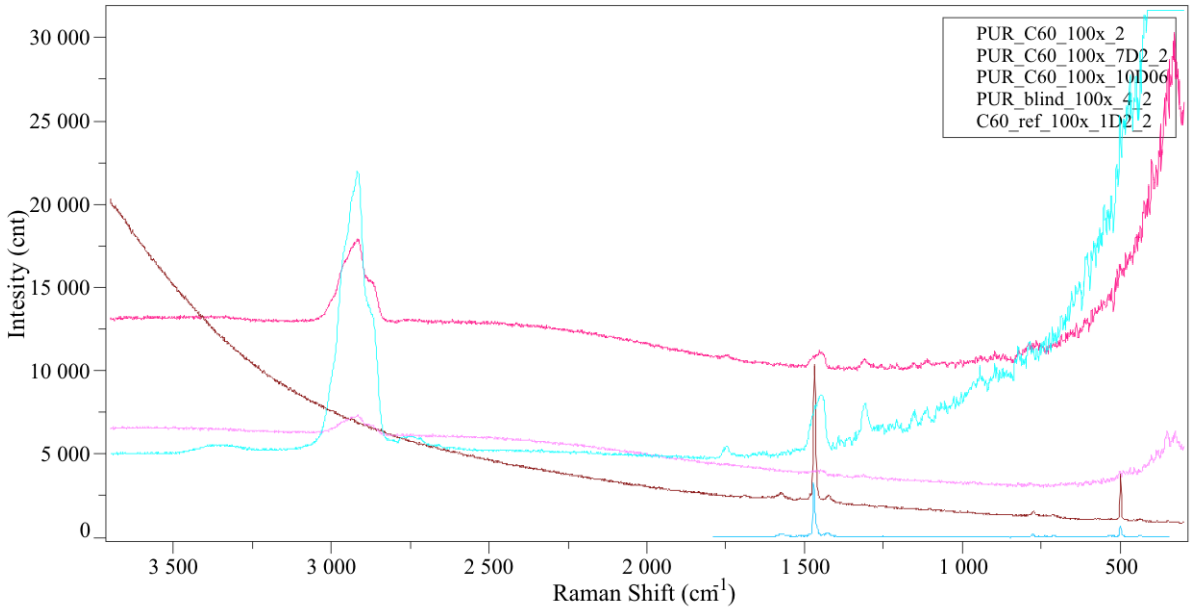

Obr.10: *Série spekter porovnávající slepý vzorek PUR nanovláken, samotné fullereny C60 a tři různá místa na kompozitním nanovlákenném materiálu PUR s přídavkem 1hm%C60.*

Sférické fullereny jsou popisovány jako dobré retardéry hoření, které mají za úkol zpomalit nebo přerušit proces hoření [102]. Proto bylo provedeno i testování tepelné odolnosti vyrobených kompozitních nanovláken s fullereny pomocí testů TGA a TG-DSC [57]. Principem těchto metod je měření úbytku hmotnosti a uvolněné spotřebované tepelné energie v závislosti na teplotě a čase. Plocha píků je přímo úměrná teplu uvolněnému nebo spotřebovanému při reakci a výška píků je přímo úměrná rychlosti reakce. Ze získaných výsledků jednoznačně vyplývá, že jak u PUR tak u PVA nanovláken přidání fullerenů vedlo ke zvýšení tepelné odolnosti. Výraznějších výsledků bylo dosaženo u nanovláken na bázi PVA. Z termické analýzy vyplývá, že přídavek fullerenů vždy zvyšuje teplotu počátku tepelného rozkladu, jak je ukázáno pro PVA i PUR v [57]. Dále je možné ukázat, že záleží i na množství fullerenů přidaných do základních polymerních nanovláken. Série vzorků s různým zastoupením fullerenů prokázala, že vyšší procento fullerenů znamená větší tepelnou odolnost, avšak nárůst není rovnoměrný. Jak je ukázáno na obr.11 u všech vzorků v sérii PVA, PVA+1hm%C60-OH, PVA+2hmC60-OH a PVA+3hm%C60-OH dochází k velmi výraznému exotermnímu ději. U vzorku PVA tento děj začíná při teplotě *220°C*, u vzorku PVA+1hm%C60-OH je to při teplotě *235°C*, u vzorků PVA+2hm%C60-OH a PVA+3hm%PVA-OH je to při teplotě nad *450°C*.

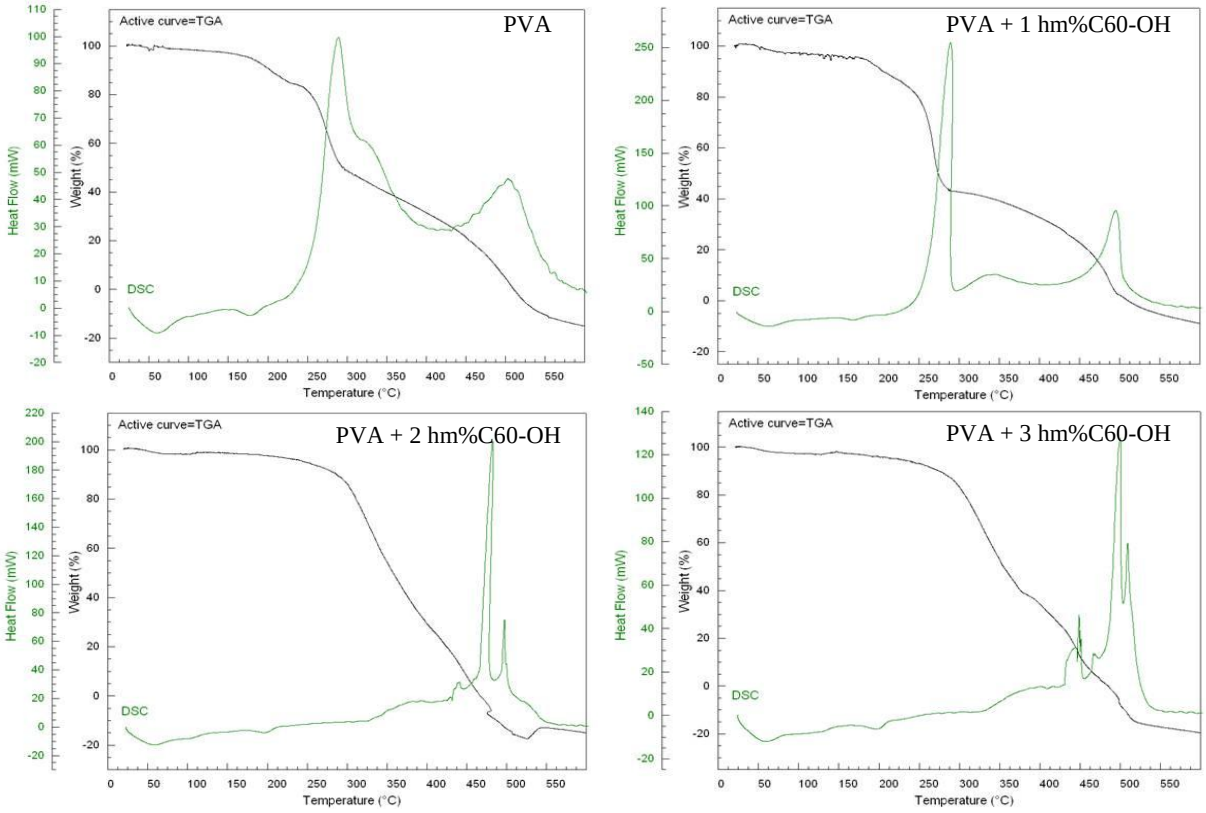

Obr.11: *Termická analýza slepého vzorku PVA nanovláken a série kompozitních elektrostaticky zvlákněných nanovlákenných materiálů s přídavkem oxiderivátu fullerenu.*

Z uvedených analýz tedy vyplývá, že inhibiční efekt fulerenu C60 a C60-OH byl jednoznačně zjištěn v průběhu thermo-oxidační degradace kompozitních nanovláken jak z PVA tak z PUR. Tento efekt se nerovnoměrně zvyšoval se vzrůstající koncentrací fullerenů uvnitř elektrostaticky zvlákněných nanovláken. Výsledné tepelné chování kompozitních nanovláken s fullereny bylo výrazně ovlivněno také přípravou roztoku, přítomností aditiv a tak dále jak je uvedeno v [57].

Uhlíkové nanočástice jsou samy o sobě velmi zajímavým materiálem nejen ze strukturního hlediska ale i ve svých dalších vlastnostech. Nicméně jejich spojení s elektrostaticky zvlákněnými nanovlákny přináší zcela nové materiály, které je možné dále zpracovávat s menšími zdravotními riziky než samotné uhlíkové nanočástice. Kontinuální výroba zejména bezjehlovým zvlákňováním ale vyžaduje důraz na přípravu roztoků hlavně na dokonalou dispergaci nanočástic v roztoku. Studium struktury i výsledných vlastností takových kompozitních materiálů vyžaduje pokročilá zařízení a netradiční postupy.

2.3 Kompozitní a nanokompozitní materiály jako scaffoldy pro tkáňové inženýrství

Kompozitní materiály zahrnující vlákenné či nanovlákenné struktury se významně uplatňují v celé řadě oblastí, a to i v medicíně. Jejich nezastupitelná role se v současné době ukazuje hlavně v oblasti tkáňového inženýrství, kde slouží jako nosiče buněk čili scaffoldy. Tkáňové inženýrství je jedinečným multidisciplinárním oborem, kde se potkávají nejen lékaři, zvěrolékaři, biochemici, biologové, fyzici atd., ale i strojní či textilní inženýři. Textilie jsou zde ceněny, hojně využívány zejména pro svou širokou variabilitu a flexibilitu. Nicméně pouze textilie jako samostatný materiál nemůže fungovat jako scaffold. Scaffoldy vyžadují kombinaci materiálů, aditiva, impregnace a tak dále, aby dosáhly zejména svými strukturními charakteristikami podobu ze strukturou nahrazované tkáně. Avšak vedle struktury je třeba hledat i mechanické, povrchové a degradační vlastnosti. Existuje celá řada specifických požadavků, které musí vhodný scaffold splňovat, aby mohl být použit pro konkrétní aplikaci. Obecně platí, že musí být biokompatibilní, biodegradabilní, netoxický a nekarcinogenní, musí mít vysokou porozitu a trojrozměrně propojené póry, musí mít specifický trojrozměrný tvar, musí mít optimální chemické a povrchové vlastnosti, musí mít určitou rychlost degradace a produkty degradace nesmí být toxické ani podporovat záněty, musí být sterilizovatelný, musí mít podobné mechanické vlastnosti jako rozvíjející se tkáň. Scaffold musí ulehčovat migraci, adhezi a proliferaci buněk.

V současné době se v oblasti tkáňového inženýrství pracuje intenzivně na možnostech výroby tkáňových náhrad pro léčbu degenerativních onemocnění chrupavky se zaměřením na uplatnění tradičních i moderních technologií. Chrupavky jsou velmi důležitou částí lidského těla a zároveň z hlediska tkáňového inženýrství relativně jednoduchou tkání, neboť neobsahují cévy ani nervy. Autorka se věnovala tématu výroby scaffoldů pro kolenní chrupavkové implantáty, které byly dále zpracovávány a testovány týmem profesora Evžena Amlera z Ústavu experimentální medicíny AV ČR a výsledky této spolupráce jsou popsány zejména v publikacích [2-4,6,8,9 a 76].

Zásadní otázkou je volba základního polymerního materiálu s ohledem na jeho vlastnosti a cenu. Prvotní volba je mezi přírodními a syntetickými polymerními materiály. Přírodní materiály, jako například kolagen, mají pro aplikaci v tkáňovém inženýrství zejména chrupavky velký potenciál [3]. Další podstatnou otázkou je volba

struktury scaffoldu - vlákenný materiál či pěna a následné úpravy. Téměř vždy je možné scaffold považovat za kompozitní materiál, neboť ve většině případů je složen z více složek, které jsou pro jeho správnou funkci nezbytné. Společně s týmem u ÚEM AVČR byly testovány materiály vyrobené autorkou jak z netkaných textilií vyráběných z různých biodegradabilních vláken klasických rozměrů pomocí technologie naplavování na laboratorním zařízení s využitím několika druhů základních biodegradabilních vláken a několika typů pojení [**2, 6**] (mechanické - vpichování, chemické - impregnace a pojivá vlákna rozpustěna po výrobě) tak elektrostaticky zvlákněné materiály [9]. Vedle vlákenných materiálů byly vyrobeny a testovány také pěnové scaffoldy vytvořené zejména technologií mechanického zpěňování a technologie salt leaching [8].

Vedle výše popsaných materiálů použitých pro podrobnější studie a publikovaných v odborných časopisech se dále autorka ve spolupráci s AV ČR věnovala a věnuje přípravě biodegradabilních pletenin impregnovaných gelem či pěnou, přípravě kompozitních pěn vyztužených krátkými úseky biodegradabilních vláken a nanovláken namletých pomocí kryogenního mlýnku, přípravě vpichovaných netkaných textilií z biodegradabilních vláken v kombinaci s nanovlákennou strukturou, integraci liposomů do "těla" nanovláken jako potenciálního nosiče léčiv, přípravě orientovaných délkových nanovlákenných útvarů pomocí elektrostatického zvlákňování na hladinu kapaliny, přípravě pěnových struktur pomocí technologie solvent casting a tak dále. Některé výsledky této spolupráce v publikacích [36-38, 44, 45, 49-51, 64-66] a užitných vzorech [68-72].

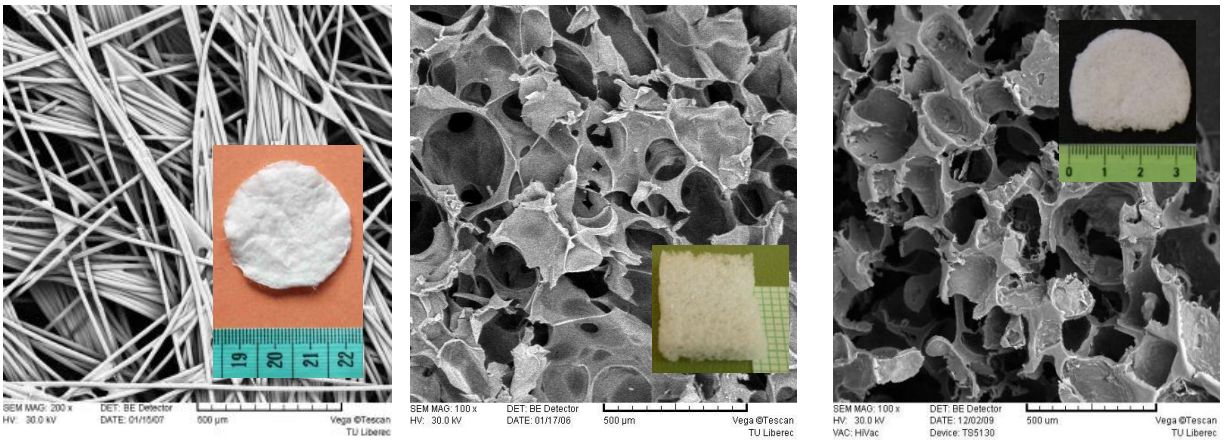

Obr.12: *SEM snímky a fotografie materiálů určených k testování jako scaffoldy pro tkáňové inženýrství kolenní chrupavky: netkaná textilie naplavovaná (vlevo), pěna vytvořená mechanickým zpěňováním (uprostřed), pěna vytvořená technologií salt-leaching (vpravo).*

2.4 Prohlášení

Ráda bych na tomto místě poděkovala všem spoluautorům prací, které jsem prezentovala jako součást této habilitační práce. Jmenovitě děkuji Ing. Janu Grégrovi (KCH, FP, TUL), Dr. Lászlo Mészárosovi a Dr. Kolosovi Molnárovi (Budapest University of Technology and Economics, Hungary), doc. Karlovi Kloudovi a Ing. Evě Zemanové (Státní úřad pro jadernou bezpečnost), Dr. Evě Filové a Dr. Michale Rampichové (ÚEM AVČR) a prof. Davidu Lukášovi vedoucímu KNT, FT, TUL. Čestně prohlašuji, že ve všech případech byl můj podíl na přípravě, realizaci a interpretaci výsledků větší nebo stejný jako ostatních spoluautorů nebo je můj podíl po domluvě s hlavním autorem článku uveden přímo u článku.

2.5 Použitá literatura

[77] Yarin, AL, Zussman, E. Polymer 2004;45:2977-80
[78] Jirsák O, et al. CZ Patent 2003-2414
[79] Jirsák O, et al. World Patent WO/2005/024101
[80] Bhushan B. Handbook of Nanotechnology, Springer 2004
[81] Tekehara, H., et al.: Experimental study of industrial scale Fullerene Production by Combustion Synthesis, Carbon, Vol. 43, Issue 2, pg.311-319, 2005
[82] Carbon Application Note 03: Carbon NanoTubes – What information does Raman bring?. New York: HORIBA Jobin Yvon Inc., 2006
[83] Baddour, C. E., Faysal, F.: A Simple thermal CVD Metod for carbon nanotube synthesis on stainless steel 304 without the adition of an external catalyst. Carbon,2008, vol. 47, s. 313–347.
[84] Gao, L., Z., Kiwi-Minsker, L. Renken, A.: Growth of carbon nanotubes and microfibers over stainless steel mesh by cracking of methane. Surface & Coatings Technology, 2008, vol. 202, no. 13, s. 3029–3042.
[85] Park, S., J., Lee, D. G.: Development of CNT–metal–filters by direct growth of carbon nanotubes.Current Applied Physics, 2006, vol. 681, s. e182–e186.
[86] Vander Wal, R., L., Hall, L., J.: Carbon nanotube synthesis upon stainless steel meshes. Carbon, 2003, vol. 41, no. 4, s. 659–672.
[87] Talapatra, S., Kar, S., Pal, S., K., et al. Direct growth of aligned carbon nanotubes on bulk metals: Nature Nanotech. 2006, vol. 1, no. 2, s. 112-116.
[88] Pal, S., K., Kar, S., Pastelka, S. et al. Importance of Cr2O3 layer for growth of carbon nanotubes on superalloys. Carbon, 2010, vol. 48, no. 3, s. 844–853.
[89] Gao, L., Peng, A., Wang, Z., Y., et al. Growth of aligned carbon nanotube arrays
on metallic substrate and its application to supercapacitors. Solid State Communications, 2008, vol. 146, no. 9–10, s. 380–383.
[90] Ko F, et al. Advance Materials 2003;15(14):1161-5
[91] Ge JJ, et al. J Am Chem Soc 2004;126:15754-61
[92] Ko FK, et al. Proc. 19th American society for composites annual technical conf USA 2004
[93] Kim GM, Michler GH, Pötschke P. Polymer 2005;46:7346-51
[94] Ye H, Lam H, Titchenal N, Gogotsi Y, Ko, F. Applied physics letters 2004;85:1775-7
[95] Kannan P, Eichhorn SJ, Young RJ. Nanotechnology 2007;18:235707
[96] Kamel S. eXPRESS Polymer Letters 2007;1:546-575
[97] Angammana, C., J., Jayaram, S., H.: Analysis of the Effect of Solution Conductivity on Electro-spinning Process and Fiber Morphology, Fellow IEEE,2008, E-ISBN : 978-1-4244-2279-1 ISSN: 0197-2618
[98] Jiang, G., Li, G.: Preparation, Characterization and Properties of Fullerene- Vinylpyrrolidone Copolymers, American Institute of Chemical Engineers, Biotechnology Progress, Vol. 28, No. 1, 2012

[99] Yang, P., Zhan, S., et al.: The fabrication fo PPV/C60 composite nanofibers with highly optoelectric response by optimization solvents and electrospinning technology, Materials Letters, vol.65, Issue 3, pg. 537-539, 2011
[100] Ma, X. et al: Fullerene C60: surface energy and interfacial interactions in aqueous systems, Langmuir, 2010;26(14);11886-93
[101] Beranová (Zemanová), E., Klouda, K.: C(60) Fullerene Derivative: Preparation of a Water-soluble Fullerene Derivative in Reaction with Peracetic Acid, Conference Proceedings Nanocon 2009, Ostrava, pg.139-148, 2009, ISBN: 978-80-87294-13-0
[102] Klouda, K., Cafourek, S.: Role fullerenu C60 při aerosolovém způsobu hašení, Požární ochrana 2009, str.1-20, 2009

3. SEZNAM PŘÍLOH

Příloha 1: článek [1]

Příloha 2: článek [2]

Příloha 3: článek [3]

Příloha 4: článek [4]

Příloha 5: článek [5]

Příloha 6: článek [6]

Příloha 7: článek [7]

Příloha 8: článek [8]

Příloha 9: článek [9]

Příloha 10: článek [10]

Příloha 11: článek [11]

Příloha 12: článek [12]

Příloha 13: článek [13]

Příloha 1

Lukáš D. Chaloupek J., Kostakova E., Pan N., Martinkova, I.: Morphological transitions of capillary rise in a bundle of two and three solid parallel cylinders, *Physica A*, **371** (2006), pp. 226-248, IF=1,373(11)

Available online at www.sciencedirect.com
ScienceDirect
Physica A 371 (2006) 226–248
PHYSICA A
www.elsevier.com/locate/physa

Morphological transitions of capillary rise in a bundle of two and three solid parallel cylinders

D. Lukáš[a,*], J. Chaloupek[a], E. Košťáková[a], N. Pan[b], I. Martinková[c]

[a]*Technical University of Liberec, Hálkova 6, Liberec 1, 461 17, Czech Republic*
[b]*Division of Textiles, Biological and Agricultural, Engineering Department, University of California, Davis, CA 95616, USA*
[c]*Internationales Hochschulinstitut, Zittau, Markt 23, 02763 Zittau, Germany*

Received 17 September 2005; received in revised form 3 April 2006
Available online 12 May 2006

Abstract

Morphological transitions here refer to the liquid-body instability of capillary rise as the spacing among cylinders changes and are studied in this paper with both theoretical analysis and experimental verifications for systems composed of two and three equidistant and parallel cylinders systems. The theory predicts cross-sectional shapes of the bounded liquid body in a bundle of cylinders, when gravity is neglected, as a function of the cylinder–cylinder separation, contact angle and the Harkinson/spreading parameter. All these morphological transitions in turn reveal the hysteresis mechanisms in the processes.

The problems dealt with cover the full spectrum of wetting behaviors, from complete wetting, to partial wetting and up to the super-hydrophobic surfaces, characterized by the corresponding contact angles and the Harkinson spreading parameters. Unlike the wetting over a flat solid surface, the wetting of bundles of cylinders exhibits much more complexities because of the geometrical curvatures and shapes involved. Various transitions and their criteria are described and derived, extensive parametric studies then followed, and the hysteresis during the transitions is analyzed. Some experimental verifications are provided at the end.

Keywords: Morphological transitions; Capillary liquid columns; Complete wetting and super-hydrophobic surface; Transition hysteresis

1. Introduction

In a series of papers published in 1960s, Princen considered the capillary rise between two vertical cylinders [1], and subsequently three-, four-, and multi-cylinder systems [2]. The last paper in the series [3] was devoted to the study of the equilibrium configurations of limited amounts of liquid in horizontal cylinder assemblies, where gravitational effects were neglected. All Princen's works were focused on partial wetting cases where the contact angles ranged within the interval $0^\circ < \theta < 180^\circ$, i.e. the Harkinson parameter, defined as $S = \gamma_{SV} - \gamma_{SL} - \gamma$, $0 > S > -2\gamma$, where γ is the liquid surface tension, and γ_{SV}, γ_{SL} are the solid–gas and solid–liquid surface tensions.

*Corresponding author.
E-mail address: david.lukas@tul.cz (D. Lukáš).

0378-4371/$ - see front matter
doi:10.1016/j.physa.2006.04.045

Princen stated in Ref. [3] that a liquid column between two horizontal cylinders can no longer maintain its circular cross-section as soon as the separation between the cylinders exceeds certain critical value; the liquid then acquires a body shape similar to that of an unduloid on a single cylinder. This abrupt change in the liquid-body shape is called a morphological transition. It was also found [3] that the liquid columns in bundles of more than two cylinders will undergo two successive morphological transitions, again depending on the cylinder–cylinder separation. If the spacing is small enough, the liquid bridges only between each pair of adjacent cylinders (forming multi-liquid columns), with the central channel left open. If the distance increases to a critical value, the liquid fills completely the open channel among the cylinders (turning into a single column). Further increasing of the distance reduces the liquid shape back to unduloid.

Such transitions to unduloids are often taken as a manifestation of the Rayleigh instability [4,5], a phenomenon commonly occurring in liquid and cylindrical solid systems. However, the Rayleigh instability is in fact the result, not the cause, of the morphology transitions, as shown for example in the experiments of both Princen's [3] and this present work. We thus believe that, when analyzing the initiation of morphological transitions between various types of long liquid columns, it is mistaken to take the Rayleigh instability into account. Rayleigh instability is mainly attributed to the tendency of a liquid body to form unduloids when spacing among cylinders is too big so the influence of the triplet solid–liquid–gas lines that maintain the integrity of the liquid is insufficient to prevent the unduloidal instability.

The above-described liquid morphology transition has become an interest in several recent studies. For instance, Lenz and Lipowsky have shown in Ref. [4] that liquid droplets on circular planar surfaces and liquid channels on striped domains exhibit several distinct morphologies and may undergo morphological transitions between different states (homogeneous pattern, heterogeneous patterns, and film states) depending on the volume of the liquid phase.

Gau et al. [6] have presented another study on the behaviors of liquid micro-channels on structured surfaces on a plate consisting of hydrophilic stripes periodically adhered on a hydrophobic substrate. The liquid channels formed in between the strips go through shape instability at certain amount of adsorbed liquid volume, from a homogeneous state with a spatially constant cross-section to a state with a single bulge.

Swain and Lipowsky have studied wetting phenomena for a slab geometry consisting of a wetting phase confined between two chemically patterned substrates in Ref. [7]. For a single pair of opposing stripes, the wetting phase either forms a bridge spanning from one surface to the other or breaks up into two separate channels. In the case of a plane substrate decorated with many stripes, a whole sequence of morphological transitions has appeared with the number of bridges decreasing as the surface separation between the stripes grows.

Capillary phenomena associated with the presence of a liquid in fibrous bundles are of great importance in a number of fields and products. More recently, fibrous structures have been chosen as scaffold in biology for organism cultivating. To prevent the liquid nutrient from detaching into isolated droplets, the spacing d or the ratio of the spacing d to fiber radius r, has to be maintained to a desirable level.

In the present study, we have extended Princen's approach in several dimensions. First of all we analytically studied the instances $0^\circ \leqslant \theta \leqslant 180^\circ$, or $0 \geqslant S \geqslant -2\gamma$, i.e. to include the cases at the boundaries. For instance, if $\theta = 0^\circ$ and $S = 0$, it is a transition to complete wetting while if $\theta = 180^\circ$ and $S = -2\gamma$, it is a transition to super-hydrophobicity. So we dealt with some wetting cases overlooked in his work, particularly the complete wetting and super-hydrophobic ones. Note that although both θ and $S = \gamma_{SV} - \gamma_{SL} - \gamma$ are used to describe the wetting behavior, the spreading parameter S covers more grounds. For example there are instances where $\theta = 0^\circ$ but $S > 0$, i.e. $\gamma_{SV} - \gamma_{SL} > \gamma$, also termed as complete wetting hereafter, which is common in such materials as iron in contact with mineral oils [8]. Likewise cases where $\theta = 180^\circ$ but $S < -2\gamma$ or $\gamma_{SL} - \gamma_{SV} > \gamma$ indicate a super-hydrophobic repulsive behavior which is explained in detail next.

Consider a complete wetting case so that $S > 0$, i.e. $\gamma_{SV} - \gamma_{SL} > \gamma$. Then image the vapor ($V$) and liquid ($L$) phases exchange the roles so that the vapor is treated as a liquid phase (L) and the liquid as vapor (V). Thus a new spreading parameter $S' = \gamma_{SL} - \gamma_{SV} - \gamma$ is defined (obviously γ is unchanged since $\gamma = \gamma_{LV} = \gamma_{VL}$). Since $S > 0$ or $\gamma_{SV} - \gamma_{SL} > \gamma$, replacing here in terms of S' will result in $S' < -2\gamma$. In other words, this is a reversed super-hydrophobic case where, instead of total spreading of a liquid over a solid in a gaseous environment, we obtain a super-hydrophobic repulsion between a gas bubble submerged into a liquid contacting a solid surface; this should be observable at least in space with absence of any gravity field.

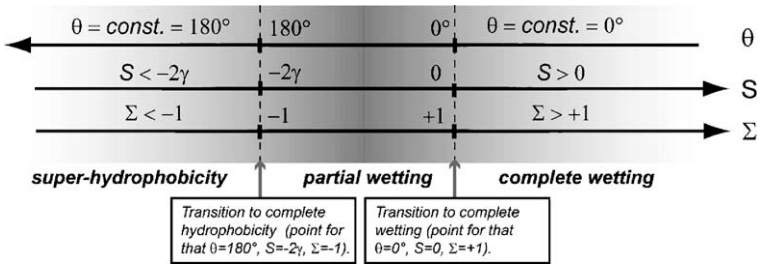

Fig. 1. Three wetting stages (super-hydrophobic, partial wetting, and complete wetting) are divided by two transition points (transition to super-hydrophobicity and transition to complete wetting).

A graphical illustration is depicted in Fig. 1 of the above-described three distinctive wetting cases, i.e., super-hydrophobic, partial wetting, and complete wetting, together with two thresholds between them. That is, a transition to super-hydrophobicity and a transition to complete wetting. These cases and transitions can be described using three parameters θ, S, and $\sum$ the last of which will be defined in Eq. (10) as $\Sigma = \left(S/\gamma + 1\right)$.

We carry out also in this work an analytical derivation of the cross-sectional shapes of the liquid columns between two- and three-cylinder bundles, which will provide us with the complete geometrical information on the relationships among the dimensionless cylinder–cylinder separation d/r, the contact angle θ or the spreading parameter S and another yet to be defined parameter angle α, so as to fully describe the liquid-column shapes.

The lengths of the liquid columns will not play any role in our analysis since the columns are long enough to neglect the effects at the column terminal fronts, where liquid body forms a complex meniscus shape. This is quite consistent with the cases dealt with by Princen in his works [1–3]. Carroll reported in Ref. [9], while studying small liquid drops adhering to a short cylindrical fiber, a different type of transition between axially symmetric and unsymmetric conformations of the droplets.

Next, we conduct a parametric study of the morphological transitions using analytical results obtained, aiming at the construction of morphology diagrams, and we also investigate the hysteresis occurring during the morphological transitions. Finally, we carry out some experimental work to yield results so as to substantiate our analytical predictions.

2. Theory

2.1. Liquid columns between two solid cylinders

Consider a mixture of limited amount of a liquid phase denoted as L with a vapor phase V. The liquid phase L is located within the gap between two narrowly spaced cylindrical solids S. (Our use of the same symbol S for denotation of both the spreading parameter and the solid phase should not cause confusion in the given context.) We will concentrate on wetting structures that are at least of the size of microns so as to ignore both the line tension, and more importantly the gravitational effects. We assume the liquid phase L forms a short bridge whose surface possesses a constant mean curvature $1/R$ (see Fig. 2). When the bridge contains sufficient amount of the phase L, it will then form a long column with constant cross-section.

For convenience, we use the same notations as used by Princen in Ref. [3]. The distance between the solid cylinders is $2d$, and the cylinder diameter is $2r$. Phases L, V and S are characterized by the liquid contact angle θ or by the Harkinson parameter S. The angle between the lines connecting the cylinder centers and the radius to the triplet L–V–S line is noted here as the 'covering angle' α. The radius R represents the curvature of the liquid surface and its value with respect to Laplace pressure is considered positive when the surface is concave, and negative otherwise [1–3]. The cross-section of such a concave long liquid column in the region of constant geometry with positive value of R is shown in Fig. 2.

Princen has treated the equilibrium columns and their surfaces using the principle of minimization of free energy in Ref. [3], whilst we prefer the mechanical concept of surface tension. Adamson and Gast argued in Ref. [8] for the mathematical equivalence of the two concepts.

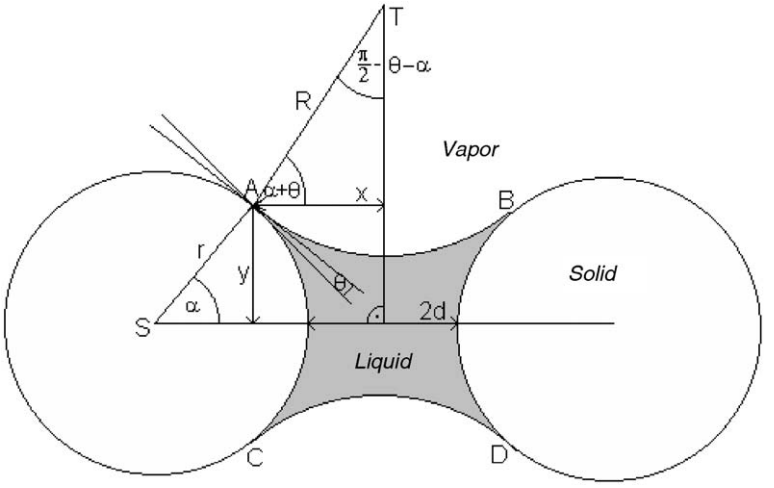

Fig. 2. The cross-section of a pair of parallel cylinders with a long stabile liquid column between them. The cylinder radius is r, the curvature of the free surface of the liquid column is denoted $1/R$, the distance between cylinders is $2d$, and the contact angle is marked by θ. The meaning of the covering angle α is evident from the figure.

To find the cross-sectional shape of the long liquid column at equilibrium between two cylinders we start with a simple case of the column geometry. From the sketch in Fig. 2, we have

$$\frac{R}{r} = \frac{1 + d/r - \cos\alpha}{\cos(\theta + \alpha)}. \tag{1}$$

Our aim however is to find the relationship between the dimensionless inter-cylinder half distance d/r on one side and angles α, and θ or S on the other. Such a relation exists, as we will show later, because R/r depends unambiguously on α and θ (or on spreading parameter S) only. To obtain the relationship we examine the force equilibrium on the liquid column front edge for a concave liquid columns surface depicted in Fig. 2.

$$F_{SV} = F_{LS} + F_{LV} + F_p, \tag{2}$$

where F_{SV} is the force of solid–vapor interface generated by the corresponding surface tension γ_{SV}. This force acts outside the liquid body and tends to spread the liquid along the cylinders. We call F_{SV} the line force because it is proportional to the length of the line, whereas γ_{SV} acting in perpendicular direction to this line and parallel with the cylinder axis. The lines in this case consists of two arcs AC and BD of identical length $L_{AC} = L_{BD} = l_{AC}r$ where $l_{AC} = 2\alpha$. For F_{SV} the following holds:

$$F_{SV} = 2\gamma_{SV} l_{AC} r. \tag{3}$$

Inwards the liquid body along the same arcs acts the force F_{SL} due to the surface tension γ_{LS} between the solid cylinder and the liquid column:

$$F_{LS} = 2\gamma_{LS} l_{AC} r. \tag{4}$$

The last line force F_{LV} is associated with the $L{-}V$ fluid interface. This force acts in the same direction as F_{LS} along the arcs AB and CD, both equal arc lengths L_{AB} and L_{CD}, i.e. $L_{AB} = L_{CD} = l_{AB}R$, where $l_{AB} = 2(\pi/2 - \theta - \alpha)$. So we have for F_{LV}

$$F_{LV} = 2\gamma l_{AB} R \tag{5}$$

Finally F_p, the last quantity in Eq. (2) is the force that has its origin from the Laplace pressure p. The value of Laplace pressure depends on the liquid surface tension γ and the main curvatures $1/R_1$ and $1/R_2$ of the L–V interface via the relation [8]

$$p = \gamma\left(\frac{1}{R_1} + \frac{1}{R_2}\right).$$

In the case of long liquid column between two cylindrical fibers, the L–V interface shares the shape of a portion of the cylinder surface, and hence one of the main curvatures is zero. Thus

$$p = \frac{\gamma}{R} \tag{6}$$

This Laplace pressure acts on the cross-sectional area A of the column, causing the force $F_p = Ap$. Convex liquid surfaces with negative R lead to positive Laplace pressure that tends to spread the liquid along the cylinder while positive radii R of concave liquid surfaces cause liquid suction with the tendency to shrink columns.

The area A can be expressed as seen in Fig. 2, as

$$A = A_{ABCD} - 2A_{AB} - 2A_{AC}, \tag{7}$$

and the areas A_{ABCD}, A_{AB} and A_{AC} satisfy

$$A_{ABCD} = a_{ABCD} rR \quad \text{where } a_{ABCD} = 4\cos(\theta+\alpha)\sin\alpha, \tag{8a}$$

$$A_{AB} = a_{AB}R^2 \quad \textit{where } a_{AB} = \frac{l_{AB}}{2} - \cos(\theta+\alpha)\sin(\theta+\alpha), \tag{8b}$$

$$A_{AC} = a_{AC}r^2 \quad \text{where } a_{AC} = \frac{l_{AC}}{2} - \sin\alpha\cos\alpha. \tag{8c}$$

Substitution of Eq. (3)–(8) together with the relation $F_p = Ap$ into Eq. (2) gives us

$$2\gamma_{SV} l_{AC} r = 2\gamma_{SL} l_{AC} r - 2\gamma l_{AB} R + \left(a_{ABCD} rR - 2a_{AB}R^2 - 2a_{AC}r^2\right)\frac{\gamma}{R}. \tag{9}$$

As opposed to Princen [1–3] as mentioned in the Introduction and in Fig. 1, we will distinguish between several different wetting instances. The first case is the partial wetting scheme with the contact angle $0^\circ < \theta < 180^\circ$, or the spreading coefficient $0 > S > -2\gamma$. Outside this interval lie the realms of complete wetting $\theta = 0^\circ$ and $S > 0$, with a transition point that divides partial wetting from complete wetting case $\theta = 0^\circ$ and $S = 0$. Another is the super-hydrophobic case $\theta = 180^\circ$ and $S < -2\gamma$, and the transition point $\theta = 180^\circ$ and $S = -2\gamma$ that divides the region of partial wetting from the super-hydrophobic area.

Using either the Young equation $\gamma_{SL} - \gamma_{SV} = -\gamma\cos\theta$ or the spreading parameter $S = \gamma_{SV} - \gamma_{SL} - \gamma$ and multiplying Eq. (9) by $R/(r^2 2\gamma)$ yields a quadratic relationship for the dimensionless parameter R/r:

$$a_2\left(\frac{R}{r}\right)^2 + 2b_2\frac{R}{r} + c_2 = 0, \tag{10}$$

where

$$a_2 = l_{AB} - a_{AB} = \left(\frac{\pi}{2} - \theta - \alpha\right) + \sin(\theta+\alpha)\cos(\theta+\alpha), \tag{10a}$$

$$\begin{aligned} b_2 &= \left(\tfrac{1}{2}a_{ABCD} - l_{AC}\cos\theta\right) = \sin\alpha\cos(\theta+\alpha) - \alpha\cos\theta \\ &= \sin\alpha\cos(\theta+\alpha) - \alpha\Sigma, \end{aligned} \tag{10b}$$

and $\sum = \left(S/\gamma + 1\right)$.

So for complete wetting (CW), i.e. $\theta = 0^\circ$, Eq. (10b) becomes

$$b_{2,CW} = \sin\alpha\cos\alpha - \alpha\Sigma = c_2 + \alpha(1-\Sigma). \tag{10bCW}$$

and for the super-hydrophobicity (SH), $\theta = 180^\circ$

$$b_{2,SH} = -\sin\alpha\cos\alpha - \alpha\Sigma = -c_2 - \alpha(1+\Sigma), \tag{10bSH}$$

where

$$c_2 = -a_{AC} = \sin\alpha\cos\alpha - \alpha, \tag{10c}$$

is universal for all wetting situations. By using the symbol $\sum$ and c_2, parameters $b_{2,CW}$ and $b_{2,SH}$ can thus be expressed in more general forms.

The solution of the quadratic Eq. (10) is

$$\left(\frac{R}{r}\right)_{1,2} = \frac{-b_2 \pm \sqrt{b_2^2 - a_2 c_2}}{a_2}, \tag{11}$$

depending on α and θ only as evidenced from the definitions of the parameters a_2, b_2, and c_2.

After substituting Eq. (11) into Eq. (1), we derive the relation between d/r and the angles α and θ:

$$\left(\frac{d}{r}\right)_{1,2} = \left(\frac{-b_2 \pm \sqrt{b_2^2 - a_2 c_2}}{a_2}\right) \cos(\theta + \alpha) + \cos\alpha - 1. \tag{12}$$

For partial wetting cases, the physically acceptable solution is the one with positive square root that ensures the positive value of d/r.

For the particular case of transition to complete wetting when $S = 0$, $\sum = 1$ and $\theta = 0^\circ$, we have $a_2 = c_2 + \pi/2$ and $b_2 = c_2$ so that

$$\left(\frac{d}{r}\right)_{S=0} = \left(\frac{-c_2 + \sqrt{-\frac{\pi c_2}{2}}}{\frac{\pi}{2} + c_2}\right) \cos\alpha + \cos\alpha - 1. \tag{13}$$

To include the complete wetting case $S \geqslant 0$ and $\theta = 0^\circ$, the wetting phenomenon is then governed by parameters $\alpha_{2,CW} = c_2 + \pi/2$ and $b_{2,CW} = c_2 - \alpha(1 - \sum)$. Then Eq. (12) reduces to

$$\left(\frac{d}{r}\right)_{CW} = \left(\frac{\alpha(\Sigma - 1) - c_2 + \sqrt{\alpha(\Sigma - 1)[\alpha(\Sigma - 1) - 2c_2] - \frac{\pi c_2}{2}}}{\frac{\pi}{2} + c_2}\right) \cos\alpha + \cos\alpha - 1. \tag{13CW}$$

When the liquid is completely repelled by cylinders, i.e. $S \geqslant -2\gamma$ and $\theta = 180^\circ$ so that $\alpha_{2,SH} = c_2 - \pi/2$, and $b_{2,SH} = -c_2 - \alpha(1 - \sum)$, only the solution of Equation (12) with the negative sign with the square root provides us with positive $(d/r)_{SH}$ values.

$$\left(\frac{d}{r}\right)_{SH} = \left(\frac{c_2 + \alpha(\Sigma + 1) - \sqrt{\alpha(\Sigma + 1)[2c_2 + \alpha(\Sigma + 1)] + \frac{\pi c_2}{2}}}{c_2 - \pi}\right) \cos\alpha + \cos\alpha - 1. \tag{13SH}$$

In Fig. 3 we have plotted d/r according to Eqs. (13), (13CW) and (13SH). Princen indicated in Ref. [3] that only the increasing parts of the d/r versus α curves in Fig. 3a are stable solutions and the rest solutions are at equilibrium but unstable, for a decreasing d/r value indicates leaking or disintegration of the liquid column.

Fig. 3a illustrates d/r versus the covering angle α for partial wetting case, where a larger α value, i.e. a wider covering arc AC of the liquid meniscus, or a smaller contact angle θ, leads to a greater d/r value, i.e. more volumetric liquid contained. Fig. 3b depicted the complete wetting situation $\theta = 0^\circ$, where in general much more water (much greater d/r) is absorbed than in the case of partial wetting; increasing either α or $\sum$ can achieve even greater liquid adsorption.

Finally Fig. 3c shows $d/r \sim \alpha$ dependences for $\sum < -1$, concerning the super-hydrophobic case. All liquid columns, one of them is shown in Fig. 3d, where we can deduce that, any combination of α and $\sum$ which lead to $d/r > 0$ will be unstable. The capillary pressure difference will accelerate the movement of the liquid column boundaries resulting in the leakage of the liquid away from the space in-between a pair of fibers. The escaped liquid body without the support of cylinders will be immediately disintegrated into droplets like a free liquid jet.

Back to the partial-wetting regime, the ultimate covering angle α_{max} yielding $(d/r)_{max}$ at different values of the contact angle θ for stable equilibrium liquid columns are plotted in Fig. 4, whereas the maximum ratio $(d/r)_{max}$ against θ are depicted in Fig. 5a. Numerical results are indicated along the curves hereafter for easy examination.

For the complete wetting case where $\theta = 0^\circ$ and $S > 0$ (i.e. $\sum > 1$) leading to $\alpha = 180^\circ$, we derived directly from (13CW) the simple formula $(d/r)_{max,CW} = 2(\Sigma - 1) + \sqrt{4\Sigma - 2}$ based on which Fig. 5b was plotted. So in this case $(d/r)_{max}$ is simply close to a linear function of the parameter $\sum$.

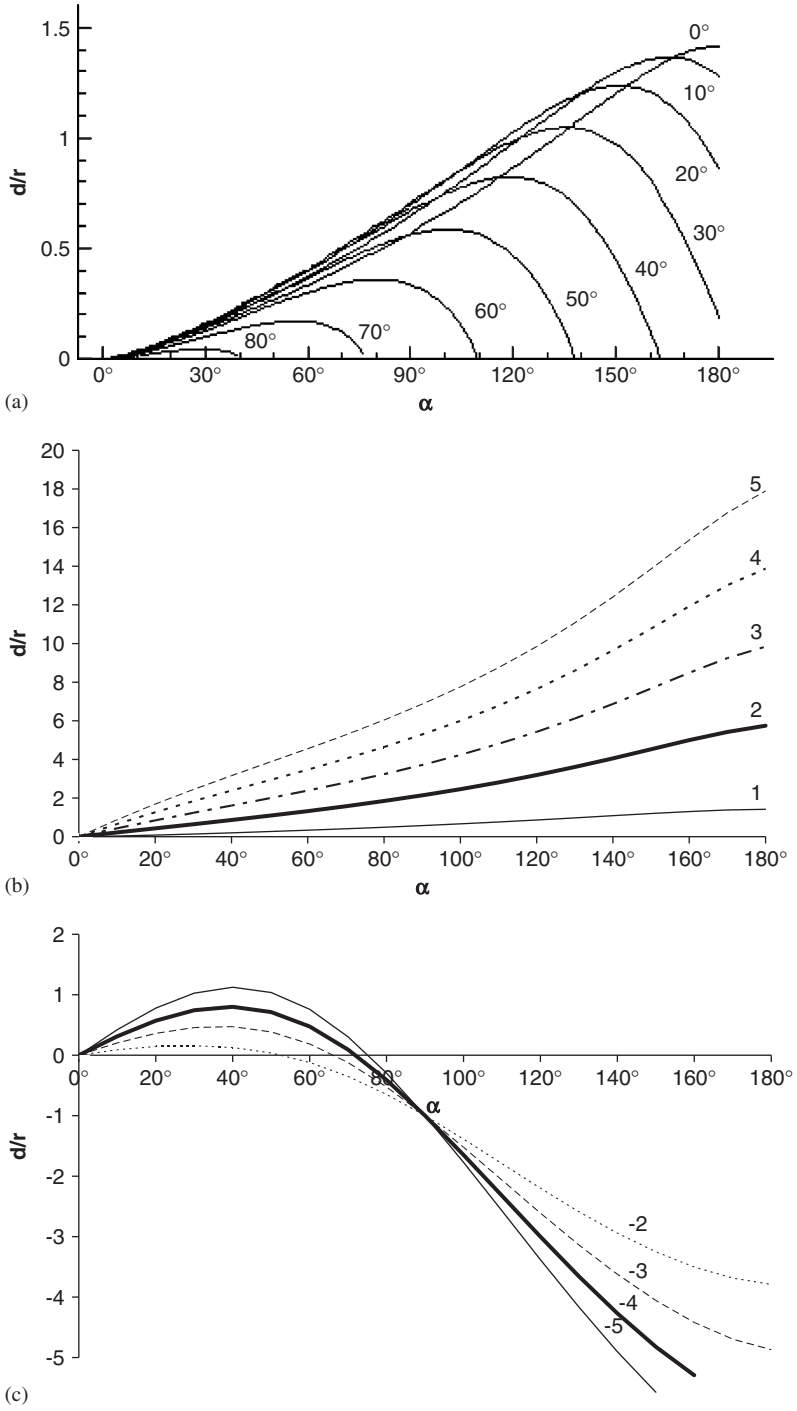

Fig. 3. (a) Relationship between d/r and α for long columns of constant cross-section between two cylinders at nine contact angles θ. These plots cover systems with partial wetting where $\theta \in (0^\circ, 180^\circ)$. (b) Plots of d/r dependence on α for various values $\sum = S/\gamma + 1$ were calculated using Eq. (13CW) for complete wetting regime. The particular $\sum$ values are typed tight to each of corresponding curves. (c) The graphs for super-hydrophobic surfaces express $d/r{-}\alpha$ dependences calculated according to the Eq. (13SH) for some chosen values $\sum$ below–1. Nonzero d/r values were obtained using the minus sign in front of the second root of solution (12). (d) A cross-section of unstable long liquid columns for super-hydrophobic pairs of cylinders. Each perturbation of cylindrical liquid boundaries will lead to its inexorable going-on thanks to a decrease of the capillary pressure on the head liquid front and its increase on the back. The movement of such perturbation is envisaged by arrows.

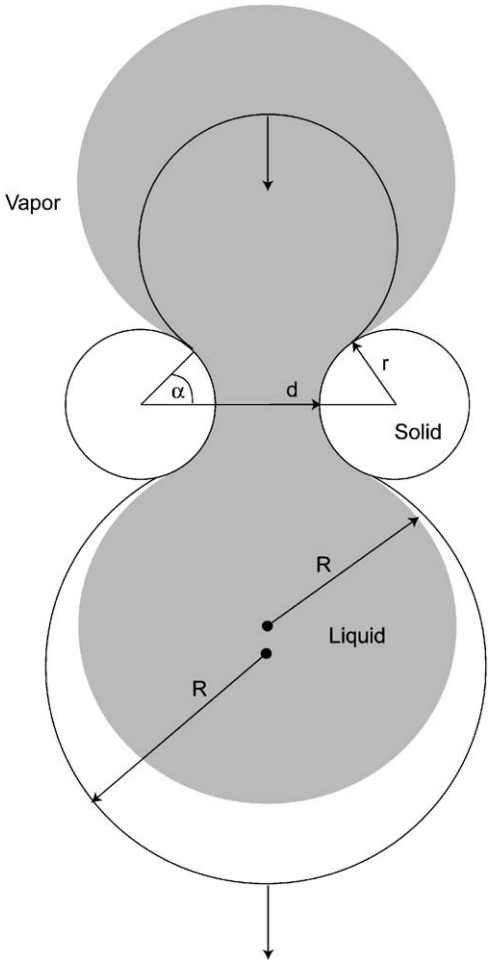

Fig. 3. (*Continued*)

Fig. 6 shows some cross-sectional shapes of the liquid column between the two cylinders for $\theta = 0^\circ$ and $\theta = 40^\circ$, respectively. The figures were plotted using Eq. (12).

We will use the above results in next section to describe the morphological transitions of the liquid columns between two cylinders and three separate columns with channel-filling liquid column.

2.2. Liquid columns among three solid cylinders

A typical cross-section of a channel-filing liquid column among three equal-distance and horizontal cylinders is shown in Fig. 7. The notations in the figure are similar to those used above for two-cylinder system, except for the definition for angle α.

The angle α is now the one between the line connecting the centers of neighboring cylinders and the radius to the L–V–S boundary. It means that the meaningful upper limit of α for non overlapping liquid surfaces is now 150°, and in three-cylinder case 2α no longer covers the entire wetted region for each cylinder, although for convenience it is still called the covering angle. To distinguish the two- and three-cylinder systems, we will use both a stroke for three-cylinder quantities and the index 3 for parameters a, b, c in the following text.

The equilibrium condition for channel-filing liquid column is the same as for that in two-cylinder system, as expressed by Eq. (2). The force F'_{SV}, driving the liquid to spread along cylinders, is composed now by three

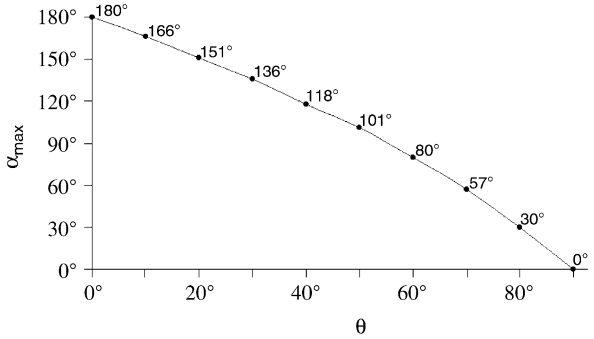

Fig. 4. The relationship between the maximal values of the covering angle α and the contact angle θ for two-cylinder bundle. Numerical values of α_{max} for chosen contact angles $\theta = \{0^0, 10^0, 20^0, 30^0, 40^0, 50^0, 60^0, 70^0, 80^0, 90^0\}$ are introduced directly in the graph.

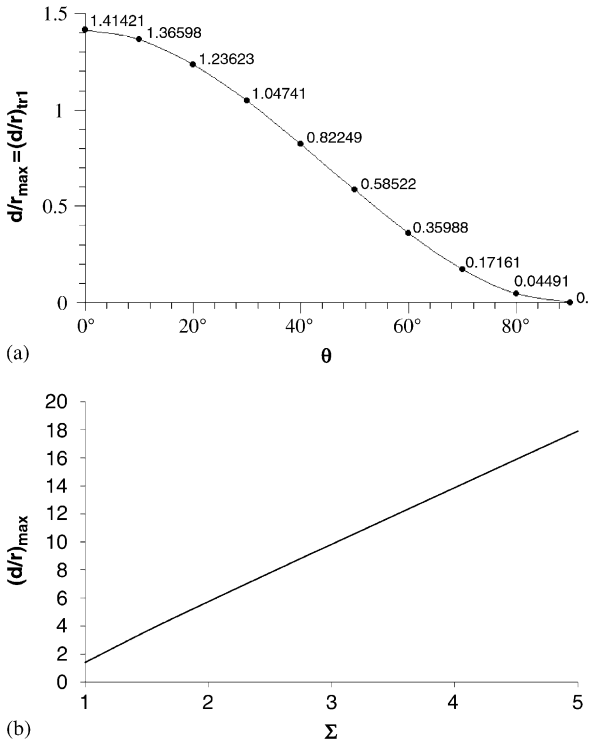

Fig. 5. (a) The dependence of the maximal values of d/r on the contact angle θ. Numerical values of $(d/r)_{max}$ for chosen contact angles $\theta = \{0^0, 10^0, 20^0, 30^0, 40^0, 50^0, 60^0, 70^0, 80^0, 90^0\}$ are shown in the figure. (b) Relationship $\left(d/r\right)_{\max,CW} = 2(\Sigma - 1)\sqrt{4\Sigma - 2}$ for maximal d/r values in the case of completely wetting pair of cylindrical fibers.

arcs of equal length $L'_{AC} = \left(l_{AC} + \pi/3\right)r$, where $l_{AC} = 2\alpha$ is the same as in the two-cylinder case. Hence for F'_{SV} due to the surface tension between the solid and the vapor we have

$$F'_{SV} = (3l_{AC} + \pi)r\gamma_{SV}. \tag{14}$$

Another force F'_{SL} acts along the same three arcs as F'_{SV}, but in opposite direction. It is due to the surface tension γ_{SL} acting on the solid–liquid interface.

$$F'_{SL} = (3l_{AC} + \pi)r\gamma_{SL}. \tag{15}$$

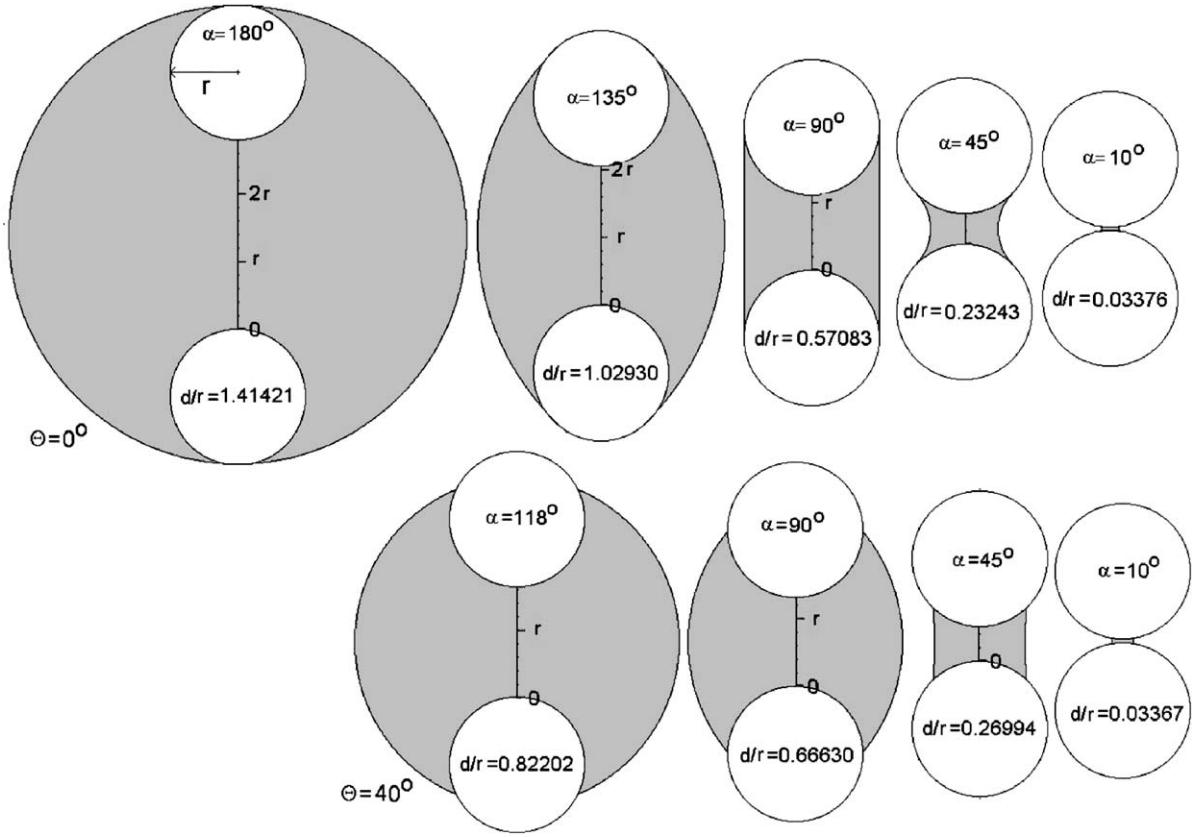

Fig. 6. Several cross-sectional shapes of liquid columns in two-cylinder system for $\theta = 0°$, and $\theta = 40°$. The first cross-sections from the left of each series represent the states with maximal values of d/r and α. The next increase of the cylinder–cylinder separation will cause abrupt change of the liquid-body shape. The long column will change into an ''unduloid''.

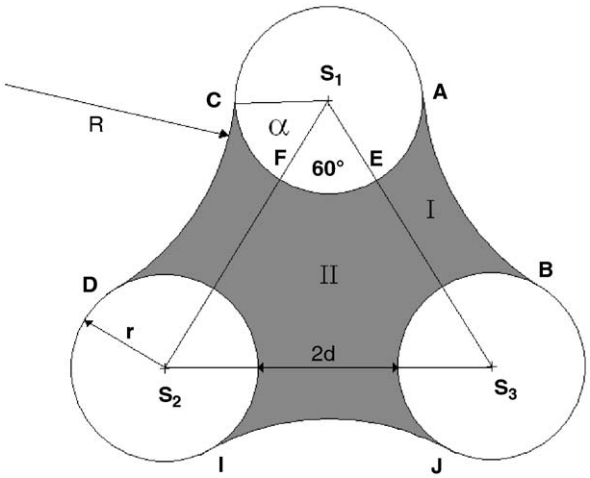

Fig. 7. The cross-section of the three-cylinder system with a channel-filling column among them. The area A of the liquid column cross-section consists of three parts (I), and the component (II).

The last line force F'_{LV} in the equilibrium equation is the one associated with the surface tension γ between the liquid and its vapor. It acts along three arcs of length $L_{AB} = l_{AB}R$, which are expressed in the same manner as in the two-cylinder assembly. Hence F'_{LV} satisfies

$$F'_{LV} = 3l_{AB}R\gamma. \tag{16}$$

Note that $l_{AB} = 2(\pi/2-\theta-\alpha)$.

The Laplace pressure force F'_p is the product of the Laplace pressure γ/R with the liquid column cross-sectional area A':

$$F'_p = A'\frac{\gamma}{R}. \tag{17}$$

The area A' can be expressed using two sub-regions denoted as (I) and (II) in Fig. 7. The sub-region (I) has the area $A_I = A/2$, where A is still the same as in Eqs. (7) and (8) for two-cylinder system. Combining these equations yields

$$A_I = \frac{1}{2}a_{ABCD}rR - a_{AB}R^2 - a_{AC}r^2. \tag{18}$$

The sub-region (II) has the area A_{II} derivable from the area of the triangle A_{S1S2S3} that has its summits in the centers of cylinder cross-sections S_1,S_2 and S_3. To obtain A_{II} we have to subtract from the triangle area A_{S1S2S3} three areas of A_{ES_1F} of the circular sector ES_1F. For A_{S1S2S3} it is apparent that

$$A_{S_1S_2S_3} = \sqrt{3}(d+r)^2 = \sqrt{3}[R\cos(\theta+\alpha) + r\cos\alpha]^20 \tag{19}$$

where we have used Eq. (1) to express $d+r$ in terms of R,θ,α and r.

The circular section ES_1F has an area

$$A_{ES_1F} = \pi r^2/6. \tag{20}$$

Hence we have for the cross-sectional area of the liquid column among three cylinders

$$\begin{aligned} A' &= 3A_I + A_{II} = 3A_I + A_{S_1S_2S_3} - 3A_{ES_1F} \\ &= \frac{3}{2}\mathrm{a}_{ABCD}rR - 3\mathrm{a}_{AB}R^2 - 3\mathrm{a}_{AB}r^2 + \sqrt{3}[R\cos(\theta+\alpha) + r\cos\alpha]^2 - \frac{\pi r^2}{2}. \end{aligned} \tag{21}$$

Substituting Eqs. (14)–(17), and (21) into (2) and using the Young equation $\gamma_{SL}-\gamma_S = \gamma\cos\theta$, we obtain the final quadratic equation:

$$a_3\left(\frac{R}{r}\right)'^2 + 2b_3\left(\frac{R}{r}\right)' + c_3 = 0, \tag{22}$$

where

$$a_3 = 3\left(\frac{\pi}{2} - \theta - \alpha\right) + 3\sin(\theta+\alpha)\cos(\theta+\alpha) + \sqrt{3}\cos^2(\theta+\alpha), \tag{22a}$$

$$b_3 = 3\cos(\theta+\alpha)\sin\alpha + \sqrt{3}\cos(\theta+\alpha)\cos\alpha - 3\alpha\cos\theta - \frac{\pi}{2}\cos\theta, \tag{22b}$$

where for complete wetting cases $\theta = 0^\circ$ and for super-hydrophobic ones $\theta = 180^\circ$.

Similar to the manipulations in the 2-cylinder cases, by connecting $\cos\theta$ with the parameter $\sum$, we derive $b_{3,CW}$ for the complete wetting ($S>0$, $\sum>1$, and $\theta = 0^\circ$) as

$$b_{3,CW} = 3\cos\alpha\sin\alpha + \sqrt{3}\cos^2\alpha - \left(3\alpha+\frac{\pi}{2}\right)\sum = c_3 - \left(3\alpha+\frac{\pi}{2}\right)\left(\sum -1\right). \tag{22bCW}$$

For the super-hydrophobic cases, $S\leqslant -2\gamma$ and $\theta = 180^\circ$ the following it holds:

$$b_{3,SH} = -3\cos\alpha\sin\alpha - \sqrt{3}\cos^2\alpha - \left(3\alpha+\frac{\pi}{2}\right)\sum = -c_3 - \left(3\alpha+\frac{\pi}{2}\right)\left(\sum +1\right). \tag{22bSH}$$

The last parameter c_3 is, similar to c_2 universal for all wetting situations.

$$c_3 = \sqrt{3}\cos^2\alpha - \frac{\pi}{2} + 3\sin\alpha\cos\alpha - 3\alpha. \tag{22c}$$

Likewise, the solutions of the quadratic Eq. (22) has two roots:

$$\left(\frac{R}{r}\right)'_{1,2} = \frac{-b_3 \pm \sqrt{b_3^2 - a_3 c_3}}{a_3}. \tag{23}$$

Again combining Eq. (23) with Eq. (1) gives

$$\left(\frac{d}{r}\right)'_{1,2} = \left(\frac{-b_3 \pm \sqrt{b_3^2 - a_3 c_3}}{a_3}\right)\cos(\theta+\alpha) + \cos\alpha - 1. \tag{24}$$

For the case with zero spreading coefficient, i.e., for the transition to complete wetting, ($S = 0$ and $\theta = 0^\circ$), Equation (24) reduces, due to relations $a_3 = c_3 + 2\pi$ and $b_3 = c_3$ following from Eqs. (22a) and (22b), into

$$\left(\frac{d}{r}\right)'_{s=0} = \left(\frac{-c_3 + \sqrt{-2\pi c_3}}{2\pi + c_3}\right)\cos\alpha + \cos\alpha - 1. \tag{25a}$$

For the complete wetting case, $S \geqslant 0$ and $\theta = 0^\circ$,

$$\left(\frac{d}{r}\right)'_{CW} = \left(\frac{\left(3\alpha+\frac{\pi}{2}\right)(\Sigma-1) - c_3 + \sqrt{\left(3\alpha+\frac{\pi}{2}\right)(\Sigma-1)\left[\left(3\alpha+\frac{\pi}{2}\right)(\Sigma-1) - 2c_3\right] - 2\pi c_3}}{2\pi + c_3}\right)\cos\alpha + \cos\alpha - 1, \tag{25CW}$$

since $a_3 = c_3 + 2\pi$ and $b_3 = c_3 - (3\alpha + \pi/2)$ ($\sum - 1$) for $S \geq 0$ and $\theta = 0^\circ$. For super-hydrophobic surfaces, it is given by

$$\left(\frac{d}{r}\right)'_{SH} = \left(\frac{c_3 + \frac{\pi}{2} + \left(3\alpha+\frac{\pi}{2}\right)(\Sigma+1) - \sqrt{\left[c_3 + \frac{\pi}{2} + \left(3\alpha+\frac{\pi}{2}\right)(\Sigma+1)\right]^2 - (c_3 - \pi)c_3}}{c_3 - \pi}\right)\cos\alpha + \cos\alpha - 1. \tag{25SH}$$

The liquid body can be perfectly cylindrical when $\alpha = 150^\circ$, $S \geq 0$ and $\theta = 0^\circ$ as will be shown below while deriving Eqs. (28).

The relationships between $(d/r)'$ and the covering angle α are illustrated for various levels of both the contact angle θ and the parameter $\sum$ in Fig. 8. Once more, the physically stable equilibrium states include only the increasing parts of the curves.

It is noticeable that for three cylinders the equilibrium dimensionless distance $(d/r)'$ reaches its maximum value as $\theta = 20^\circ$ (in Fig. 8a), not $\theta = 0^\circ$ as in the two-cylinder case. The behavior of systems for complete wetting is depicted in Fig. 8b, and for super-hydrophobic surfaces in Fig. 8c, where for positive d/r values the negative sign in Eq. (24) has to be taken. Stable liquid columns are those with $\alpha < 0^\circ$ Fig. 8d depicts cross-sectional shapes of stable and unstable liquid bodies for a super-hydrophobic situation. Similar comments on the stable ranges for θ and $\sum$ can be made as in 2-cylinder cases.

Also for three-cylinder system the liquid absorbed is usually higher than that for the system of two cylinders, as visible from comparison of Fig. 6 with Fig. 9, where the cross-sectional shapes of liquid bodies are illustrated for the two systems, respectively, at chosen levels of θ.

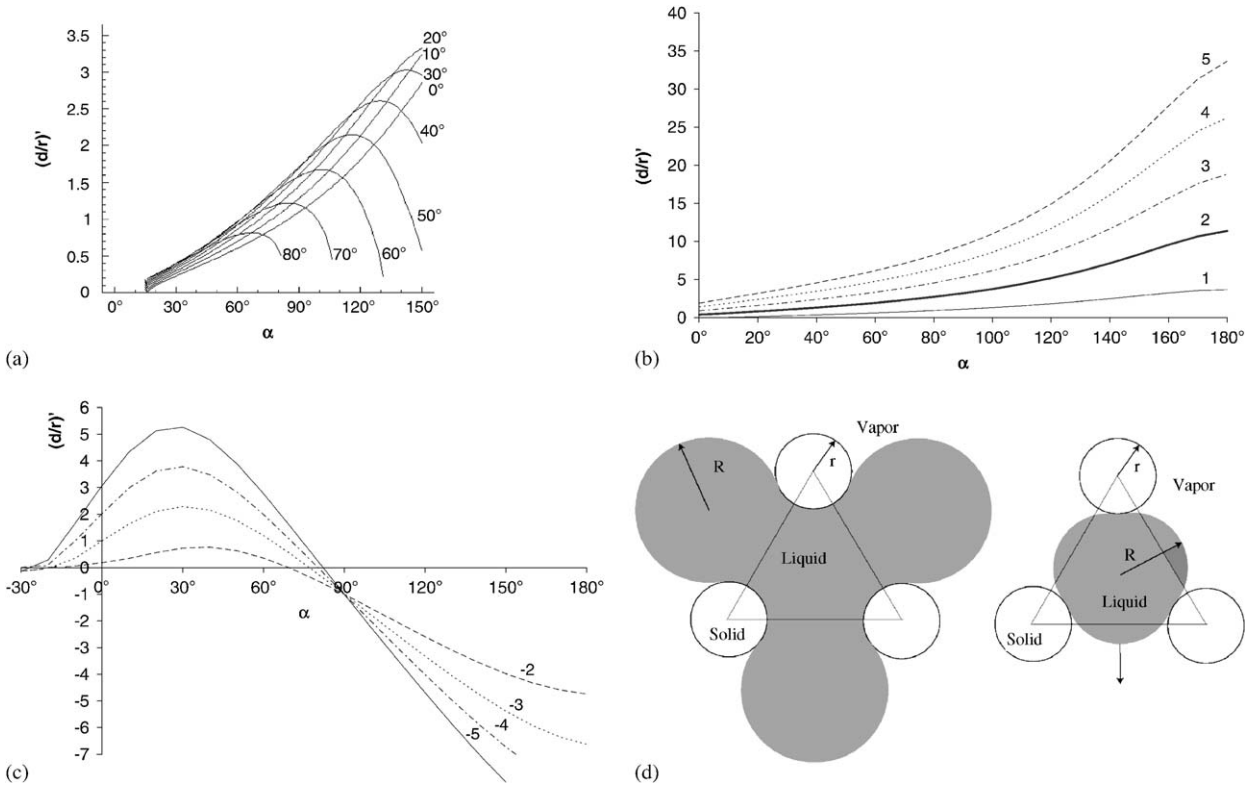

Fig. 8. (a) The graphs show the dependence of the dimensionless cylinder–cylinder separation $(d/r)'$ on the covering angles θ for various contact angles θ for three-cylinder bundles. (b) The dependences of $(d/r)'$ on α for complete wetting instances are depicted for chosen values $\sum = \{1, 2, 3, 4, 5\}$. (c) Dependences of the dimensionless parameter $(d/r)'$ on α for super-hydrophobic cylinder surfaces. Individual curves belong to five chosen values $\sum = \{-1, -2, -3, -4, -5\}$. (d) Drawings of cross-sections of an unstable (left-hand side) and a stable (right-hand side) long liquid columns for high values of contact angle $\theta \approx 180^o$ or for super-hydrophobic surfaces, i.e. $S < -2\gamma$, $\sum < -1$.

3. Morphological transitions

3.1. Liquid body morphological transition in two-cylinder systems

When the cylinder–cylinder separation between two cylinders becomes greater than a certain threshold value $(d/r)_{tr}$, the liquid column between the two cylinders can no longer maintain a single cross-section and will instead turn into a shape similar to a sessile droplet, or unduloid, on a single fiber. The threshold or transition value $(d/r)_{tr}$ depends on among other things the values of α or θ or S. It is in fact obvious that $(d/r)_{tr} = (d/r)_{max}$.

The covering angle leading to $(d/r)_{tr}$ is α_{max} which is related to the contact angle θ as shown in Fig. 4. The special case of the transition to complete wetting $S = 0$ is provided by Eq. (13) for $\alpha = \alpha_{max} = 180^\circ$ and $c_2 = -\pi$. Hence the value $(d/r)_{max,S=0} = \sqrt{2} = 1.41421$ is the upper limit to which the liquid column can still reverse back to the original stable state.

For spreading parameter values greater than zero, i.e. for the complete wetting case, inter-cylinder distance obeys the formula $(d/r)_{max,CW} = 2(\Sigma - 1) + \sqrt{4\Sigma - 2}$ that has been derived in the Section 2.1. The relative water absorbed d/r has evidently no theoretical limit for its growth with increasing S as seen in Fig. 5b.

Conversely, on starting with a ratio $d/r > (d/r)_{tr}$ and drawing the cylinders closer, we suppose the threshold shape of a limited amount of liquid will be a long cylinder encircling the two cylinders as shown in Fig. 10. There is then a simple expression for the area A of the cross-section as the area of a circle with the radius R from which we subtract two circle areas each of the radius r. The Laplace force F_p is now $-\pi(R^2 - 2r^2)\gamma/R$ and

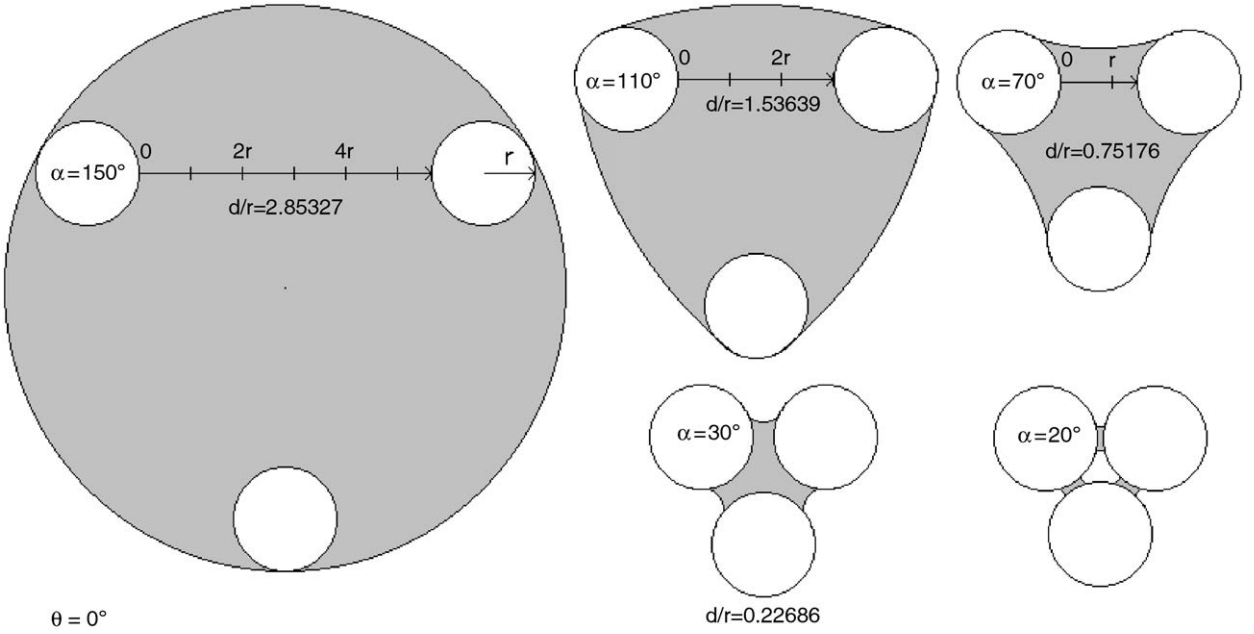

Fig. 9. Several cross-sectional shapes of liquid columns in three-cylinder system for $\theta = 0^\circ$. The first cross-section from the left represents the state with maximal value of d/r and α. Next increase of the cylinder–cylinder separation will cause the abrupt change of the liquid body shape. The long column will turn into the "unduloid".

the Eq. (2) reduces to

$$4\pi r\gamma_{SV} = 4\pi r\gamma_{LS} + 2\pi R\gamma - \pi\left(R^2 - 2r^2\right)\frac{\gamma}{R}, \tag{26}$$

where a negative R has been used due to the convex shape of the cylindrical liquid body. Relation (26) provides us with the quadratic equation (27)

$$\left(\frac{R}{r}\right)'^2 + 4\cos\theta\left(\frac{R}{r}\right)'^2 + 2 = 0 \tag{27}$$

with the solutions $\left(R\Big/r\right)'_{1,2} = -2\cos\theta \pm \sqrt{2}\sqrt{2\cos^2\theta - 1}$. A physical sense requires $|R| \geqslant 2r$, i.e., the negative sign before the second term be taken. The covering angle α is 180° as illustrated in Fig. 10 so that holds– $R = 2r + d$. Substituting this relation into Eq. (27) we obtain the relationship between $(d/r)'_{tr2}$ and θ. For partial wetting region with θ ranges over (0°, 180°)

$$\left(\frac{d}{r}\right)'_{tr2} = 2(\cos\theta - 1) + \sqrt{4\cos^2\theta - 2}. \tag{28}$$

The case of complete wetting ($S > 0$, i.e. $\sum > 1$) is governed by the following relationship:

$$\left(\frac{d}{r}\right)_{tr2,CW} = 2(\Sigma - 1) + \sqrt{4\Sigma^2 - 2}. \tag{28CW}$$

The special transition for $S = 0$ ($\theta = 0^\circ$) occurs when $\left(d/r\right)'_{tr2} = 2(1-1) + \sqrt{2} = \sqrt{2}$ as derived directly from both Eqs. (28) and (28CW). This result is identical to the above transition value $(d/r)_{tr1}$ from Eq. (13).

The hysteresis of the transitions for partial wetting area emerges as the result of the difference between the values $(d/r)_{tr1}$ calculated directly from Eq. (12) and the threshold values $(d/r)_{tr2}$ from Eq. (28). Both transition curves are plotted in Fig. 11 to evaluate the difference between them.

Assume one starts with a cylinder–cylinder separation greater than the threshold value $2(d/r)_{tr1}$ with the liquid originally forming an unduloid. While the distance between cylinders decreases, the unduloid

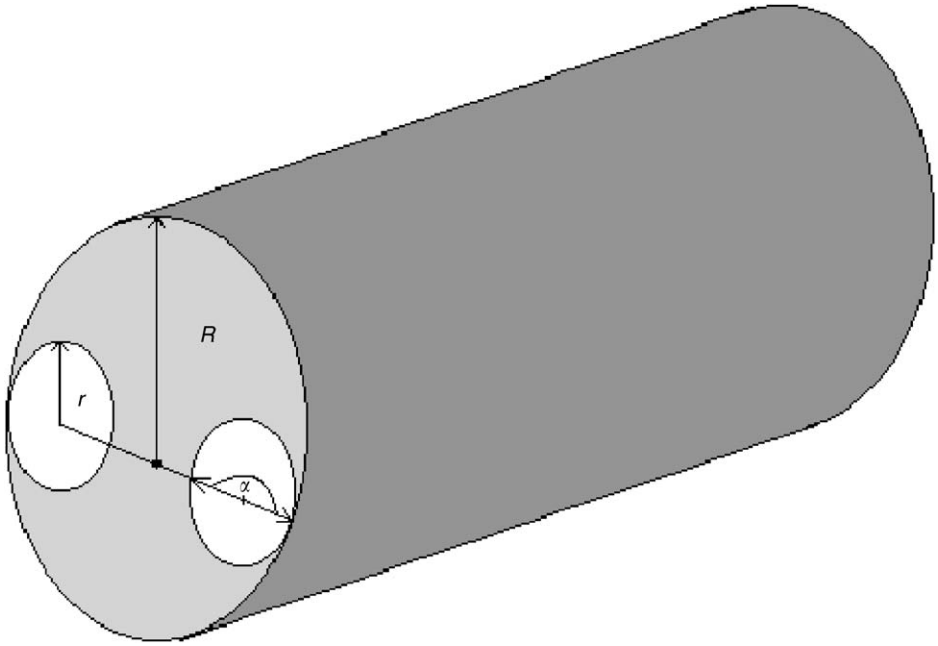

Fig. 10. System composed of two cylinders with long liquid column of the cylindrical shape. The cylinders are touching the liquid body from the inside. The situation on the figure belongs to the threshold $(d/r)_{tr2}$.

gradually prolongs until it suddenly turns into a cylindrical liquid body upon touching the two solid cylinders in one point. This transition is governed by Eq. (28). Moving the two cylinders even closer to each other, the dry areas on each cylinder will appear. Then if the cylinders are slowly separated again to complete the hysteresis loop, the previously dry cylinder surfaces are now coated by a liquid film so that Eq. (12) becomes effective. These different transition conditions during the reversal in fact are the causes for the hysteresis.

3.2. Transition from multiple columns to channel-filling column in three cylinder system

Princen in his work [3] made an assumption that at small cylinder–cylinder distance $2d$, the liquid column in between the three cylinders disintegrates into three separate columns, one between each pair of the adjacent cylinders. Thus, a hole forms all along the center of the disappeared column. Princen has offered two alternative justifications. The first is based on the comparison of surface free energies of the channel-filling and disintegration morphologies of columns. The second one is by considering liquid flows in the case of coexistence of both morphologies in the same system; the coexistence will cause the liquid flow from higher pressure regions to the lower ones. The result of the flow is the extinction of the higher pressure column shape.

The pressure difference is governed by the Laplace pressure formulas. That is why the transition between separate columns and channel-filling column occurs under the condition of equal values of curvatures $1/R$ of the liquid bodies. The numerical solution for a general contact angle θ in the case of partial wetting is obtained by equating Eq. (11) to Eq. (23), i.e.,

$$\frac{-b_2+\sqrt{b_2^2-a_2c_2}}{a_2}=\frac{-b_3+\sqrt{b_3^2-a_3c_3}}{a_3}. \tag{29}$$

The resultant transition curve based on this relation is sketched as the curve no.1 in the morphology diagram in Fig. 12.

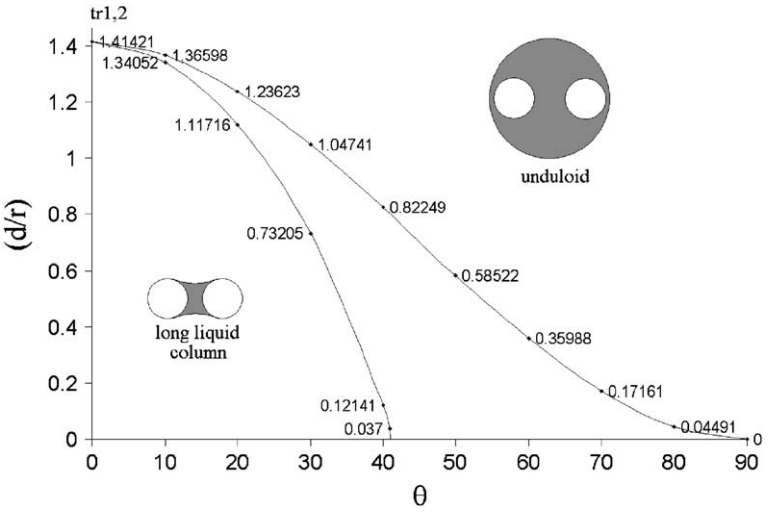

Fig. 11. The morphology diagram for transitions between long liquid columns and "unduloids" for two parallel cylinders under the conditions of partial wetting. The d/r–θ relationship curve (1) depicts transitions from long liquid columns to "unduloids" and is identical with the one shown in Fig. 5, while curve (2) describes morphological changes from a perfectly cylindrical liquid-body shape to a long liquid column.

When $S = 0$ ($\theta = 0^\circ$), i.e. at the complete wetting threshold, Eq. (29) turns into

$$\frac{-c_2 + \sqrt{-\frac{\pi c_2}{2}}}{\frac{\pi}{2} + c_2} = \frac{-c_3 + \sqrt{-2\pi c_3}}{2\pi + c_3}. \tag{30}$$

After the substitution $c_3 = 4c_3'$ we can rewrite Eq. (30) into

$$\frac{-c_2 + \sqrt{-\frac{\pi c_2}{2}}}{\frac{\pi}{2} + c_2} = \frac{-c_3' + \sqrt{-\frac{\pi c_3'}{2}}}{\frac{\pi}{2} + c_3'}. \tag{31}$$

According to Eqs. (10c) and (22c), values of c_2 and c_3' are both negative for α from intervals $\alpha \in (0, \pi)$ and $\alpha \in (0.25, 5\pi/6)$, respectively. These c's values are then fall into corresponding intervals $c_2 \in (0, -\pi)$ and $c_3' \in (0, -3\pi)$. On the joint interval $c_2, c_3' \in (0, -\pi)$ are both functions given by the terms on RHS and LHS of Eq. (31) positive and monotonically decreasing.

So Eq. (31) is true only if $c_2 = c_3'$. Thus, the threshold condition for $S = 0$ is reached. The threshold value α'_{tr1} for zero contact angle θ and zero spreading parameter S, i.e. on the threshold to complete wetting, is therefore given by

$$\sqrt{3}\cos^2 \alpha'_{tr1} - \sin \alpha'_{tr1} \cos \alpha'_{tr1} + \alpha'_{tr1} = \frac{\pi}{2}. \tag{32}$$

The numerical solution shows $= \alpha'_{tr1} = 0.333305\,\text{rad} = 1/3\,\text{rad}$ or $(d/r)'_{tr1} = 0.07869$. The complete wetting region with S>0 and $\sum > 1$ leads to more complicated relation that has to be solved numerically, since Eqs. (13CW) and (25CW) that contain the information about R/r, have to be used in their general forms.

Morphological transition between the channel-filling liquid column and the separate liquid columns also has a hysteresis as noted in Ref. [3], confirmed by the above-derived threshold values. Assume one starts with a cylinder–cylinder separation greater than the threshold value $2(d/r)'_{tr1}$ with the liquid column originally filing the channel. When the distance is decreased a hole will form and the channel-filling liquid column starts to split (when $\theta = 0^\circ$ and $S = 0$ this transition occurs for $(d/r)'_{tr1} = 0.07869$ as mentioned before). If the cylinders are subsequently separated again, i.e., the distance is increased to complete the hysteresis loop, previously split liquid columns survive until α increases to 30° when the separated liquid columns connect each other again at $(d/r)_{tr2}$, and the central hole disappears. These different transition conditions in fact are the cause for the hysteresis.

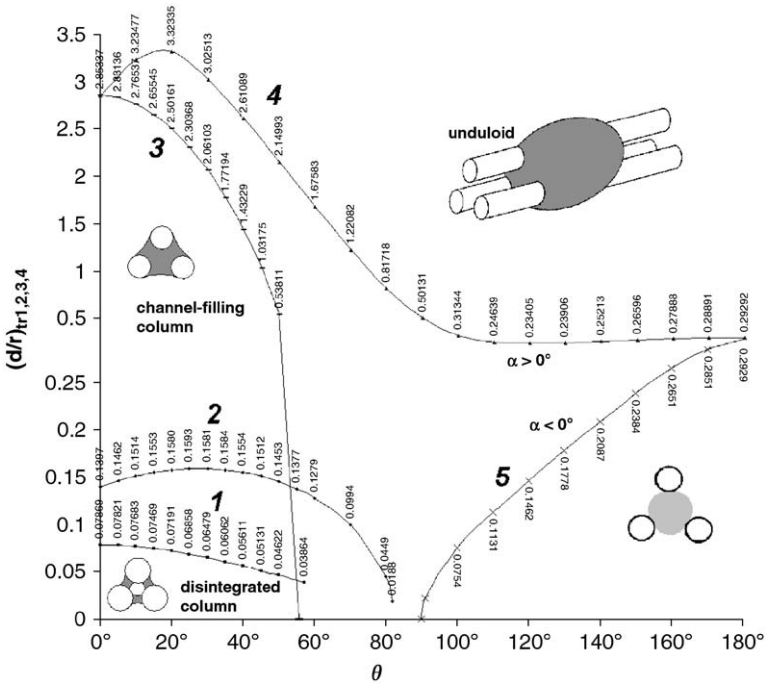

Fig. 12. The morphology diagram for three-cylinder systems. The curve (1) describes the transition from channel-filling columns to disintegrated ones. The points marked by triangles on the curve (2) denote the reversed transition from disintegrated columns to channel-filling columns. The transition from channel-filling column to the "unduloid" is described by the curve (3), while the last $(d/r)'_{tr4}$–θ relationship denotes the morphology transition from the "unduloid" to the channel-filling column with points (4). Curves (3) and (4) are plotted for $S = 0$. Stable columns for $\theta > 90^\circ$ belong to the curve (5), while unstable ones to the curve (4), viz. Fig. 8d. The scale of the $(d/r)'_{tr}$ axis is divided into two parts with different unit lengths. The first ranges from 0 to 0.2 is more detailed while the second has a less minute scale.

The threshold values $(d/r)'_{tr2}$ for filling the central hole can be obtained from Equation (24) by substituting both $\alpha = 30^\circ$ and a chosen contact angle θ or $\sum$ The zero contact angle together with the condition $S = 0$ means we are dealing with the transition from partial wetting to complete wetting just now, provides the threshold value $(d/r)'_{tr2,\ S=0} = 0.13972$. The corresponding transition curve no. 2 is drawn in Fig. 11 as the morphology diagram, together with the $(d/r)'_{tr1}$–θ relationship.

3.3. Transition from the channel-filling column to an unduloid in three-cylinder system

Another stable state of the wetting phase among three cylinders is akin to the unduloid. When the cylinder–cylinder distance exceeds a certain value, the long liquid column disintegrated into unduloids as the only equilibrium configuration. The reason for this second kind of morphological transition in the system in question is based on the fact that the upper limit of α in three-cylinder case is 150°, as a larger covering angle α would require overlap of the two liquid surfaces in contact with each of the cylinder. Corresponding transition values $(d/r)'_{tr3}$ result from Equation (24) by substituting $\alpha = 150^\circ$ and a chosen value of the contact angle θ. Considering zero contact angle and concurrently zero spreading coefficient, we obtain from Eq. (25) the threshold value $\left(d/r\right)'_{tr3,S=0} = \sqrt{3} + 3/\sqrt{2} - 1 \cong 2.85337$. This transition sets in when the distance between three cylinders with channel-filling column, which is originally below $(d/r)'_{tr3}$, increases.

Another transition value $(d/r)'_{tr4}$ occurs when the distance between three cylinders with an "unduloid", i.e., the original distance among the cylinders is greater than $(d/r)'_{tr4}$, reduces. This threshold $(d/r)'_{tr4}$ can be derived from the assumption that the transitional liquid morphology has perfectly circular cross-section with cylinders touching the liquid from the inside.

Owing to the simple cylinder symmetry of the liquid body, Eq. (2) reduces into a simple form that is the equivalent of Eq. (27) for three-cylinder bundle:

$$3 \times 2\pi r\gamma_{SV} = 3 \times 2\pi r\gamma_{SL} + 2\pi R\gamma - \left(\pi R^2 - 3\pi r^2\right)\frac{\gamma}{R}. \tag{33}$$

Note the negative value of the liquid surface radius R for convex liquid body. The third term on the RHS of Eq. (33) is due to the Laplace pressure that acts, for convex surfaces, outward of the liquid. Using again the Young equation $\gamma_{SV} = \gamma_{SL} + \gamma\cos\theta$ one obtains from Eq. (33)

$$\left(\frac{R}{r}\right)'^2 + 6\cos\theta\left(\frac{R}{r}\right)' + 3 = 0. \tag{34}$$

Solutions of this quadratic equation are $\left(R/r\right)'_{1,2} = -3\cos\theta \pm \sqrt{9\cos^2\theta - 3}$. Hence from the minimal value required for $|R| > r + 2r/\sqrt{3}$, we exclude the solution with positive root term and obtain the relation between $(d/r)'_{\mathrm{tr4}}$ and θ under which an unduloid to a channel-filling column transition takes place. Similar to the derivation of Eq. (28) from Eq. (27) we postulate here the liquid column has the shape of the ideal cylinder that touches outer points of the bundle of three solid cylinders. From Eqs. (1) and (34), we have

$$\left(\frac{d}{r}\right)'_{tr4} = \left(3\cos\theta + \sqrt{9\cos^2\theta - 3}\right)\cos\left(\theta + \frac{5\pi}{6}\right) - \frac{\sqrt{3}+2}{2}. \tag{35}$$

Both zero contact angle θ and zero spreading coefficient S lead to the resultant value $(d/r)'_{tr4,\ S=0} = \sqrt{3} + 3/\sqrt{2} - 1 = 2.85337$, which is the same as $(d/r)'_{tr3}$ for the zero contact angle θ and $S = 0$. The corresponding transition curves nos.3 and 4 for $(d/r)'_{\mathrm{tr3}}$ and $(d/r)'_{\mathrm{tr4}}$ are shown in Fig. 12.

For a complete wetting area with $\theta = 0^\circ$ and $S \geq 0$ the term $\cos\theta$ in Eq. (35) has to be substituted by $\sum$ providing us with the relation

$$\left(\frac{d}{r}\right)'_{tr4,CW} = \left(3\Sigma + \sqrt{9\Sigma^2 - 3}\right)\frac{\sqrt{3}}{2} - \frac{\sqrt{3}+2}{2}. \tag{35CW}$$

There exists a great gap between transition curves nos. 3 and 4 in Fig. 12. A channel-filling column cannot be created from an unduloid for contact angles higher than about 54° via drawing solid cylinders nearer to each other, as is visible from curve no. 3. On the other had such a rode-like channel-filling column can be created when the liquid body starts to be fed from inside, for instance by the injection of liquid into the space among a triplet of cylinders, and it remains to be trapped among them like in a birdcage even up to great values of the contact angle, as is obvious from the shape of the curves no. 4 and no. 5. The curve no. 5 is plotted using Eq. (24) for $\alpha < 0^\circ$ and $\theta > 90$.

The last described configuration of thinly spread completely non wetting liquid along the solid substrate is quite unusual and deserves next investigation with another theoretical tools than those used in this work. Of primary importance should be the stability of such configuration. According to Figs. 8c and d it is obvious that stable as well as unstable long liquid columns exist for super-hydrophobic surfaces of cylinders. Stable are those which cowering angle α values less than 0°.

4. Experimental verifications

To validate our theoretical results, we have conducted a series of experiments for both two- and three-cylinder systems. Polypropylene rods of radius 1.5 mm were chosen as the cylinders to meet the requirements of smooth and homogenous surface. Moreover their radius is small enough to minimize the effects of the gravity. A two-component epoxy resin consisting of a mixture of alkylenpolyamids was chosen as the liquid. The time necessary for the resin to solidify is 48 h. So the employment of the resin enabled us to thoroughly examine the sample systems after the resin solidified, as well as to adjust the viscosity and contact angle by altering the resin compositions.

To ensure the equal distances between neighboring pairs of cylinders, wires of certain radii d were used, and arranged into a rose of angles of 120°. These roses were fastened on a glass base. The straws were then located

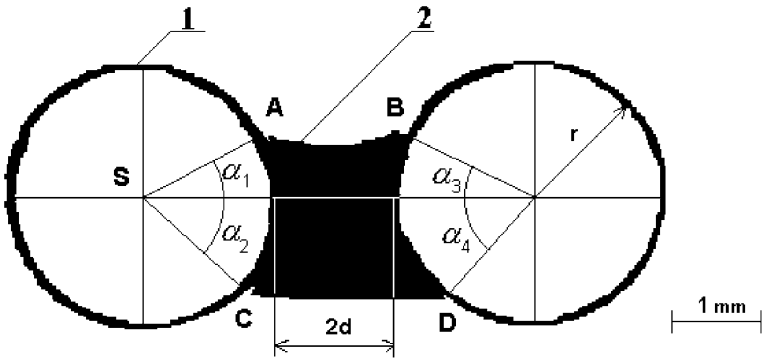

Fig. 13. The cross-section of the two straw systems with solidified resin between them. The straw (1) radius is denoted by r. The distance between straws is $2d$. The long column of resin (2) creates the triplet points A, B, C, and D that provide us with four angles α_1, α_2, α_3, α_4 the average of which is taken as the estimation of the covering angle α.

perpendicular to this bed close to the wire rose by their lower edges. Hence the distance $2d$ between cylinders was secured.

To further minimize the gravitational effects the glass base with the cylinders and applied resin was turned into horizontal position and slowly rotated all around the cylinder bound axis via a special apparatus during resin setting. Once the resin becomes hardened, the cylinder systems with "frozen" liquid columns were examined using a stereo-microscope with digital imaging system for angles and distances. We have prepared and examined more than 150 samples in this study.

A result for two-cylinder system with the "frozen" liquid processed by image analysis is shown in Fig. 13. The measured parameters include: the cylinder–cylinder separation $2d$, fiber radii r, wetting angles θ, and the covering angle α. Resultant values based on these measurements were utilized in constructing d/r–α graphs as shown in Fig. 14 for contact angles $\theta = 45^\circ$, and $\theta = 25^\circ$, respectively. The points represent the experimental data with standard deviations σ for the angle α and distance d, in comparison with the theoretical prediction in solid lines. It is obvious from Fig. 13 that gravity still affected the measurements of angles α because angles α_1 and α_2 in Fig. 13 were systematically larger than α_3 and α_4. To bypass this deviation from the theoretical assumption, we took the average values of all these four α's in plotting Fig. 14, and calculated the standard deviations for particular measurement using these four angles. So a general consistency is shown in between the experiment data and the predictions in both Fig. 14(a) for $\theta = 45^\circ$ and Fig. 14(b) for $\theta = 25^\circ$.

Systems composed of three cylinders were investigated with respect to the transition between split and channel-filling liquid columns. The distance $2d$, diameter $2r$, and the appearance of the hole in the center of the systems as shown in Fig. 15 were our main interests. All experiments have been done for various d/r values at the interval of contact angles within 25° and 45°.

The experimental data are then incorporated into the morphology diagrams in Fig. 16. An empty circle denotes the hole in the center due to the liquid-column disintegration while a filled one denotes the existence of the channel-filling liquid column. The predicted transition curves for $(d/r)'_{tr1}$, and $(d/r)'_{tr2}$ are plotted by solid lines. We can see in the Fig. 16(a) that the disintegration empty circles appeared mostly below the transition curve $(d/r)'_{tr1}$ (Line 1), and rarely between $(d/r)'_{tr1}$ (Line 1) and $(d/r)'_{tr2}$ (Line 2), never above the $(d/r)'_{tr2}$ (Line 2), validating nicely the predictions by the theory. On the other hand however, experimental channel-filling columns occurred even under the transition curve $(d/r)'_{tr1}$ (Line 1) as shown in Fig. 15(b), which is actually forbidden by the theory!

All the contact angle θ values 25°, 30°, 35°, 40°, and 45° used in plotting Fig. 16 were experimentally determined as shown in Fig. 17. A rod was perpendicularly plunged into the resin and the contact angle was measured directly by constructing a tangent line to the liquid surface in the triplet (liquid, solid, and air) point.

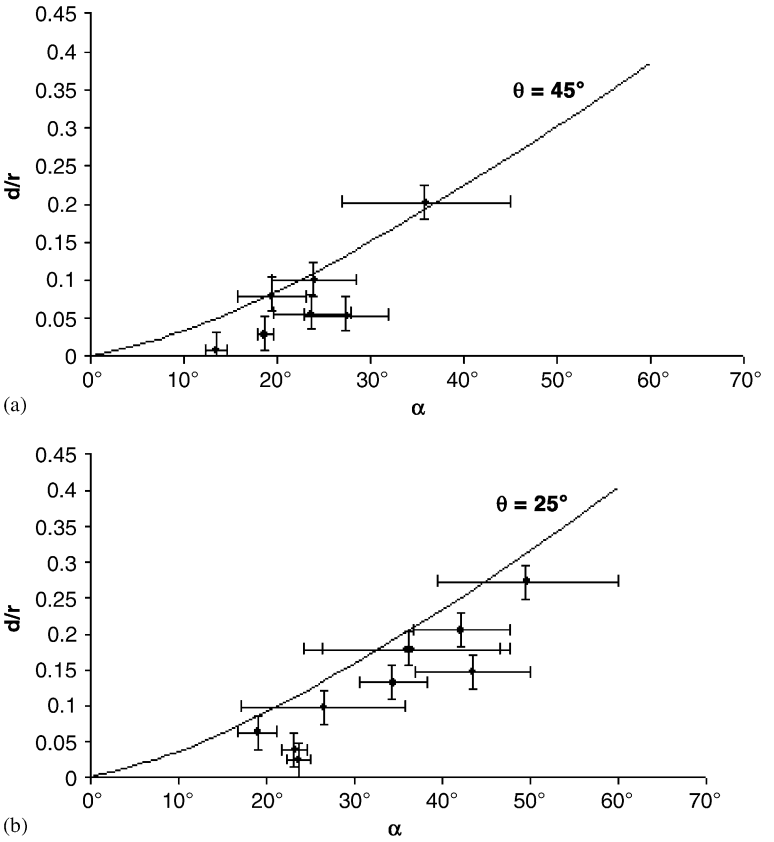

Fig. 14. Experimental data for the relationships between the dimensionless distance (d/r) on the covering angle α in two-straw systems are plotted with their standard deviations σ. The solid lines plot curves predicted by the theory. Fig. 14(a) is for the contact angle $\theta = 45^\circ$, while Fig. 14(b) depicted the relationship for $\theta = 25^\circ$.

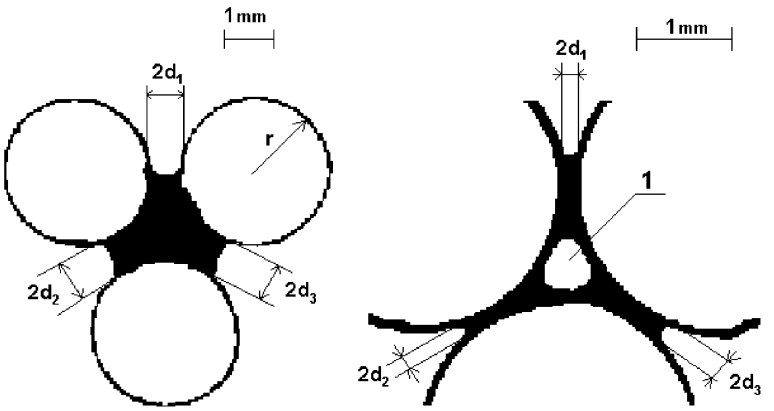

Fig. 15. The cross-sections of two three-straw systems with the solidified resin among them. The left part of the figure represents the channel-filling columns, while the right hand side belongs to the disintegrated ones. The straw–straw separation $2d$ from each experiment was obtained as the average value of three measurements of d_1, d_2, and d_3.

5. Concluding remarks

We have investigated the transitional wetting phenomenon occurring for both two, and three equidistant, parallel cylinders. As opposed to Princen's works [1–3] we extended our analysis to the complete wetting

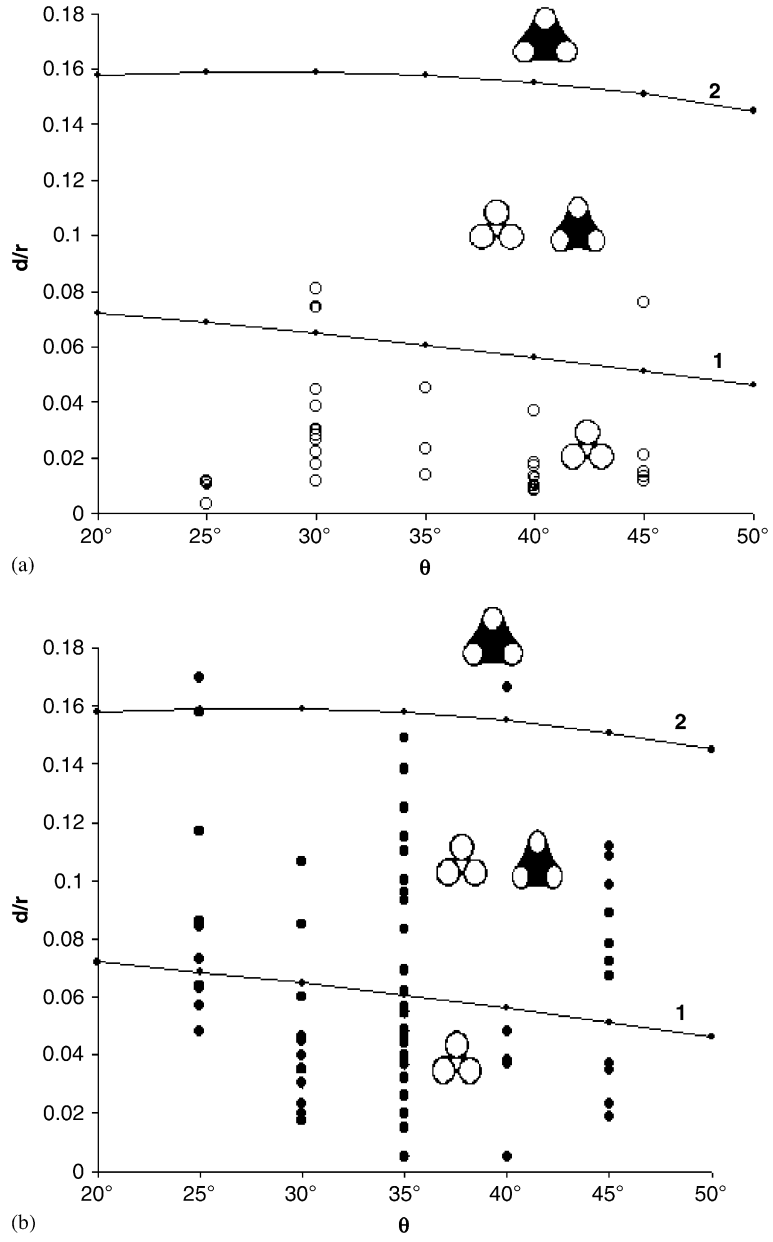

Fig. 16. Morphology diagrams of the transitions between disintegrated column and channel-filling column. These threshold values of d/r are denoted in the theory as $(d/r)'_{tr1}$ (the curve no. 1), and $(d/r)'_{tr2}$ (the curve no. 2). The empty circles in Fig. 16(a) reflect the disintegrated columns, whereas the filled points in Fig. 16(b) represent the channel-filling columns. The investigated interval of contact angles θ ranges from 25° to 45°.

instances, where $S>0$, and to the hypothetic situations $S<-2\gamma$. We have shown that unstable long liquid columns, in the regime of super-hydrophobicity, can exist theoretically even between pairs of parallel cylinders. The three-cylinder systems in this "completely non wetting" area exhibit both unstable and stable long liquid columns.

We have shown that a number of different morphologies of the wetting phase are possible. For instance for two-cylinder systems, liquid columns and unduloids are the only two alternatives; whereas three

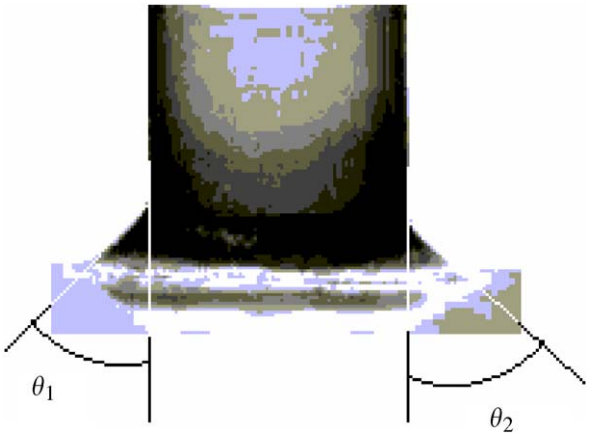

Fig. 17. The image of the straw partly plunged into the resin. This kind of images was used for the measurements of contact angles θ. Two contact angles θ_1 and θ_2 can be obtained from each image and averaged to give θ.

morphologies, multiple liquid columns, channel-filling column and unduloids, can be observed for the three-cylinder systems. With the theory developed in this work, we are able to predict the morphological transitions processes between different types of liquid columns and unduloids. All transition curves predicted in morphology diagrams exhibit transition hysteresis.

Our experiments provided data to verify our predictions. We focused on the dependence of the covering angle α on the dimensionless cylinder–cylinder distance d/r for systems composed of two-cylinders, and transition of the channel-filling liquid column to split columns for three-cylinder systems. The experimental data show consistency with the predictions on the morphological transitions, except in the case of channel-filling columns. This discrepancy can be attributed to the sensitivity of the experiments to impurities and alignment of cylinders that are supposed to be perfectly parallel with each other. We contemplate next to carry out a Monte Carlo simulation, based for instance on our works [10–13], to demonstrate the existence of transition hysteresis.

Acknowledgement

Lukáš, Chaloupek, and Košťáková would like to express their thanks to The Ministry of Education of the Czech Republic for the support of this work from the project CEP1-1M0554 in the frame of The Research Center for Advanced Conservation Technologies.

References

[1] H.M. Princen, Capillary Phenomena in assemblies of Parallel Cylinders: Capillary Rise between Two Cylinders, J. Colloid Interface Sci. 30 (1969) 69.
[2] H.M. Princen, Capillary Phenomena in Assemblies of parallel Cylinders: II. Capillary Rise in Systems with More Than Two Cylinders, J. Colloid Interface Sci. 30 (1969) 359.
[3] H.M. Princen, Capillary Phenomena in Assemblies of Parallel Cylinders: III. Liquid Columns between Horizontal Parallel Cylinders, J. Colloid Interface Sci. 34 (1970) 171.
[4] P.-G. de Gennes, F.D. Wyart-Brochard, D. Quere, Capillarity and Wetting Phenomena; Drops, Bubbles, Pearls, Waves, Springer, New York, Berlin, 2003.
[5] P. Lenz, R. Lipowsky, Morphological Transitions of Wetting Layers on Structured Surfaces, Phys. Rev. Lett. 80 (1998) 1920.
[6] Ryong-Joon Roe, Wetting of Fine Wires and Films by a Liquid Film, J. Colloid Interface Sci. 50 (1975) 70.
[7] H. Gau, S. Herminghaus, P. Lenz, R. Lipowsky, Liquid Morphologies on Structured Surfaces: From Microchannels to Microchips, Science 283 (1999) 46.
[8] P.S. Swain, R. Lipowsky, Wetting between Structured Surfaces: Liquid Bridges and Induced Forces, Europhys. Lett 49 (2000) 203.
[9] A.W. Adamson, A.T. Gast, Physical Chemistry of Surfaces, Wiley, New York, 1997.

[10] B.J. Carroll, Equilibrium Conformations of Liquid Drops on Thin Cylinders under Forces of Capillarity: A Theory for the Roll-up Process, Langmuir 2 (1985) 248.
[11] D. Lukas, E. Glazyrina, N. Pan, Computer Simulation of Liquid Wetting Dynamics in Fiber Structures Using the Ising Model, J. Text. Inst. 88 (1997) 149.
[12] D. Lukas, N. Pan, Wetting of a Fiber Bundle in Fibrous Structures, Polymer Composites 24 (2003) 314.
[13] D. Lukas, V. Soukupova, N. PAN, Computer Simulation of 3-D Liquid Transport in Fibrous Materials, Simulation 80 (2004) 547.

Příloha 2

Rampichova, M., Filova, E., Kolacna, L., Kostakova, E., Ocheretna, L.,Lukas, D., Lytvynets A., Amler, E.: Improved biological properties of non-woven PGA/PVA scaffolds for artificial cartilage, *FEBS Journal*, Vol 273, Suppl 1, June 2006, p. 269, IF = 3,790 (11)

M. Rampichova (35%), E. Filova (20%), L. Kolacna (2%), ***E. Kostakova (25%)****, L. Ocheretna (3%), D. Lukas (5%), A. Lytvynets (4%), E. Amler (6%)*

cytoplasmic (6.4%), centromere (3.4%) and mixed (11.3%). Anti-ENA ($n = 76$) and anti- ds DNA ($n = 145$) tests were performed in ANA positive serum samples. Anti-ENA detected by line immunoassay and Crithidia luciliae coated slides were used for detection of anti-ds DNA. Anti-ENA results are as follow; anti-SSA 4.1%, anti-Ro-52 10.8%, anti-RNP 2.7%, anti-Sm 1.4%, anti-Scl70 4.1%, anti-Cenp-B 1.4% anti-M2 1.4% and two or more pattern 37.8% . Anti-dsDNA found in 6.9% positive. In Conclusion, the data from this analysis are useful in estimating the probabilities of detecting specific ANA in our province.

Biocompatibility of Materials for Advanced Therapies

PP-710
In vitro cytotoxicity and genotoxicity of metallic and polymeric materials

S. Gülçe[1], S. İ. Gürhan[1], N. Hasırcı[2] and T. Endoğan[2]
[1]*Department of Bioengineering, Ege University, Izmir, Turkey*
[2]*Department of Chemistry, Middle East Technical University, Ankara, Turkey E-mail: sultangulce@yahoo.com*

Biomaterials are the materials that can replace whole or a part of the body tissues or organs. The most important property of the biomaterials is its biocompatibility. Tests to ensure the biological compatibility of materials have been specified by regulatory organizations. In this study; different metallic and polymeric materials were tested due to the test protocols of ISO and OECD. Metallic materials tested were; Ti grade 4, alloy 625, alloy 304 L, and alloy 321; and also three different polymeric materials, PMMA, PMMA + MMA and PMMA + MMA + HA were tested. Those consists of polymethylmetacrylate polymer, polymethylmetacrylate and methylmetacrylate monomer and, polymethylmetacrylate plus methylmetacrylate monomer and hydroxyapatite polymer respectively. To determine *in vitro* cytotoxicity of materials, cytotoxicity test with biomaterial extract and cell attachment tests were done. To determine genotoxicity of biomaterials, *in vitro* micronucleus assay with human peripheral blood lymphocytes were done. As a general result, metallic materials are more biocompatible than polymeric ones. If the metallic materials are compared among each other, Ti grade 4 is the least cytotoxic and genotoxic one; alloy 625, alloy 304 L, and alloy 321 (most toxic) follows it. And if we compare the polymeric materials among each other, PMMA is the most toxic one, PMMA + MMA + HA polymer found to be the least toxic. HA addition as a compound reduces cytotoxic and mutagenic effects of MMA monomers.

PP-711
Inhibitory effect of *Morus alba* L. on 3-hydroxy-3-methylglutaryl-coa(HMG-CoA) reductase

S.H. Kim[1], S.K. Oh[1], D.Y. Kwon[1], J.H. Seo[2], S.Y. Ryu[2], Y.S. Kim[2], **M.S. Koo**[1]
[1]*Food Functional Research Division, Korea Food Research Institute, Songnam-Si, Korea(South)* [2]*Korea Research Institute of Chemical Technology, Daejeon, Korea(South)*
E-mail: kiimmy@hanmail.net

HMG-CoA reductase catalyzes the first committed step in lipid (sterol, isoprenoide) biosynthesis. Therefore, inhibition of this enzyme is widely applied to the therapeutic method on the prevention of cardiovascular diseases (hypertension, coronary artery disease, stroke, bone and joint disease, cancer etc.) Syrian Hamster HMG-CoA reductase was overexpressed in *E. coli* and purified. The HMG-CoA reductase inhibitory activity was assayed spectrophotometrically which measured the rate of decrease in absorbance at 340 nm due to the oxidation of NADPH. The methanol extract of *Morus alba* L. was evaluated on the inhibitory effect of HMG-CoA reductase and partitioned to methylene chloride, ethyl acetate (EtOAc) and water soluble fraction. The EtOAc fraction of *Morus alba* L. exhibited a remarkable inhibitory effect of HMG-CoA reductase with 85% inhibition at the concentration of 40 μg/ml. The chromatographic separation of the EtOAc fraction of *Morus alba* L. led to the isolation of three compounds, sanggenon C, mordacin P, and daucosterol. Their structures were established by chemical and spectroscopic methods. Sanggenon C and mordacin P showed significant inhibitory effect on HMG-CoA reductase with 73%, 90% inhibition at the concentration of 40 μg/ml. These results indicate that sanggenon C and mordacin P are to be active compounds of *Morus alba* L. with HMG-CoA reductase inhibitory action.

PP-712
Improved biological properties of non-woven PGA/PVA scaffolds for artificial cartilage

M. Rampichova[1], E. Filova[2], L. Kolacna[2], E. Kostakova[3], L. Ocheretna[3], D. Lukas[3], A. Lytvinets[4] and E. Amler[5]
[1]*Institute of Experimental Medicine, Academy of Sciences of the Czech Republic, Prague, Czech Republic Institute of Physiology, Academy of Sciences of the Czech Republic, Prague, Czech Republic,* [2]*Institute of Experimental Medicine, Academy of Sciences of the Czech Republic, Prague, Czech Republic,* [3]*Faculty of Textile Engineering, Technical University of Liberec, Liberec, Czech Republic,* [4]*Institute of Physiology, Academy of Sciences of the Czech Republic, Prague, Czech Republic,* [5]*Institute of Experimental Medicine, Academy of Sciences of the Czech Republic, Prague, Czech Republic Institute of Biophysics, 2nd Faculty of Medicine, Charles University, Prague, Czech Republic.*
E-mail: m.rampichova@centrum.cz

Polyglycolic acid (PGA) and polyvinylalcohol (PVA) are biodegradable polymers commonly used in medical practice. Our study was focused on PGA and PVA scaffolds for artificial cartilages. The scaffolds were prepared by the wet-laid method. PGA/PVA scaffolds were subsequently treated with PVA solution (PVA/PGA/PVA scaffolds), PGA scaffolds with hyaluronic acid solution (PGA/HA scaffolds) and/or subsequently processed by needle punching (PGA/PVA and PGA/HA scaffolds). Supplementation with nanofibres was also employed. Chondrocytes cultured on polystyrene (PS) were used as a control. Rabbit chondrocytes were cultured for 28 days and seeded onto the scaffolds at a density of 8×104 cells/cm^2. Proliferation and viability of chondrocytes were tested using the MTT test, fluorescence and confocal microscopy. The absorbance of PVA/PGA/PVA, PGA and PS cultured cells 24 h after seeding was significantly higher compared with the other scaffolds. After 7, 14, and 21 days, scaffolds containing PVA (PVA/PGA, PVA/PGA/PVA) showed the highest proliferation rate, comparable with polystyrene cultures. A good pH stability of culture medium was observed. On the other hand, scaffolds prepared with HA showed the lowest proliferation of chondrocytes, accompanied by acidification of the culture medium. In this study, the best proliferation of chondrocytes on three-dimensional non-woven PVA/PGA, PVA/PGA/

PVA scaffolds was shown. These results prove their potential for cartilage repair utilization.

PP-713
Investigation of the model protein interaction with novel di-block copolymers

A. Asady and M. N. Sarbolouky
Institute of Biochemistry and Biophysics, University of Tehran, Tehran, Iran. E-mail: asady@ibb.ut.ac.ir

Amphiphilic di-block copolymers are typical nonionic polymeric surfactants with tunable hydrophilic and hydrophobic segments (synthesized here) was used to study of their effects on bovine serum albumin and lysozyme as a model proteins. Effects of different biodegradable di-block copolymers on the thermal stability and conformation of proteins in aqueous solution was studied by UV-Vis, flouresence and (near and far) UV-CD spectroscopic techniques. Results showed that these polymers have negligible effects on structure and a little or no increase thermal stability of these proteins. It can be concluded that these polymers are compatible for proteins and hence may be used as additives for several proteins and good candidates for drug delivery purposes and protein pharmaceuticals

Parasitic Diseases

PP-714
New approach aimed at investigation of genomic polymorphism of the Russian *M. tuberculosis* population

N. A. Gvozdevskiy[1], T. L. Azhikina[1], A. O. Botvinnik[1], I. Y. Evsyukova[1], I. G. Shemyakin[2] and E. D. Sverdlov[1]
[1]Russian Academy of Science, Shemyakin-Ovchinnikov Institute of Bioorganic Chemistry, Moscow, Russia, [2]State Research Center for Applied Microbiology, Obolensk, Moscow reg., Russia. E-mail: zasulich80@yahoo.com

Mycobacterial population are characterized by considerable genetic heterogeneity. The purpose of our work was identification of genomic differences among various strains of *M. tuberculosis* that would help to better understand mechanisms of their functional differences. We compared genomes of four clinical strains widespread in Russia with the laboratory strain H37Rv by subtractive hybridization. The majority of the found insertions were shared by all the strains, with remarkable exception for 1540 that possess a peculiar genes, absent from other clinical strains. It is significant that among the strains under study 1540 reveals the highest virulence. Two of the differential genes encode putative membrane proteins and may be supposed to change the way of *Mycobacterium* interaction with a host cell, enhancing virulent properties of the strain. With the differences obtained using genomic PCR method we developed diagnostic tool called ID-typing aimed at identification of mycobacterial strains. 172 Russian clinical strain were analysed with the technique to characterize the population structure. We demonstrated good general correlation of the grouping results obtained by ID-typing with other methods in use such as spoligotyping and IS RFLP-typing. Since identification of unknown strains can be achieved quickly and at low cost in terms of consumables and equipment, ID typing may serve as a powerful complement to the existing epidemiological tools for the *M. tuberculosis* complex.

PP-715
L-proline and glucose transport in intracellular forms of *Trypanosoma cruzi*.

A. M. Silber[1], R. R. Tonelli[2], W. Colli[2] and M. J. Manso Alves[2]
[1]Departamento de Fisiologia, Instituto de Biociências, Universidade de São Paulo, São Paulo, Brasil, [2]Departamento de Bioquímica, Instituto de Química, Universidade de São Paulo, São Paulo, Brasil. E-mail: asilber@iq.usp.br

Trypanosoma cruzi, the etiological agent of Chagas' disease affecting 16–18 million people in the Americas and with 80–100 million people at risk, has an obligatory intracellular cycle in the mammalian host. This intracellular cycle initiates with the invasion of mammalian cells by trypomastigotes (TRY) followed by a sequence of differentiation steps into amastigotes (AMA), intracellular epimastigote (IE), and again into TRY. The uptake of glucose and proline, the main energy and carbon sources of the parasite, and the intracellular free proline concentration were determined along the intracellular cycle of *T. cruzi*. Employing the host cell line CHO-K_1 (auxotrophic for this amino acid) it was established that proline is important for the differentiation of IE to TRY and, consequently, for the burst of TRY. IE has the highest proline transport activity (30 and 13 times higher than TRY and AMA, respectively) and the lowest free proline concentration (0.7 mM, in comparison to 6.6 mM for AMA and 2.7 mM for TRY). Conversely, the transport of glucose is 3.5 higher in TRY than in IE. No glucose transport was detected in AMA. Thus: (a) L-proline is essential for the differentiation of IE to TRY; (b) along the mammalian infection a metabolic switch occurs in the parasite from a glucose to a proline-based metabolism. These facts point to the proline transport and metabolism as targets for the development of therapeutic drugs.
Acknowledgment: Supported by: FAPESP and CNPq.

PP-716
Odorant-binding protein (OBP) genes in mosquitoes

M. S. Sengul and Z. Tu
Department of Biochemistry, Virginia Polytechnic Institute and State University, Blacksburg, VA, USA. E-mail: msengul@vt.edu

Olfaction plays a crucial role in host-seeking behaviour of mosquitoes. Odorant-binding proteins (OBPs) are one of the key components of the olfactory pathways in insects and are believed to bind and transport odorants to odorant receptors in olfactory sensory neurons. Little is known of the structural and functional properties as well as the regulation of OBP genes in mosquitoes. Here we report the identification of the selected OBP genes among different mosquito species by bacterial artificial chromosome (BAC) library screening. Multi-species comparison of the upstream regions of the orthologous OBP genes identified conserved non-coding regions, which might be potential regulatory elements of these genes. We characterized the complete gene structure of two OBP genes in Anopheles stephensi, named Ast-OBP1 and Ast-OBP7 because of its high amino acid similarity with Anopheles gambiae AgOBP1 and AgOBP7 respectively. The genome segments containing these two genes share conservation of gene order among mosquitoes as well. We also determined

Příloha 3

Kolacna, L., Bakesová, J., Varga, F., Kostakova, E., Planka, L., Necas, A., Lukas, D., Amler, E., Pelouch, V.: Biochemical and biophysical aspects of collagen nanostructure in the extracellular matrix, Physiol. Res.; 56 (Suppl. 1) Biophysics in Mecial Research, pg.51-60. (2007), IF = 1,555 (11)

Koláčná 40 %, Bakešová 3 %, Varga 15 %, ***Košťáková 3 %,*** *Plánka 3 %, Nečas 3 %, Lukáš 3 % , Amler 15 %, Pelouch 15 %*

Physiol. Res. 56 (Suppl. 1): S51-S60, 2007

Biochemical and Biophysical Aspects of Collagen Nanostructure in the Extracellular Matrix

L. KOLÁČNÁ[1,2], J. BAKEŠOVÁ[3], F. VARGA[1], E. KOŠŤÁKOVÁ[4], L. PLÁNKA[6], A. NEČAS[7], D. LUKÁŠ[4], E. AMLER[1,2], V. PELOUCH[3,5]

[1]Institute of Biophysics, Second Faculty of Medicine, Charles University, Prague, [2]Laboratory of Tissue Engineering, Institute of Experimental Medicine, Academy of Sciences of the Czech Republic, Prague, [3]Department of Medical Chemistry and Biochemistry, Second Faculty of Medicine, Charles University, Prague, [4]Department of Nonwoven Textiles, Faculty of Textile Engineering, Technical University, Liberec, [5]Center for Cardiovascular Research, Prague, [6]Department of Pediatric Surgery, Orthopedics and Traumatology, Masaryk University, Brno and [7]Department of Surgery and Orthopedics, Small Animal Clinic, Faculty of Veterinary Medicine, University of Veterinary and Pharmaceutical Sciences Brno, Czech Republic

Received May 23, 2007
Accepted May 29, 2007
On-line available May 31, 2007

Summary

ECM is composed of different collagenous and non-collagenous proteins. Collagen nanofibers play a dominant role in maintaining the biological and structural integrity of various tissues and organs, including bone, skin, tendon, blood vessels, and cartilage. Artificial collagen nanofibers are increasingly significant in numerous tissue engineering applications and seem to be ideal scaffolds for cell growth and proliferation. The modern tissue engineering task is to develop three-dimensional scaffolds of appropriate biological and biomechanical properties, at the same time mimicking the natural extracellular matrix and promoting tissue regeneration. Furthermore, it should be biodegradable, bioresorbable and non-inflammatory, should provide sufficient nutrient supply and have appropriate viscoelasticity and strength. Attributed to collagen features mentioned above, collagen fibers represent an obvious appropriate material for tissue engineering scaffolds. The aim of this minireview is, besides encapsulation of the basic biochemical and biophysical properties of collagen, to summarize the most promising modern methods and technologies for production of collagen nanofibers and scaffolds for artificial tissue development.

Key words

Collagen • Extracellular matrix • Nanofibers • Biomechanical properties • Scaffold

The extracellular matrix (ECM) plays a substantial role in both prenatal and postnatal development of organs and in rebuilding of organs during many pathological situations (Pelouch *et al.* 1995, Adamcova *et al.* 2003, Simko *et al.* 2005, Vanhoutte *et al.* 2006). Its biochemical and biophysical properties are responsible for integrity of individual cells, migration, adhesion, nutrition and differentiation of cells,

angiogenesis and formation of intracellular contacts. Moreover, ECM forms contact sites between (cardio)myocytes and fibroblasts both in skeletal and myocardial muscles and participates also in the migration of some specified cells as well as in proteolysis (via apoptosis). Therefore, ECM plays an active role in both physiological and pathophysiological remodelations (Herget *et al.* 1996, Kolar *et al.* 1998).

ECM composition and biochemistry

ECM is composed of collagenous (different collagen types) as well as non-collagenous proteins, such as elastin, fibronectin, laminin or entactin. Most of them are glycosylated with sugar content ranging between 5 and 10 %. There is also a significant content of proteoglycans (e.g., perlecan) in ECM (Pelouch *et al.* 1993, Pelouch *et al.* 1995). The synthesis of those proteins is predominantly under the effect of many growth factors, catecholamines and cytokines. Their degradation, on the other hand, is due to the effect of metalloproteinases (MMPs) – enzymes containing Zn^{2+} and they need Ca^{2+} ions for their activation). The family of MMPs could be divided into a few groups (e.g. collagenases, gelatinases) – they either cleave the molecule of different collagen types or other ECM proteins into very precisely defined fragments or MMPs splitting off only previously formed fragments; for details see Kukacka *et al.* (2005), Janssens and Lijnen (2006), Vanhoutte *et al.* (2006). The turnover all ECM proteins is very slow.

The principal structural elements of ECM are, however, formed by collagens. They play a dominant role in maintaining the biological and structural integrity of various tissues and organs, including bone, skin, muscle, tendon, blood vessels, and cartilage. Collagens are a family of closely related but distinct extracellular matrix proteins. Collagen type I usually consists of three coiled subunits: two α1(I) and one α2(I) chains forming fibrils of 50 nm in diameter; collagen type II is composed of three identical α1(II) chains forming fibrils less than 80 nm in diameter; collagen type III fibrils are formed from three α1(III) chains resulting in diverse fibril diameters between 30 and 130 nm (Bowlin 2002, Matthews *et al.* 2002, Matthews *et al.* 2003). The important role of collagens in maintaining the extracellular structure resulted in numerous tissue engineering applications, employing collagen as an ideal scaffold or matrix for cell growth and proliferation (Yang *et al.* 2004).

Family of collagens

The family of collagens is mainly composed of fibrillar collagens, collagens with globular domains and other collagen structures. A total of 44 genes for 26 collagen types were described up to now; they are divided according to their supramolecular structure into 9 groups; most collagens are associated either with different proteins of ECM or with a another collagen type. The primary sequence of amino acids is characteristic: -*GLY-X -Y* -; every third amino acid is glycine, in position X there are different amino acids; however, proline is typical of this position, in the Y position there are different amino acids but approximately every seventh position of Y is occupied by hydroxyproline. Three α-chains form the polypetide structure of each collagen type: they are either identical (homotrimer) or only two chains are the same (two times α1) and the last chain is different (α2) = heterotrimer. Alpha-chains are characteristic for each collagen type: the chains are numbered according to the respective collagen type.

The structure of three major collagen types is given as examples: $[\alpha1(III)_3]$ is the structure of homotrimer in collagen III, $[\alpha1(I)_2\ \alpha2(I)]$ is the structure of heterotrimer in collagen I,

$[\alpha1(I)]_3$ is the structure of homotrimer in collagen I. Both heterotrimer of collagen I (up to 80 %) and homotrimer of collagen III (up to 10 %) are the major collagen types in adult tissues of different organs (e.g. muscle, skin, bone). During embryonic life, a relatively high amount of collagen III, together with homotrimer of collagen I, was detected in different organs (Pakkanen *et al.* 2003).

Biosynthesis of collagen molecules is a stepwise procedure; it starts in the endoplasmic reticulum where different posttranslational reactions occur. The first step is hydroxylation; it is the effect of different enzymes: both prolyl-4-hydroxylase and prolyl-3-hydroxylase (formation of hydroxyproline - HYP) and lysyl-hydroxylase (formation of hydroxylysine - HYL). The second step is N-glycosylation (transfer of either glucose or galactose to some HYL) via transferase mechanisms; these steps prepare three collagen chains for the procollagen structure. Finally, both N- and C-terminal proteinases remove the sequences from both collagen ends. Furthermore, there comes the association of three molecules of collagen of appropriated propeptides. Then the new structure is transferred into the extracelular compartment. Moreover, covalent cross-links arise among different both inter- and intramolecular chains of

collagens; it is due to the effect of enzyme: lysyloxidase (Pelouch *et al.* 1993, Maki and Kivirikko 2001, Myllyharju and Kivirikko 2004).

The high stability of collagen molecules is caused by the presence of an -OH group in HYP on the pyrollidine ring; however, it is not due to hydrogen bridges or to the water net around the molecules. Oxygen in -OH group stabilizes the peptide bond despite the inductive effect and so higher thermal stability of three-stranded polypeptide units; the evidence for it was provided by experiments where several 4-HYP were exchanged for 4-fluoroproline (Holmgren *et al.* 1998). Fibrillar collagens are synthesized from their procollagen; carboxy- and amino- terminal propeptides are cleaved.

Prolyl-4-hydroxylase (P4H) (EC 1.14.11.2) is the key enzyme of collagen synthesis: it catalyzes hydroxylation of proline on 4-HYP. There are two isoforms of this P4H: the first one is localized in luminal ER, the second one in either the cytosol or in the nuclear compartment where it hydrolyzes HIF (hypoxia-inducible factor); PH4 is a tetramer ($\alpha_2\beta_2$) – thw α-subunit has three isoforms (I, II, III; however, I is dominant), the β-subunit is identical with proteindisulfidic isomerase (PDI, EC 5.3.4.1). Hydroxylation of proline to hydroxyproline by P4H occurs in the presence of oxygen only. Moreover, decarboxylation of 2-oxoglutarate requires both Fe^{2+} and ascorbate and the minimum sequence of *-X-Pro-Gly-*.

Lysylhydroxylase (EC 1.14.11.4) is a protein tightly bound to the ER membrane; three isoforms of the enzyme are responsible for hydroxylation of some lysine to hydroxylysine (HYL – in both collagen and other ECM proteins). This procedure is the same as was described above and the minimum sequence for enzyme action is *-X-Lys-Gly-*; the function of HYL is both stabilization of intramolecular cross-linking and of the newly formed -OH groups; these groups can bind monosaccharides (galactose or glucosylgalactose). Hydroxylated and glycosylated chains are organized into triads, using the same mechanism of disulfide bridges in the presence of PDI as was described for the β-subunit of P4H. The functional reason is still a matter of speculations but the formation of ECM fibrils and specific properties of basal membrane occurring in collagen IV are known to be due to thesugar moiety (Rautavuoma *et al.* 2002).

Other ECM proteins and cytoskeletal structures

Fibronectin is localized in both the extracellular matrix of different cells and extracellular fluid (blood plasma). Its dimer is composed of two subunits bound together in the C-terminal parts by disulfide bridges; various amounts of sugar contamination were found in different organs (Kim *et al.* 1999, Sharma *et al.* 1999). Fibronectin has an important role in the organization of ECM. *Laminins*, the most important non-collagenous glycoproteins in ECM, are composed of three different chains connected by disulfide bridges. They participate in both cell adhesion and differentiation. Laminins, often bound to collagen type IV, are responsible for both selective filtration of different metabolites and connections between the cell and the ECM (Paulsson *et al.* 1991, Nomizu *et al.* 1994, Kim *et al.* 1999). *Perlecan* is a typical proteoglycan of basal membranes; the structure of this protein is responsible for cell adhesion and regulation of cell growth (Murdoch *et al.* 1992). There are many other ECM proteins, such as *desmin*. Desmin is responsible for the structural properties of ECM in different muscles and for connection of neighboring sarcomeres. Then there are *tubulin, vinculin, vimentin, dystrofin, actin, talin* or *spectrin*. Their physiological and pathological roles remain still not fully understood (Heling *et al.* 2000).

Collagen nanostructure tissue engineering aspects

Collagen fibers seem to be crucial for tissue engineering also from the biophysical point of view. They transmit forces, dissipate energy, prevent premature mechanical failure and provide biological signals to adjacent cells that regulate functional responses (Huang *et al.* 2001). Moreover, collagen is resorbable, it has high water affinity, low antigenicity, very good cell compatibility and ability to promote tissue regeneration. The most abundant collagens in the ECM are collagen types I, II and III. Other substances, such as proteoglycans, glycosaminoglycan and various minerals, are important components of ECM (Teo *et al.* 2006).

The modern tissue engineering task is to develop three-dimensional scaffolds of appropriate biological and biomechanical properties, at the same time mimicking the natural ECM and promoting tissue regeneration. The scaffold should permit cell adhesion, infiltration, and proliferation for ECM synthesis. Furthermore, it should be biodegradable, bioresorbable and non-inflammatory, should provide sufficient nutrient supply and have appropriate viscoelasticity and strength. Attributed to collagen features mentioned above, collagen fibers represent an obvious appropriate material for tissue engineering scaffolds.

Electrospinning, a suitable technique for the production of small-diameter fibers. It has been developed in the first half of the 20th century (Formhals 1932, Taylor 1969). Recently, Reneker and coworkers have investigated the process in more detail (Reneker and Chun 1996, Reneker *et al.* 2000). It uses an electrical field to control the formation and deposition of polymer fibers on a target surface. It is remarkably efficient, rapid and inexpensive (Matthews *et al.* 2002). A polymer solution is injected through a thin needle opposite to a collecting target. At a critical voltage, the charge imbalance overcomes the surface tension of the polymer solution, forming an electrically charged jet. Within the electric field, the jet is directed toward the grounded target, the solvent evaporates, the jet becomes thinner via its whipping and fibers are formed. On the grounded target, the single fibers are deposited as a non-woven highly porous mesh (Bowlin 2002, Buttafoco *et al.* 2006). Placing a rotating collector between the needle and the grounded plate allows deposition of the fibers on the collector with a certain alignment. Fiber orientation involves proper interaction with the cellular environment as well as strength and function of the engineered tissue (Deitzel *et al.* 2001, Xu *et al.* 2004, Zhong *et al.* 2006). Synthetic non-biodegradable polymers, biodegradable polymers, natural polymers, composites and even ceramic precursors can be electrospun to form nanofibers.

During the last decay a lot of effort has been spent to enhance electrospinnig productivity via the development of so-called needle-less methods. Needle-less electrospinning concerns self-organization of polymeric jets on free liquid surfaces and is a result of electrohydrodynamics on the surface. Electrohydro-dynamic analysis reveals the development of unstable surface waves, depending on the strength of the external electrostatic field. Although physically similar, theoretical considerations show substantial differences between needle and needle-less electrospinning. The dependence of critical field strength on the polymeric solution surface tension, self-organization of jets and the fact that jetting density in the instance of needle-less electrospinning depends on the field strength value, are notable. The needle-less electrospinning is supported with various electric field strength concentrators. Thus, the polymeric materials are spread on cylindrical surfaces (Jirsak *et al.* 2005) or on spikes of magnetic liquids (Yarin and Zussman 2004).

The electrospinning process has the potential to produce collagen fibrils that closely mimic and at some point may even fully reproduce the structural and biological properties of the natural fiber. *In vitro* and *in vivo* experiments demonstrate that electrospun scaffolds hold great potential for tissue engineering applications.

Fiber size was shown to be crucial for proper interaction of the scaffold with cell and tissue formation (i.e. for cell morphology, adhesion, migration, proliferation, and differentiation). The wide range of possible fiber diameters permits a large variation in the production of tissue engineering scaffolds via electrospinning (Bowlin 2002). The possibility to produce meshes with a high surface area makes electrospinning an ideal procedure for scaffold design in tissue engineering (Li *et al.* 2002). Furthermore, the architecture of the produced non-woven meshes is similar to extracellular matrices (Xu *et al.* 2004). Nanofibrous scaffolds are highly porous. The pore size, much smaller than the normal cell size, inhibits cell migration. In spite of this fact, the results indicate the capacity of nanofibrous meshes to infiltrate cells (Zhang *et al.* 2005). The cells entering into the matrix through ameboid movement to migrate through the pores can push the surrounding fibers aside to expand the pore. The dynamic architecture of the fibers allows the cells to adjust according to the pore size and grow into the nanofiber matrices. In spite of producing typical electrospun fibers in the form of two-dimensional non-woven meshes, three-dimensional scaffolds consisting of aligned fibers and tubular scaffolds can be made. Synthetic materials with superior mechanical strength lack the cell-recognition signal (Kim and Mooney 1998); scaffold constructed from naturally occurring proteins in the ECM, such as collagen, allows much better infiltration of cells into the scaffold. For many tissue engineering applications nanofiber modifications are necessary to achieve the required scaffold properties. Polymer blending, co-electrospinning, multilayering and mixing for nanofiber production or cross-linking, surface modifications and coating of the scaffold can improve the stability and biocompatibility.

Many surface modifications were used to modify the synthetic polymer and to bring ECM components onto the scaffold surface. Collagen-coated poly(L-lactic acid)-*co*-poly(ε-caprolactone) nanofiber mesh with mechanical properties suitable for vascular graft enhanced endothelialization and preserved phenotype of human coronary artery endothelial cells, as shown by increased spreading, cell viability, attachment and phenotypic maintenance (He *et al.* 2005a, b).

Blended nanomaterials possess the potential of adding various ingredients (e.g. growth factors) according to cell-type requirements. Blended nanoscaffold, prepared from collagen with chondroitin sulfate, exhibited after cross-linking excellent biocompatibility when seeded with rabbit conjunctiva fibroblasts. Combination of nanofibrous collagen-glycosaminoglycan scaffold prepared from natural ECM components seems to mimic closely the ECM and thus has a great potential in tissue engineering applications (Zhong *et al.* 2005).

In multilayering electrospinning, after electrospinning the first component, the second polymer is sequentially electrospun on the same target producing a multilayerd meshes with hierarchically ordered layers made from particular fibers. For example, a trilayered electrospun mesh, composed from type I collagen, styrenatedgelatin, and segmented polyurethane were prepared; a bilayered tubular construct composed of a thick segmented polyurethane microfiber mesh as an outer layer and a thin type I collagen nanofiber mesh as an inner layer was fabricated (Kidoaki *et al.* 2005).

Different polymers are simultaneously electrospun from different syringes under special conditions in the mixing electrospinning. The produced fibers are mixed on the same collector, resulting in the formation of a mixed fiber mesh, e.g. mixed electrospun-fiber mesh composed of segmented polyurethane and polyethylene oxide (Kidoaki *et al.* 2005). Scaffolds can better mimic the extracellular matrix and thus promote tissue regeneration.

The aligned nanofibrous collagen scaffold with distinct fiber alignment fabricated using a rotational wheel collector was used to evaluate the alignment effect on cell orientation. Collagen nanofibers were cross-linked in glutaraldehyde vapor and seeded with rabbit conjunctiva fibroblasts. Decreased cell adhesion but increased proliferation were found on aligned collagen scaffold when compared with random collagen. Most cells on aligned scaffold adhere and elongate themselves along the nanofiber alignment direction, while the random scaffold provided cell spread in all directions. The elongated proliferation pattern of the cells coincides with the native tissue cell morphology (Zhong *et al.* 2006).

Collagen types I, II and III were successfully electrospun (Buttafoco *et al.* 2006, Casper *et al.* 2007). The fiber diameter and structural properties produced by electrospinning depend on the collagen type, tissue origin and concentration (Matthews *et al.* 2002, Matthews *et al.* 2003). Optimizing conditions for calf-skin type I collagen produced a matrix composed of 100-nm fibers that exhibited the 67-nm banding pattern that is characteristic of native collagen (Matthews *et al.* 2002). Because of the solubility of collagen fibers, different methods of fiber cross-linking are used to stabilize fibrous scaffolds (Kidoaki *et al.* 2005, Li *et al.* 2005, Buttafoco *et al.* 2006, Casper *et al.* 2007). Some applications of collagen nanofibrous scaffolds are mentioned below.

Cartilage grafts. Cartilage is predominantly composed of collagen type II. Matthews *et al.* (2003) report electrospun chicken sternal cartilage collagen type II to form fibers 0.11–1.8 μm in diameter. The scaffold fixed in glutaraldehyde vapor support cell growth, human articular chondrocytes can freely penetrate the matrix and are readily infiltrated.

A significant difference was identified between the noncross-linked and the cross-linked scaffolds when comparing scaffold thickness and fiber diameter (Shields *et al.* 2004). The electrospun noncross-linked scaffolds were stiffer but were not able to attain as high a tensile strength as native cartilage. Vapor-glutaraldehyde cross-linked scaffolds seeded with human articular chondrocytes revealed the potential of the scaffold for articular cartilage repair.

Three-dimensional nanofibrous matrices from poly-L-lactic acid and poly(ε-CBZ-lysine) (carbobenzoxy-protected L-lysine) with free NH_2 groups for the covalent binding of recombinant collagen II variants were prepared and human chondrocyte attachment to collagen type II with differently deleted D periods was analyzed (Fertala *et al.* 2001).

Skin grafts. With collagen type I nanofibers cross-linked by glutaraldehyde vapor, a relatively low adhesion of human oral keratinocytes was observed (Rho *et al.* 2006). ECM protein coating of this matrix, specifically treatment with type I collagen or laminin, promoted cell adhesion and spreading of cells as a consequence of the great surface area available for cell attachment and of the restoration of biological and structural properties of natural ECM proteins. Polycaprolactone (PCL) and collagen represent a favorable matrix for preparing a dermal substitute for engineering skin. PCL nanofiber membrane coated with collagen shows good growth, proliferation and migration inside the matrix of human dermal fibroblasts (Venugopal and Ramakrishna 2005). Venugopal *et al.* successfully used blended collagen type I and PCL nanofibers for culture of human dermal fibroblasts (Venugopal *et al.*

2006). Matrices promoted cell adhesion, proliferation and spreading and have the potential for skin defect and burn wound healing. Two different methods of nanofiber coating were investigated for human dermal fibroblast skin graft preparation – coaxial electrospinning with collagen type I as shell material and wrapped PLC core component, and post-coating by immersing the PLC nanofibrous scaffold into collagen solution (Zhang *et al.* 2005). Coaxial electrospinning resulted in individually surface-coated nanofibers, while a rough surface coating was accomplished by soaking nanofibers in a coating medium. Individually collagen-coated nanofibers resembled the natural ECM rather than the rough collagen coating and encouraged human dermal fibroblast migration into the scaffold and cell proliferation.

Cardiovascular grafts. In tissue engineering of blood vessels, collagen constructs have a limited applicability due to lack of structural integrity when subjected to intraluminal physiological pressure. Electrospinning of blended solutions of collagen and elastin results in materials of high porosity, surface area and fibers with extraordinary mechanical properties. Furthermore, electrospinning of solutions separately can be utilized for the production of multilayered scaffolds with controlled morphology and/or mechanical properties (Buttafoco *et al.* 2006). Besides the required biomechanical properties, cell proliferation and adhesion parameters, vascular grafts should have anti-coagulant activity until the endothelial cell lining is fully achieved.

Vascular graft scaffolds have been fabricated using electrospun polymer blends of collagen type I, elastin and poly(D,L-lactide-*co*-glycolide) with a length of 12 cm and a thickness of 1 mm. The scaffolds possess tissue composition and mechanical properties similar to native vessels. The electrospun vessel matrix is biocompatible for bovine endothelial and smooth muscle cells, seeded separately or on either side, as well as *in vivo* subcutaneously implanted in mice (Stitzel *et al.* 2006). The equimolar copolyester poly(L-lactide-*co*-ε-caprolactone) (PLCL) was co-electrospun with collagen type I. The tensile strength was decreased with increasing collagen content. Human umbilical vein endothelial cells were highly elongated and well spread on the fibrous matrices containing 5 and 10 % collagen, while round or restricted spread cells were observed on the 30–50 % collagen-blended PLCL scaffolds (Kwon and Matsuda 2005). On the other hand, collagen-blended PLCL (70:30) nanofibers supported endothelialization – enhanced the viability, spreading, and attachment of human coronary artery endothelial cells and preserved the phenotype (He *et al.* 2005a, b). Homogeneous fibers were prepared from calf skin collagen type I and elastin solution with addition of poly(ethylene oxide) and NaCl. On scaffolds, cross-linking with N-(3-dimethylamino-propyl)-N´-ethylcarbodiimide hydrochloride and N-hydroxysuccinimide, smooth muscle cells were successfully cultured and a confluent layer of cells was observed after 2 weeks on the surface (Buttafoco *et al.* 2006).

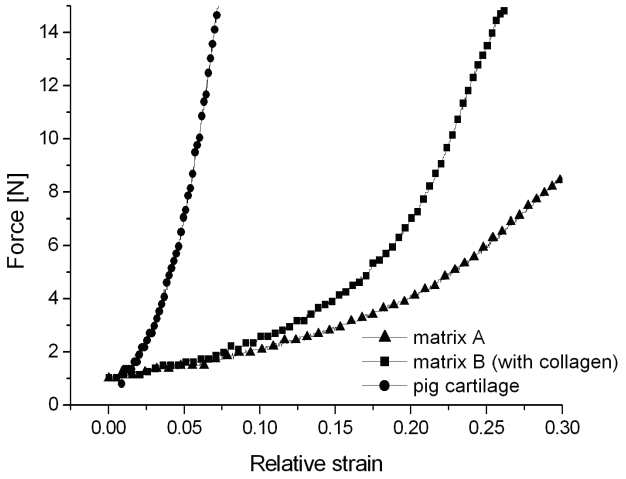

Fig. 1. Loading diagrams of native pig joint cartilage and fibrin-glue-based matrices A and B, where matrix B contains 9 % of collagen in volume.

Collagen in native tissue seems to be a key element for the cartilage structural network. Collagen fibers provide the cartilage with its tensile stiffness and strength. On the other hand, collagen fibers show only a little resistance to compression or shear. Different orientation of collagen fibrils, however, can significantly influence the mechanical properties of individual native cartilage layers (cartilage anisotropy). Random orientation of collagen fibers implies a lower tensile modulus than their parallel orientation. Though the role of proteoglycans is reported to be crucial for compressive properties of cartilage tissue, involvement of collagen is undoubtedly important as well. Different chemical composition and different techniques of scaffold preparation can significantly modify the biomechanical properties of the scaffold and, consequently, after cell seeding also of artificial tissue.

The essential role of collagen on cartilage biomechanics is presented in Fig. 1. There were three samples tested: native cadaveric pig joint cartilage and two different fibrin matrices. The matrices were formed from fibrin glue based on Tissuecol® Kit, one of them

(matrix B) containing 9 % of collagen in volume. Mechanical properties were tested according to Varga *et al* (2007); the resulting mean force-displacement curves are shown in Fig. 1. The data clearly demonstrate the basic role of collagen for biomechanical properties of fibrin gel structures which are very commonly used for tissue engineering. When collagen was added to fibrin matrix, overall sample stiffness was increased. Collagen fibers formed internal structure of higher porosity which resulted in less linear course of loading curve (more resembling the properties of viscoelastic material). It should be stated that the presence of collagen in fibrin gel shifted biomechanical properties of the scaffold closer to the native tissue. While the fibrin matrix showed a relatively low value of derivation of the force/strain dependence (Fig. 1, line A) compared to the much higher value of the derivation for the native cartilage from pig knee (Fig. 1, line C), simple presence of collagen can significantly improve the biomechanical properties of the fibrin gel and "shift" these properties toward the properties of native tissue (Fig. 1, line B).

Appropriate determination of biomechanical properties of artificial tissue and scaffolds is, therefore, one of the crucial steps in tissue engineering. Testing of native or artificial tissue for biomechanical properties is not easy from several points of view. First of all, we have mostly to deal with a very tiny sample which is rather difficult to examine. Second, in spite of several methods that have been already employed for the determination of biomechanical properties (e.g. Young modulus), there are rather large drawbacks which still need to be overcome to establish a quick and reliable detection method.

Most common approaches for material mechanical properties testing employ commercially available testing machines. Though these devices usually offer a limited interval of applicable loading rates and face difficulties with attaching and subsequent testing of humid and slippy samples of limited size, they are still most frequently used for the evaluation of cartilage tissue biomechanical properties. Some alternatives have been proposed to yield more comprehensive knowledge about cartilage mechanics, e.g. nanoindentation (Hu *et al.* 2001), ultrasonic (Saarakkala *et al.* 2004) or dynamic impact loading (Repo and Finlay 1977).

Acknowledgements

This work was supported by the Grant Agency of AS CR grants No. 1ET400110403 and IAA500390702, the Grant Agency of the Charles University in Prague grants No. 121/2005/B-BIO/2.LF, the Ministry of Education, Youth and Sport of the Czech Republic grants No. 1M6798582302 and NPV II 2B06130 and Research Plans of AS CR Institutes No. AVOZ 50390512 and AVOZ 50390703.

References

ADAMCOVA M, PELOUCH V, GERSL V, KAPLANOVA J, MAZUROVA Y, SIMUNEK T, KLIMTOVA I, HRDINA R: Protein profiling in daunorubicin-induced cardiomyopathy. *Gen Physiol Biophys* **22**: 411-419, 2003.

BOWLIN GL: Electrospinning Collagen Scaffolds. *Sci Med* **8**: 292-293, 2002.

BUTTAFOCO L, KOLKMAN NG, ENGBERS-BUIJTENHUIJS P, POOT AA, DIJKSTRA PJ, VERMES I, FEIJEN J: Electrospinning of collagen and elastin for tissue engineering applications. *Biomaterials* **27**: 724-734, 2006.

CASPER CL, YANG W, FARACH-CARSON MC, RABOLT JF: Coating Electrospun Collagen and Gelatin Fibers with Perlecan Domain I for Increased Growth Factor Binding. *Biomacromolecules*, 2007.

DEITZEL JM, KLEINMEYER J, HARRIS D, TAN NCB: The effect of processing variables on the morphology of electrospun nanofibers and textiles. *Polymer* **42**: 261-272, 2001.

FERTALA A, HAN WB, KO FK: Mapping critical sites in collagen II for rational design of gene-engineered proteins for cell-supporting materials. *J Biomed Mater Res* **57**: 48-58, 2001.

FORMHALS A: *Improvements in or relating to Processes and Apparatus for the Production of Artificial Filaments*. United Kingdom patent no. 364, 780; 1932.

HE W, MA Z, YONG T, TEO WE, RAMAKRISHNA S: Fabrication of collagen-coated biodegradable polymer nanofiber mesh and its potential for endothelial cells growth. *Biomaterials* **26**: 7606-7615, 2005a.

HE W, YONG T, TEO WE, MA Z, RAMAKRISHNA S: Fabrication and endothelialization of collagen-blended biodegradable polymer nanofibers: potential vascular graft for blood vessel tissue engineering. *Tissue Eng* **11**: 1574-1588, 2005b.

HELING A, ZIMMERMANN R, KOSTIN S, MAENO Y, HEIN S, DEVAUX B, BAUER E, KLOVEKORN WP, SCHLEPPER M, SCHAPER W, SCHAPER J: Increased expression of cytoskeletal, linkage, and extracellular proteins in failing human myocardium. *Circ Res* **86**: 846-853, 2000.

HERGET J, PELOUCH V, KOLAR F, OSTADAL B: The inhibition of angiotensin converting enzyme attenuates the effects of chronic hypoxia on pulmonary blood vessels in the rat. *Physiol Res* **45**: 221-226, 1996.

HOLMGREN SK, TAYLOR KM, BRETSCHER LE, RAINES RT: Code for collagen's stability deciphered. *Nature* **392**: 666-667, 1998.

HU K, RADHAKRISHNAN P, PATEL RV, MAO JJ: Regional structural and viscoelastic properties of fibrocartilage upon dynamic nanoindentation of the articular condyle. *J Struct Biol* **136**: 46-52, 2001.

HUANG L, APKARIAN RP, CHAIKOF EL: High-resolution analysis of engineered type I collagen nanofibers by electron microscopy. *Scanning* **23**: 372-375, 2001.

JANSSENS S, LIJNEN HR: What has been learned about the cardiovascular effects of matrix metalloproteinases from mouse models? *Cardiovasc Res* **69**: 585-594, 2006.

JIRSAK O, SANETRNIK F, LUKAS D, KOTEK V, MARTINOVA L, CHALOUPEK J: *A Method of Nanofibres Production from A Polymer Solution Using Electrostatic Spinning and A Device for Carrying out The Method*. WO2005024101; 2005.

KIDOAKI S, KWON IK, MATSUDA T: Mesoscopic spatial designs of nano- and microfiber meshes for tissue-engineering matrix and scaffold based on newly devised multilayering and mixing electrospinning techniques. *Biomaterials* **26**: 37-46, 2005.

KIM BS, MOONEY DJ: Development of biocompatible synthetic extracellular matrices for tissue engineering. *Trends Biotechnol* **16**: 224-230, 1998.

KIM H, YOON CS, KIM H, RAH B: Expression of extracellular matrix components fibronectin and laminin in the human fetal heart. *Cell Struct Funct* **24**: 19-26, 1999.

KOLAR F, PAPOUSEK F, PELOUCH V, OSTADAL B, RAKUSAN K: Pressure overload induced in newborn rats: effects on left ventricular growth, morphology, and function. *Pediatr Res* **43**: 521-526, 1998.

KUKACKA J, PRUSA R, KOTASKA K, PELOUCH V: Matrix metaloproteinases and their function in myocardium. *Biomed. Pap. Med. Fac. Univ. Olomouc* **149**: 225-236, 2005.

KWON IK, MATSUDA T: Co-electrospun nanofiber fabrics of poly(L-lactide-co-epsilon-caprolactone) with type I collagen or heparin. *Biomacromolecules* **6**: 2096-2105, 2005.

LI M, MONDRINOS MJ, GANDHI MR, KO FK, WEISS AS, LELKES PI: Electrospun protein fibers as matrices for tissue engineering. *Biomaterials* **26**: 5999-6008, 2005.

LI WJ, LAURENCIN CT, CATERSON EJ, TUAN RS, KO FK: Electrospun nanofibrous structure: a novel scaffold for tissue engineering. *J Biomed Mater Res* **60**: 613-621, 2002.

MAKI JM, KIVIRIKKO KI: Cloning and characterization of a fourth human lysyl oxidase isoenzyme. *Biochem J* **355**: 381-387, 2001.

MATTHEWS JA, BOLAND ED, WNEK GE, SIMPSON DG, BOWLIN GL: Electrospinning of Collagen Type II: A Feasibility Study. *Journal of Bioactive and Compatible Polymers* **18**: 125-134, 2003.

MATTHEWS JA, WNEK GE, SIMPSON DG, BOWLIN GL: Electrospinning of collagen nanofibers. *Biomacromolecules* **3**: 232-238, 2002.

MURDOCH AD, DODGE GR, COHEN I, TUAN RS, IOZZO RV: Primary structure of the human heparan sulfate proteoglycan from basement membrane (HSPG2/perlecan). A chimeric molecule with multiple domains homologous to the low density lipoprotein receptor, laminin, neural cell adhesion molecules, and epidermal growth factor. *J Biol Chem* **267**: 8544-8557, 1992.

MYLLYHARJU J, KIVIRIKKO KI: Collagens, modifying enzymes and their mutations in humans, flies and worms. *Trends Genet* **20**: 33-43, 2004.

NOMIZU M, OTAKA A, UTANI A, ROLLER PP, YAMADA Y: Assembly of synthetic laminin peptides into a triple-stranded coiled-coil structure. *J Biol Chem* **269**: 30386-30392, 1994.

PAKKANEN O, HAMALAINEN ER, KIVIRIKKO KI, MYLLYHARJU J: Assembly of stable human type I and III collagen molecules from hydroxylated recombinant chains in the yeast Pichia pastoris. Effect of an engineered C-terminal oligomerization domain foldon. *J Biol Chem* **278**: 32478-32483, 2003.

PAULSSON M, SALADIN K, ENGVALL E: Structure of laminin variants. The 300-kDa chains of murine and bovine heart laminin are related to the human placenta merosin heavy chain and replace the a chain in some laminin variants. *J Biol Chem* **266**: 17545-17551, 1991.

PELOUCH V, DIXON IM, GOLFMAN L, BEAMISH RE, DHALLA NS: Role of extracellular matrix proteins in heart function. *Mol Cell Biochem* **129**: 101-120, 1993.

PELOUCH V, MILEROVA M, OSTADAL B, HUCIN B, SAMANEK M: Differences between atrial and ventricular protein profiling in children with congenital heart disease. *Mol Cell Biochem* **147**: 43-49, 1995.

RAUTAVUOMA K, TAKALUOMA K, PASSOJA K, PIRSKANEN A, KVIST AP, KIVIRIKKO KI, MYLLYHARJU J: Characterization of three fragments that constitute the monomers of the human lysyl hydroxylase isoenzymes 1-3. The 30-kDa N-terminal fragment is not required for lysyl hydroxylase activity. *J Biol Chem* **277**: 23084-23091, 2002.

RENEKER DH, CHUN I: Nanometre diameter fibres of polymer, produced by electrospinning. *Nanotechnology* **7**: 216-223, 1996.

RENEKER DH, YARIN AL, FONG H, KOOMBHONGSE S: Bending instability of electrically charged liquid jets of polymer solutions in electrospinning. *Journal of Applied Physics* **87**: 4531-4547, 2000.

REPO RU, FINLAY JB: Survival of articular cartilage after controlled impact. *J Bone Joint Surg Am* **59**: 1068-1076, 1977.

RHO KS, JEONG L, LEE G, SEO BM, PARK YJ, HONG SD, ROH S, CHO JJ, PARK WH, MIN BM: Electrospinning of collagen nanofibers: effects on the behavior of normal human keratinocytes and early-stage wound healing. *Biomaterials* **27**: 1452-1461, 2006.

SAARAKKALA S, KORHONEN RK, LAASANEN MS, TOYRAS J, RIEPPO J, JURVELIN JS: Mechano-acoustic determination of Young's modulus of articular cartilage. *Biorheology* **41**: 167-179, 2004.

SHARMA A, ASKARI JA, HUMPHRIES MJ, JONES EY, STUART DI: Crystal structure of a heparin- and integrin-binding segment of human fibronectin. *EMBO J* **18**: 1468-1479, 1999.

SHIELDS KJ, BECKMAN MJ, BOWLIN GL, WAYNE JS: Mechanical properties and cellular proliferation of electrospun collagen type II. *Tissue Eng* **10**: 1510-1517, 2004.

SIMKO F, PELOUCH V, TOROK J, LUPTAK I, MATUSKOVA J, PECHANOVA O, BABAL P: Protein remodeling of the heart ventricles in hereditary hypertriglyceridemic rat: effect of ACE-inhibition. *J Biomed Sci* **12**: 103-111, 2005.

STITZEL J, LIU J, LEE SJ, KOMURA M, BERRY J, SOKER S, LIM G, VAN DYKE M, CZERW R, YOO JJ, ATALA A: Controlled fabrication of a biological vascular substitute. *Biomaterials* **27**: 1088-1094, 2006.

TAYLOR G: Electrically Driven Jets. *Proceedings of the Royal Society of London Series a-Mathematical and Physical Sciences* **313**: 453, 1969.

TEO WE, HE W, RAMAKRISHNA S: Electrospun scaffold tailored for tissue-specific extracellular matrix. *Biotechnol J* **1**: 918-929, 2006.

VANHOUTTE D, SCHELLINGS M, PINTO Y, HEYMANS S: Relevance of matrix metalloproteinases and their inhibitors after myocardial infarction: a temporal and spatial window. *Cardiovasc Res* **69**: 604-613, 2006.

VARGA F, DRŽÍK M, HANDL M, CHLPÍK J, KOS P, FILOVÁ E, RAMPICHOVÁ M, NEČAS A, TRČ T, AMLER E: Biomechanical characterization of cartilages by a novel approach of blunt impact testing. *Physiol Res* **56** (Suppl 1)*:* S61-S68, 2007 (This issue).

VENUGOPAL J, RAMAKRISHNA S: Biocompatible nanofiber matrices for the engineering of a dermal substitute for skin regeneration. *Tissue Eng* **11**: 847-854, 2005.

VENUGOPAL JR, ZHANG Y, RAMAKRISHNA S: In vitro culture of human dermal fibroblasts on electrospun polycaprolactone collagen nanofibrous membrane. *Artif Organs* **30**: 440-446, 2006.

XU CY, INAI R, KOTAKI M, RAMAKRISHNA S: Aligned biodegradable nanofibrous structure: a potential scaffold for blood vessel engineering. *Biomaterials* **25**: 877-886, 2004.

YANG C, HILLAS PJ, BAEZ JA, NOKELAINEN M, BALAN J, TANG J, SPIRO R, POLAREK JW: The application of recombinant human collagen in tissue engineering. *BioDrugs* **18**: 103-119, 2004.

YARIN AL, ZUSSMAN E: Upward needleless electrospinning of multiple nanofibers. *Polymer* **45**: 2977-2980, 2004.

ZHANG YZ, VENUGOPAL J, HUANG ZM, LIM CT, RAMAKRISHNA S: Characterization of the surface biocompatibility of the electrospun PCL-collagen nanofibers using fibroblasts. *Biomacromolecules* **6**: 2583-2589, 2005.

ZHONG S, TEO WE, ZHU X, BEUERMAN R, RAMAKRISHNA S, YUNG LY: Formation of collagen-glycosaminoglycan blended nanofibrous scaffolds and their biological properties. *Biomacromolecules* **6**: 2998-3004, 2005.

ZHONG S, TEO WE, ZHU X, BEUERMAN RW, RAMAKRISHNA S, YUNG LY: An aligned nanofibrous collagen scaffold by electrospinning and its effects on in vitro fibroblast culture. *J Biomed Mater Res A* **79**: 456-463, 2006.

Corresponding author

V. Pelouch, Department of Medical Chemistry and Biochemistry, Second Faculty of Medicine, Charles University, V Úvalu 84, 150 06 Prague 5, Czech Republic. E-mail: vaclav.pelouch@lfmotol.cuni.cz

Příloha 4

Filova E, Rampichova M, Handl M, Lytvynets A, Halouzka R, Usvald D, Hlucilova J, Prochazka R, Dezortova M, Rolencova E, Kostakova E, Trc T, Stastny E, Kolacna L, Hajek M, Motlik J, Amler E. Composite hyaluronate-type I collagen-fibrin scaffold in the therapy of osteochondral defects in miniature pigs, Physiol. Res.; 56 (Suppl. 1): pg.5-16 (2007), IF =1.555 (11)

Filova E 19%, Rampichova M 14%, Handl M 4%, Lytvynets A 4%, Halouzka R 14%, Usvald D 5%, Hlucilova J 5%, Prochazka R 4%, Dezortova M 4%, Rolencova E 4%, ***Kostakova E 3%,*** *Trc T 3%, Stastny E 2%, Kolacna L 3%, Hajek M 4%, Motlik J 4%, Amler E 4%.*

Physiol. Res. 56 (Suppl. 1): S5-S16, 2007

Composite Hyaluronate-Type I Collagen-Fibrin Scaffold in the Therapy of Osteochondral Defects in Miniature Pigs

E. FILOVÁ[1, 2], M. RAMPICHOVÁ[1, 2], M. HANDL[3], A. LYTVYNETS[4], R. HALOUZKA[5], D. USVALD[6], J. HLUČILOVÁ[6], R. PROCHÁZKA[6], M. DEZORTOVÁ[7], E. ROLENCOVÁ[7], E. KOŠŤÁKOVÁ[8], T. TRČ[3], E. ŠŤASTNÝ[3], L. KOLÁČNÁ[1, 2], M. HÁJEK[7], J. MOTLÍK[6], E. AMLER[1, 2]

[1]Institute of Experimental Medicine of the Academy of Sciences of the Czech Republic, Prague, [2]Institute of Biophysics, Second Faculty of Medicine, Charles University, Prague, [3]Orthopedic Clinic, University Hospital Motol, Prague, [4]Institute of Physiology of the Academy of Sciences of the Czech Republic, Prague, [5]Institute of Pathological Morphology, Faculty of Veterinary Medicine, University of Veterinary and Pharmaceutical Sciences, Brno, [6]Institute of Animal Physiology and Genetics of the Academy of Sciences of the Czech Republic, Liběchov, [7]MR-Unit, ZRIR, Institute for Clinical and Experimental Medicine, Prague, [8]Technical University of Liberec, Faculty of Textile Engineering, Liberec, Czech Republic

Received May 23, 2007
Accepted May 29, 2007
On-line available May 31, 2007

Summary

The potential of novel scaffold containing sodium hyaluronate, type I collagen, and fibrin was investigated in the regeneration of osteochondral defects in miniature pigs. Both autologous chondrocyte-seeded scaffolds and non-seeded scaffolds were implanted into two defects located in the non-weight-bearing zone of the femoral trochlea (defect A was located more distally and medially, defect B was located more proximally and laterally). Control defects were left untreated. Twelve weeks after the operation, the knees were evaluated *in vivo* using MRI. Six months after the implantation, the defects were analyzed using MRI, histological, and immunohistochemical analysis. In the A defects of chondrocyte-seeded scaffold group, hyaline cartilage and fibrocartilage was formed, containing type II collagen, acidic and neutral glycosaminoglycans while the non-seeded scaffold group was predominantly filled with fibrocartilage. Defects in the control group were predominantly filled with fibrous tissue. Histomorphometric analysis of photomicrographs revealed a significantly higher amount of hyaline cartilage in the cell-seeded scaffold group in A defects than in other groups. Both scaffold groups in A defects showed significantly less fibrous tissue than cell-seeded defects B and the control group. Both histological and MRI analysis proved that the novel composite scaffold has a potential to regenerate osteochondral defects within six months.

Key words

Osteochondral defect • Fibrin • Autologous chondrocytes • Cartilage regeneration

Introduction

Isolated chondral or osteochondral defects, when left untreated, fail to heal. Moreover, large defects can progress to symptomatic degeneration of the joint. Therefore, the treatment of selected isolated defects may prevent or delay the development of osteoarthritis. Standard surgical techniques, such as debridement, drilling or microfracturing of subchondral bone, osteotomy, mosaicplasty, transplantation of autographs from non-weight bearing zone into former defect area, and soft tissue grafts, such as perichondrial, periosteal flap, joint capsule, or fascia have the potential to stimulate formation of new articular surface, and may decrease symptoms and improve the joint function (Niedermann *et al.* 1985, Hoikka *et al.* 1990, Buckwalter and Mankin 1998a). However, they are not able to restore normal articular cartilage (Buckwalter and Mankin 1998a).

One of the modern techniques involves autologous chondrocytes injected into the defect that is covered by periosteal flap sealed with fibrin glue (Brittberg *et al.* 1994, Breinan *et al.* 1997, 2001). However, in animal models, a positive effect of ACI was observed only three months after the implantation (Breinan *et al.* 2001), but no effect was observed after 12 and 18 months (Breinan *et al.* 1997). That may be explained by the lack of retention of the cells in the defect due to possible displacement of the periosteal flap, and the location of the defect.

The second generation of ACI technique (or ACT) involves autologous chondrocytes injected under a three-dimensional biodegradable scaffold such as collagen bilayer membrane (Chondro-Gide™ membrane, Geistlich Biomaterials) (Marlovits *et al.* 2006).

The third generation of ACT is based on autologous chondrocyte-seeded biomaterials as cell carriers (MACT). Hyaluronan derivative fleece, type-I/III collagen membrane, and polylactin and polyglactin are intensively examined in clinical studies (Pavesio *et al.* 2003, Marlovits *et al.* 2005, Trattnig *et al.* 2005, Marlovits *et al.* 2006). In comparison with the second generation of ACT, this technique allows chondrocytes to redifferentiate and to produce their own extracellular matrix. Subjective and objective improvement has been observed in 76 % to 100 % of patients. In spite of these promising results, incomplete filling (Trattnig *et al.* 2005) and rare detachment of the scaffold have occurred (Marlovits *et al.* 2005).

Hydrogels mimic the natural highly hydrated cartilage that contains above 90 % of water (Buckwalter and Mankin 1998b). They include naturally derived biopolymers, such as collagen, fibrin, chitosan, agarose, alginate, hyaluronic acid derivatives (Drury and Mooney 2003, Ng *et al.* 2005), or synthetic polymers, such as polyvinyl alcohol, polyethylene oxide, and polyethylene glycol (Bryant and Anseth 2002, Kobayashi *et al.* 2003). Crosslinked hydrogels (Bryant and Anseth 2002), or porous scaffolds prepared from hydrogels by cross-linking and/or by freeze-drying exhibit increased stiffness and reduced degradation velocity (Chang *et al.* 2003). They allow preparing scaffolds of variable composition, biological, and biomechanical properties, especially when they are combined with other hydrogels, woven or non-woven scaffolds, and other polymer scaffolds (Minoura *et al.* 1998). In our previous study, we developed a novel composite scaffold consisting of sodium hyaluronate, type I collagen and fibrin, and proved its ability to regenerate osteochondral defects in rabbits within six weeks. The purpose of this study was to prove the long-time efficacy of the same scaffold in cartilage regeneration in miniature pigs.

Methods

Animal care

The investigation was approved by the Expert Committee of the Institute of Physiology, Academy of Sciences, Prague, and conformed with the Czech Animal Protection Law № 246/92. Animals were premedicated with intramuscular 2.0 mg/kg azaperonum and 1 mg Atropin Biotika *pro toto* in the same syringe (posterior thigh – semitendinous and semimembranous muscles). Marginal auricular vein was used for anesthetic induction drugs (ketamine 20 mg/kg). Animals were intubated with 2.5F tracheal tube without cuff. Anesthesia was maintained with 1.5 % isoflurane at 2 l/min constant flow. During *in vivo* MRI measurement the general anesthesia was done by continual infusion into marginal auricular vein with ketamine (20 mg/kg).

Chondrocyte isolation and cell culture

Small pieces of cartilage were taken from the left femoral trochlea of three miniature pigs (total of nine miniature pigs) under general anesthesia. After enzymic digestion, chondrocytes were collected and cultured for 14 days in Iscove´s Modified Dulbecco´s Medium supplemented with 15 % fetal bovine serum (FBS), 3 g/l

$NaHCO_3$, 100 IU/ml penicillin, 100 µg/ml streptomycin, 4 mM L-glutamine, 20 µg/ml L-ascorbate-2-phosphate sesquimagnesium salt, 50 ng/ml insulin-like growth factor (IGF-I, human recombinant (hr), Sigma), 10 ng/ml basic fibroblast growth factor (bFGF, hr, Roche Applied Science), and 1 ng/ml transforming growth factor β2 (TGF-β2 from porcine platelets, Sigma-Aldrich). During the subsequent 9 days the cells were cultured in the same medium but containing 10 % FBS. The cells were incubated at 37 °C in a humidified atmosphere with 5 % CO_2. The culture was passaged always before confluence was reached and the medium was exchanged every three days.

Scaffold preparation

The scaffolds were prepared in the wells of a 24-well plate at about 4 °C by mixing 33 µl of sodium hyaluronate (10 mg/ml, 1500 kDa, kindly provided by CPN, CR) with 49.4 µl of 1 mg/ml type I collagen in 0.1 M acetic acid (Collagen type I from calf skin, acid soluble, Sigma) and neutralized with 1 M KOH. 66 µl of cell suspension (4.3×10^6 chondrocytes) or 66 µl of media, respectively, was then added. Into this medium containing five times higher concentrations of growth factors compared to culture medium and 20 % FBS, we added 0.16 ml of Tissucol solution in aprotinin (fibrinogen 70-110 mg/ml, aprotinin 3000 kallidinogenase-inactivator units/ml), and 0.16 ml of thrombin solution (4 IU/ml) in $CaCl_2$ (40 µmol/ml, Tissucol® Kit, Baxter). Two identical scaffolds were prepared for each animal. The gel was formed at 37 °C. Subsequently, the culture medium was added and the scaffold was placed in an incubator with a humidified atmosphere, 5 % CO_2 at 37 °C for one day.

MRI examination

Twelve weeks after the implantation, *in vivo* MRI evaluation of the knees was performed under general anesthesia, euthanasia of miniature pigs was performed twenty-four weeks after the implantation by intravenous anesthetic thiopental overdosing, and the entire knees were evaluated using MRI. MRI examination was performed on a whole-body MR system Siemens Vision 1.5 T (Erlangen, Germany) using a standard CP head coil. Subjects were measured in a supine position with the knee in the middle of the head coil. MR images were obtained in sagittal orientation using T1-weighted spin echo (TR/TE = 500/12 ms) and FLASH (TR/TE = 999/11 ms) sequence, FOV = 280 mm, slice thickness 3 mm. The same T1-weighted sequence was repeatedly applied after contrast agent (Gd-DTPA) application.

Histological examination and immunohistochemistry

Femoral trochleas were taken away and fixed in 10 % phosphate-buffered formalin for 48 h for histological and immunohistochemical analysis. Briefly, after 48-h fixation, the samples were washed in water and decalcified in 8 M formic acid for seven days. After decalcification, the samples were put into a 5 % sodium sulfate solution for 8 h and subsequently washed using tap water for 24 h. The samples were embedded in paraffin and 4 µm thick sections were stained with hematoxylin-eosin. Staining with Alcian blue at pH 2.5 and the PAS reaction was done to verify acidic and neutral GAG synthesis. The preparations were dehydrated and embedded in Canadian balsam. Immunohistochemical staining was done to identify type II collagen using a monoclonal antibody against type II collagen, clone II-II6B3, obtained from Developmental Studies Hybridoma Bank, University of Iowa, Iowa City. Subsequently, the biotinylated secondary antibody and streptavidin-peroxidase (both Immunotech) were used. Reactions were visualized using the DAB Chromogen Kit (Immunotech). The slides were counterstained with hematoxylin.

Histological and histochemical scoring system

The repair of osteochondral defects in all groups was compared by the scoring system for histological and histochemical results with maximum 24 points, modified from van Susante *et al.* (1999). The blinded analysis was performed by two authors.

Histomorphometric analysis

Histomorphometric analysis of photomicro-graphs of the histological preparations was performed using several randomly selected areas of each defect (Microscope IX 51, Olympus). The amount of hyaline cartilage, fibrocartilage, and fibrous and/or fibrovascular tissue was measured as their percentage of the total area of defect. Total area of the defect was measured by marking the borders of the defect to the defect base and the adjacent cartilage. The blinded analysis was performed by two authors using software Ellipse (ViDiTo, Kosice, Slovakia). The evaluation of hyaline cartilage, fibrocartilage and fibrous tissue was performed according to Breinan 2001.

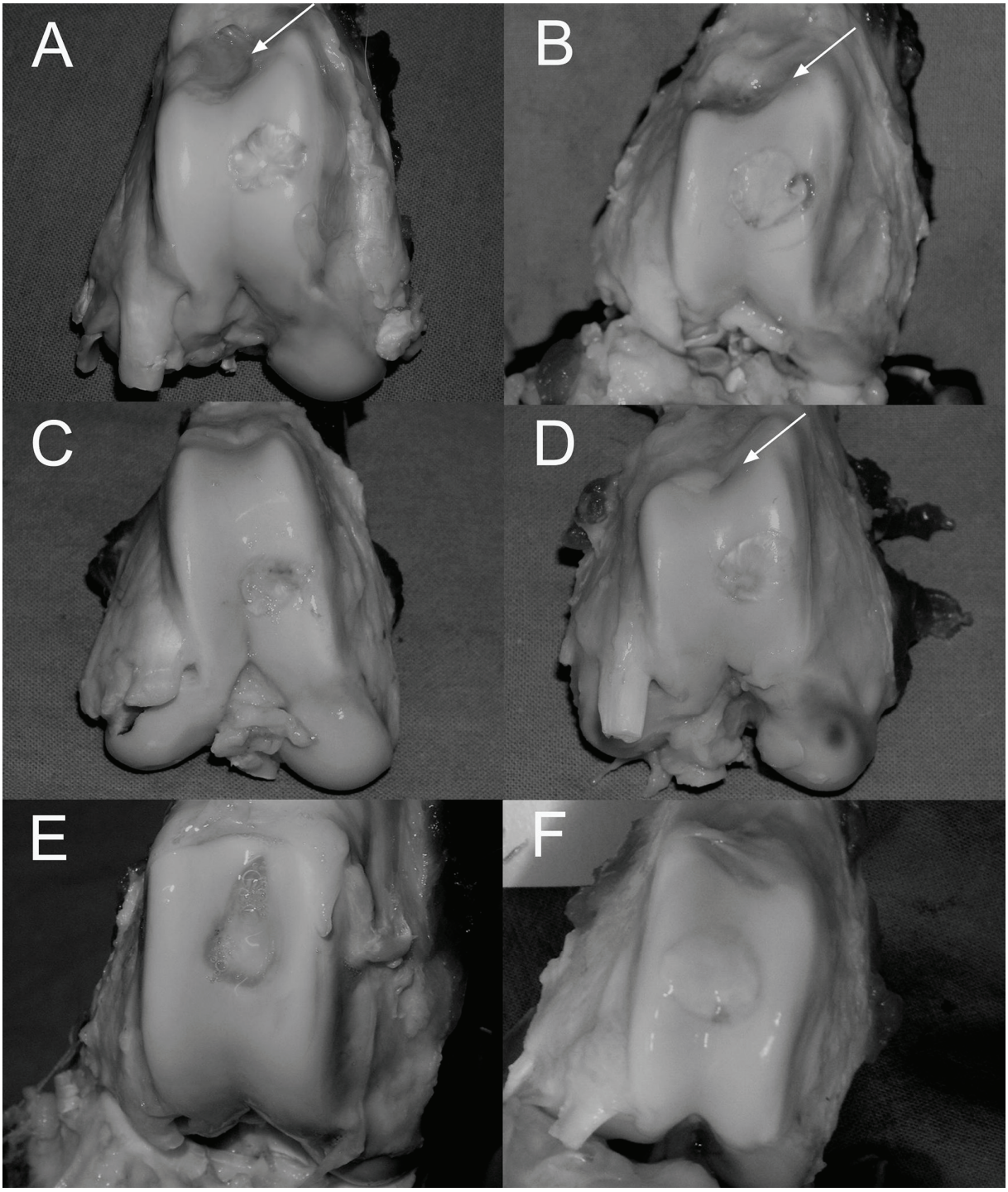

Fig. 1. Femoral trochlea of miniature pigs 24 weeks after the implantation. Defect A was located more distally and medially; defect B was located more proximally and laterally. Arrows show the positions of defect B. (A and B – chondrocyte-seeded scaffold group; C, D – non-seeded scaffold group; E, F – control group)

Statistical analysis

Quantitative data of histomorphometric analysis were presented as mean ± SEM (standard error of the mean). Statistical analysis was performed using One Way Analysis of Variance (ANOVA) and Student-Newman-Keuls Method. The level of significance was set at 0.05. Only groups with 3 animals were analyzed.

Results

Defect simulation and treatment

Patella was dislocated on the lateral site after medial arthrotomy of the knee-joint. Menisci remained untouched. Two experimental circular lesions were created by a 6-mm (diameter) and 2-mm (depth) drill

harvester approaching the subchondral bone in the non-weight-bearing zone in the upper part of medial condyle. To follow the complex effect of cell implantation and knee loading for healing processes, two localizations of cartilage lesion were investigated in the present study. Defect A was located more distally and medially (closer to the weight-bearing zone); defect B was located more proximally and laterally, and farther from the non-weight-bearing zone.

The defects were filled with two pieces of scaffold (as sandwich) containing cultured autologous chondrocytes in three animals (chondrocyte-seeded scaffold group), with two pieces of scaffold without cells in three animals (non-seeded scaffold group). In the control group of three animals, defects A were created and left untreated. The scaffolds were glued to the adjacent tissue and subchondral bone with Tissucol® fibrin glue. Wound healing proceeded without any complication in all cases during the whole post-operation period. Miniature pigs were not limited in their movement after surgery.

Macroscopic evaluation

Chondrocyte-seeded scaffold group. The composite scaffold (hyaluronate/type I collagen/fibrin) seeded with autologous chondrocytes in miniature pigs resulted in almost completely filled defect A after six months. Tissue visually resembled hyaline cartilage (Figs 1A and 1B). The surface was predominantly homogeneous; in one animal the medial edge was irregular and incompletely filled with repaired tissue. The contours of the defect were visible. Defects B were partially filled with the white tissue in distal part adjacent to hyaline cartilage. The proximal yellow part adjacent to fibrous tissue (fibrous capsule) was not filled with the tissue and resembled fibrous tissue (Figs 1A and 1B).

Non-seeded scaffold group. Defects A were filled completely with white tissue, and one defect was filled only partially (Figs 1C and 1D). The color and surface were not homogeneous and the repaired tissue partially resembled the adjacent cartilage. Defects B were done in two animals. The defects were partially filled with white tissue; the proximal part of the defect was not filled and resembled fibrous tissue (Fig. 1D).

Control group. The defect was filled in one case and weakly filled in two animals; the color was white-yellowish with uneven surface and distinct contours (Figs 1E and 1F).

Histological and histochemical score

Structural characteristics of the repaired tissue (Table 1) revealed a higher score in the A defects of chondrocyte-seeded scaffold group (total score – 26, 21, and 23) in comparison with chondrocyte-seeded scaffold in defects B (total score – 16, 9, and 9), and slightly higher than other groups (total score – 16, 19, and 21 of defects A; 19, and 19 of defects B) of non-seeded scaffold group; control group (total score – 13, 14, and 20). Its improvement was observed in all tested parameters. Chondrocyte-seeded scaffold in defects B revealed a lower score than non-seeded scaffold in defect A (total score – 16, 18, and 21).

Histomorphometric analysis

Defects A of chondrocyte-seeded scaffold group contained significantly more hyaline cartilage than other groups. Non-seeded scaffold in defect A revealed significantly more fibrocartilage compared to chondrocyte-seeded scaffold in defects B. However, both defects B of chondrocyte-seeded scaffold group and control group had significantly more fibrous tissue than both types of scaffolds in defects A. (Table 2)

Magnetic resonance images

Three months after the implantation, defects A with chondrocyte-seeded scaffolds were well visible with minimal edema in all cases. Joint cartilages were slightly inhomogeneous without signs of synovitis. In the non-seeded scaffold group, defects A were distinct with prominent edema in the adjacent bone; joint cartilage was inhomogeneous. After application of the contrast agent, the tissue saturation was moderate, and predominantly at the basis of the defects. Synovium was slightly thicker with signs of synovitis. Defects in the control group were clearly visible without high edema and rather inhomogeneous. The signal of the defects slightly enhanced after contrast agent application and the basis showed signs of synovitis.

Six months after the implantation, defects A implanted with chondrocyte-seeded scaffolds remained still visible, without signs of edema in the adjacent bone. The joint cartilage was slightly inhomogeneous. In the non-seeded scaffold group, defects A were clearly visible with sclerotic basis that could lead to slower regeneration. Edema decreased and the cartilage remained slightly inhomogeneous. In the controls, the cartilage has become homogeneous, the edema decreased. The defects were not unambiguously differentiated.

Table 1. Histological and histochemical scoring system, modified from van Susante *et al.* (1999); (AC, BC – chondrocyte-seeded scaffolds implanted in defects A, and B, respectively; A, B – non-seeded scaffolds implanted in defects A, and B, respectively; control – defects without treatment)

Characteristic		AC	BC	A	B	Control
Nature of predominant tissue						
Cellular morphology (I)						
Hyaline articular cartilage	(4)	2	0	0	0	0
Incompletely differentiated	(2)	1	0	3	2	1
Fibrous tissue and bone	(0)	0	3	0	0	2
Alcian blue staining of the matrix (II)						
Normal or near normal	(3)	2	0	1	0	0
Moderate	(2)	1	0	2	2	1
Slight	(1)	0	3	0	0	2
None	(0)	0	0	0	0	0
Structural characteristics						
Surface regularity (III)						
Smooth and intact	(3)	3	0	1	2	0
Superficial horizontal lamination	(2)	0	2	2	0	3
Fissures, 25-100% of the thickness	(1)	0	0	0	0	0
Severe disruption or fibrillation	(0)	0	1	0	0	0
Structural integrity (IV)						
Normal	(2)	1	0	0	0	0
Slight disruption, including cysts	(1)	2	2	3	2	3
Severe disintegration	(0)	0	1	0	0	0
Thickness (V)						
100% of normal adjacent cartilage	(2)	2	0	1	0	0
50-100% of normal cartilage	(1)	1	3	2	2	3
0-50% of normal cartilage	(0)	0	0	0	0	0
Bonding to the adjacent tissue (VI)						
Bonded at both sides and subchondral bone	(2)	3	2	3	2	3
Bonded partially	(1)	0	1	0	0	0
Not bonded	(0)	0	0	0	0	0
Freedom from cellular changes of degeneration						
Hypocellularity (VII)						
None	(3)	3	1	2	2	1
Slight	(2)	0	1	1	0	0
Moderate	(1)	0	1	0	0	2
Severe	(0)	0	0	0	0	0
Chondrocyte clustering (VIII)						
None	(2)	2	1	1	0	2
<25% of cells	(1)	1	1	2	2	1
25-100% of cells	(0)	0	1	0	0	0
Freedom from degenerative changes in adjacent cartilage (IX)						
Normal cellularity, no clusters, normal staining	(3)	2	0	0	0	1
Normal cellularity, mild clusters, moderate staining	(2)	1	3	2	2	2
Mild or moderate hypocellularity, slight staining	(1)	0	0	1	0	0
Severe hypocellularity, poor or no staining	(0)	0	0	0	0	0

Table 2. Histomorphometric analysis of photomicrographs of the defects. Content of hyaline cartilage, fibrocartilage, and fibrous and/or fibrovascular tissue in the defect was determined as a percentage of the total defect area (mean ± S.E.M.). (AC, BC – chondrocyte-seeded scaffolds implanted in the defects A, and B, respectively, A, and B – non-seeded scaffolds implanted in defect A, and B, respectively, control – defects without treatment)

	AC (%)	BC (%)	A (%)	B (%)	Control (%)
Hyaline cartilage	48.72 ± 17.27	0	16.68 ± 8.92	30.80 ± 6.03	0
Fibrocartilage	32.65 ± 6.14	19.23 ± 10.39	66.89 ± 7.41	49.70 ± 13.46	31.23 ± 11.94
Fibrous/ fibrovascular tissue	18.63 ± 11.2	80.77 ± 10.39	16.43 ± 14.35	19.50 ± 19.50	68.77 ± 11.94

Histological examination and immunohistochemistry

Chondrocyte-seeded scaffold group. Defects A were twice thicker than normal cartilage, approaching the subchondral bone (Fig. 2A). Repaired cartilaginous tissue filled the defects; the repaired tissue was slightly disintegrated. The collagen fibers were horizontally oriented on the surface and vertically in the deep part of the defects. All tissues revealed more intense staining of acidic GAGs than neutral GAGs (Figs 2C and 2E). The new repaired tissue was well integrated to both adjacent cartilage and bone. Type II collagen was present in all samples; intense staining was found both in the middle and the deep part of the defects (Fig. 2G). Defects B, however, were filled with fibrovascular and lipid tissue with synovium at the surface (Fig. 2B). Tissue formation was irregular, and PAS-positive substances were present in subchondral bone (Fig. 2D and 2F). In one defect, inflammatory cells were present in the repaired tissue. Type II collagen staining was negative in the repaired tissue (Fig. 2H).

Non-seeded scaffold group. Defects A were flat and filled with mature fibrocartilage or cartilage (Fig. 3A), in one sample with superficial inflammatory infiltration. Alcian-blue- positive substances were observed in the surface area (Figs 3C and 3E); type II collagen staining with moderate intensity was predominantly present in the central part of the defect and in tissue adjacent to the subchondral bone (Fig. 3G). The repaired tissue was well integrated to adjacent bone and cartilage. Some fissures were present in one defect. Defects B were filled with flat fibrocartilaginous tissue that was horizontally structured with good binding to adjacent tissues (Fig. 3B). Acidic GAGs were present in the upper part of the defect. The intense or moderate PAS positive staining (Fig. 3D and 3F) was observed together with moderate type II collagen staining (Fig. 3H); they were concentrated in the deeper regions of the repaired tissue.

Control group. Two defects were partially filled with chaotic sparse fibrous tissue that revealed both GAG and type II collagen staining negative (Figs 4A and 4B and 4C). The third defect was filled with fibrocartilaginous tissue where some fissures were observed. Moreover, moderate Alcian blue and type II collagen staining were observed in the subchondral bone or in the tissue adjacent to the subchondral bone (Fig. 4 D).

Discussion

Chondral defects are reported not to regenerate but to be filled by fibrous tissue (Shortkroff *et al.* 1996). In addition, also treatment of chondral defects with chondroitinase ABC, and fibrin glue containing growth factors resulted in development of fibrous tissue (Hunziker and Rosenberg 1996). On the other hand, osteochondral defects are able to regenerate without treatment by producing a higher amount of proteoglycans, type I and II collagen within six to eight weeks. Later, a decreasing amount of proteoglycans and higher amount of collagen was observed till six months after the operation (Furukawa *et al.* 1980).

Scaffolds seeded with chondrocytes and cultured *in vitro* support the production of extracellular matrix by chondrocytes, mainly GAGs, and type II collagen (Pavesio *et al.* 2003, Trattnig *et al.* 2005). Our aim was to prepare a scaffold supporting cell proliferation, differentiation, and thus regeneration of the defects.

Heterologous chondrocyte-seeded fibrin implanted into the osteochondral defect in the weight-bearing zone was so far reported to repair the defect to a very limited extent. From three weeks after the implantation, many dead cells were observed in the central part of the defects. This was accompanied by

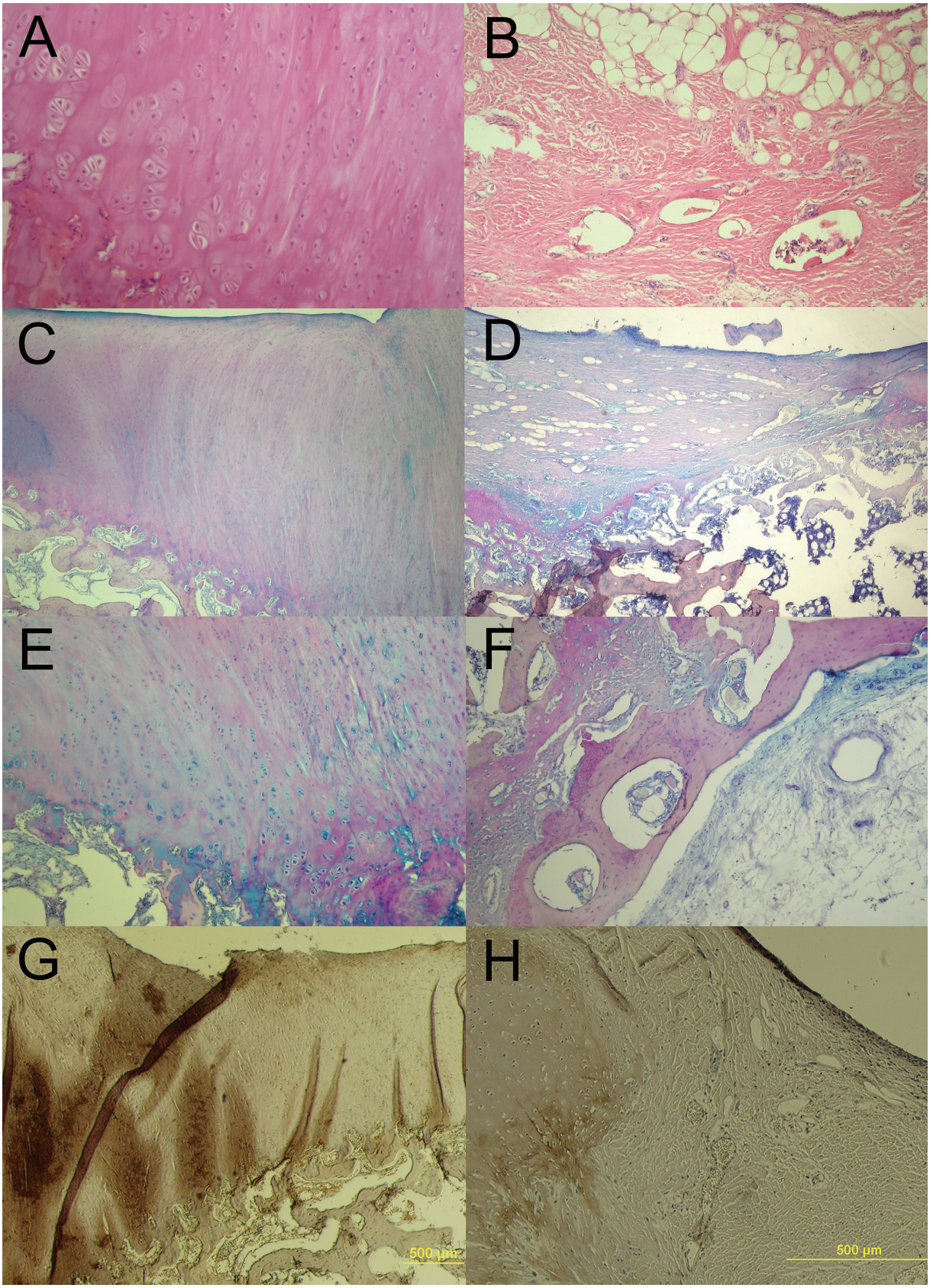

Fig. 2. Histology of osteochondral defects A (A, C, E, G), and defects B (B, D, F, H) of the chondrocyte-seeded scaffold group after 24 weeks using HE staining (A, B), Alcian blue staining and PAS reaction at pH 2.5 (C, D, E, F), and immunohistochemical staining using monoclonal antibody against type II collagen (G, H). Magnification × 200 (A), × 100 (B, E, F, H), × 40 (D, G).

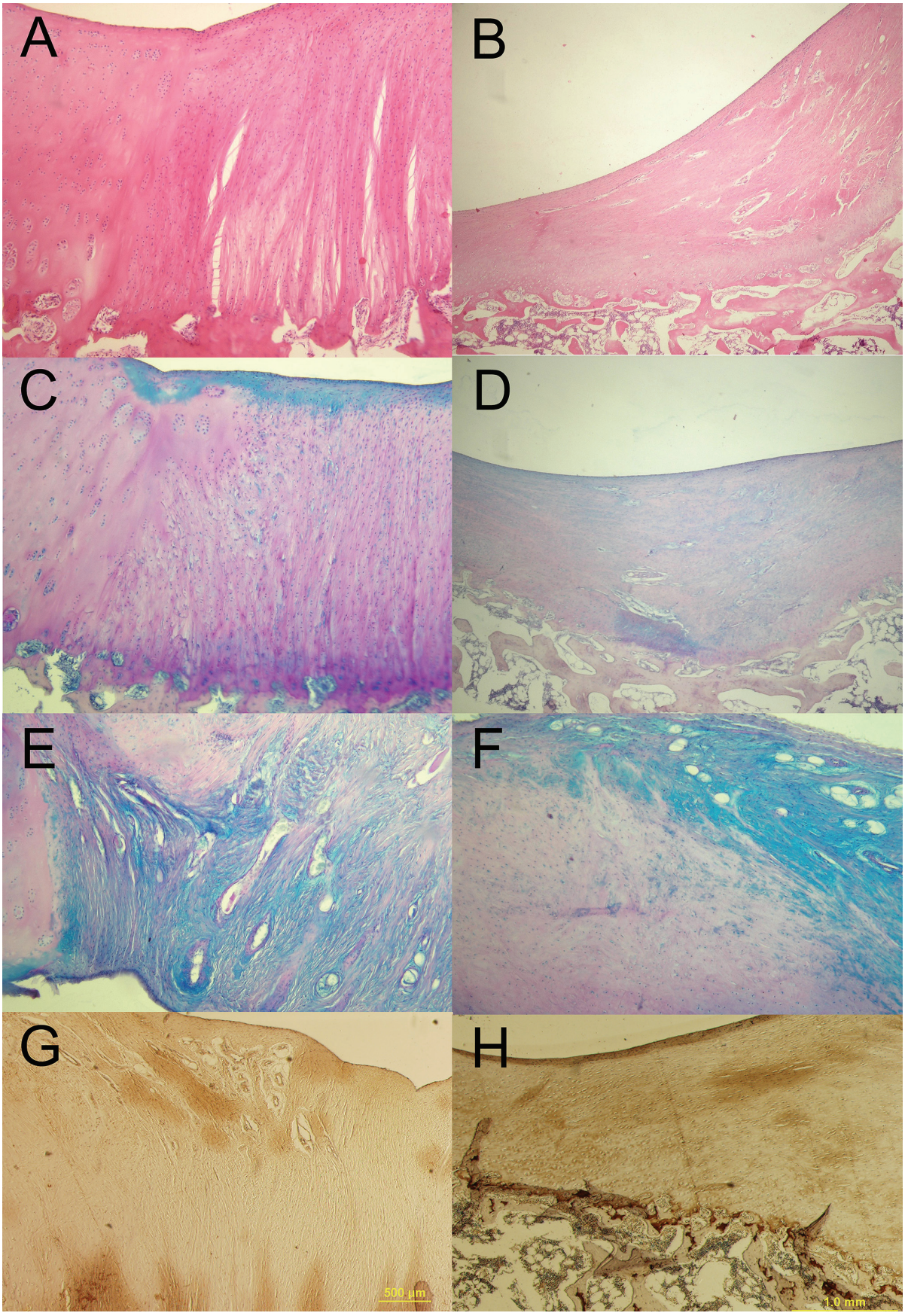

Fig. 3. Histology of osteochondral defects A (A, C, E, G), and B (B, D, F, H) of the non-seeded scaffold group after 24 weeks using HE staining (A, B), Alcian blue staining and PAS reaction at pH 2.5 (C, D, E, F), and immunohistochemical staining using monoclonal antibody against type II collagen (G, H). Magnification × 100 (A, C, E, F), × 40 (B, D, G, H).

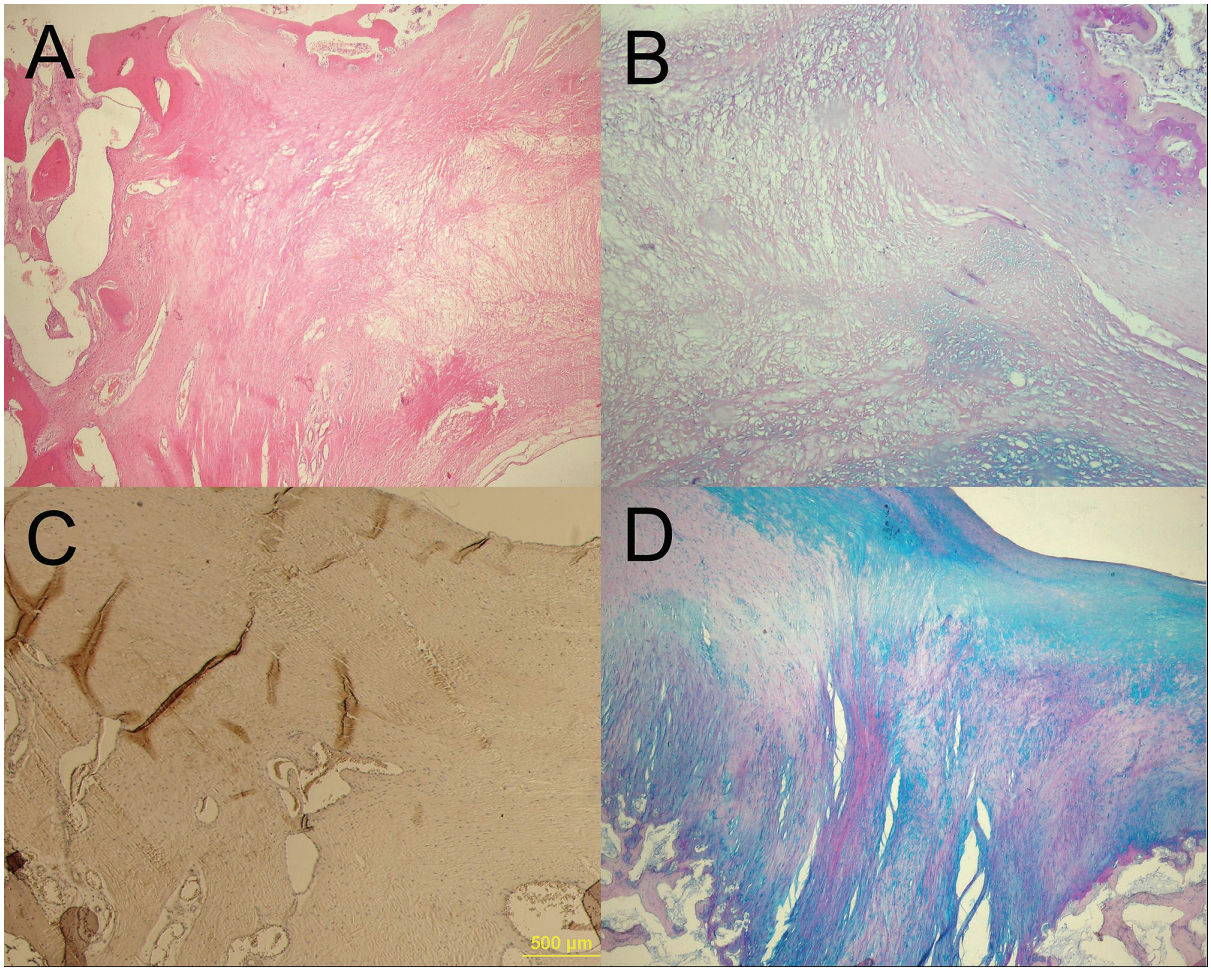

Fig. 4. Histology of osteochondral defects of the control group after 24 weeks using HE staining (A), Alcian blue staining and PAS reaction at pH 2.5 (B, D), and immunohistochemical staining using monoclonal antibody against type II collagen (C) which showed chaotic sparse fibrous tissue with negative both GAG and type II collagen staining (A, B, C). Magnification × 40 (A, C, D), × 100 (B).

inflammatory cell migration into progressively degraded fibrin, and subsequently, fibrocartilage formation (van Susante *et al.* 1999). To improve the biomechanical and biological properties of fibrin, we developed a composite scaffold containing type I collagen, hyaluronic acid, and fibrin. The regenerative potential of the scaffold was already proved in a six-week study in rabbits (data not published yet) where hyaline cartilage was predominantly formed in osteochondral defects. This long-term study proved the healing potential of the method, but also a positive effect of joint loading on regeneration process. Defects A (in the middle of *condylus medialis*) were located more closely to the weight-bearing zone of the joint. They were subjected to higher passive loading compared to the defects located in the proximal part of femoral trochlea (defects B), while the defects B were primarily subjected to shear stress. In the cell-seeded scaffolds in defects A, regenerated tissue was predominantly filled with hyaline and fibrocartilaginous tissue, while the non-seeded scaffolds formed predominantly fibrocartilage, and defects in the control group contained fibrous tissue. In the cell-seeded group, the hyaline tissue was present predominantly near the base of the lesion and at the borders; fibrocartilage was predominantly found in the central part of the defects, and fibrous tissue was located on the surface. The same distribution of tissue types was observed in ACI treated osteochondral defects three and six months after the implantation (Breinan *et al.* 2001). Our results are also in accordance with our previous six-week rabbit experiment where the defects were also situated in the non-weight-bearing zone of femoral condyle. On the other hand, the repair of the proximal defects was diminished probably due to decreased hydrostatic pressure and increased shear stress. Some hypotheses maintain that shear stress and strain applied to cells result in fibrous tissue formation while compression of the cells by hydrostatic pressure results in hyaline cartilage formation (McMahon *et al.*

2004, Kelly and Prendergast 2005).

Interestingly, bioreactor utilizing intermittent pressure and perfusion significantly stimulated both the collagen and GAG synthesis by chondrocytes (Carver and Heath 1999), In contrast, in a spinner flask, the shear stress applied to chondrocytes increased the synthesis of type I collagen, and the fibroblast-like phenotype of chondrocytes at the scaffold periphery (Vunjak-Novakovic *et al.* 1999).

In conclusion, the composite scaffold prepared from sodium hyaluronate, type I collagen and fibrin proved its ability to regenerate the osteochondral defect of miniature pigs in a six-month study. The best regeneration of hyaline cartilage and fibrocartilage was observed in the autologous chondrocyte-seeded scaffold group while the non-seeded scaffold group and control group revealed fibrocartilage and fibrous tissue formation, respectively. According to these results we suggest that the novel composite scaffold is promising for treatment of osteochondral defects.

Acknowledgements

This work was supported by the Grant Agency of AS CR grants No. 1ET400110403 and IAA500390702, the Grant Agency of the Charles University in Prague grants No. 121/2005/B-BIO/2.LF and and the Ministry of Education, Youth and Sport of the Czech Republic grants No. 1M6798582302 and NPV II 2B06130. Internal Grant Agency of the Ministry of Health of the Czech Republic (IGA), grant number: 8122 - 3/2004; Grant Agency of the Czech Republic, grant 304/05/0327; Research Projects, grant numbers: AV0Z50390512 and AV0Z 50110509; We are grateful to Prof. MVDr. František Jelínek, CSc., Dipl. ECVP for the immunohistochemical analysis.

Abbreviations

MRI – magnetic resonance imaging; ACI – autologous chondrocytes implantation; ACT – autologous chondrocytes transplantation; MACT – matrix-associated autologous chondrocyte transplantation; GAG – glycosaminoglycan.

References

BREINAN HA, MINAS T, HSU HP, NEHRER S, SHORTKROFF S, SPECTOR M: Autologous chondrocyte implantation in a canine model: change in composition of reparative tissue with time. *J Orthop Res* **19**: 482–492, 2001.

BREINAN HA, MINAS T, HSU HP, NEHRER S, SLEDGE CB, SPECTOR M: Effect of cultured autologous chondrocytes on repair of chondral defects in a canine model. *J Bone Joint Surg Am* **79**: 1439–1451, 1997.

BRITTBERG M, LINDAHL A, NILSSON A, OHLSSON C, ISAKSSON O, PETERSON L: Treatment of deep cartilage defects in the knee with autologous chondrocyte transplantation. *N Engl J Med* **331**: 889–895, 1994.

BRYANT SJ, ANSETH KS: Hydrogel properties influence ECM production by chondrocytes photoencapsulated in poly(ethylene glycol) hydrogels. *J Biomed Mater Res* **59**: 63–72, 2002.

BUCKWALTER JA, MANKIN HJ: Articular cartilage: degeneration and osteoarthritis, repair, regeneration, and transplantation. *Instr Course Lect* **47**: 487–504, 1998a.

BUCKWALTER JA, MANKIN HJ: Articular cartilage: tissue design and chondrocyte-matrix interactions. *Instr Course Lect* **47**: 477–486, 1998b.

CARVER SE, HEATH CA: Influence of intermittent pressure, fluid flow, and mixing on the regenerative properties of articular chondrocytes. *Biotechnol Bioeng* **65**: 274–281, 1999.

DRURY JL, MOONEY DJ: Hydrogels for tissue engineering: scaffold design variables and applications. *Biomaterials* **24**: 4337–4351, 2003.

FURUKAWA T, EYRE DR, KOIDE S, GLIMCHER MJ: Biochemical studies on repair cartilage resurfacing experimental defects in the rabbit knee. *J Bone Joint Surg Am* **62**: 79–89, 1980.

HOIKKA VE, JAROMA HJ, RITSILA VA: Reconstruction of the patellar articulation with periosteal grafts. 4-year follow-up of 13 cases. *Acta Orthop Scand* **61**: 36–39, 1990.

HUNZIKER EB, ROSENBERG LC: Repair of partial-thickness defects in articular cartilage: cell recruitment from the synovial membrane. *J Bone Joint Surg Am* **78**: 721–733, 1996.

CHANG CH, LIU HC, LIN CC, CHOU CH, LIN FH: Gelatin-chondroitin-hyaluronan tri-copolymer scaffold for cartilage tissue engineering. *Biomaterials* **24**: 4853–4858, 2003.

KELLY DJ, PRENDERGAST PJ: Mechano-regulation of stem cell differentiation and tissue regeneration in osteochondral defects. *J Biomech* **38**: 1413–1422, 2005.

KOBAYASHI M, TOGUCHIDA J, OKA M: Preliminary study of polyvinyl alcohol-hydrogel (PVA-H) artificial meniscus. *Biomaterials* **24**: 639–647, 2003.

MARLOVITS S, STRIESSNIG G, KUTSCHA-LISSBERG F, RESINGER C, ALDRIAN SM, VECSEI V, TRATTNIG S: Early postoperative adherence of matrix-induced autologous chondrocyte implantation for the treatment of full-thickness cartilage defects of the femoral condyle. *Knee Surg Sports Traumatol Arthrosc* **13**: 451–457, 2005.

MARLOVITS S, ZELLER P, SINGER P, RESINGER C, VECSEI V: Cartilage repair: generations of autologous chondrocyte transplantation. *Eur J Radiol* **57**: 24–31, 2006.

MCMAHON LA, BARRON V, PRINA-MELLO A, PRENDERGAST PJ: The state-of-the-art in cartilage bioreactors. In: *Topics in Bio-Mechanical Engineering*. PJ PRENDERGAST and PE MCHUGH (eds), Trinity Centre for Bioengineering & National Centre for Biomedical Engineering Science, Dublin & Galway, 2004, pp 94–146.

MINOURA N, KOYANO T, KOSHIZAKI N, UMEHARA H, NAGURA M, KOBAYASHI K-I: Preparation, properties, and cell attachment/growth behavior of PVA/chitosan-blended hydrogels. *Mater Sci Engineer: C* **6**: 275–280, 1998.

NG KW, WANG CCB, MAUCK RL, KELLY T-AN, CHAHINE NO, COSTA KD, ATESHIAN GA, HUNG CT: A layered agarose approach to fabricate depth-dependent inhomogeneity in chondrocyte-seeded constructs. *J Orthop Res* **23**: 134–141, 2005.

NIEDERMANN B, BOE S, LAURITZEN J, RUBAK JM: Glued periosteal grafts in the knee. *Acta Orthop Scand* **56**: 457–460, 1985.

PAVESIO A, ABATANGELO G, BORRIONE A, BROCCHETTA D, HOLLANDER AP, KON E, TORASSO F, ZANASI S, MARCACCI M: Hyaluronan-based scaffolds (Hyalograft C) in the treatment of knee cartilage defects: preliminary clinical findings. *Novartis Found Symp* **249**: 203–217; discussion 229–233, 234–208, 239–241, 2003.

SHORTKROFF S, BARONE L, HSU HP, WRENN C, GAGNE T, CHI T, BREINAN H, MINAS T, SLEDGE CB, TUBO R, SPECTOR M: Healing of chondral and osteochondral defects in a canine model: the role of cultured chondrocytes in regeneration of articular cartilage. *Biomaterials* **17**: 147–154, 1996.

TRATTNIG S, BA-SSALAMAH A, PINKER K, PLANK C, VECSEI V, MARLOVITS S: Matrix-based autologous chondrocyte implantation for cartilage repair: noninvasive monitoring by high-resolution magnetic resonance imaging. *Magn Reson Imaging* **23**: 779–787, 2005.

VAN SUSANTE JL, BUMA P, SCHUMAN L, HOMMINGA GN, VAN DEN BERG WB, VETH RP: Resurfacing potential of heterologous chondrocytes suspended in fibrin glue in large full-thickness defects of femoral articular cartilage: an experimental study in the goat. *Biomaterials* **20**: 1167–1175, 1999.

VUNJAK-NOVAKOVIC G, MARTIN I, OBRADOVIC B, TREPPO S, GRODZINSKY AJ, LANGER R, FREED LE: Bioreactor cultivation conditions modulate the composition and mechanical properties of tissue-engineered cartilage. *J Orthop Res* **17**: 130–138, 1999.

Corresponding author

E. Filová, Institute of Experimental Medicine**,** CzAcadSci, Vídeňská 1083, 142 20 Prague 4, Czech Republic. E-mail: evafil@biomed.cas.cz

Příloha 5

Kostakova, E., Meszaros, L., Gregr,J.: Composite nanofibers produced by modified electrospinning method; Material Letters, Vol.63, pg.2419-2422 (2009), IF = 2,307 (11)

Materials Letters 63 (2009) 2419–2422

Contents lists available at ScienceDirect

Materials Letters

journal homepage: www.elsevier.com/locate/matlet

Composite nanofibers produced by modified needleless electrospinning

Eva Kostakova [a,*], Laszlo Meszaros [b], Jan Gregr [a]

[a] Technical University of Liberec, Czech Republic
[b] Budapest University of Technology and Economics, Hungary

ARTICLE INFO

Article history:
Received 5 October 2007
Accepted 7 August 2009
Available online 14 August 2009

Keywords:
Nanocomposites
Nanomaterials
Nanofibers
Electrospinning

ABSTRACT

A needleless electrospinning method was used to prepare poly(vinyl alcohol) nanofibers with a content of single walled (SWCNTs) and multi walled carbon nanotubes (MWCNTs). The needleless process of electrospinning from free surface of polymeric solution requires perfect solutions of polymers and additives (carbon nanotubes in the case). The solutions were prepared by sonication method and by usage of surface modified carbon nanotubes. The presence of carbon nanotubes inside the electrospun nanofibrous materials were proved by means of Raman spectroscopy. This process example can be modified for other polymer solutions to produce nanocomposite fibrous structures by electrospinning in mass scale.

1. Introduction

Nowadays, the electrospinning methods and their nanofibrous products have been studied all over the world. The technology uses electrostatic forces for self-organization of polymer solution/melt into a nanofibrous layer as is generally known [1]. Presently, the most of electrospinning techniques used for production of nanofibrous materials is based on capillary electrospinning. On the other hand, the electrospinning from free surface (or almost free surface) of liquid was named as a needleless electrospinning by Yarin [2]. However before that, the needleless modification for continuous production of nanofibers was patented [3,4], Fig. 1. This modified technology is called Nanospider™. A polymer solution is for spinning supplied into the electric field using a surface of a rotating charged cylindrical electrode. Thus no syringes, capillaries, nozzles or needles are needed. The main advantages of the technology are: (i) continuous mass production, (ii) high production capacity (up to 1 g min^{-1} m^{-1} of one spinning electrode) and (iii) ease of upkeep.

There is also well known carbon nanotubes have potentially excellent mechanical, electrical and thermal properties. One of the best ways to realize these properties is to incorporate them in composites [5]. The materials originated thanks to connection of carbon nanotubes and electrospun nanofibers are also in the center of the scientific researches. Here are remarks from several exemplary publications dedicated to this type of composite nanofibers [6–12]. All of these publications present nanofibrous materials electrospun from capillary electrospinners or other non industrial methods of electrospinning.

The presenting study wants to show that nanotubes can be at specific conditions “pulled out” from a polymer solution by creating nanofibers during needleless electrospinning process from almost a free surface of a polymer solution, even though that there is no assurance nanotubes stay in the surface layer during electrospinning. The focusing on the mass production of composite nanofibrous materials is obvious in term of cost effectiveness. Raman spectroscopy gave a proof of carbon nanotubes' presence in the composite nanofibrous materials. The spectroscopy as a powerful tool for the characterization of carbon nanotubes even in polymer electrospun nanofibrous material was used in several research works, for example here [12–14].

2. Experimental part

For the presenting contribution, there were chosen three different samples (plus “blind” sample) from a complete set of tested solutions with integrated nanotubes. These other solutions (containing in general pure multi walled carbon nanotubes with no surface treatment) have not been possible electrospun by the modified electrospinning method. Thus they are not described below.

Basic poly(vinyl alcohol) (PVA) water solution (10 wt.%) plus crosslinking agents (glyoxal 2.5 wt.% and phosphoric acid 2.5 wt.% of PVA) was electrospun and subsequently crosslinked at 140 °C for 10 min. It was the “blind” sample. The basic solution plus addition of water solution of 0,1 wt.% of single walled carbon nanotubes (SWCTs) with COOH surface modification (Nanocyl, Belgium) presents the second type of introduced samples. The third type used the same basic solution plus addition of 0.1 wt.% of multi walled carbon nanotubes (MWNTs) with OH surface modification (Nanocyl, Belgium). The last, i.e. the forth, set of samples was prepared by electrospinning of PVA solution in mixture of water and ethanol (4:3) plus addition of

* Corresponding author.
E-mail address: eva.kostakova@tul.cz (E. Kostakova).

0167-577X/$ – see front matter © 2009 Elsevier B.V. All rights reserved.
doi:10.1016/j.matlet.2009.08.014

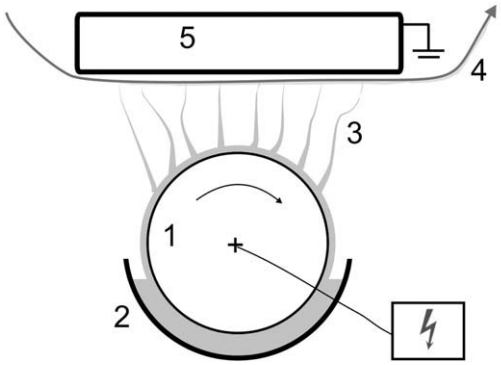

Fig. 1. Modified electrospinning method — basic principle: 1 — metal roller (positive charged); 2 — reservoir of the polymer solution; 3 — direction of fiber formation; 4 — nonwoven substrate (support material for creating nanofibers); 5 — grounded collector.

0.1 wt.% of MWNTs with OH surface modification (Nanocyl, Belgium). All three solutions with modified carbon nanotubes were mixed 1 min by sonication to completely separate agglomerates of nanotubes inside the solutions. There were used device Couptiss Ultra Sons HS30 with power 30 W and frequency 30 kHz (Calemard, France). The crosslinking process after electrospinning was the same for all types of composites. Images from scanning electron microscope of these four electrospun materials can be seen at Fig. 2. The nanofibrous layers were collected on spun-bond material for subsequent better separation. All samples were prepared by modified electrospinning method called Nanospider™. A distance between a grounded collector and a charging rotating cylinder in bath of polymer solution was 8 cm, voltage was 45–53 kV and speed of the collecting nonwoven textile was 0.1 m/min. The surface density of these samples is 5 g m^{-1}. There is expected that the final amount of nanotubes inside all three final composite nanofibrous materials is approximately 1 wt.% of PVA.

The used device for Raman spectroscopy was Horiba JOBIN Yvon — LabRam IR with microscope Olympus BX41. The area of measuring point was in 1.2 μm in diameter. The surface morphology was studied by a 6380LVa scanning electron microscope (JEOL, Japan). The tested materials are not good conductive materials, so they can overload with electrons that can cause bad pictures. There wasn't used golden on the surface, not to increase the diameter of the fibers. This is why there was necessary to a little change voltage during scanning electron microscope observation (between 20 and 24 kV).

3. Results and discussion

There is obvious that an addition of nanotubes and using different solvent changes the properties of solutions for electrospinning. It results in a slight increasing of an average fiber diameter for the second and the third type of produced material and an evident increasing of an average fiber diameter for the fourth type of the electrospun composite material (see Fig. 2). The average diameters of fibers inside studied materials were: for the basic electrospun nanofibrous layer 191 ± 87 nm; for the second type 222 ± 123 nm; for the third type 246 ± 80 nm; and for the fourth type 463 ± 266 nm.

Figs. 3–5 prove a presence of carbon nanotubes inside electrospun PVA nanofibers. There were done also spectra of pure SWNTs and MWNTs. The characteristic spectra for carbon nanotubes usually have two peaks. One of them is around wavelength of 1350 cm^{-1} (known as the D-band peak) and second one about 1590 cm^{-1} (known as the G-band peak) [15]. The first peak represents impurities and also fullerens or half-fullerens at the end of carbon nanotubes. The D-mode is expected to be observed in MWNTs. However when it is observed in SWNTs one assumes that it is due to defects in the tubes. The second one is connected with G-bands in graphen sheets. The G-mode corresponds to the trenching mode of the–C–C–bond in the graphite plane.

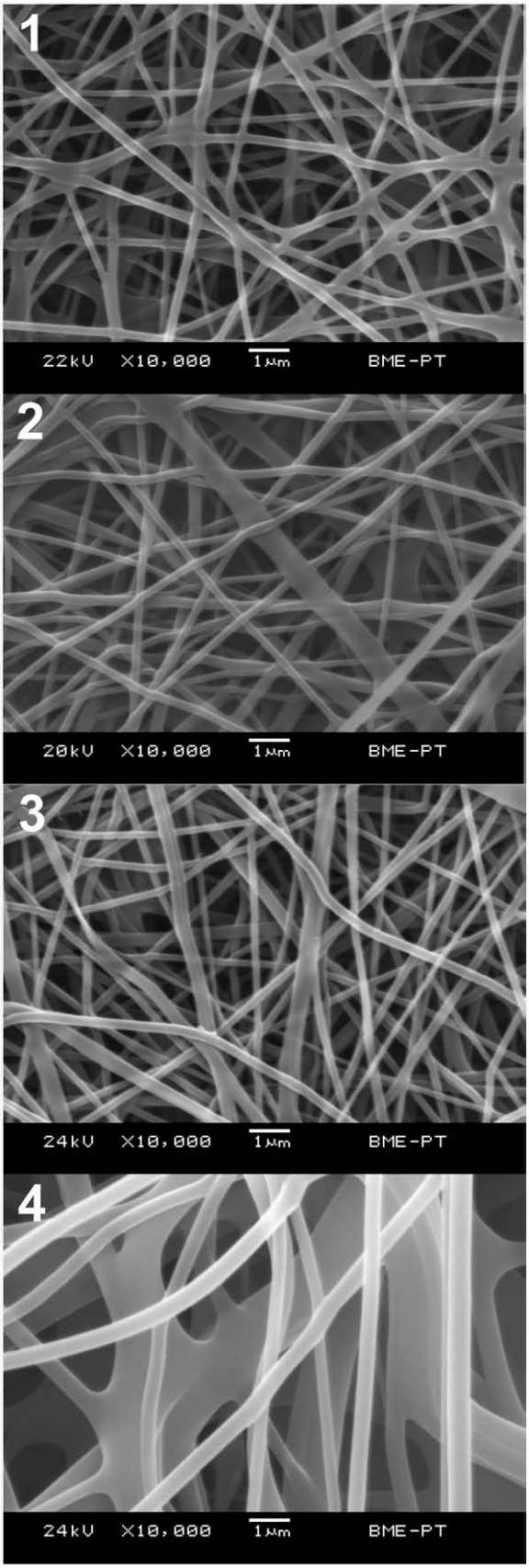

Fig. 2. SEM images of all tested PVA electrospun materials: 1 — without nanotubes; 2 — with SWNTs with COOH modification; 3 — with MWNTs with OH modification; 4 — with MWNTs with OH modification from solution with ethanol. It is visible that in the first three cases the diameters of the samples are in submicron range. The forth samples contains fibers in submicron and also micron range.

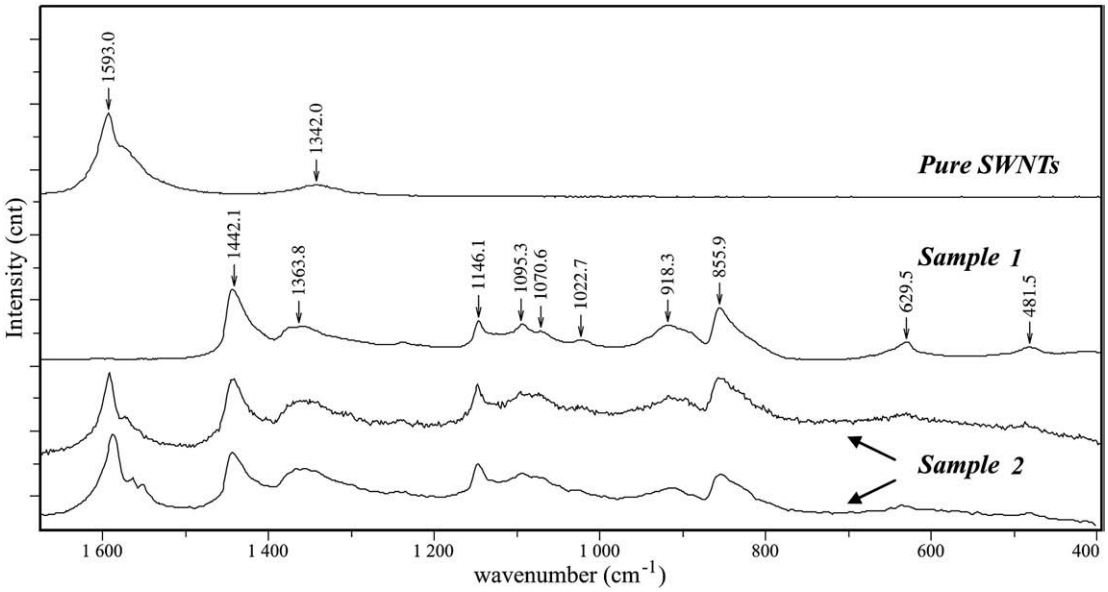

Fig. 3. Raman spectra shows comparison between the spectra of SWNTs, the spectra of the sample without nanotubes and two curves of different parts of sample with SWNTs with surface COOH modification.

It is interesting that the Raman spectra of the third and fourth sample are different (Figs. 4 and 5), however they has to be similar, because of the composition of them are the same. It can be explained by the different rate of the nanotubes containing. In the fourth sample case the diameter of the fibers are higher, it means that they can include more nanotubes, and also agglomerates of them. It means that in the Raman spectra the peaks of the nanotubes is more characteristic while the PVA has less intensive peaks.

4. Conclusions

It is obvious from Raman spectra that carbon nanotubes are in all three cases inside electrospun nanofibers. Thus the study proved that a mass production of electrospun nanocomposite materials by modified needleless method is possible. For usage of water soluble polymer in the mass electrospinning technology, it is necessary to use carbon nanotubes with surface modification (in the case by COOH or OH groups). The main reason is creating of polar bonds and hydrogen bonds between parts of nanotubes and polymer chains. Also extremely long stability of the solutions is apparently the cause of these bonds. These solutions can be used even half-year after their mixing. Of course it is necessary to use the sonication to break up the agglomerations of the nanotubes inside polymer solution.

Future work obviously should be mainly devoted to optimalization of the electrospinning process for a particular required type of usage of these materials and particular testing of result properties of these nanocomposite materials.

Acknowledgment

This research was supported by the Czech–Hungarian intergovernmental research support KONTAKT (No. CZ-4/2007), as well as the

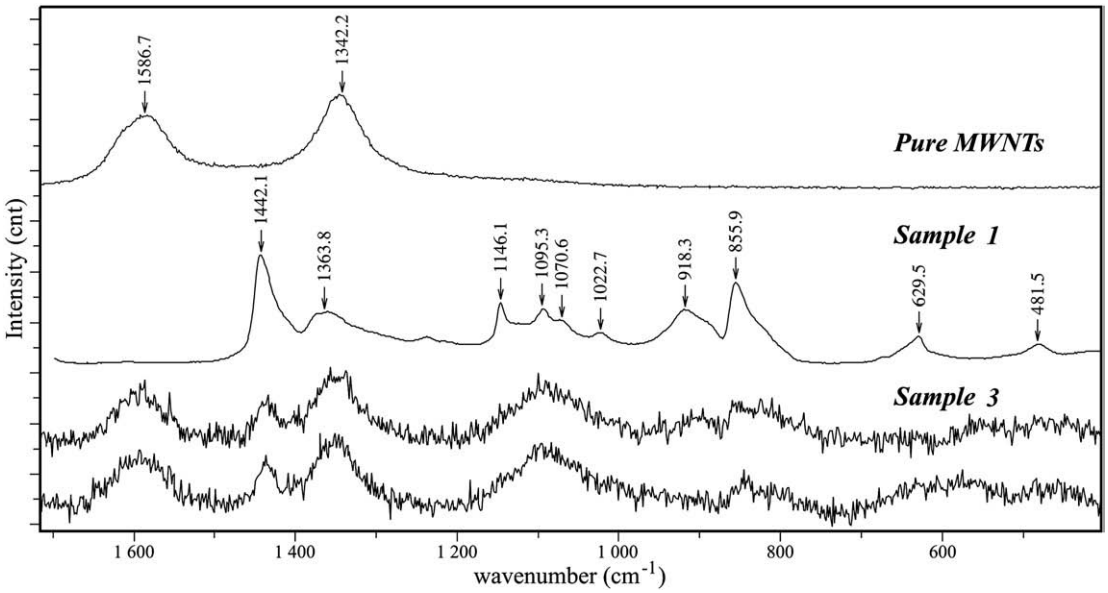

Fig. 4. Raman spectra shows comparison between the spectra of MWNTs, the spectra of the sample without nanotubes and two curves of different parts of sample with MWNTs with surface OH modification.

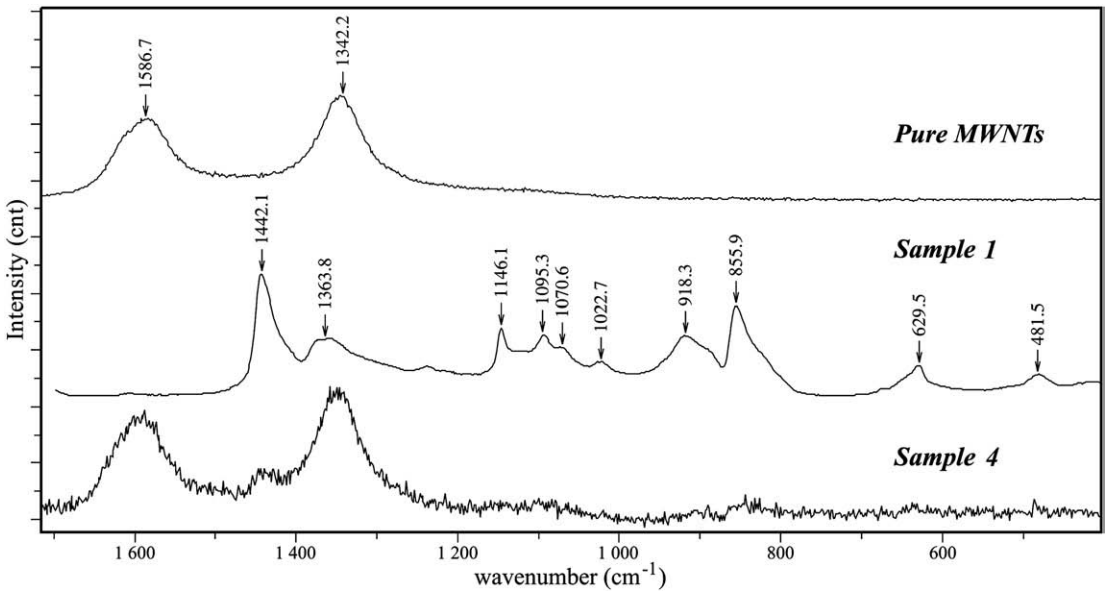

Fig. 5. Raman spectra shows comparison between the spectra of MWNTs, the spectra of the sample without nanotubes and spectra of sample with MWNTs with surface OH modification from solution with ethanol.

Hungarian Research Fund (OTKA NI 62729 and OTKA F 67897) and by the grant of Ministry of Industry and Trade of the Czech Republic, No. MPO — 1M 0553, 1H PK-2/46.

References

[1] Huang ZM, Zhang YM, Kotaki M, Ramakrishna S. Compos Sci Technol 2003;63: 2223–53.
[2] Yarin AL, Zussman E. Polymer 2004;45:2977–80.
[3] Jirsak O, Sanetrnik F, Lukas D, Kotek V, Martinova L, Chaloupek J. CZ Patent 2003–2414.
[4] Jirsak O, Sanetrnik F, Lukas D, Kotek V, Martinova L, Chaloupek J. World Patent WO/2005/024101.
[5] Du J-H, Bai J, Cheng H-M. eXPRESS Polym Lett 2007(1):253–73.
[6] Ko F, Gogotsi Y, Ali A, Naguib N, Ye H, Yang GL, et al. Adv Mat 2003;15(14):1161–5.
[7] Ge JJ, Hou H, Li Q, Graham MJ, Greiner A, Reneker DH, et al. J Am Chem Soc 2004;126:15754–61.
[8] Ko FK, Khan S, Ali A, Gogotsi Y, Naguib N, Yang G, et al. Proc. 19th American Society for Composites Annual Technical Conf USA; 2004.
[9] Kim GM, Michler GH, Pötschke P. Polymer 2005;46:7346–51.
[10] Ye H, Lam H, Titchenal N, Gogotsi Y, Ko F. Appl Phys Lett 2004;85:1775–7.
[11] Kannan P, Eichhorn SJ, Young RJ. Nanotechnology 2007;18:235707.
[12] Kamel S. eXPRESS Polym Lett 2007(1):546–75.
[13] Zussman E, Chen X, Ding W, Calabri L, Dikin DA, Quintana JP, et al. Carbon 2005;43:2175–85.
[14] Sundaray B, Subramanian V, Natarajan TS. Appl Phys Lett 2006;88:14314.
[15] Saito R, Jorio A, Souza Filho AG, Grueneis A, Pimenta MA, Dresselhaus G, et al. Physica B 2002;323:100–6.

Příloha 6

Rampichová M, Košťáková E, Filová E, Prosecká E, Ocheretná L, Lytvynets A, Lukáš D, Amler E. Non-woven PGA/PVA Fibrous Mesh as an Appropriate Scaffold for Chondrocyte Proliferation; Physiol. Res.; Vol.59, Issue 5; pg.773-781 (2010), ISSN: 0862-8408, IF =1.555 (11)

Rampichová M 30%, ***Košťáková E 25%,*** *Filová E 20%, Prosecká E 5%, Plencner M 3%, Ocheretna L 3%, Lytvynets A 4%, Lukáš D 5%, Amler E. 5%*

Physiol. Res. 59: 773-781, 2010

Non-Woven PGA/PVA Fibrous Mesh as an Appropriate Scaffold for Chondrocyte Proliferation

M. RAMPICHOVÁ[1,2], E. KOŠŤÁKOVÁ[3], E. FILOVÁ[1], E. PROSECKÁ[1,2], M. PLENCNER[1,2], L. OCHERETNÁ[3], A. LYTVYNETS[1], D. LUKÁŠ[3], E. AMLER[1,2,4]

[1]Laboratory of Tissue Engineering, Institute of Experimental Medicine, Academy of Sciences of the Czech Republic, v. v. i., Prague, Czech Republic, [2]Institute of Biophysics, Second Faculty of Medicine, Charles University in Prague, Prague, Czech Republic, [3]Faculty of Textile Engineering, Technical University of Liberec, Liberec, Czech Republic, [4]Centre for Cardiovascular Research, Second Faculty of Medicine, Charles University in Prague, Prague, Czech Republic

Received September 10, 2009
Accepted February 19, 2010
On-line April 20, 2010

Summary

Non-woven textile mesh from polyglycolic acid (PGA) was found as a proper material for chondrocyte adhesion but worse for their proliferation. Neither hyaluronic acid nor chitosan nor polyvinyl alcohol (PVA) increased chondrocyte adhesion. However, chondrocyte proliferation suffered from acidic byproducts of PGA degradation. However, the addition of PVA and/or chitosan into a wet-laid non-woven textile mesh from PGA improved chondrocyte proliferation seeded *in vitro* on the PGA-based composite scaffold namely due to a diminished acidification of their microenvironment. This PVA/PGA composite mesh used in combination with a proper hydrogel minimized the negative effect of PGA degradation without dropping positive parameters of the PGA wet-laid non-woven textile mesh. In fact, presence of PVA and/or chitosan in the PGA-based wet-laid non-woven textile mesh even advanced the PGA-based wet-laid non-woven textile mesh for chondrocyte seeding and artificial cartilage production due to a positive effect of PVA in such a scaffold on chondrocyte proliferation.

Key words

PGA • PVA • Non-woven textile • Chondrocyte • Tissue engineering

Corresponding author

Evžen Amler, Charles University, Second Faculty of Medicine, Department of Biophysics, V Úvalu 84, 150 06 Prague 5, Czech Republic. E-mail: evzen.amler@lfmotol.cuni.cz, Fax: +420 257 296 355.

Introduction

Cells seeded in a biodegradable scaffold that slowly dissipates and is gradually replaced by new functional tissue, this is a promising approach in regenerative medicine. Implantation of such an artificial tissue, namely artificial cartilage based on autologous chondrocytes, is already currently applied in clinical practice for osteoarthritis treatment. Three-dimensional highly porous and preferentially fibrous constructs are inevitable in modern tissue engineering. These scaffolds grant the cells not only with suitable environment for their proliferation and differentiation, but also with a proper mechanical and morphological support. Several hydrogels from biopolymers have been reported to create suitable environment for chondrocytes and to provide three-dimensional immobilization of the cells (Benya and Shaffer 1982, Brittberg *et al.* 1997, Radice *et al.* 2000, Drury and Mooney 2003, Ng *et al.* 2005). Despite many positive features of hydrogels, several serious limitations constrain them for broader application. Optimal biomechanical properties belong among the most significant shortcomings. Consequently, development of more favorable scaffolds fully complying with both biocompatibility and biomechanical requirements is a key task of modern tissue engineering.

Application of composite scaffolds that are formed, besides of hydrogels, also from other compounds like biocompatible polymers seems to be a promising

approach. A number of biodegradable polymers were reported. Polyglycolic acid (PGA), known as a resorbable suture in surgery and as ligament fixation in orthopedics, is frequently used (Freed *et al.* 1994, Rokkanen *et al.* 2000, Schaefer *et al.* 2000, Lee and Shin 2007). Different structures and forms of PGA were already published ranging from foams to nanofibers. Non-woven PGA meshes were also used for chondrocyte proliferation *in vitro* and for extracellular matrix (ECM) production (Freed *et al.* 1994, Schaefer *et al.* 2000). However, inflammatory and nonbacterial foreign-body reactions of PGA *in vivo* were described in several studies (Bostman and Pihlajamaki 2000). These inflammatory reactions were probably caused by acid byproducts of PGA degradation (Athanasiou *et al.* 1995). Thus, combination of PGA with other material seems to be inevitable namely for a broader *in vivo* application.

A higher amount of poly(lactic acid) (PLA) reportedly diminishes PGA degradation both *in vitro* and *in vivo* (Lu *et al.* 1999, Lu *et al.* 2000). Buffers or different basic compounds, such as calcium carbonate, sodium bicarbonate, calcium hydroxyapatite, wollastine or bioglass 45S5, were also examined as an alternative approach for pH control of PGA-based implants (Agrawal and Athanasiou 1997, Ara *et al.* 2002, Day *et al.* 2004, Li and Chang 2005).

In the present study, biocompatibility of different novel PGA-based non-woven composite scaffolds was tested for chondrocyte adhesion and proliferation. Particular attention was devoted to the positive effect of a nontoxic, water-soluble, biocompatible and biodegradable synthetic polymer – polyvinyl alcohol (PVA), which is widely used in the biomedical field (Jia *et al.* 2007). In addition, hyaluronic acid (HA), a polysaccharide commonly present in synovial fluid and extracellular cartilage matrix, and chitosan, another natural biodegradable biopolymer, were applied in our non-woven composite scaffolds to compensate the negative inflammatory properties of PGA scaffolds and to prepare the optimum environment for chondrocyte seeding and for development of artificial cartilage.

Materials and Methods

Materials

The scaffolds were produced from poly(glycolic acid) (PGA) fibers (surgical thread from Chirmax, Ltd., Czech Republic, fiber average diameter 15 μm), polyvinyl alcohol (PVA) fibers (Kuralon K-II, Kuraray Europe GmbH, Germany, fiber average diameter 15 μm), and chitosan fibers (Weifang Young Deok Chitosan CO., LTD, China). Primary antibody against type II collagen (clone II-II6B3, DSHB, USA) and secondary antibody Cy 3-conjugated Donkey Anti-Mouse IgG (H+L) (Jackson ImmunoResearch) were used.

Preparation of the scaffolds

The fiber scaffolds were prepared by the so-called wet-laid process of non-woven production. The fibers were swollen and thoroughly dispersed in low voluminous concentration in various liquid media. The suspension was subsequently transported by a liquid flux on a screen, where a web was formed as a result of filtration-like process. The samples were finally dried and bonded.

There were prepared five different wet-laid non-woven scaffolds with area density 283 g/m^2:

PGA fibers were wet-laid in distilled water into a non-woven scaffold (**PGA**);

A blend of PGA fibers (50 %) and PVA fibers (50 %) was wet-laid in n-butanol and mechanically bonded by needle-punching (**PGA/PVA**);

A blend of PGA fibers (50 %) and PVA fibers (50 %) was wet-laid in n-butanol and consequently impregnated by distilled water. This solvent moderately dissolves PVA fibers that are unstable in water and thus PVA fibers served as a binder for the PGA ones (**PVA/PGA/PVA**);

PGA fibers were wet-laid in a water solution of 0.1 % sodium hyaluronate (w/w) (M_r = 1.5 × 10^6 Da) (**PGA/HA**);

A blend of PGA fibers (1/3), PVA fibers (1/3) and chitosan fibers (1/3) was wet-laid in n-butanol and impregnated with distilled water. Dissolved PVA fibers served as a binder for PGA and chitosan fibers (**PGA/PVA/CH**).

Scaffolds were cut to circular pieces with a diameter of 6 mm and sterilized using hydrogen peroxide gas plasma. Sterilization by plasma was used because of PGA sensitivity to heat and moisture. In addition, hydrogen peroxide residuals are nontoxic and noncarcinogenic.

Cells and cell culture conditions

Chondrocytes were isolated from the condyle of femur of a three-month-old New Zealand white rabbit under general anesthesia (60 mg/kg ketamine and

4 mg/kg xylazine). The cartilage was cut to small pieces (1 × 1 mm), put into a collagenase solution (0.9 mg/ml, collagenase crude 816 PSZ) and incubated in a humidified incubator (37 °C, 5 % CO_2) for 14 h. Then the cells were centrifuged at 300 *g* for 5 min and seeded into culture flasks. The chondrocytes were cultivated in Iscove's Modified Dulbecco's Medium supplemented with 10 % fetal bovine serum (FBS), penicillin/streptomycin (100 IU/ml and 100 μg/ml, respectively), 400 mM L-glutamine, 100 nM dexamethasone, 40 μg/ml ascorbic acid-2-phosphate and ITS-X (10 μg/ml insulin, 5.5 mg/l transferrin, 6.7 μg/l sodium selenite, 2 mg/l ethanolamine. Chondrocytes were seeded on scaffolds at a density of 80 $\times 10^3$ /cm^2; the medium was changed every 3 days.

Cell proliferation analysis by MTT test

The MTT test is widely used for *in vitro* measurement of the metabolic activity and proliferation of cells. MTT [3-(4,5-dimethylthiazol-2-yl)-2,5-diphenyl-2*H*-tetrazolium bromide] is reduced to purple formazan by mitochondrial dehydrogenase in cells indicating normal metabolism. 50 μl of MTT (1 mg/ml in a phosphate-buffered saline (PBS) pH 7.4) was added to the medium (150 μl) and samples were further incubated at 37 °C for 4 h. Formazan crystals were solubilized with 100 μl of 50 % *N,N*-dimethylformamide/20 % sodium dodecyl sulfate (SDS) /H_2O, pH 4.7. A volume of 200 μl of suspension was removed to the new well and the optical density of formazan was measured (λ_{sample} 570 nm, $\lambda_{reference}$ 690 nm). Absorbance of samples incubated without cells was deducted from cell-seeded samples. Cells seeded on tissue culture plastic (TCP) were used as control.

Fluorescence and confocal microscopy

Cells were stained using propidium iodide and visualized using fluorescence and confocal microscopy. Cells were fixed by frozen ethanol (–20 °C), rinsed with PBS and then propidium iodide (5 μg/ml in PBS) was added for 10 min, rinsed with PBS again and visualized using a confocal microscope (Leica SP2 AOBS (λ_{exc}=514 nm and λ_{em}=610-645 nm) and a fluorescence microscope (Olympus IX51, U-RFL-T).

Indirect immunofluorescence staining was used to detect type II collagen. Samples were fixed with 10 % formaldehyde/PBS for 10 min, washed in PBS and then incubated in 3 % FBS in PBS/0.1 % Triton at room temperature. Primary antibody (mouse anti type II collagen) was diluted 1:20 and added to samples for 1 hour at room temperature. Then samples were washed with PBS/0.05 % Tween for 3, 10 and 15 min. Secondary antibody (Cy 3-conjugated Donkey Anti-Mouse IgG (H+L), was diluted 1:300 and added for 45 min at room temperature. After washing, an antifading solution was added (PBS/90 % glycerol/2.5 % 1,4-diazabicyclo(2,2,2) octane (DABCO). Type II collagen staining was visualized using confocal microscope Leica SP2 AOBS (λ_{exc}=488 nm, λ_{em}=555-620 nm).

In vitro degradation of the scaffolds

The weight in dry and wet conditions, and water absorption of every group of scaffolds was measured. Three specimens of each group were dried to constant weight and weighed. Then each specimen was put into 70 % ethanol for 10 min and then into PBS for 1 h. Surface water was wiped off with filter paper and the wet weight of samples was measured. Water absorption (WA) was calculated from the Eq. (1),

$$WA = 100 \times (M_w - M_d)/M_d, \quad (1)$$

where M_w is the weight in wet condition, M_d in dry condition.

Five specimens of each group were used for pH measurement. Each sample was put into 20 ml of PBS in a separate bottle without stirring and refreshing. Samples were placed in an incubator (37 °C) and cultivated for 42 days. The pH was measured every two days (pH-meter HANNA HI 92240).

Statistics

Quantitative data were presented as mean ± SD (Standard Deviation). Results were evaluated statistically using one-way analysis of variance (ANOVA), and the Student-Newman-Keuls test. The level of significance was set at 0.05.

Results

Chondrocytes adhere well to wet-laid non-woven scaffolds from PGA

Chondrocyte adhesion on wet-laid non-woven scaffolds from different PGA mixtures was measured by the MTT test 24 h after seeding. In general, chondrocytes adhered well to all PGA-based scaffolds. The best adhesion (absorbance in MTT test A=0.41±0.06), was observed on both wet-laid non-woven scaffolds from

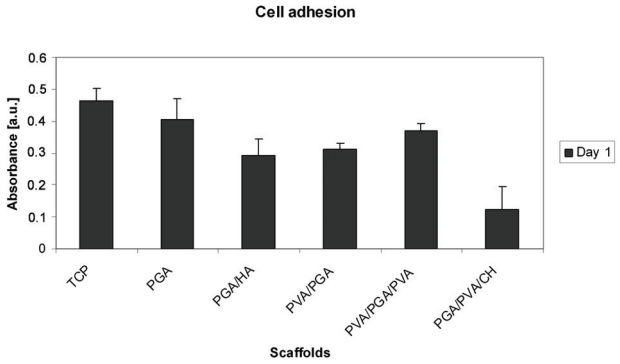

Fig. 1. Chondrocyte adhesion (MTT test) one day after scaffold seeding (significant differences between measured values are described in the text; $p<0.05$).

PGA without any additive (see Fig. 1) and the control TCP sample (A=0.47±0.04). The addition of PVA to the mixture significantly diminished chondrocyte adhesion, except PVA/PGA/PVA. Absorption of composite scaffolds from PVA/PGA/PVA decreased to 0.37±0.02 and for PGA/PVA even to 0.32±0.02.

Curiously, the presence of hyaluronic acid in the PGA mixture did not improve cell adhesion. Absorption remained on the same statistical level with the PGA/PVA mixture (0.29±0.05). This rather surprising finding supports the results of fluorescence confocal microscopy where propidium iodide staining was used to visualize chondrocytes adhered on scaffold fibers (Fig. 2).

Presence of chitosan in the scaffold mixture resulted in the lowest chondrocyte adhesion of all the tested scaffolds. Absorption of the chitosan-containing scaffold (0.12±0.07) was significantly lower not only than the control sample but also than the PVA-containing scaffolds as well than the mesh from PGA/HA mixture.

PVA but not hyaluronic acid improves chondrocyte proliferation on wet-laid non-woven scaffolds from PGA

Despite lower adhesion, the presence of PVA in wet-laid non-woven PGA scaffolds significantly improved chondrocyte proliferation. MTT tests performed on the 7th and 14th day after seeding indicated that the originally lower cell number adhering to fibers on the first day was significantly amplified by very good proliferation. Already 7 days after seeding, the highest cell number was observed on PVA/PGA (0.93±0.06). A somewhat lower value was observed after 7 days of cultivation on PVA/PGA/PVA and also on the control TCP (0.78±0.23 and 0.64±0.09, respectively). A lower absorbance 7 days after seeding was found for the PGA-containing scaffold. Absorbance (0.33±0.16) was significantly lower both in the control TCP sample and in the PVA/PGA scaffold. Interestingly, the presence of hyaluronic acid did not improve chondrocyte proliferation at this early stage and, thus, a similar pattern and a significantly lower cell number compared to TCP and PVA containing scaffolds was observed also for the PGA /HA mixture (0.30±0.03).

In spite of the worst adhesion, the presence of chitosan in the wet-laid non-woven scaffold markedly improved proliferation. While 7 days after seeding our MTT test suggested a good proliferation (absorption 0.45±0.01) but there was still no significant increase compared with the PGA or PGA/HA scaffolds, the PGA/PVA/CH showed a different outline after 14 days of cultivation. The amount of cells increased significantly (1.05±0.14 on day 14) and reached the same level as the control TCP sample (1.12±0.12) (Fig. 3).

This clearly suggested a positive effect of PVA but also chitosan presence in wet-laid non-woven scaffolds on chondrocyte proliferation.

Confocal fluorescence microscopy of wet-laid non-woven scaffolds from PGA mixtures

The positive effect of PVA presence in wet-laid non-woven scaffolds from PGA mixtures on chondrocyte proliferation was proved by the MTT test. However, to confirm this conclusion and to verify suitable proliferation of chondrocytes along the fibers of wet-laid PVA-containing non-woven scaffolds, visualization by confocal microscopy was employed. Cells started to spread along the fibers already 7 days after seeding. On day 14 and 21, large proliferation of cells was observed, mainly on PGA/PVA/CH and PVA/PGA/PVA (Fig. 4).

A key point for successful preparation of artificial cartilage seems to be the preparation of chondrocytes in their optimum condition for transplantation. Only under these circumstances chondrocytes can produce the protein of extracellular matrix. Under these conditions, the production of type II collagen as typical extracellular marker for hyaline cartilage, was observed. Extracellular matrix started to be produced by proliferating chondrocytes on our wet-laid non-woven PGA/PVA scaffolds already during the first week after seeding. Using indirect immunofluorescence of anti-type II collagen, we visualized a developing extracellular matrix by confocal microscopy on days 7 and 14 (Fig. 5). Increasing presence of type II collagen, as a marker of the hyaline cartilage extracellular matrix, is clearly demonstrated.

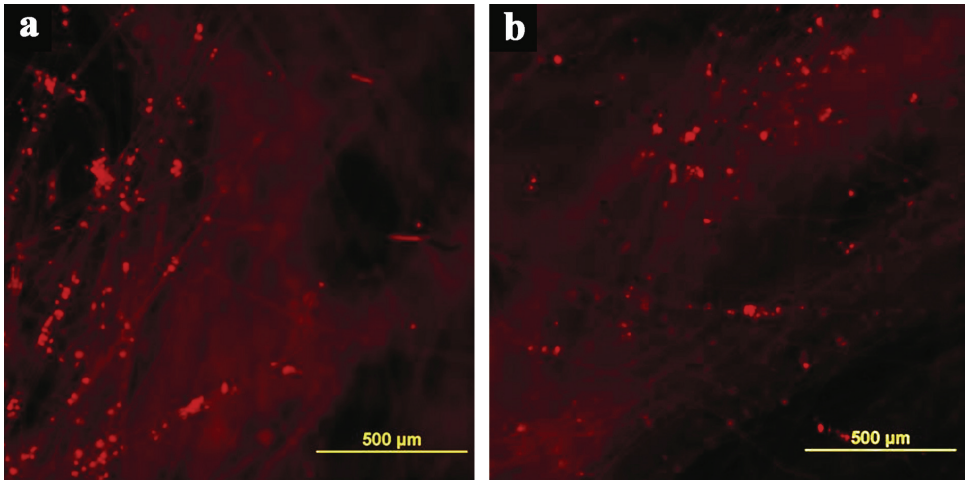

Fig. 2. Fluorescence and confocal microscopy – chondrocyte adhesion on **(a)** PGA/PVA and **(b)** PGA/HA scaffold one day after scaffold seeding.

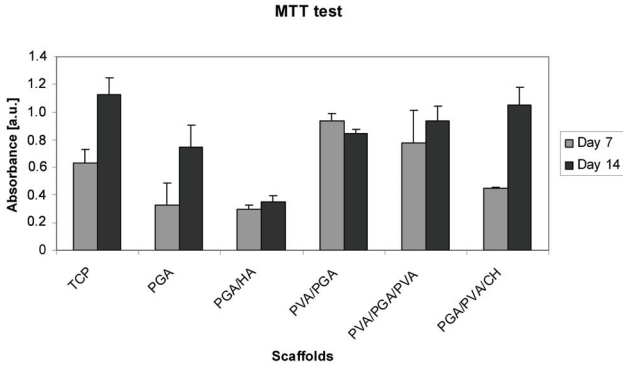

Fig. 3. Chondrocyte proliferation (MTT test) 7 and 14 days after scaffold seeding (significant differences between measured values are described in the text; $p<0.05$).

Scaffolds containing PVA lead to pH stabilization

The time-dependent pH course in the incubation solution over a 42-day period was followed for all tested wet-laid non-woven scaffolds (Fig. 6). A significant pH drop for all PGA-containing scaffolds was found. The largest pH decrease was observed immediately after putting in solution. Despite the comparable initial pH decrease for all tested samples, medium acidification did not continue in the same manner. Acidification of the medium with scaffolds containing PVA continued only very moderately, especially for the PGA/PVA/CH. Conversely, samples containing only PGA or PGA in combination with HA prolonged considerable acidification over the whole 42-day period. This suggested a higher presence of degradation products in the incubation solution.

Wettability of the scaffold influenced scaffold degradation

Slower scaffold degradation of composite PVA-containing wet-laid non-woven scaffolds was also accompanied by another important characteristic: higher water retention inside the scaffolds. Presence of PVA in the mixture increased several times the water absorption in all wet-laid non-woven scaffolds (Table 1). The highest water retention was shown by the PVA/PGA scaffold, three times higher than the PGA scaffold. On the other hand, the addition of hyaluronic acid substantially lowered the water content in the scaffold compared to the PGA scaffold. Notably, samples characterized by higher water retention showed also less pronounced pH dependence. In addition, higher water retention in our samples correlates well not only with the pH dependence but also with improved chondrocyte proliferation while the decreased water content in the PGA/HA sample correlated with their worse proliferation.

Discussion

Chondrocytes adhere well but poorly proliferate on PGA non-woven textile mesh

Polyglycolic acid is commonly known as a resorbable substance frequently used in tissue engineering (Freed *et al.* 1994, Rokkanen *et al.* 2000, Schaefer *et al.* 2000, Lee and Shin 2007). Many different forms and structures of PGA were reported for application in regenerative medicine and tissue engineering but only a few reports are related to non-woven PGA meshes and chondrocyte proliferation (Freed *et al.* 1994, Schaefer *et al.* 2000). In accordance with previously reported data, we found PGA non-woven textile mesh as a proper material for chondrocyte adhesion. Interestingly, presence of PGA in composite scaffolds seemed to be dominant for chondrocyte adhesion to non-woven textile mesh. Neither hyaluronic

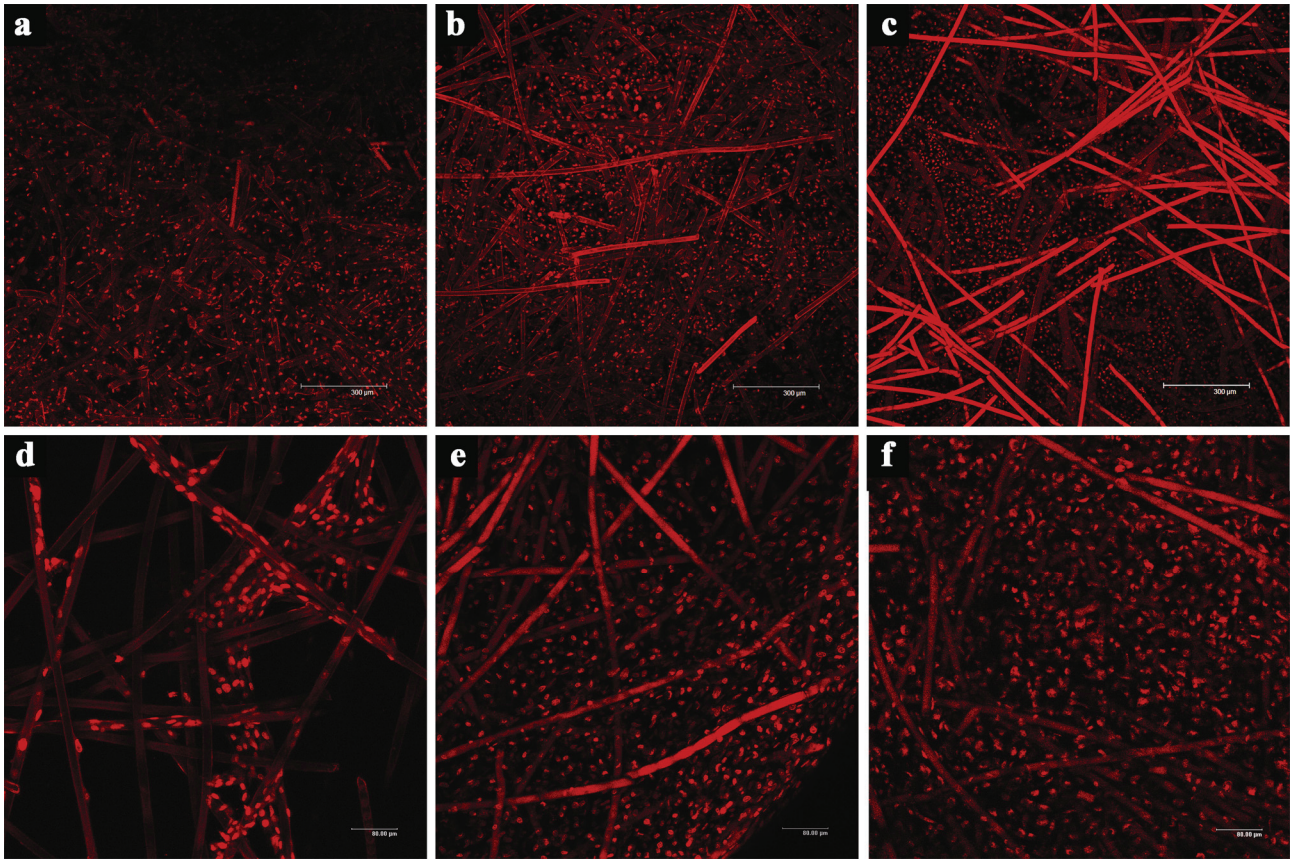

Fig. 4. Fluorescence confocal microscopy of proliferated chondrocytes. Chondrocytes are stained by propidium iodide, which is bound on cell DNA. Fibers of scaffold are also visible for their autofluorescence. PGA/PVA/CH scaffold – **(a)** 7, **(b)** 14, **(c)** 21 days after seeding, PVA/PGA/PVA scaffold – **(d)** 7, **(e)** 14, **(f)** 21 days after seeding.

acid nor chitosan nor PVA increased chondrocyte adhesion in any composite scaffold tested in the present study. Thus, our study confirmed the previously reported results that the mesh from polyglycolic acid (no matter whether in a single-component form or as a composite scaffold) is suitable material for chondrocyte adhesion. However, chondrocyte proliferation on wet-laid non-woven PGA fibers significantly suffers from acidic degradation products. Naturally, hydrolysis of PGA causes its bulk degradation to glycolic acid which is followed by further transformation in the tricarboxylic acid cycle. Final degradation products are excreted as carbon dioxide and water (Athanasiou *et al.* 1995, Agrawal and Athanasiou 1997).

Elevated concentration of acidic by-products could be solved *in vitro* by pH control and/or incubation solution exchange. This approach, however, can be applied neither *in vivo* nor *in vitro* for composite scaffolds where mesh from polyglycolic acid is immobilized in gels or other similar materials. Nevertheless, these composite scaffolds attract growing attention particularly due to the possibility of tuning up their properties to make them more appropriate for cell seeding and proliferation. Consequently, better understanding of PGA degradation processes and especially improved knowledge of their modulation is highly important.

Addition of PVA improves chondrocyte proliferation on PGA non-woven textile mesh

Although our composite scaffolds based on PGA non-woven textile mesh did not show any improved chondrocyte adhesion, their application in tissue engineering seems to be very promising. A proper additive can modify accordingly the biomechanical properties of the scaffold. Biomechanical properties are modified by presence of type II collagen as was detected in our study by immunofluorescence staining and subsequent visualization by confocal microscopy. Despite of less sensitivity of this method compared to PCR, type II collagen was detected in the vicinity of chondrocytes on day 7 and 14. There was a production of both type II collagen and glycosaminoglycans (GAG) which are typical indicators of chondrogenic character of cells that

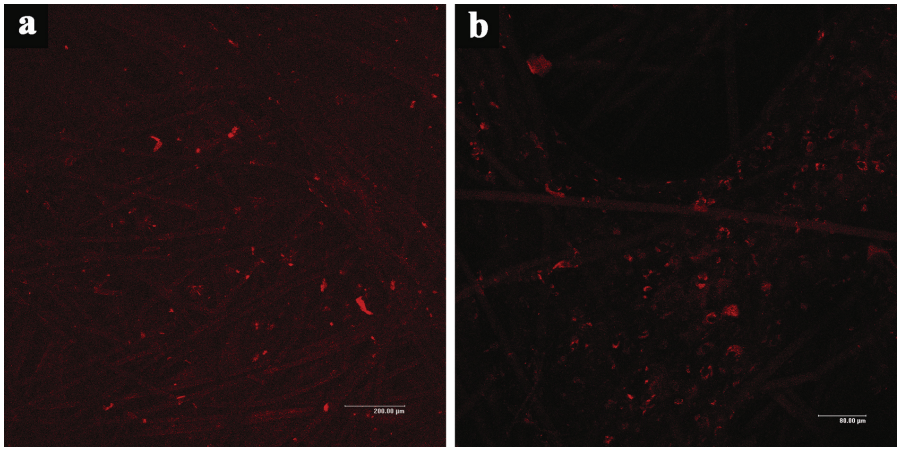

Fig. 5. Fluorescence confocal microscopy of proliferated chondrocytes – immunofluorescent detection of type II collagen. PVA/PGA/PVA scaffold **(a)** 7 and **(b)** 14 days after seeding.

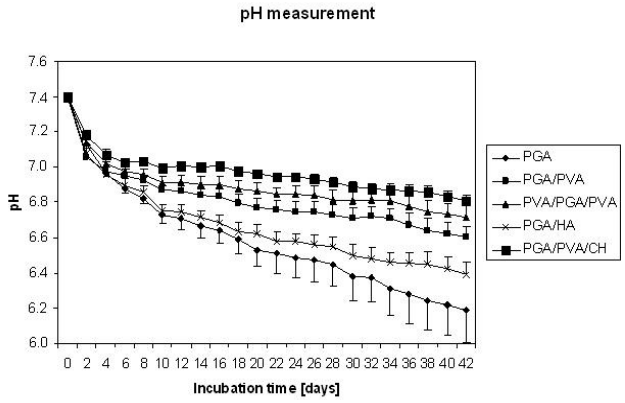

Fig. 6. Time-dependent acidification of scaffolds from PGA mixtures.

Table 1. Scaffold wettability.

Scaffold	Dry weight (mg)	Wet weight (mg)	Water absorption (%)
PGA	4.2 ± 0.9	9.5 ± 1.6	141 ± 46
PVA/PGA	4.4 ± 0.2	22.5 ± 1.2	416 ± 26
PVA/PGA/PVA	4.5 ± 0.3	5.5 ± 0.6	23 ± 10
PGA/HA	3.9 ± 0.5	6.7 ± 0.8	73 ± 13
PGA/PVA/CH	5.3 ± 0.3	18.3 ± 2.3	242 ± 22

For calculation details see Methods.

appear in conjunction. These components are synthesized by chondrocytes and diffused to the extracellular matrix (ECM) of hyaline cartilage. Joint synthesis of both GAG and type II collagen were commonly detected (Benya and Shaffer 1982, Vunjak-Novakovic *et al.* 1999, Deng *et al.* 2003). Consequently, diffusion of type II collagen from chondrocytes as well as collagen crosslinking decreased by the inhibition of GAG incorporation in the newly formed ECM (Bastiaansen-Jenniskens *et al.* 2009).

Appropriate biomechanical properties of artificial scaffolds are currently a considerable obstacle in the construction of artificial cartilages. In addition, composite scaffolds can adjust the lifetime of biodegradation. Last but not least, apposite compounds can adapt scaffold biocompatibility. We clearly proved in our study a positive effect of PVA addition in wet-laid non-woven scaffolds from PGA on chondrocyte proliferation. A slightly lower chondrocyte adhesion in PVA-containing textile mesh was overcome already during the first week of incubation. Improved proliferation was also accompanied by a higher pH stability of incubation media. This suggested a moderate appearance of acidic biodegradation products in scaffolds resulting in a more favorable environment for chondrocyte proliferation. Notably, the presence of chitosan in wet-laid non-woven scaffolds from PGA/PVA did not significantly modify the positive effect of PVA on chondrocyte proliferation. However, such additives can modify the biomechanics and biodegradability of composite scaffolds. However, the influence of additives on these parameters could be only hardly predicted, as follows from the effect of hyaluronic acid which is one of the key substances of the hyaline extracellular matrix. Consequently, proper scaffold composition as well as the way of preparation remain to be experimentally tested.

Composite scaffold preparation is certainly an important feature dramatically influencing composite scaffold application. We found that the presence of PVA significantly increases water retention. This is one of the key points in the hypothetical explanation of improved chondrocyte proliferation – higher water retention leads to better supply of chondrocytes with nutrients and also

to a quicker disappearance of all kinds of degradation products. Such a scaffold structure needs a firmer connection between the fibers and has to be characterized by a more hydrophilic interior with larger pores for water penetration but also for cell seeding. Firmer and more solid scaffolds could be achieved either chemically or using physical means. Our attempts for a physical way of connection (mechanical puncturing) failed so far. However, we present here a successful chemical approach – an application of PVA as a suitable chemical fiber connection in wet-laid non-woven scaffolds from PGA.

Chitosan but not hyaluronic acid is another component improving chondrocyte proliferation on PGA scaffolds

Besides PVA, we also tested the effect of other compounds that could improve chondrocyte seeding and proliferation, i.e. hyaluronic acid and chitosan. HA is a biocompatible and biodegradable polysaccharide which is a very common component of synovial fluid and extracellular matrix (ECM). It plays an important role in tissue hydration. HA is commonly used in medicine and tissue engineering for its physicochemical properties (Hahn *et al.* 2007) and was reported to improve *in vitro* substrate adhesion ability and proliferative activity of human chondrocytes (Patti *et al.* 2001). Interestingly, an attempt to apply HA in our PGA wet-laid non-woven composite scaffold with the aim of connecting PGA fibers failed. The presence of hyaluronic acid in the PGA mesh did not result in any improvement of chondrocyte proliferation compared to PVA scaffold. Notably, the presence of HA in our sample did not also improve water retention. This suggests that rather the size of pores and not the hydrophilicity of the surface component in wet-laid non-woven scaffolds can play a crucial role for proper cell proliferation.

The presence of chitosan, however, resulted in different properties of the PGA composite scaffold. Chitosan is an at least partly deacetylated form of chitin, the second most abundant form of organic resource found in nature next to cellulose. These biopolymers have a good biocompatibility and biodegradation as well as various favorable antithrombogenic, homeostatic, immunity-enhancing or wound-healing properties (Jia *et al.* 2007). We applied chitosan in our PGA composite scaffold. While the presence of chitosan significantly deteriorated chondrocyte adhesion, chondrocyte proliferation was greatly enhanced after the first week, and especially during the second week of cultivation. Consequently, chitosan, beside PVA seems to be a promising compound for preparing composite scaffolds based on wet-laid non-woven PGA textile mesh intended for chondrocyte tissue engineering. However, it is necessary to state clearly that the properties of chitosan can sharply depend on its source and purity.

Conflict of Interest

There is no conflict of interest.

Acknowledgements

Supported by the Academy of Sciences of the Czech Republic (institutional research plans AV0Z50390703 and AV0Z50390512), Ministry of Education, Youth and Sports of the Czech Republic (research programs NPV II 2B06130 and 1M0510), Grant Agency of the Academy of Sciences grant No. IAA500390702, by Czech Science Foundation grants No. GA202/09/1151 and P304/10/1307, EU project BIOSCENT ID number 214539, and the Grant Agency of the Charles University grant No. 119209.

References

AGRAWAL CM, ATHANASIOU KA: Technique to control pH in vicinity of biodegrading PLA-PGA implants. *J Biomed Mater Res* **38**: 105-114, 1997.

ARA M, WATANABE M, IMAI Y: Effect of blending calcium compounds on hydrolytic degradation of poly(DL-lactic acid-co-glycolic acid). *Biomaterials* **23**: 2479-2483, 2002.

ATHANASIOU KA, NIEDERAUER GG, AGRAWAL CM, LANDSMAN AS: Applications of biodegradable lactides and glycolides in podiatry. *Clin Podiatr Med Surg* **12**: 475-495, 1995.

BASTIAANSEN-JENNISKENS YM, KOEVOET W, JANSEN KM, VERHAAR JA, DEGROOT J, VANOSCH GJ: Inhibition of glycosaminoglycan incorporation influences collagen network formation during cartilage matrix production. *Biochem Biophys Res Commun* **379**: 222-226, 2009.

BENYA PD, SHAFFER JD: Dedifferentiated chondrocytes reexpress the differentiated collagen phenotype when cultured in agarose gels. *Cell* **30**: 215-224, 1982.

BOSTMAN O, PIHLAJAMAKI H: Clinical biocompatibility of biodegradable orthopaedic implants for internal fixation: a review. *Biomaterials* **21**: 2615-2621, 2000.

BRITTBERG M, SJOGREN-JANSSON E, LINDAHL A, PETERSON L: Influence of fibrin sealant (Tisseel) on osteochondral defect repair in the rabbit knee. *Biomaterials* **18**: 235-242, 1997.

DAY RM, BOCCACCINI AR, SHUREY S, ROETHER JA, FORBES A, HENCH LL, GABE SM: Assessment of polyglycolic acid mesh and bioactive glass for soft-tissue engineering scaffolds. *Biomaterials* **25**: 5857-5866, 2004.

DENG Y, LIN XS, ZHENG Z, DENG JG, CHEN JC, MA H, CHEN GQ: Poly(hydroxybutyrate-co-hydroxyhexanoate) promoted production of extracellular matrix of articular cartilage chondrocytes in vitro. *Biomaterials* **24**: 4273-4281, 2003.

DRURY JL, MOONEY DJ: Hydrogels for tissue engineering: scaffold design variables and applications. *Biomaterials* **24**: 4337-4351, 2003.

FREED LE, VUNJAK-NOVAKOVIC G, BIRON RJ, EAGLES DB, LESNOY DC, BARLOW SK, LANGER R: Biodegradable polymer scaffolds for tissue engineering. *Biotechnology (N Y)* **12**: 689-693, 1994.

HAHN SK, PARK JK, TOMIMATSU T, SHIMOBOJI T: Synthesis and degradation test of hyaluronic acid hydrogels. *Int J Biol Macromol* **40**: 374-380, 2007.

JIA Y-T, GONG J, GU X-H, KIM H-Y, DONG J, SHEN X-Y: Fabrication and characterization of poly (vinyl alcohol)/chitosan blend nanofibers produced by electrospinning method. *Carbohydrate Polymers* **67**: 403-409, 2007.

LEE SH, SHIN H: Matrices and scaffolds for delivery of bioactive molecules in bone and cartilage tissue engineering. *Adv Drug Deliv Rev* **59**: 339-359, 2007.

LI H, CHANG J: pH-compensation effect of bioactive inorganic fillers on the degradation of PLGA. *Composites Sci Technol* **65**: 2226-2232, 2005.

LU L, GARCIA CA, MIKOS AG: In vitro degradation of thin poly(DL-lactic-co-glycolic acid) films. *J Biomed Mater Res* **46**: 236-244, 1999.

LU L, PETER SJ, LYMAN MD, LAI HL, LEITE SM, TAMADA JA, UYAMA S, VACANTI JP, LANGER R, MIKOS AG: In vitro and in vivo degradation of porous poly(DL-lactic-co-glycolic acid) foams. *Biomaterials* **21**: 1837-1845, 2000.

NG KW, WANG CCB, MAUCK RL, KELLY T-AN, CHAHINE NO, COSTA KD, ATESHIAN GA, HUNG CT: A layered agarose approach to fabricate depth-dependent inhomogeneity in chondrocyte-seeded constructs. *J Orthopaed Res* **23**: 134-141, 2005.

PATTI AM, GABRIELE A, VULCANO A, RAMIERI MT, DELLA ROCCA C: Effect of hyaluronic acid on human chondrocyte cell lines from articular cartilage. *Tissue Cell* **33**: 294-300, 2001.

RADICE M, BRUN P, CORTIVO R, SCAPINELLI R, BATTALIARD C, ABATANGELO G: Hyaluronan-based biopolymers as delivery vehicles for bone-marrow-derived mesenchymal progenitors. *J Biomed Mater Res* **50**: 101-109, 2000.

ROKKANEN PU, BOSTMAN O, HIRVENSALO E, MAKELA EA, PARTIO EK, PATIALA H, VAINIONPAA SI, VIHTONEN K, TORMALA P: Bioabsorbable fixation in orthopaedic surgery and traumatology. *Biomaterials* **21**: 2607-2613, 2000.

SCHAEFER D, MARTIN I, SHASTRI P, PADERA RF, LANGER R, FREED LE, VUNJAK-NOVAKOVIC G: In vitro generation of osteochondral composites. *Biomaterials* **21**: 2599-2606, 2000.

VUNJAK-NOVAKOVIC G, MARTIN I, OBRADOVIC B, TREPPO S, GRODZINSKY AJ, LANGER R, FREED LE: Bioreactor cultivation conditions modulate the composition and mechanical properties of tissue-engineered cartilage. *J Orthop Res* **17**: 130-138, 1999.

Příloha 7

D. Lukas, N. Pan, A. Sarkar, M. Weng, J. Chaloupek, E. Kostakova, L. Ocheretna, P. Mikes, M. Pociute, E. Amler, Auto-model based computer simulation of Plateau–Rayleigh instability of mixtures of immiscible liquids, Physica A (2010),doi:10.1016/j.physa.2010.01.046, IF=1,373 (11)

Physica A 389 (2010) 2164–2176

Contents lists available at ScienceDirect

Physica A

journal homepage: www.elsevier.com/locate/physa

Auto-model based computer simulation of Plateau–Rayleigh instability of mixtures of immiscible liquids

D. Lukas [a,b,*], N. Pan [c], A. Sarkar [a], M. Weng [d], J. Chaloupek [a], E. Kostakova [a], L. Ocheretna [a], P. Mikes [a,b], M. Pociute [e], E. Amler [f,g]

[a] Technical University of Liberec, Faculty of Textile Engineering, Department of Nonwovens – Nanoscience Centre, Studentska 2, Liberec 1, 461 17, Czech Republic
[b] Clemson University, School of Materials Science and Engineering, Clemson, SC, 29634, United States
[c] University of California, Division of Textiles and Clothing, Biological and Agricultural Engineering Department, Davis, CA, 95616, United States
[d] Key Laboratory of Advanced Textile Materials and Manufacturing Technology (Zhejiang Sci-tech University), Ministry of Education, Hangzhou, 310018, PR China
[e] Kaunas University of Technology, Faculty of Design and Technologies, LT-51424 Kaunas, Lithuania
[f] Laboratory of Tissue Engineering, Institute of Experimental Medicine, Academy of Sciences of the Czech Republic, Prague, Czech Republic
[g] Institute of Biophysics, 2nd Faculty of Medicine, Charles University in Prague, Czech Republic

ARTICLE INFO

Article history:
Received 2 December 2009
Received in revised form 24 January 2010
Available online 7 February 2010

Keywords:
Rayleigh instability
Liquid mixture
Auto-model
Markov Random Field

ABSTRACT

The classic theory to derive the characteristic Rayleigh wavelength, i.e., the distance between neighbouring droplets into which an originally cylindrical liquid body disintegrates, as a consequence of Rayleigh instability, is analysed in terms of the phenomenon of self-organization due to the mechanism of 'fastest forming instability'. The paper aims at simulating this self-organization with Monte Carlo dynamics while accounting spatial interactions in lattices of Markov Random Fields that enable also modelling of Plateau–Rayleigh instability of instable mixtures of dispersed immiscible liquids. The Hammersley and Clifford theorem, concerning the general form of energy function, belonging to Markov Random Fields, is introduced for detailed classification of a simple model used for computer simulation. The relevant Auto-model, with Kawasaki dynamics, is chosen to investigate the liquid jet and the instability of the liquid's cylindrical film. The computer-simulated outputs show encouraging agreement with the classic analytical predictions on main features of the Rayleigh instability. The model is also used as a foundation stone for developing a simple analytical approach for the estimation of Rayleigh wavelength of jets and cylindrical films, composed of instable mixtures of immiscible liquids. Qualitatively, the theory agrees with both computer simulation and experiment.

1. Introduction

Interactions of liquids, polymer melts and polymer solutions with fibrous systems, having highly curved surfaces and formation of tiny liquid jets is critical in numerous commercial applications, such as, fibre manufacturing processes, including electrospinning, wet chemical processes of fabrics, protective coating of wires, nonwoven fabrication, etc. Furthermore, such interactions play a vital role in determining the performance of products, like, baby diapers, surgical wipes, feminine hygiene products, hair cosmetics, scaffolds for tissue engineering and paper printings. In spite of wide and common applications, it is quite surprising to find the theoretical description of wetting of fibrous systems to be still in its early stage of development [1].

* Corresponding author at: Technical University of Liberec, Faculty of Textile Engineering, Department of Nonwovens – Nanoscience Centre, Studentska 2, Liberec 1, 461 17, Czech Republic. Tel.: +420 48 535 3146; fax: +420 48 535 3146.
E-mail address: david.lukas@tul.cz (D. Lukas).

0378-4371/$ – see front matter © 2010 Elsevier B.V. All rights reserved.
doi:10.1016/j.physa.2010.01.046

Liquid interacts with a cylindrical surface less readily as compared to a flat surface of the same material [2]. Furthermore, once a liquid film coats a fibre, the film will soon break down into small droplets, more or less regularly spaced along the fibre, except for extremely thin liquid films that are stabilized by the intermolecular forces, such as, the Van der Waals forces. It is well known that in homogeneous liquids, structure of such a chain of droplets, i.e. the typical dimension of the droplets and the distance between them is nearly independent of the associated surface tension, γ, liquid viscosity, and is governed almost completely by the initial radius, r_0, of the cylindrical liquid column. In other words, wetting behaviour of fibres is typified by the instability or breakdown of the liquid columns, coating the fibre, that resembles the breakdown of free cylindrical liquid columns, as initially described by Plateau [3] and Rayleigh [4]. Rayleigh showed the disintegration of a liquid jet with radius, r_0, occurred due to perturbation caused by waves of various wavelengths, λ on the surface of the liquid column, where λ is always greater than $2\pi r$. Disintegration of the liquid's cylindrical film develops at an avalanching rate, obeying the mechanism of fastest forming instability. This phenomenon, called Plateau–Rayleigh instability, was later studied by numerous researchers, both theoretically and experimentally, out of which reported here are those of Roe [2], Tomotikov [5] and Meister [6], respectively.

The present analysis studies the break down of a continuous liquid cylinder, either in the form of a free liquid jet or, a film covering a fibre, and the resultant detachment of the fragmented liquid into droplets with a particular emphasis to study disruptive behaviour of instable mixtures of immiscible liquids. Initially, surfaces of revolution, called as H-surfaces, with constant mean curvature, will be introduced to establish a stability criterion of various liquid bodies. Subsequently, derivation of the wavelength, λ_e, critical to the onset of the breakdown of the liquid jets, will be estimated using conservation of the system's free energy. It will be shown as to why the wavelength of the dynamic phenomenon of the Plateau–Rayleigh instability cannot be derived accurately on the basis of this simplified approach. Thereafter, the original analysis of Rayleigh [4] will be slightly modified to interpret detachment of liquid columns in the frame of self-organization by the mechanism of the fastest forming instability. The succeeding paragraph introduces noteworthy Hammersley and Clifford theorem for deeper classification of the computer simulation model used for the purpose. Furthermore, a computer algorithm, based on both Monte Carlo method and so-called Auto-model, with Kawasaki dynamics, will be described to investigate the Plateau–Rayleigh instability for homogeneous liquid and instable liquid mixture. Eventually, the computer-simulated outputs will be compared with the existing results and newly developed theoretical approach.

2. *H*-surfaces of revolution

In absence of external fields, like the gravity field, liquid jets or liquid films, covering cylindrical fibres possess, as a rule, axial symmetry. A uniform capillary pressure everywhere inside the liquid body defines the equilibrium in such cases, except in the very vicinity of the fibre surface, where the intermolecular forces inflict additional disjoining pressure [1]. For mathematical simplicity, this disjoining pressure will be disregarded in the current analytical context of Rayleigh instability. According to Young [7] and Laplace [8], the capillary pressure value, p_c, depends on the two principal radii R_1 and R_2 of a curved liquid–air interface, as given by

$$p_c = \gamma \left(\frac{1}{R_1} + \frac{1}{R_2} \right). \tag{1}$$

An immediate consequence of this relation for mechanical equilibrium of a liquid body is the constant value of the mean curvature, $K = (1/R_1 + 1/R_2)/2$, along the surface of the body. Rotationally symmetric surfaces of constant mean curvature are called H-surfaces of revolution [9,10]. Plateau [3] demonstrated that there exist only six different species of such H-surfaces of revolution: the flat plane, and catenoid with zero curvature; the sphere, the cylinder, the unduloid, and the nodoid with nonzero value of the mean curvature.

The morphological changes of a liquid film on an isolated, straight and cylindrical fibre occur, particularly, between cylinder and unduloid [11], as in the case of a droplet. Continuous cylindrical columns of liquid jets start disintegrating and continue to do so till detached spheres are formed. Hence, original, as well as, resultant surfaces of liquid bodies, considered in Plateau–Rayleigh instability, belong to the family of H-surfaces. So, only slow morphological changes, without any vigorous manifestations of inertia, are normally considered and hence, Monte Carlo dynamics, used in our computer simulation, seem to be appropriate to describe the development of the fastest forming instability.

3. Energy conservation and Rayleigh instability

A rough analysis of the Plateau–Rayleigh instability of free liquid columns can be done by associating the initial shape of a liquid jet, which is originally cylindrical, with the final form of a chain of droplets, each with identical volume. So, for an incompressible liquid holds:

$$\pi r_0^2 \lambda_e = \frac{4}{3} \pi r_d^3, \tag{2}$$

where, λ_e is the length of the cylinder with original radius, r_o, that is converted into one droplet of radius, r_d. The volume conservation between the cylinder and the sphere is assumed here. The value of λ_e, obtainable from the volume and surface energy conservation laws, will be taken as the approximation of the Rayleigh wavelength, λ. The free energy of the liquid is composed of two components. Firstly, one is associated with the surface tension, γ, i.e. the surface energy, γS, while the

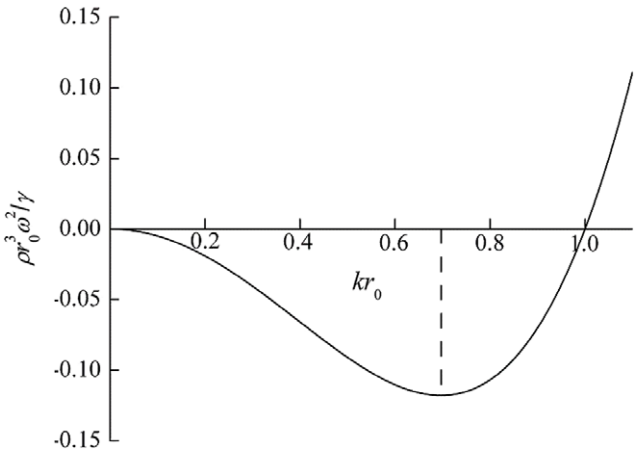

Fig. 1. Dispersion law for the Rayleigh instability plots dimensionless angular frequency $\omega^2\rho r_0^3/\gamma$ against the dimensionless wave-number kr_0. The fastest forming mode occurs for $\partial\omega^2/\partial\,(kr_0) = 0$ providing with the wavelength $\lambda = 2.87\pi r_0$.

last one is associated with the mechanical energy by means of capillary pressure, p_c, and volume V, i.e., $p_c V$. The last one will be further referred to as pressure energy. Quantities, S and V are respectively the surface area and the volume of the liquid bodies. A liquid column will spontaneously form a droplet/unduloid if its free energy is higher than the free energy of a probable subsequent shape, approximated as sphere.

$$2\pi r_0\lambda_e\gamma + \pi r_0\lambda_e\gamma \geq 4\pi r_d^2\gamma + \frac{8}{3}\pi r_d^2\gamma. \tag{3}$$

According to the previous remark, the left hand side of the Eq. (3) represents a cylinder's free energy, while the right hand side is the free energy belonging to the cylindrical liquid jet. From Eqs. (3) and (2), λ_e may be expressed as:

$$\lambda_e \geq \frac{5^3 4}{3^4} r_0 \approx 1.96\pi r_0. \tag{4}$$

A well known similar inequality was firstly established experimentally by Plateau [3], while observing the onset of instability, marked with formation of spherical drops of oil in water, mixed with alcohol, from an elongated initial cylindrical shape. According to Plateau, the instability started when the cylinder's length, i.e. wavelength, λ_e, is between $1.99\pi r_0$ and $2.02\pi r_0$, quite close to the present estimation. A similar study [12] ended up with the well-known inequality, $\lambda_e > 2\pi r_0$. Thus, conclusively, a drop cannot be formed, when the wavelength is shorter than $2\pi r_0$, since the surface energy of the drop is always lower than that of the original smooth cylinder.

It is noteworthy that the exact value of the wavelength of the Rayleigh instability cannot be derived based merely on the conservation of free energy. Transformation of the liquid body shape is coupled with dynamic mutation of its shape and surface area, causing changes of both surface and kinetic energies. Some authors also mentioned entropy changes at the liquid–gas interface [13]. Thus, the success of computer simulations of the Rayleigh instability, using the Auto-model, as introduced later on, is, rather, due to the appropriate "quantum" dynamics represented by Markov Chain of states that dissipates appropriately energy, than due to the ability of Auto-models to reveal Newtonian dynamics of the studied system.

The Plateau–Rayleigh instability of liquid jets is the consequence of a temporal development and magnification of originally tiny perturbations, commonly known as the capillary waves [14,15]. Assuming that the perturbations are harmonic surface waves, with assigned wavelengths, the following relation for one-dimensional propagation of the wavy perturbation along the original cylindrical liquid column, coinciding with x-axis of cylindrical coordinate system, holds true:

$$r = r_o + \varepsilon \exp\left[\mathrm{i}(kx - \omega t)\right]. \tag{5}$$

In this relation, r is the radius of the liquid body as a function of space, x, and time, t. The symbol r_o denotes original radius of a perfectly cylindrical column, and ε is the initial amplitude of the perturbation. The angular frequency of the surface wave is ω, and k is the wave-number ($k = 2\pi\lambda^{-1}$, where λg is the wavelength).

Starting with Euler equation in cylindrical coordinates that describes mechanical dynamics of ideal fluids, and subsequently applying appropriate boundary conditions, where balance of normal stress on free liquid surface plays a critical role, one comes to a dispersion relation (6) [14], that indicates the dependence of the angular frequency ω on the wave-number, k.

$$\omega^2 = \frac{\gamma}{\rho r_0^3}\frac{I_1(kr_0)}{I_0(kr_0)} kr_0\left(1 - k^2 r_0^2\right). \tag{6}$$

Liquid mass density is here denoted as ρ, while $I_0(x)$ and $I_1(x)$ are modified Bessel functions of the zero and first order. The relationship among dimensionless quantities $\omega^2\rho r_0^3/\gamma$ and kr_0 is depicted in Fig. 1. The parameter kr_0 has a critical value at 1

and, hence, the critical, previously mentioned, Plateau wavelength is $\lambda_r = 2\pi r_0$. Beyond this lower limit the square of the angular frequency, ω^2, is negative and so, ω starts to be purely imaginary. The negative value of ω^2 causes the imaginary part of i.e., $q = Im(\omega) = -i\omega$, to play the role of a growing factor of the amplitude. When $\omega^2 < 0$ the wave becomes stationary, since, the imaginary argument of the exponential function in Eq. (5) loses its dependence on time, and the amplitude with positive growing factor, q, starts to grow instantaneously as εe^{qt}.

$$r = r_o + \varepsilon e^{qt} \exp[i(kx)]. \tag{7}$$

Self-organization, i.e. the detachment of a liquid column into equidistantly located droplets, governed by the mechanism of the fastest forming instability, is due to the selection of the extreme value of the growing factor, q, that belongs to the minimal value of ω^2. It is usually accepted that the resulting instability is entirely determined by the earliest state of the perturbations, for which the Eq. (6) holds. As indicated in Fig. 1, the fastest forming mode occurs for $\partial\omega^2/\partial(kr_0) = 0$, when the wavelength is $\lambda = 2.87\pi r_0$. This value is called Rayleigh wavelength. As will be shown in Section 4, it is noteworthy that the chosen Auto-model and, particularly, its Monte Carlo dynamics follow this rule, obtained on the basis of hydrodynamic analysis of a liquid column. This fact is surprising since the Auto-model does not involve any information about liquid density, particle velocity, inertia and kinetic energy belonging to liquid motion, as opposed to the conventional methodology to derive governing equations of Rayleigh instability, e.g., using dispersion law, as in Eq. (6).

4. Random Fields and the Markov Random Fields

It is believed that one of the great progresses in the field of statistical physics is the ability to combine the physics with the informatics [16]. Here an attempt is presented to connect the mathematical description of Random Fields and Markov Random Fields, used often for image recognition, with the models and methods used in Statistical physics to deal with the present problem of Plateau–Rayleigh instability of immiscible liquids to demonstrate the robustness of such a combined approach.

A Random Field may be briefly described through a lattice consisting of a set $S = \{s_1, s_2, \ldots, s_n\}$ of n nodes (or sites). Any two different nodes can be differentiated with their node indices, i and j. Each node, s_i, from the set, S, is assigned a random variable X_i. For a discrete random variable, a local state space, Λ_i, at a node, s_i, may be defined, by a set of all local random variable values $\{x_i, y_i, \ldots, z_i\}$. Local state spaces of all nodes form a global state space, Λ, in which each random variable, X_i, is assigned an actual random variable value, x_i, in each node s_i. Then, a configuration vector, $\vec{x}$, corresponding to the global state space, Λ, is composed of all the random variable values $\vec{x} = (x_1, x_2, \ldots, x_n)$. The probability, $P(\vec{x})$, that the system appears in the particular configuration, $\vec{x}$, is referred to as the joint probability [17–19].

In Random Fields, all nodes interact with each other, while Markov Random Fields have a reduced set of interactions between the nodes. Hence, for Markov Random fields, the probability that a variable, X_i, acquiring a value $x_i \in \Lambda_i$ is, and only is, conditional upon values of x_j's at the neighbourhood $N_i \subset S$ of the node, s_i, where a neighbourhood, N_i, is composed solely of nodes, s_j's, that interact directly with the node s_i. According to the definition, the node s_i is not an element of its own neighbourhood. Due to the complete set of interactions between all the nodes in a Random Field, the concept of local conditional probabilities $p(x_i|x_1, x_2, \ldots, x_{i-1}, x_{i+1}, \ldots, x_n)$ can be introduced to define the probability of occurrence of a random local configuration, x_i, at the node s_i, under the condition that all other nodes, s_j's, are configured with a certain pattern of x_j's. For simplifying the analysis, all the neighbourhoods are considered, further, to be symmetric wherein any node, s_j, belongs to the neighbourhood of a node, s_i, if and only if, the node s_i belongs to the neighbourhood of the node s_j.

In the early 1970's, Besag [20] formulated on the basis of Bayes' rule [21] a proposition for Random Fields in which he showed that the joint probabilities, $P(\vec{x})$, are uniquely determined by their local conditional probabilities, p's. Specifically, for any two given global configurations, $\vec{x} = (x_1, x_2, \ldots, x_n)$, $\vec{y} = (y_1, y_2, \ldots, y_n) \in \Lambda$, the following relation may be derived.

$$\frac{P(\vec{x})}{P(\vec{y})} = \prod_{1 \le i \le n} \frac{p(x_i|y_1, y_2, \ldots, y_{i-1}, x_{i+1}, \ldots, x_{n-1}, x_n)}{p(y_i|y_1, y_2, \ldots, y_{i-1}, x_{i+1}, \ldots, x_{n-1}, x_n)}. \tag{8}$$

However, the problem of determining the most general probability structure of $P(\vec{x})$ for a symmetric neighbourhood of each site arises. The first approach to this problem, made by Hammersley and Clifford [22], was commented by Besag [20] as, "circuitous and requires the development of an operational calculus (the 'blackening algebra')". On the contrary, the main idea involved in pioneering Hammersley and Clifford's approach, to factorise global probabilities into 'clan functions', served as the main hint to solve the problem in question. As a result, the said theorem was, thenceforth, coined with the names of Hammersley and Clifford. Besag proposed a simpler approach to this issue [20], based on investigation of changes in joint probability due to alterations in local configurations.

Derivation of the Hammersley and Clifford theorem appropriately demands introduction of the notion of 'clan' ('clique') [18,20]. A clan, c, may be defined as a set of mutually interacting nodes, i.e. every node of a clan is a neighbour of all other nodes belonging to the same clan. Moreover, each node is considered to make a clan, though, physically it does not belong to its own neighbourhood. So, a solitary node creates a 1-clan, while a group of k mutually interacting nodes makes a k-clan. Random Fields have a complete set of interactions, i.e., clans, while Markov Random Fields possess reduced number of clans, corresponding to their system of neighbourhoods.

Using the notion of a clan, Hammersley and Clifford theorem may be effectively formulated, since each clan c in a Markov Random Field may be assigned a g-function. In arguments of g-functions appear random variable values of all the nodes that belong to a particular clan. The g-functions, then, determine joint probabilities, $P(\vec{x})$, according to the formula

$$P(\vec{x}) = \prod_{1\le i\le n} g_i(x_i) \cdot \prod_{1\le i<j\le n} g_{i,j}(x_i, x_j) \cdot \prod_{1\le i<j<k\le n} g_{i,j,k}(x_i, x_j, x_k) \cdots . \tag{9}$$

The Hammersley and Clifford theorem states, that the $g_{i,j,\ldots,k}$-function may disappear from the factorisation of the joint probability at the right hand side of Eq. (9) if and only if the nodes $\{s_i, s_j, \ldots, s_k\}$ do not make a clan in a Markov Random Field. Subjected to this restriction, the g-functions may be chosen as arbitrary functions of random variables [18,20].

Merging of Hammersley and Clifford theorem with classic statistical physics requires definition of an energy function, $Q(\vec{x}) = \ln P(\vec{x})$, to obtain the following expression directly from Eq. (9):

$$Q(\vec{x}) = \sum_{i=1}^{n} q_i(x_i) + \sum_{1\le i<j\le n} q_{i,j}(x_i, x_j) + \sum_{1\le i<j<k\le n} q_{i,j,k}(x_i, x_j, x_k) + \cdots . \tag{10}$$

Two objectives are achieved at by defining an energy function — these are to transform the multiplicative form of g-functions in Eq. (9) into additive form, and to maintain equivalence between the results obtained from the theories of Markov Random Fields and Gibbs potentials in Statistical physics. More details about this equivalence were discussed in Refs. [16,18]. The energy function, $Q(\vec{x})$, for physical systems, investigated from point of view of statistical physics, vide Boltzmann law as Eq. (14), is defined as negatively taken system's total energy, $-E(\vec{x})$, normalized by the statistical temperature τ as $Q(\vec{x}) = -E(\vec{x})/\tau$.

The simplest Markov Random Fields are the ones that belong to non-interacting particles. The example of such system is the ideal gas in statistical physics.

$$P(\vec{x}) = \sum_{1\le i\le n} q_i(x_i) . \tag{11}$$

The Auto-models, the non-trivial Markov Random Field models, including Ising model, are defined to have an energy function $Q(\vec{x})$, composed of g-functions, belonging, at the most, to 2-clans, as given below:

$$P(\vec{x}) = \sum_{1\le i\le n} q_i(x_i) + \sum_{1\le i<j\le n} q_{i,j}(x_i, x_j) . \tag{12}$$

The first term in relation (12) represents interactions of individual nodes with external fields or self-interaction of individual nodes, while the last term expresses interactions between pairs of nodes.

For computer simulation of the Rayleigh instabilities of free liquid columns and of liquid layers on a fibre, as introduced further in the work, the energy function of the Auto-model is written as:

$$Q(\vec{x}) = \sum_{1\le i<j\le n}^{n} q_{i,j}(x_i, x_j) = -\frac{1}{\tau} \sum_{1\le i<j\le n}^{n} E(x_i, x_j), \tag{13}$$

where, τ is the statistical temperature.

5. Computer simulation

The Markov Random Field used here for investigation of the Rayleigh instability is composed of a cubical simulation box of lattice-nodes having dimensions of $N = N_X \times N_Y \times N_Z = 600$ l.u. $\times$ 20 l.u. $\times$ 20 l.u., and volume of 24×10^4 (l.u.)^3, where l.u. represents a length unit that is chosen as the nearest-neighbour inter-node distance in the lattice. The distance of one l.u. will be called further as lattice constant b. In each node, a random variable, X_i, is assigned a value of 0, when the node is filled by air, a value of 1 when filled by liquid, and a value of 2, when the node is occupied by solid (fibre). The neighbourhood for each node is composed of 26 neighbouring nodes that together with the central node form a super-cube of 27 nodes. The number of interactions, belonging to a particular node, is also called as coordination number z. One crucial aspect of the particular form of energy function, $Q(\vec{x})$, as in Eq. (13), in the present context is the easiness with which it can be interpreted in terms of the concrete physical meaning of Hamiltonian, $E(\vec{x})$ (total system energy). The Hamiltonian depends on a particular set of interaction energies, $E(x_i, x_j)$'s, of neighbouring particles, represented by random variable values in nodes of the lattice. To concretise the energy function, the shape of the right hand side of Eq. (13) may be considered. Assuming, that the contributions to the energy function, regarding the Hammersley and Clifford theorem, are only from $q_{i,j}(x_i, x_j)$, where random variable values, x_i and x_j, belong to the neighbouring nodes, s_i and s_j, that make the 2-clan. The energy function, $Q(\vec{x})$, of physical systems is also supposed to be homogeneous, i.e. $q_{i,j}$ does not depend on the selected node pairs, s_i and s_j, i.e. $q_{i,j}(x_i, x_j) = q_{k,l}(x_k, x_l)$ for each $x_i = x_k$ and $x_j = x_l$. Thus, there is no need to distinguish exchange energies using nodal indices. Hence, one may write $E_{i,j}(x_i, x_j) = E(x_i, x_j)$. The particle interaction energies are assumed to be symmetric and, hence, holds $E(x_i, x_j) = E(x_j, x_i)$. The energy function contributions, $q(x_i)$'s of 1-clans are considered as zero, thus implying, that the influence of external fields such as gravity, electrical field, etc. are neglected. So, one can construct

Table 1
Interaction energies are symmetric functions of their two variables $E(x_i, x_j) = E(x_j, x_i)$ and represent the energies belonging to mutual interaction of neighbouring nodes i and j where random variables X_i and X_j have values x_i and x_j.

Interaction energies $E(x_i, x_j)$ in (e.u.)	Gas $x_i = 0$	Liquid $x_i = 1$	Fibre $x_i = 2$
Gas $x_j = 0$	−40	−10	20
Liquid $x_j = 1$	−10	−26	−10
Fibre $x_j = 2$	20	−10	0

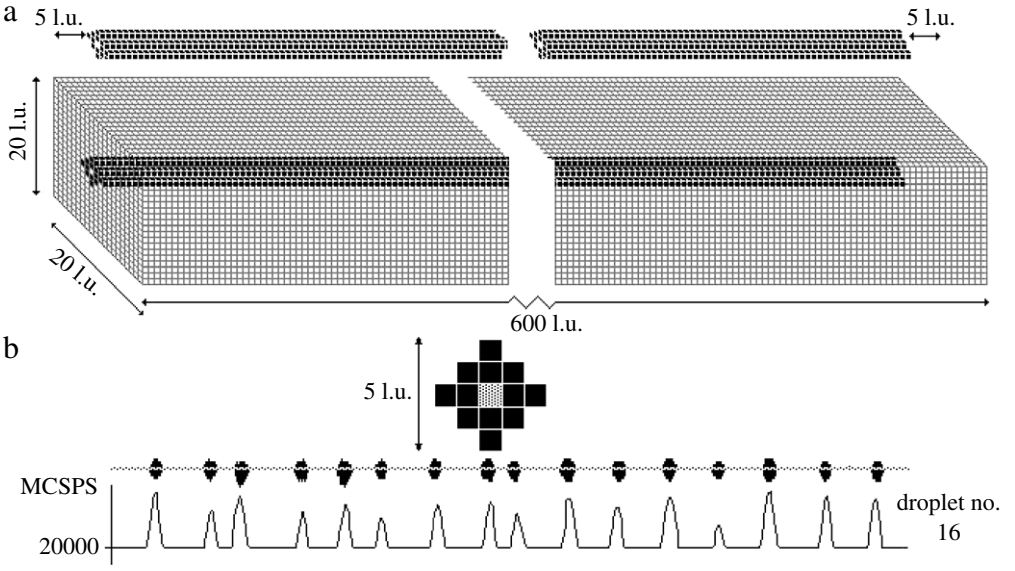

Fig. 2. (a) The original longitudinal and cross sectional configurations of the liquid coated fibre; the cubical simulation box of lattice-nodes has dimensions of $N = N_X \times N_Y \times N_Z = 600\,\text{l.u.} \times 20\,\text{l.u.} \times 20\,\text{l.u.} = 24 \times 10^4\,(\text{l.u.})^3$. (b) Detailed cross sectional shape of the original liquid layer on a fibre and the liquid nodes distribution along the fibre axis after the detachment into individual unduloids at the time of MCSPS=20,000.

the contribution $q(x_i, x_j)$ to energy function $Q(\vec{x})$ in the language of statistical physics [23] as $q(x_i, x_j) = -E(x_i, x_j)/\tau$. The statistical temperature, denoted as τ, has physical dimension of energy, and so, $-E(\vec{x})/\tau$ is a dimensionless energy function, $Q(\vec{x})$. These are the arguments that led to the used energy function, introduced in Eq. (13), for the computer simulations.

The statistical temperature, τ, for the carried out computer simulations, is assigned a value of 50 e.u., where e.u. is the energy unit of the model. The values of particle interaction energies, $E(x_i, x_j)$, are provided in Table 1. Free boundary conditions, as defined earlier [23], are used. Initially all liquid nodes are configured into chains, parallel to the fibre axis to simulate liquid columns or liquid films on straight fibres. The initial configuration of the system is depicted in Fig. 2. Two systems are studied in this work: liquid jets and liquid coatings (layers) on a fibre. For liquid jet simulation, all non-gassy nodes are initially filled with the liquid to have $x_i = 1$. For the case of liquid coating a fibre, the central chain of nodes inside a liquid column represents the solid fibre with all x_i's equal to 2. Various cross sections of the systems, i.e. various liquid columns with different radii, to be studied are shown further.

Monte Carlo dynamics, based on Metropolis algorithm and Kawasaki dynamics for short-range exchange [23], has been used in computer simulations. A pair of nodes in this method has been chosen at random, and within this chosen pair, the particles try to exchange their positions so that a new configuration is attained. To realize that, the Hamiltonian values, $E(\vec{x})$'s are firstly calculated for both the configurations: before (denoted further by index 1) and after (index 2) exchange trials. The change of configuration from the original to the new one is accepted surely if the total energy, $E(\vec{x}_2)$, for the new configuration is lower than that of the original one $E(\vec{x}_1)$, i.e. if $E(\vec{x}_1) > E(\vec{x}_2)$. If the aforementioned condition is not accomplished, the exchange occurs only with a certain *exchange probability* of $W_{1\to2}$. The exchange probability $W_{1\to2}$ is expressed as, $W_{1\to2} = \exp\left[-\left(E(\vec{x}_2) - E\left(\vec{x}_1\right)\right)/\tau\right]$. This probabilistic transition is simulated by the generation of a uniform random number, z, within the interval $\langle 0, 1\rangle$ and the acceptance of a new system configuration is done under the condition, $z < W_{1\to2}$. Detailed information about Model dynamics are given by Binder and Lukas [23–25].

Generally, simulation outcomes of Monte Carlo dynamics vary with respect to the criteria used for exchange of nodal random variable values, i.e. exchange of particles. Present simulations use the Kawasaki dynamics for short-range exchange [23], where the paired particles for the exchange are chosen among the neighbours, i.e. neighbouring nodes. The simulation algorithm iterates the described steps and terminates after the liquid film disintegrates into individual droplets. As a time unit for Monte Carlo dynamics, Monte Carlo Step per Site/Node (MCSPS) [23] is used, corresponding to average one exchange trial for each node in the simulation box. Presently there are 24×10^4 trials for node exchange in each MCSPS.

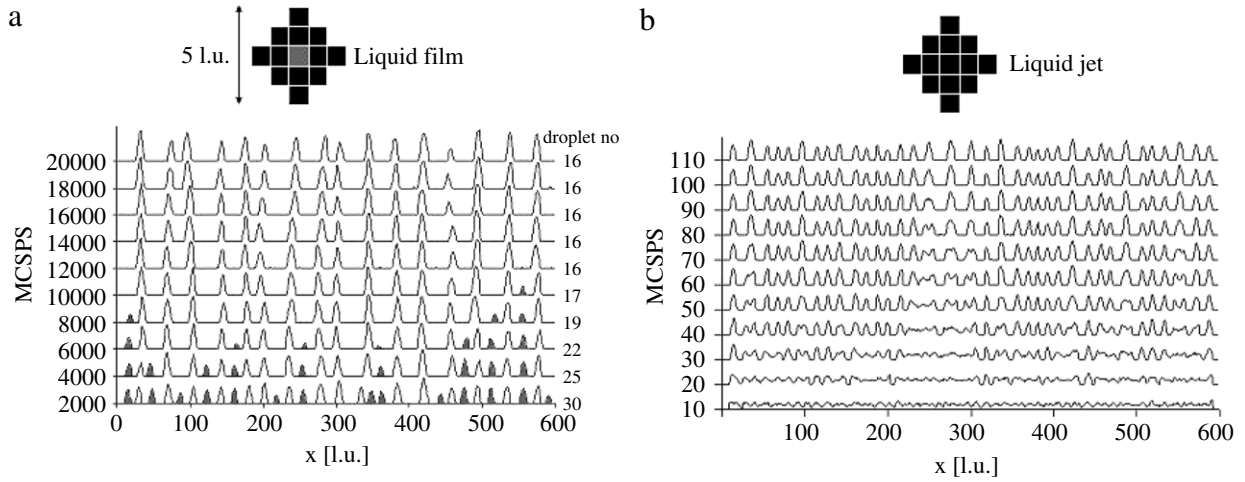

Fig. 3. The time versus the droplet numbers for (a) the liquid coating the fibre; (b) the pure liquid jet. Unduloids on the fibre merge and those, which disappeared, are marked in grey.

It is well established [23] that the aforementioned temporal Markov chain of system states assures the convergence of the process to the equilibrium probability distribution of configurations, $P_{eq}\left(\vec{x}\right)$, where

$$P_{eq}(\vec{x}) = \frac{1}{Z}\exp\left(\frac{-E\left(\vec{x}\right)}{\tau}\right). \tag{14}$$

Here, Z is the partition function. The chosen Kawasaki dynamics for particle exchange conserves the number of particles as well as the fixed positions of fibres in the present model and impose constraints on the original formulation of the Markov Random Field. Some of these issues mentioned above, are also discussed in more details by Paget [18] and Moussouris [26].

6. Computer simulation outputs

Computer simulation outputs of a liquid film coating the fibre is sketched in Fig. 2. The original longitudinal and cross sectional configurations of the liquid coated fibre is depicted in part (a). The part (b) illustrates the liquid distribution along the fibre axis at the time of MCSPS = 20,000. The liquid particle counts in a cross section, perpendicular to the original liquid column axis at various positions along the fibre axis, represent the droplet localizations, as is shown in the inserted graph.

More informative simulation outputs are provided in Fig. 3a for liquid coating a fibre; and in Fig. 3b for free liquid jet. These graphs plot positions of the liquid droplets along the x-axis, corresponding to their coordinates. In both the cases, the number n of droplets along the fibre axis changes with the iteration time, i.e. with MCSPS. It is obvious, from these figures that the number of detached droplets indeed undergoes a temporal change, driven by the previously described Monte Carlo dynamics. The dynamics of the liquid film, coating a fibre is nearly perpetual because the droplets can continuously communicate with neighbours to exchange liquid particles via sessile liquid films on a fibre between neighbouring droplets. As a result, some neighbouring droplets merge to minimize the system surface energy. So, the temporal development of this system is vital for detecting the *first* complete break down of the originally cylindrical liquid bodies, to compare this early-detached configuration with Rayleigh's prediction, $\lambda = 2.87\pi r_0$. The detection of these early-detached configurations has been done here using figures with a series of graphs, like the ones in Fig. 3a, obtained at equidistant steps of 2000 MCSPS time scale. On the contrary, number of droplets created from a free liquid jet has no temporal development after the complete detachment takes place because isolated droplets can't exchange liquid particles effectively.

By comparing Fig. 3a and b, the pure liquid jet takes much less MCSPS, than the liquid coating the fibre, to disintegrate. The time development of the droplet number, averaged over five such trials, for the liquid coating a fibre is plotted in Fig. 4. The figure shows that a temporal decrement of n, caused by mutual merging of neighbouring droplets, can be described by a logarithmic dependence, $\ln(n) = A * \text{MCSPS} + B$, where $A = -0.000039$ and $B = 3.364$, with the correlation coefficient, as high as $R^2 = 0.97$.

The computer-simulated outputs are compared with the analytical results for the Rayleigh instability. The Rayleigh wavelength, $\lambda = 2.87\pi r_o$, is considered as the characteristic distance between neighbouring droplets that fits the earliest state of complete detachment of the cylindrical liquid films and jets. By varying the thickness of the liquid film (or radii of the liquid jet), r_o, the simulations generate data for plots λ against r_0. Fig. 5a shows the cross sections for pure liquid jets and liquid films with cross sectional area values, A, in l.u.^{2} and the radii, r_0, in l.u. of the corresponding cylinders that satisfy the condition, $r_0 = \sqrt{A/\pi}$. The Rayleigh wavelength, λ, versus the original radius, r_0, as predicted by the analytical Rayleigh theory (solid line), and by the computer simulation outputs (points) are plotted in Fig. 5b and c. The plot for the pure liquid jets is provided in Fig. 5b, while Fig. 5c represents the relationship for liquid coating a fibre.

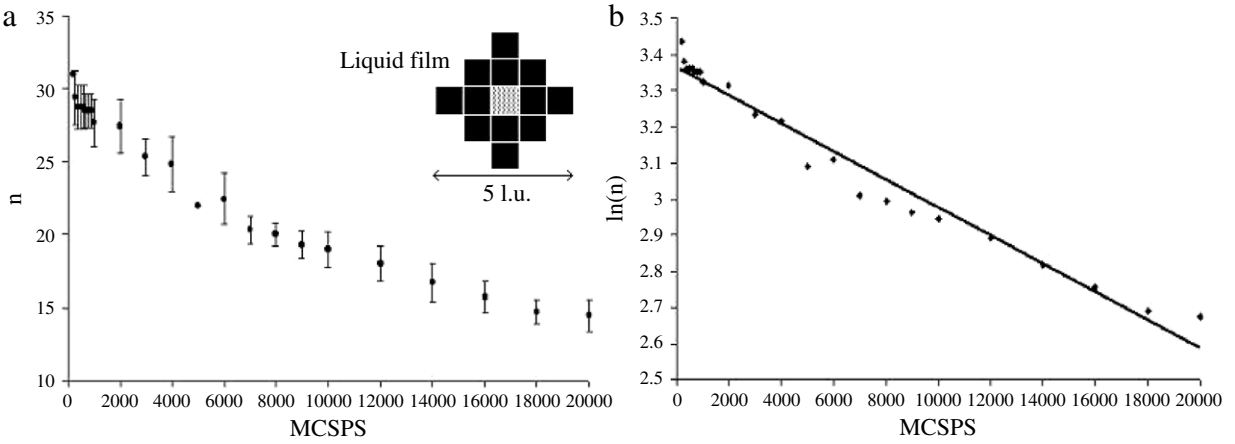

Fig. 4. The time versus the droplet numbers for the system of liquid coating fibre with the original cross section sketched. (a) The droplet numbers n versus MCSPS; (b) $\ln(n)$ versus MCSPS.

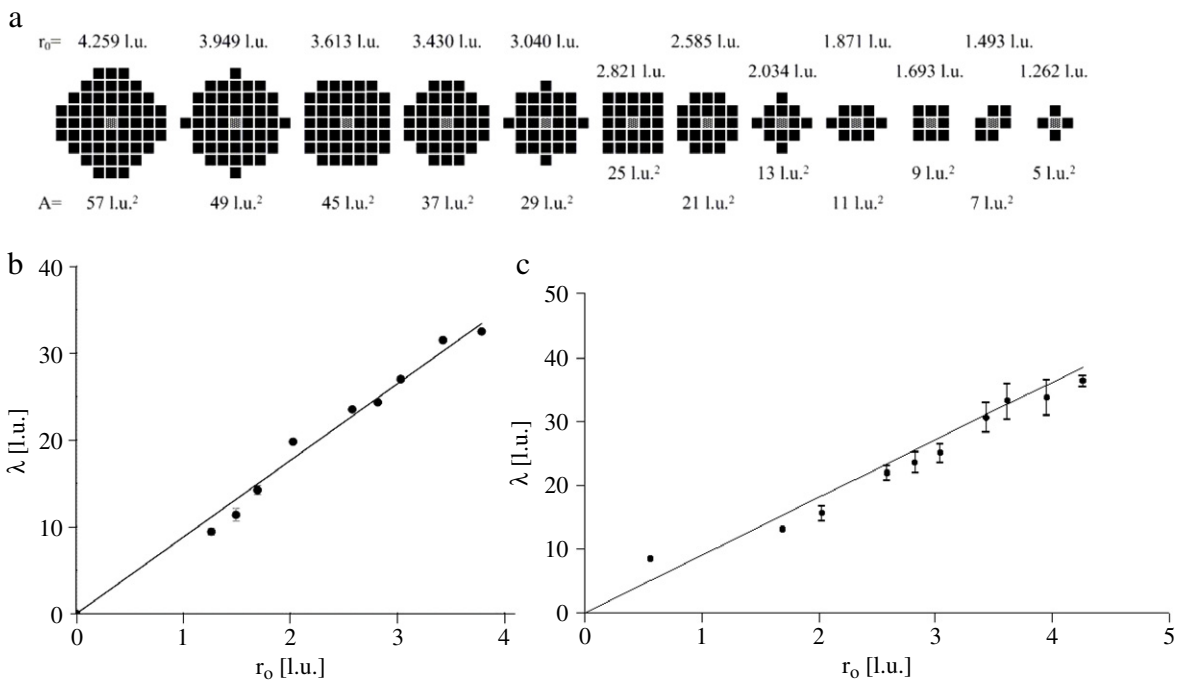

Fig. 5. (a) The cross sectional areas A in l.u.^{2} and the corresponding radii of cylinders r_o are displayed next to each cross section. The Rayleigh wavelength λ versus the original radius r_o as predicted by the analytical theory, i.e. $\lambda = 2.87\pi r_0$, (solid line) and our computer simulations (points) are plotted in parts (b) and (c); (b) is for pure liquid jet and (c) for liquid coating a fibre.

7. Immiscible liquids

In this section the way to use the Auto-model and the relevant Monte Carlo simulation to investigate the films of an instable immiscible complex liquid, i.e., liquid mixture, formed with the original random mixture/dispersion of liquid L_1 and a "new" liquid L_2, is demonstrated. All the rules regarding assigning values to the lattice variable X_i remain the same, as in the previous simulation. Therefore, in each node the lattice variable $X_i = 2$ when it is filled by solid fibre, $X_i = 1$ when filled by liquid no. 1, and $X_i = 0$ when filled by gas. In addition, the lattice variable obtains the value $X_i = 3$ when filled by the liquid L_2. Similar original configuration has been used here, as before, for the particular radius of the liquid film, $r_0 = 3$ l.u. Interaction energies for the gas, the liquid L_1, liquid L_2 and the solid fibre are introduced in Table 2. In the table are also provided the surface energies of the investigated system between all interfaces (gas–liquid L_1, gas–liquid L_2, gas–solid fibre, liquid L_1–liquid L_2, liquid L_1–solid fibre, and liquid L_2–solid fibre). These surface energies are determined by a procedure briefly described further and in Ref. [25].

Table 2
The first part of the table introduces all interaction energies used for the simulation of the behaviour of the mixed liquid film on the fibre. All parameters concerning the liquid no.1 are the same as for simulation of the disintegration of the homogeneous liquid film. Second part introduces all surface energies of the system.

Interaction energies in (e.u.)	Gas $x_i = 0$	Liquid no. 1 $x_i = 1$	Liquid no. 2 $x_i = 3$	Fibre $x_i = 2$
Gas $x_j = 0$	−40	−10	−12	20
Liquid no. 1 $x_j = 1$	−10	−26	−15	−10
Liquid no. 2 $x_i = 3$	−12	−15	−26	−30
Fibre $x_j = 2$	20	−10	−30	−60
Surface energies in (e.u./l.u.^{2})	Gas $x_i = 0$	Liquid no. 1 $x_i = 1$	Liquid no. 2 $x_i = 3$	Fibre $x_i = 2$
Gas $x_j = 0$	–	23	21	70
Liquid no. 1 $x_j = 1$	23	–	11	33
Liquid no. 2 $x_i = 3$	21	11	–	13
Fibre $x_j = 2$	70	33	13	–

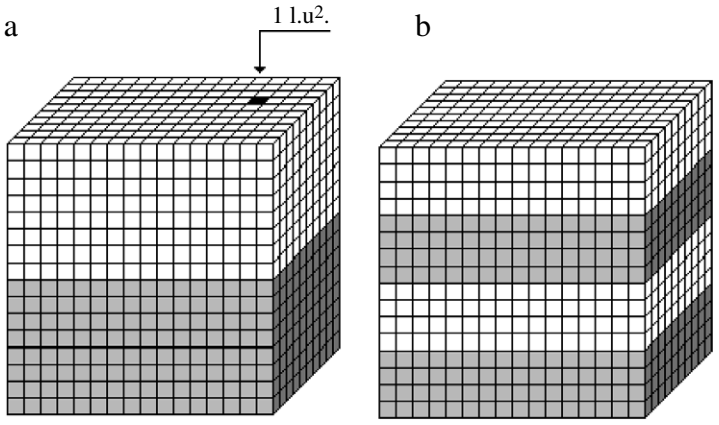

Fig. 6. Simulation box with absolutely flat interfaces between regions occupied by two different types of liquids. There is only one such interface in (a), but three interfacial planes in (b), where different cells of liquids interact to create the surface energy E_S. The total number of cells, as well as numbers of cells occupied by the two liquids, remains constant in both the configurations. Comparing interaction energies between all interfacial planes in both configurations leads to the conclusion that the total energy of the three interface configurations in (b) minus the energy of the one interface configuration in (a) per cell is $2C(X_1, X_2) - [C(X_1, X_1) + C(X_2, X_2)]$.

One may imagine a prismatic simulation box filled partly by two different types of liquids L_1 and L_2, with a flat interface between them. Then, a new configuration could be created simply by moving a slab of liquid L_1 into a space, originally occupied by the liquid L_2, in a manner such that the total numbers of cells for both the liquids are conserved. The system rearrangement is sketched in Fig. 6. Subtracting the energy of the second configuration from the first, the increase of the energy per unit surface $b^2 = 1\,\text{l.u.}^2$ could be obtained as $2C(X_1, X_2) - [C(X_1, X_1) + C(X_2, X_2)]$. This increase is due to the creation of the two new surfaces and, hence, their surface energy, E_S, has the value

$$E_S = C(X_1, X_2) - \frac{1}{2}\left[C(X_1, X_1) + C(X_2, X_2)\right]. \tag{15}$$

Such estimation of the surface energy has to be considered as a zero-temperature limit of its value, since no thermal fluctuations on interfaces are admitted. In Table 2 the units for all surface energies are in e.u./l.u.^{2}. From the table it is obvious the following relation exists among the surface tensions of various interfaces in the system

$$\gamma_{F,G} > \gamma_{F,L1} > \gamma_{G,L1} > \gamma_{G,L2} > \gamma_{F,L2} > \gamma_{L1,L2}, \tag{16}$$

The indices F, G, L_1, L_2 denote the fibre, the gas, the liquids L_1, and L_2, respectively The interaction energies, $C\left(X_i, X_j\right)$'s are chosen so that the lowest surface tension is between the liquids and the highest is between the fibre and the gas. Thus, the surface tensions may be tuned according to actual properties of the systems. From the first part of Table 2, it is quite clear that the liquid L_2 is bonded to the fibre stronger than liquid L_1. Also, the interactions between identical liquid cells are stronger ($C(X_1, X_1) = C(X_2, X_2) = -26$ e.u.) than those between the liquid cells of different types ($C(X_1, X_2) = -15$ e.u.), thereby reflecting the nature of immiscible liquids.

The outputs of the computer simulation, showing the disintegration and coalescence of the instable liquid mixture, are graphically expressed in Figs. 7 and 8. It is obvious from Fig. 7 that both pure liquids L_1 and L_2 have their Rayleigh wavelength close to 25 l.u., while the immiscible liquid results in a lower wavelength with the minimum value close to 17 l.u., at a concentration close to 30%. It is also interesting to note that the curve is not symmetric. One may conclude that the immiscible liquid with the chosen exchange energies will disintegrate with Rayleigh wavelength, smaller than that is

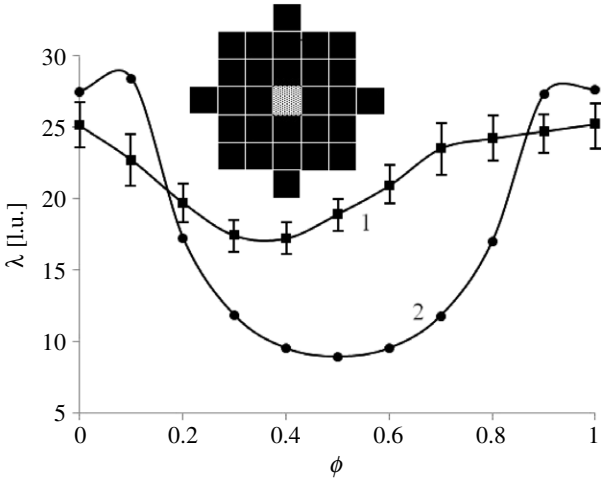

Fig. 7. Rayleigh wavelength, λ, versus the concentration, ϕ, of the liquid L_2 in the liquid L_1 for the disintegration process of the immiscible liquids film on a fibre. The curve (1) belongs to the computer simulation, while the dependence (2) represents an estimation provided by the theoretical approach, using Eq. (26).

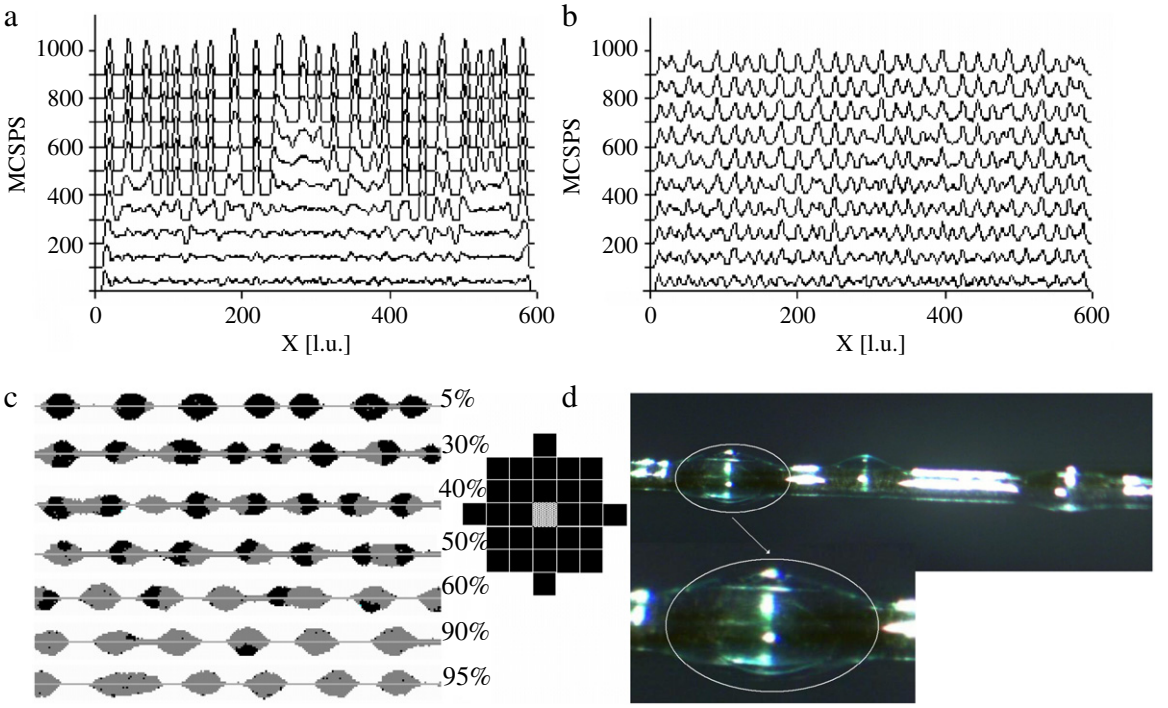

Fig. 8. The effect of the concentration of liquid L_2 on the temporal evolution of number of droplets. (a) The time development of the system with liquid L_1 only. (b) The time development of the system with the 40% of the liquid L_2. (c) The computer simulation output for the mixed liquid where the concentration of the liquid L_2 varies from 5% up to 95%. (d) A real system composed of a mixture of water and oil.

predicted for homogeneous liquids. Moreover, the process of the disintegration is much quicker for the immiscible liquids. Graphical comparison of results between the pure liquid L_1 and a liquid, blend with 40% concentration of the liquid L_2, is depicted in Fig. 8a and b, and the structure of detached droplets made by the composite liquid is shown in Fig. 8c, while Fig. 8d demonstrates the behaviour of a real system composed originally of an instable mixture of water and oil.

Based on the present computer simulation, a following analytical approach to the estimation of the wavelength of Rayleigh instability of immiscible liquids is derived. When a liquid jet/film consists originally of an instable mixture two immiscible liquids L_1 and L_2, a typical detached droplet of individual volume $V = 4/3\pi r_d^3$ is formed out of two distinguished volumes V_1 and V_2, corresponding to the liquid L_1 and the liquid L_2 respectably as a consequence of coalescence. Such final droplet compositions are obtained in computer simulation outputs and also found in the real system observations as depicted in Fig. 8c and d respectively, since relaxation time of Rayleigh instability is greater than the relaxation time of

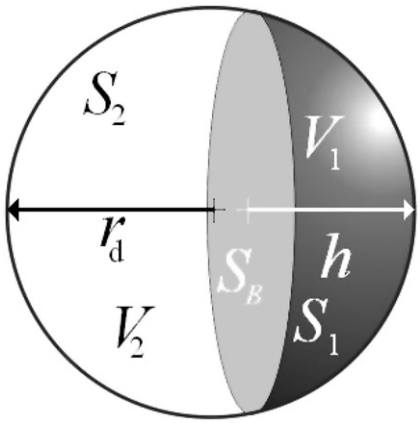

Fig. 9. A detached droplet of individual volume, $V = 4/3\pi r_d^3$, is composed of two distinguished volumes V_1 and V_2, containing the liquid L_1 and the liquid L_2, respectively. Surface of the spherical cap is S_1, the rest of the sphere has surface area S_2 and the base of the spherical cap is of surface area S_B. The height of the spherical cap is denoted as h.

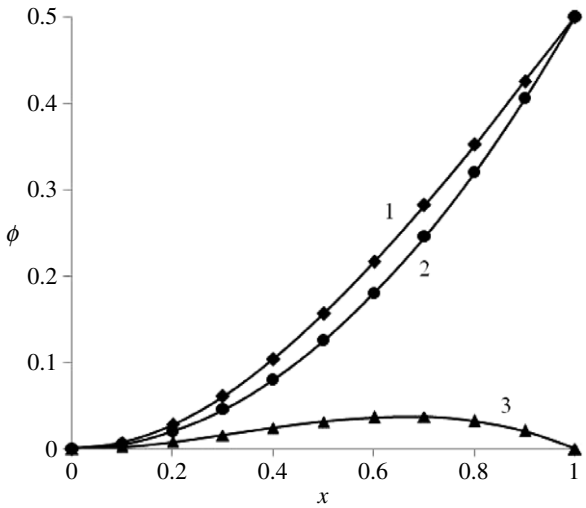

Fig. 10. The accurate dependence of ϕ on x, i.e., $\phi = 3x^2/4 - x^3/4$, is depicted as a curve no. (1). The estimation of this dependence using $\phi \cong x^2/2$ is plotted as a curve no. (2), while the difference of previous function values is depicted as a curve no (3).

coalescence. The ratio V_1/V is defined as concentration or, volume fraction, ϕ, of the liquid L_1 in the mixture. If $V_1 \leq V_2$, and composite droplets are perfectly spherical, where a spherical cap of height h is made by liquid L_1, the associated surface areas of all interfaces in the droplet, i.e., of the spherical cap of area, S_1, of the rest of the area of the sphere, S_2, and of the base area of the spherical cap, S_B, as functions of the volume fraction, ϕ, could be estimated. Quantities V_1, V_2, S_1, S_2, S_B and h are graphically introduced in Fig. 9. For ϕ holds:

$$\phi = \frac{\pi h^2 (r_d - h/3)}{\frac{4}{3}\pi r_d^3} = \frac{3}{4}\frac{h^2}{r_d^2} - \frac{1}{4}\frac{h^3}{r_d^3} \cong \frac{x^2}{2}, \tag{17}$$

where $x = h/r_d$. The estimation of ϕ as $\phi \cong x^2/2$ in a closed interval $x \in \langle 0, 1\rangle$ seems to be quite reasonable and satisfactory. The dependence of ϕ on x, as $\phi = 3x^2/4 - x^3/4$, its estimation $\phi \cong x^2/2$ and the difference of both are depicted in Fig. 10. The expression for the estimation of the spherical cap surface S_1 using Eq. (17) is straightforward, as given below:

$$S_1 = 2\pi r_d h = 2\pi r_d^2 x \cong 4\pi r_d^2 \sqrt{\frac{\phi}{2}}. \tag{18}$$

Estimations of the rest of the spherical surface S_2, that is complementary to the surface of the cap, and the surface S_B of the cap's base, follows immediately from the relation (18).

$$S_2 \cong 4\pi r_d^2 \left(1 - \sqrt{\frac{\phi}{2}}\right), \tag{19}$$

$$S_B \cong \pi\left(2r_d h - h^2\right) = 4\pi r_d^2\left(\sqrt{\frac{\phi}{8}} - \frac{\phi}{8}\right). \tag{20}$$

A free energy, F_d, of one detached droplet is composed of two parts: the surface energy of all droplet's interfaces and the pressure energy, i.e., the product of pressure and volume. The pressure energy of a droplet consisting of two spherical caps made by liquids L_1 and L_2 is estimated here using an average surface tension, γ, derived from the following simple fraction law:

$$\gamma = \gamma_1\phi + \gamma\,(1-\phi)\,. \tag{21}$$

Therefore, the pressure energy term of the droplet $pV = (2\gamma/r_d)\,V$ is given as $8/3\pi r_d^2\,[\gamma_1\phi + \gamma_2\,(1-\phi)]$. One can assess the free energy, F_d, of one detached droplet with the aid of the previously done considerations as:

$$\begin{aligned} F_d &\cong 4\pi r_d^2\left[\sqrt{\frac{\phi}{2}}\gamma_1 + \left(1-\sqrt{\frac{\phi}{2}}\right)\gamma_2 + \left(\sqrt{\frac{\phi}{8}} - \frac{\phi}{8}\right)\gamma_{12} + \frac{2}{3}\left(\gamma_1\phi + \gamma_2\,(1-\phi)\right)\right] \\ &= 4\pi r_d^2\left[\left(\frac{2}{3}\phi + \sqrt{\frac{\phi}{2}}\right)\gamma_1 + \left(\frac{5}{3} - \frac{2\phi}{3} - \sqrt{\frac{\phi}{2}}\right)\gamma_2 + \left(\sqrt{\frac{\phi}{8}} - \frac{\phi}{8}\right)\gamma_{12}\right]. \end{aligned} \tag{22}$$

Free energy of the original cylindrical jet, F_0, having the length, λ, also consists of surface energy and pressure energy term similarly as the right hand side of relation (3). The fraction law, $\gamma = \gamma_1\phi + \gamma\,(1-\phi)$, for the surface tension of random liquid mixture is assumed to be in force also in this case.

In addition to relation (3), the surface energy of inner interfaces in the instable liquid mixture bulk is involved in F_0. This additional term that is proposed here, has a simplified shape in the parlance of lattice models of mixing. In these models free energy difference, ΔF, i.e. free energy of mixing [27], is expressed as $\Delta F = \Delta U - \tau\Delta\sigma$, where ΔU is the change of internal energy, i.e. internal energy of mixing. The term $\tau\Delta\sigma$ represents the entropic contribution to the change of a system's free energy. Entropy of mixing is denoted as $\Delta\sigma$ in this term. The internal energy of mixing, ΔU, is expressed using so-called interaction parameter, $\chi = z\Delta\varepsilon/\tau$, with z being a coordination number introduced above, and $z = 26$ here. The quantity $\Delta\varepsilon = 1/2\,(E_{11} - 2E_{12} + E_{22})$ is so-called exchange energy with E's having similar meaning of interaction energies, $E\left(x_i, x_j\right)$, as in the previous section. Hence, $\Delta\varepsilon = \gamma_{12}b^2$, where b is the lattice constant, in the present model or, a characteristic dimension of islands of a liquid L_1 dispersed in a sea of a liquid L_2 in actual experiments. Taking into account that $\Delta\varepsilon$ is considered here without any temperature dependence, the internal energy of mixing turns into $\Delta U = N\tau\phi\,(1-\phi)\,\chi$, where N is the total number of particles in a system. This total number could be estimated as V/b^3, while V is the aforementioned volume of the investigated liquid. Using previous arguments, the total internal energy of mixing, ΔU, can be written as:

$$\Delta U = \pi r_0^2\lambda b^{-1} z\phi\,(1-\phi)\,\gamma_{12}. \tag{23}$$

For the mixing entropy per one lattice cell $\tau\Delta\sigma/N$ holds $\tau\Delta\sigma/N = -\tau\,[\phi\ln\phi + (1-\phi)\ln(1-\phi)]$, as introduced for instance in Ref. [27]. Hence, the total entropy contribution to mixing free energy is

$$\tau\Delta\sigma = -\tau\pi r_0^2 b^{-3}\lambda\,[\phi\ln\phi + (1-\phi)\ln(1-\phi)]\,. \tag{24}$$

Foregoing arguments about terms involving mixing, together with the surface energy $2\pi r_0\lambda\,[\gamma_1\phi - \gamma_2\,(1-\phi)]$, and the pressure energy term, $\pi r_0^2\lambda\,[\gamma_1\phi + \gamma_2\,(1-\phi)]/r_0$, lead to the following expression for the initial free energy, F_0, of the cylindrical jet/film of the length, λ, plus the free energy of mixing ΔF.

$$\begin{aligned} F_0 + \Delta F &= 3\pi r_0\lambda\,[\gamma_1\phi - \gamma_2\,(1-\phi)] + [\Delta U - \tau\Delta\sigma\,] \\ &= \pi r_0\lambda\left[3\,[\gamma_1\phi + \gamma_2\,(1-\phi)] + r_0 z b^{-1}\gamma_{12}\,[\phi\,(1-\phi)] + \tau r_0 b^{-3}\,[\phi\ln\phi + (1-\phi)\ln(1-\phi)]\right]. \end{aligned} \tag{25}$$

The free energies of the original cylindrical system plus the free energy of mixing, $F_0 + \Delta F$, could be now equated with the free energy of the resultant droplet system, F_d, keeping in mind the volume conservation, expressed previously via the Eq. (2). The conservation equation provides with the relationship $r_d^2 = \left(3/4r_0^2\lambda\right)^{\frac{2}{3}}$, using which will be eliminated r_d from the relationship (22). From $F_0 + \Delta F = F_d$ is ultimately and easily obtained an estimation of the Rayleigh length, λ, of instable mixtures of immiscible liquids as

$$\lambda \cong \frac{2.87}{1.96}36\,r_0\left[\frac{\left(\frac{2}{3}\phi + \sqrt{\frac{\phi}{2}}\right)\gamma_1 + \left(\frac{5}{3} - \frac{2\phi}{3} - \sqrt{\frac{\phi}{2}}\right)\gamma_2 + \left(\sqrt{\frac{\phi}{8}} - \frac{\phi}{8}\right)\gamma_{12}}{3\,[\gamma_1\phi + \gamma_2\,(1-\phi)] + r_0\gamma_{12}b^{-1}z\,[\phi\,(1-\phi)] + \tau r_0 b^{-3}\,[\phi\ln\phi + (1-\phi)\ln(1-\phi)]}\right]^3, \tag{26}$$

where the coefficient 2.87/1.96 is due to the used approach based on conservation of the system's free energy, see Eq. (4), and the exact value of the Rayleigh wavelength. A comparison of computer simulation outputs with theoretically predicted values of λ is depicted in Fig. 7. The coordination number z was reduced to 17, estimated from an average number of liquid nodes in the neighbourhood of a typical liquid node inside the original cylindrical liquid jet taken for the computer simulation.

8. Conclusions

The great advantage of the Monte Carlo simulation, based on Auto-models is that they work, as opposed to traditional analytical approaches, for highly disordered systems with complex geometry and boundary conditions. This study shows that, the Monte Carlo dynamics of the Auto-model is capable of predicting nearly identical results, compared to the ones, established by classical analytical hydrodynamic theory of Rayleigh instability of homogeneous liquid jets or, liquid columns sessile to cylindrical bodies. The Hamiltonian for the computer simulations is composed of the 2-clan terms of the Hammersley and Clifford expansion. As has been shown in this work, the Rayleigh wavelength, λ, obtained through computer simulations, based on previously described Auto-model, is quite comparable with the analytical result, $\lambda = 2.87\pi r_0$.

It seems that this kind of simulation accounting a statistics of spatial interactions in lattices could offer results that are similar to that of soft matters in experimental arrangements under very complex conditions like was demonstrated in works [28,29] for mesoscopic predictions of the effective thermal conductivity for microscale random porous media using a lattice Boltzmann algorithm. This work shows that the Auto-models are robust in investigating behaviour of liquid film and liquid jet instability. Authors are convinced about efficacy of the developed approach in situations where a system loses its axial symmetry, i.e., curvilinear fibres, influence of external fields, roughness of fibre surface, liquid blends and mixtures etc.

A simple estimation of Rayleigh length for columns, composed of instable mixtures of immiscible liquids was introduced. This derivation rooted from comparison between surface and pressure energy of original and final state of the system with addition of terms involving internal energy and entropy of mixing as a consequence of coalescence, i.e., liquid mixture decomposition. The obtained prediction is qualitatively similar to the computer-simulated results.

Hopefully, the results achieved in this work, would attract more attention for applying the theory of Markov Random Fields, and Auto-models for various issues in the investigation of immiscible liquid mixtures.

Acknowledgements

The authors are very thankful to Konstantin Kornev from Clemson University, SC, and to Ales Linka from the Technical University of Liberec (TUL), for consultations and inspiration on the theory of Markov Random Fields respectively. The authors are also obliged to Miroslav Brezina from TUL for the introduction to the theory of H-surfaces of revolution. This work was supported by the Grant Agency of AS CR grant no. IAA500390702. D.L. and J.C. are also thankful to The Ministry of Education of the Czech Republic for their support in the frame of "The Research Centre for Advanced Conservation Technologies" (the project CEP1-1M0554). N.P. and D.L. acknowledge the support from NTC Grant M02-CD03 which supported their joint work at UC Davis. A.S. has been supported by GACR Grant no. 102/08/H081 "Advanced Application of Physical Fields". The next co-author (M.P.) is thankful for the support granted by a "Research Center — TEXTILE, TUL", Grant No. LN00B090. L.O. and P.M. thank Cummins Filtration for their support and interest in this work.

References

[1] A.V. Neimark, Thermodynamic equilibrium and stability of liquid films and droplets on fibers, J. Adhes. Sci. Technol. 13 (1999) 1137–1154.
[2] Roe Ryong-Joon, Wetting of fine wires and films by a liquid film, J. Colloid Interface Sci. 50 (1957) 70–79.
[3] J. Plateau, Statique experimentale et theoretique des liquids soumis aux seriles forces molecularies, Gauthier-Villars, Paris, 1873.
[4] L. Rayleigh, On the instability of jets, Proc. London Math Soc. 10 (4) (1878).
[5] S. Tomotika, On the instability of a cylindrical thread of a viscous liquid surrounded by another viscous fluid, Proc. Roy. Soc. A 150 (1935) 322–337.
[6] B.J. Meister, G.F. Scheele, Generalized solution of the Tomotika stability analysis for a cylindrical jet, AIChE J. 13 (1967) 682.
[7] T. Young, in: G. Peacock (Ed.), Miscellaneous Works, J. Murray, London, vol. I, 418, 1855.
[8] P.S. de Laplace, Mechanique celeste, Supplement to Book 10 (1806).
[9] S. Hildebrandt, A. Tromba, The shape and form in the natural world, in: The Parsimonious Universe, Copernicus, Springer-Verlag, New York, 1995.
[10] C. Delaunay, Sur la surface de revolution, dont la courbure moyenne est constant, J. Math. Pures Appl. 6 (1841) 309–315.
[11] F. Brochard, Spreading of liquid drops on thin cylinder: The manchon/droplet transition, J. Chem. Phys. 84 (1986) 4664.
[12] P.G. de Gennes, F. Wyart-Brochard, D. Quere, Capillarity and Wetting Phenomena; Drops, Bubbles, Pearls, Waves, Springer-Verlag, New York, Berlin, 2003.
[13] A.I. Grigor'ev, S.O. Shir'aeva, Mechanism of electrostatic polydispersion of liquid, J. Physica D: Appl. Phys. 23 (1990) 1361–1370.
[14] S. Chandrasekhar, Hydrodynamic and Hydromagnetic Instability, Clarendon Press, Oxford, 1961.
[15] A.W. Adamson, A.P. Gast, Physical Chemistry of Surfaces, John Wiley & Sons, New York, 1997.
[16] B. Prun, J.C. Fort, Stochastic processes on a lattice and Gibbs measures, in: Mathematical Physics Studies, vol. 11, Kluwer Accademic Publishers, Dordrecht, Boston, London, 1991.
[17] D. Geman, Random Fields and inverse problems in imagining, in: Lecture Notes in Mathematics, vol. 1427, Springer-Verlag, 1991, pp. 113–193.
[18] R.D. Paget, Nonparametric Markov Random Field models for natural images, Ph.D. thesis, The University of Queensland, Australia (1999).
[19] M.N.M. van Lieshout, Markov Point Processes and Their Applications, Imperial College Press, London, 2000.
[20] J.E. Besag, Spatial interaction and the statistical analysis of lattice systems, J. Roy. Statist. Soc. Ser. B 36 (1974) 192–236.
[21] N.G. Van Kampen, Stochastic Processes in Physics and Chemistry, North-Holland, Amsterdam, New York, 1991.
[22] J.M. Hammersley, P. Clifford, Markov fields on finite graphs and lattices, unpublished, 1971.
[23] K. Binder, D.W. Heermann, Monte Carlo Simulation in Statistical Physics, Springer, Berlin, 1997.
[24] D. Lukas, V. Soukupova, N. Pan, D.V. Parikh, Computer simulation of 3-D liquid transport in fibrous materials, SIMULATION: Trans. SMS 80 (2004) 547–557.
[25] D. Lukas, E. Kostakova, A. Sakar, Computer simulation of moisture transport in fibrous materials, in: N. Pan, P. Gibson (Eds.), Thermal and Moisture Transport in Fibrous Materials, Woodhead Publishing Limited, Cambridge, 2006, pp. 469–541.
[26] J. Moussouris, Gibbs and Markov random systems with constrains, J. Statist. Phys. 10 (1974) 11–33.
[27] P.C. Hiemenz, T.P. Lodge, Polymer Chemistry, CRC Press, New York, 2007.
[28] M. Wang, J. Wang, N. Pan, S. Chen, Mesoscopic predictions of the effective thermal conductivity for microscale random porous media, Phys. Rev. E 75 (2007) 036702–10.
[29] M. Wang, N. Pan, J. Wang, S. Chen, Mesoscopic simulations of phase distribution effects on the effective thermal conductivity of microgranular porous media, J. Colloid Interface Sci. 311 (2007) 562–570.

Příloha 8

Filova, E., Burdikova, Z., Rampichova, M., Bianchini, P., Čapek, M., Košťáková, E., Amler, E., Kubínová, L.: Analysis and three-dimensional visualization of collagen in artificial scaffolds using non-linear microscopy techniques; Journal of Biomedical Optics; Vol.15, No.6; (2010), IF =3,157 (11)

Filova, E. 20%, Burdikova Z. 15%, Rampichova, M. 12%, Bianchini, P. 12%, Čapek, M. 11%, ***Kostakova, E. 10%,*** *Amler, E. 10%, Kubinová, L. 10%*

Analysis and three-dimensional visualization of collagen in artificial scaffolds using nonlinear microscopy techniques

Eva Filová
Institute of Experimental Medicine
Academy of Sciences of the Czech Republic
Vídeňská 1083
14220 Prague, Czech Republic

Zuzana Burdíková
Institute of Physiology
Academy of Sciences of the Czech Republic
Department of Biomathematics
Vídeňská 1083
14220 Prague, Czech Republic

Michala Rampichová
Institute of Experimental Medicine
Academy of Sciences of the Czech Republic
Vídeňská 1083
14220 Prague, Czech Republic
and
Charles University in Prague
Second Faculty of Medicine
Institute of Biophysics
V Úvalu 84
15006 Praha 5, Czech Republic

Paolo Bianchini
Italian Institute of Technology
Nanophysics
via Morego 30
I16163 Genova, Italy

Martin Čapek
Institute of Physiology
Academy of Sciences of the Czech Republic
Department of Biomathematics
Vídeňská 1083
14220 Prague, Czech Republic
and
Czech Technical University in Prague
Faculty of Biomedical Engineering
Sítná 3105
27201, Kladno, Czech Republic

Eva Košťáková
Technical University of Liberec
Faculty of Textile Engineering
Studentská 2
46117 Liberec, Czech Republic

Evzen Amler
Institute of Experimental Medicine
Academy of Sciences of the Czech Republic
Vídeňská 1083
14220 Prague, Czech Republic
and
Charles University in Prague
Second Faculty of Medicine
Institute of Biophysics
V Úvalu 84
15006 Praha 5, Czech Republic

Lucie Kubínová
Institute of Physiology
Academy of Sciences of the Czech Republic
Department of Biomathematics
Vídeňská 1083
14220 Prague, Czech Republic

Abstract. Extracellularly distributed collagen and chondrocytes seeded in gelatine and poly-ε-caprolactone scaffolds are visualized by two-photon excitation microscopy (TPEM) and second-harmonic generation (SHG) imaging in both forward and backward nondescanned modes. Joint application of TPEM and SHG imaging in combination with stereological measurements of collagen enables us not only to take high-resolution 3-D images, but also to quantitatively analyze the collagen volume and a spatial arrangement of cell-collagen-scaffold systems, which was previously impossible. This novel approach represents a powerful tool for the analysis of collagen-containing scaffolds with applications in cartilage tissue engineering. [DOI: 10.1117/1.3509112]

Keywords: second-harmonic generation imaging; multiphoton microscopy; tissue engineering; artificial scaffolds; collagen.

Paper 10041RR received Jan. 27, 2010; revised manuscript received Sep. 16, 2010; accepted for publication Sep. 21, 2010; published online Dec. 23, 2010.

1 Introduction

Multiphoton microscopy is an evolving high-resolution technique that has been successfully applied in many fields of biomedicine.[1–3] Nonlinear microscopy can employ two different types of signals, fluorescence and second-harmonic generation (SHG), to image biological structures with subcellular resolution. Two-photon excited fluorescence imaging is a powerful technique for monitoring the dynamic behavior of chemical components of tissues, whereas SHG imaging provides novel ways to study their spatial distribution.[4] Two-photon excitation (TPE) of fluorescent molecules is a process that involves the simultaneous absorption of two photons whose total energy equals the energy for producing a molecular transition to an excited state, while the SHG is a coherent nonlinear process that takes place in certain mesoscopic structures lacking centrosymmetry—such as collagen, myosin, and microtubules—when excited by an extremely intense light.[5] To achieve the required photon density while maintaining an average laser power at a reasonable level, the laser light is concentrated into short pulses (about 200 fs) with a repetition rate of about 80 MHz. The wavelength of the emitted light is exactly one half of the excitation wavelength, and the emission intensity is proportional to the square of the excitation radiation intensity in the focal point.[6] The advantages of SHG imaging include

Address all correspondence to: Lucie Kubínová, Institute of Physiology, Academy of Sciences of the Czech Republic, v.v.i., Tel: +420 296 442 314; Fax: +420 241 06 2 488; E-mail: kubinova@biomed.cas.cz.

1083-3668/2010/15(6)/066011/7/$25.00 © 2010 SPIE

high sensitivity and resolution, absence of photobleaching, lack of autofluorescence, and non-destructive imaging of native tissues.

SHG imaging has been used for the identification of type I collagen in fascia;[7] tendon;[8,9] skin;[5,10] and liver, where it was also used as a marker of liver cirrhosis.[11] Structural details of different types of collagen as well as its morphological changes observed during aging or disease were also studied by SHG imaging.[12]

The major components of extracellular matrix in hyaline cartilage include type II collagen (≈60% of the dry weight), hyaluronic acid, and proteoglycans.[13] Cartilage damage as a consequence of diseases such as osteoarthritis is characterized by a decreased concentration of aggrecan, a shorter length of glycosaminoglycan chains, increased water content, and collagen degradation or altered organization. These changes result in an increase of tissue permeability and reduced cartilage stiffness.[14,15]

The aim of regenerative medicine is renovation or reconstruction of missing tissues; thus, it is largely dependent on progress in tissue engineering. Innovative scaffolds as well as application of novel visualization methods are hence extensively studied in many laboratories. Implantation of biodegradable scaffolds seeded with chondrocytes is an example of a promising technique used in modern therapy of osteochondral defects. The quality of implanted cell-seeded scaffolds, which is characterized by differentiated cells as well as extracellular matrix production, is an important factor for cartilage regeneration.[16,17] Therefore, highly sensitive rapid visualization of collagen and cells is highly demanded to assess the quality of prepared implants.

Different scaffolds are characterized by differences in autofluorescence, TPE microscopy (TPEM), or SHG signals.[18] Both confocal laser-scanning microscopy (CLSM) and TPEM enable visualization of collagen using immunohistochemical staining. However, the fibrous or homogenous character of the collagen cannot be observed, since the antibodies are bound to the epitopes on the surface. On the other hand, SHG visualizes the whole collagen fibers even in the deeper part of the scaffold, which enables a spatial characterization with high sensitivity of the collagen in scaffolds of high thickness. The visualization of cells on the scaffold as well as extracellular matrix formation makes it possible to assess the proliferation and differentiation state of cells as well as collagen production and is of prime importance in tissue engineering. Simultaneous application of CLSM, TPEM, and SHG yielded imaging in great detail. The aim of the presented study was to test the sensitivity of nonlinear microscopic techniques for visualization of cells together with collagen and to quantitatively analyze collagen distribution.

2 Methods

2.1 *Sample Preparation and Seeding*

The scaffolds were produced from gelatine (Gelita Imagel BT, Type 68 917, gel 270 g Bloom, Gelita AG, Germany). A gelatine scaffold was prepared using 5% (w/w) gelatine solution in distilled water at 40°C. The solution was thoroughly stirred in an agitator; subsequently, the foam was dried at room temperature for 48 h. Samples were then crosslinked using 0.7% (w/w) N-(3-dimethylaminopropyl)-N′-ethylcarbodiimide hydrochlorid (type 03450, Sigma-Aldrich) in acetone/water (8:2 ratio) for 24 h at room temperature, and dried at room temperature for 48 h. The samples were then washed with distilled water to remove unwanted chemicals.

A poly-ε-caprolactone (PCL) foam scaffolds were prepared by salt-leaching techniques using 7% (w/w) PCL (Mw 80×10^3, Sigma-Aldrich) dissolved in ethanol/chloroform mixture (1:9). NaCl particles were mixed with the solution mechanically. After solvent evaporation, salt particles were removed by stirring in distilled water.

2.2 *Chondrocyte Isolation and Culture*

Small pieces of cartilage were taken from the left femoral trochlea of a rabbit under general anesthesia. After a 14-h digestion period in 1 mg/mL collagenase solution (collagenase crude 816 PZS/g, Sevapharma), chondrocytes were collected and cultured for 14 days in Iscove's modified Dulbecco's medium (IMDM) supplemented with 10% foetal bovine serum (FBS), penicillin/streptomycin (100 IU/mL and 100 μg/mL, respectively), 400 mM L-glutamine, 100 nM dexamethasone, 40 μg/mL ascorbic acid-2-phosphate, and ITS-X (10 μg/mL insulin, 5.5 mg/L transferrin, 6.7 μg/L sodium selenite, and 2 mg/L ethanolamine). Chondrocytes were seeded on 5% gelatine foams and PCL foams at a density of 8.0×10^5 and 3.0×10^5 cells/scaffold, respectively (scaffold diameter = 6 mm, height = 1 mm). The cells were incubated at 37°C in a 5% CO_2 atmosphere for 14 days.

2.3 *Sample Staining*

Scaffolds or cartilage samples were fixed by ethanol (–20°C) and stained by propidium iodide [5 μg/mL in phosphate-buffered saline (PBS)]. Indirect immunofluorescence staining was used to detect type II collagen. Samples were fixed with 10% formaldehyde in PBS for 10 min, washed in PBS, and then incubated in 3% FBS in PBS/0.1% Triton X-100 at room temperature for 30 min.

The samples were incubated with the primary antibody against type II collagen, clone II-II6B3, obtained from Developmental Studies Hybridoma Bank developed under the auspices of the National Institute of Child Health and Human Development (NICHD) and maintained by the University of Iowa, Department of Biological Sciences (Iowa City, IA 52242) (dilution 1:20; 1-h incubation at room temperature). After three washes with PBS/0.05% Tween 20 after 3, 10, and 15 min, the samples were incubated with a secondary antibody Cy3-conjugated Donkey Anti-Mouse IgG (H + L) (dilution 1:300; 45-min incubation at room temperature, light protected). Samples were again washed with PBS/0.05% Tween 20 and once with PBS; subsequently, antifading solution was added [PBS/90% glycerol/2.5% 1,4-diazabicyclo(2,2,2)octane (DABCO)].

2.4 *Image Acquisition*

All images were acquired by a Leica TCS SP2 acousto-optical beamsplitter (AOBS) multiphoton confocal laser scanning

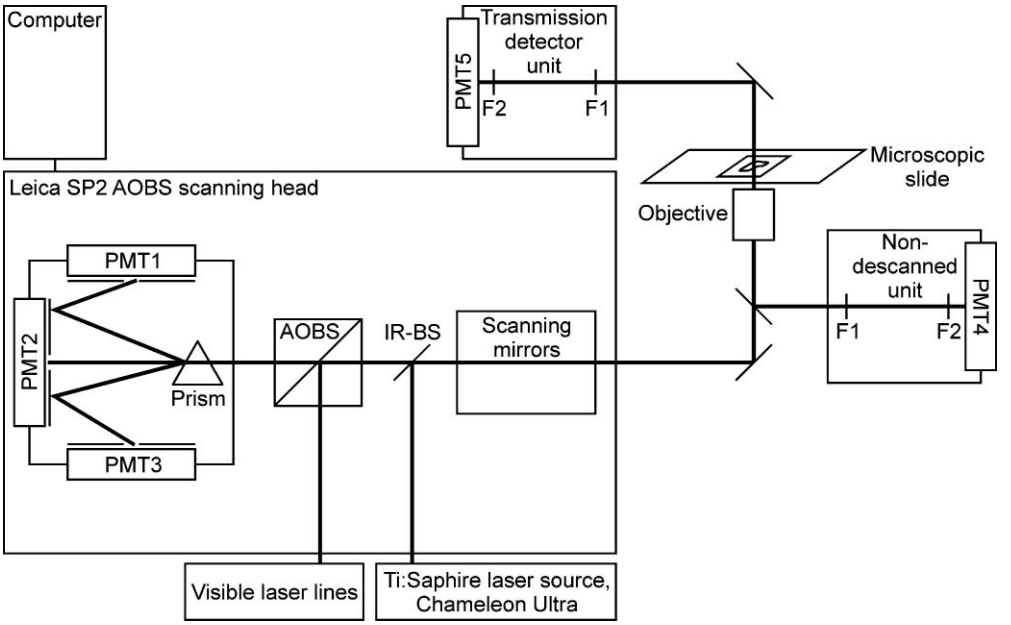

Fig. 1 Diagrammatic layout of the experimental setup based on a confocal laser scanning microscope Leica SP2 AOBS equipped with one- and two-photon lasers. PMT1, PMT2, and PMT3, photomultiplier tubes in the scanning head for descanned detection of one- and two-photon imaging of fluorescence or autofluorescence signal; PMT4, photomultiplier for nondescanned detection of SHG signal in the backward mode; PMT5, transmission detector for nondescanned detection of SHG signal in the forward mode; F1, E700SP short-pass filter; F2, 430DF15 bandpass filter; IR-BS, infrared beamsplitter.

microscope based on Leica DM IRE2 inverted microscope and equipped with the following light sources: Ar laser (458 nm/5 mW, 476 nm/5 mW, 488 nm/20 mW, 514 nm/20 mW), HeNe lasers (543 nm/1.2 mW, 633 nm/10 mW) for one-photon excitation, and a mode-locked Ti:Sapphire Chameleon Ultra laser (Coherent Inc., Santa Clara, California), tuneable from 690 to 1040 nm for TPE (Fig. 1).

2.4.1 *Imaging of fluorescence signal using one-photon excitation*

Images of structures stained by propidium iodide were acquired using one-photon excitation ($\lambda_{exc} = 543$ nm and $\lambda_{em} = 610$ to 645 nm) via a photomultiplier located in the scanning head (Fig. 1). Type II collagen stained by Cy3 was examined at $\lambda_{exc} = 514$ nm and $\lambda_{em} = 555$ to 600 nm, also using an internal detector. The gelatine and PCL scaffold thicknesses were 214 ± 75 and 195 ± 37 μm, respectively [mean and standard deviation (SD)].

2.4.2 *SHG imaging*

In our setup shown in Fig. 1, the SHG signal was detected in three ways: (1) the backward descanned mode when the signal passed through the scanning head of the confocal microscope to PMT1, (2) the backward nondescanned mode when the signal was collected directly behind the objective by PMT4, and (3) the forward nondescanned mode when the signal passed through the sample into PMT5. For collagen detection the laser was tuned at the wavelength of 860 nm, hence the SHG signal was expected at 430 nm. In the descanned mode, the SHG signal was detected in the range of 420 to 440 nm. In a nondescanned configuration, which is supposed to improve the signal-to-noise ratio in the acquired images, the external detector was placed behind a 700-nm short-pass filter, which attenuates IR light, followed by a 430-nm bandpass filter with a bandwidth of 15 nm. To confirm the detection of the SHG signal we ensured that the signal disappeared when the excitation wavelength was changed to 800 nm, then reappeared after setting up a bandpass filter to 400 nm.

2.4.3 *Imaging fluorescence signal using TPE*

The fluorescence of the stained cells and/or autofluorescence of the scaffolds was also detected by TPEM using the internal detectors (in the descanned mode, see Fig. 1). An excitation wavelength of 860 nm was used to enable a simultaneous acquisition of the SHG signal. For detection, different wavelength ranges were applied using lambda scans to get as strong as possible autofluorescence of the samples.

2.5 *Three-Dimensional Reconstructions*

Further information on the spatial arrangement of tissues was obtained from three-dimensional (3-D) reconstructions based on series of optical sections of the specimen.[19] The 3-D visualization utilized a maximum intensity projection of these series using Leica LCS software and, further, volume rendering by the Volume plug-in module developed in Ellipse3D software environment (ViDiTo, Košice, Slovakia).

3 Results

SHG imaging was used for the identification of type II collagen in an extracellular matrix. To observe and detect

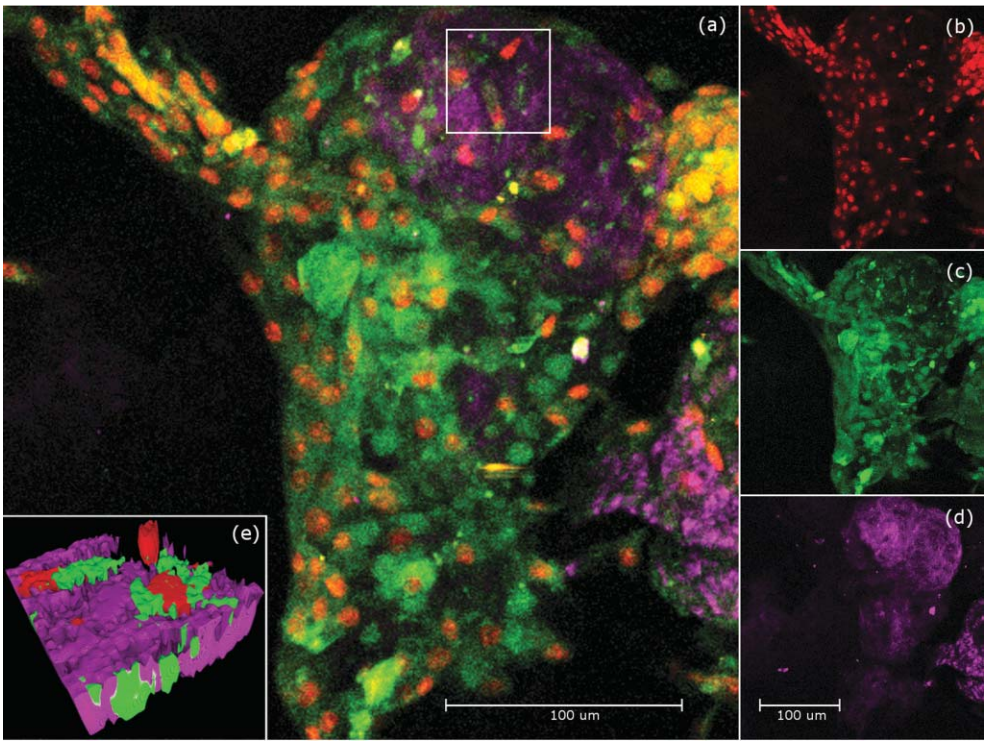

Fig. 2 Detection of collagen in PCL scaffold. (a) Maximum intensity projection of a 30-μm-thick stack of images [overlay of (b), (c), and (d)], 20×objective, 2×zoom, scale = 100 μm. The white square marked region of interest with detected collagen of the size of 36×36×19 μm^3 is shown in more detail using a 3-D reconstruction (e). (b) Cell nuclei stained by propidium iodide (red) detected by TPE in the descanned mode; (c) procollagen labeled with Cy3 detected by TPE in a green channel; and (d) collagen detected by SHG imaging in the backward mode (magenta), autofluorescence of the scaffold is also detected.

collagen, chondrocytes were seeded on gelatine and PCL foams. The cell densities on 5% gelatine foam and the PCL scaffolds were 1.4×10^4 and 5.5×10^4 cells/mm^3, respectively. Chondrocytes adhered well to the surface of PCL [Fig. 2(a)] and gelatine scaffolds (Fig. 3). As expected, cells proliferated effectively on scaffolds and were approximately 80 μm deep after 5 days. The cells were found to be grouped in large islands or formed continuous layers in pockets [Figs. 2(a), 2(b) and 3(a)].

Chondrocyte proliferation was linked to production of the extracellular matrix proteins. Collagen as a typical extracellular cartilage protein was visualized, first, by CLSM using fluorescently labeled monoclonal antibodies against type II collagen. Fluorescence staining clearly revealed only a sparse presence of collagen in gelatine foams, however, a high amount of type II collagen was detected in PCL scaffolds [Fig. 2(c)]. We performed stereological measurements of collagen volumes in five 100-μm-deep series acquired from three PCL scaffolds. The measurements revealed $5.6\pm1.8\%$ (7.49×10^5 μm^3) and $2.6\pm2.3\%$ (3.43×10^5 μm^3) (mean and SD) of collagen volume related to volume of one series acquired from the scaffold (140.57×10^5 μm^3) using nondescanned and descanned modes, respectively.

Conventional confocal microscopy images were compared with the SHG imaging in both forward and backward nondescanned modes. Well detectable signals were observed in PCL and gelatine scaffolds (Figs. 2 and 3). Detection of collagen by SHG imaging corresponded well with collagen detection by immunohistochemical staining (Figs. 3 and 4). The autofluorescence signal was collected with the aim to visualize the scaffold structure. The collagen signal was detected at sites of high chondrocyte density on the scaffold.

Fluorescence collagen signal was acquired using CLSM [Fig. 4(c)]. An SHG signal of high intensity was detected in the extracellular matrix of cartilage as well as in the close vicinity of cells, indicating newly synthesized collagen. Beside collagen, chondrocytes and scaffolds were also visualized using a simultaneous acquisition of SHG and TPEM signals [Figs. 2(a), 3(b1) and 3(c1)].

The volume of visualized collagen (backward versus forward mode SHG signal) produced by cells in scaffolds was measured. Gray-scale-level thresholding of the 3-D image data was applied to identify regions of high-intensity SHG signal. Volumes of these regions were then calculated from the number of their voxels. Using threshold of 30 (0 to 255 gray scale), the volumes of collagen detected in backward and forward modes were 5.36×10^5 μm^3 and 1.54×10^5 μm^3, respectively. The volume of the whole series was 140.57×10^5 μm^3. This indicated a slightly higher sensitivity of the backward mode to collagen compared to the forward one.

A combination of TPEM signals (propidium iodide, scaffold autofluorescence) and SHG signal from collagen was used for 3-D reconstructions. These multimodal 3-D images simultaneously revealed both collagen and scaffold architecture, and cell localization [Figs. 2(e), 3(b2), 3(c2) and Videos 1, 2, and 3].

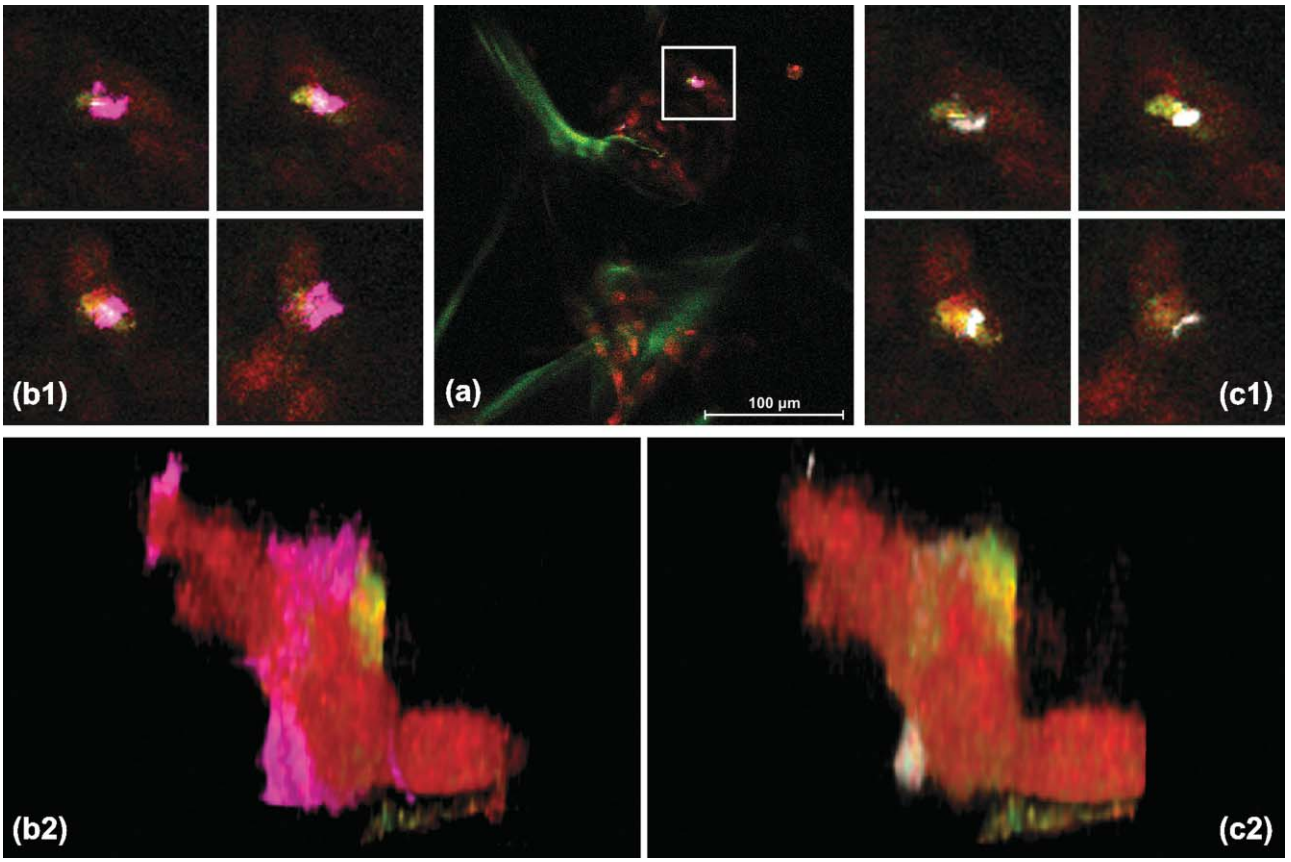

Fig. 3 Gelatine scaffold imaging by SHG in the backward and forward modes. (a) An optical section using TPE; cell nuclei stained by propidium iodide (red), scaffold autofluorescence (green), and SHG imaging in the backward mode (magenta), scale = 100 μm. The white-square-marked region of interest is shown in more detail in four optical sections of the image stack, 10 μm apart: (b1) SHG imaging in the backward mode (magenta), (c1) SHG imaging in the forward mode (cyan). The 3-D image of the region of interest shown in (a) demonstrates a stronger SHG signal detected in the backward mode (b2) when compared to the forward mode (c2). The dimensions of the reconstructed volumes were 60×60×70 μm^3; 20× objective.

4 Discussion

SHG imaging was used for the analysis of various collagen-containing tissues, such as skin, tendon, muscles, cartilage, fascia, and endometrium.[7–12] Structural changes of collagen in cryopreserved cartilage demonstrated by SHG imaging were also reported.[12]

Our SHG images of cartilage showed a homogeneous signal from collagen in the extracellular matrix [Figs. 4(a) and 4(b)]. This is in accordance with immunohistochemical staining of type II collagen [Fig. 4(c)].

The optimal technique of detecting SHG signal of collagen in scaffolds was investigated in the presented study, and both the backward and forward modes were tested. In general, SHG

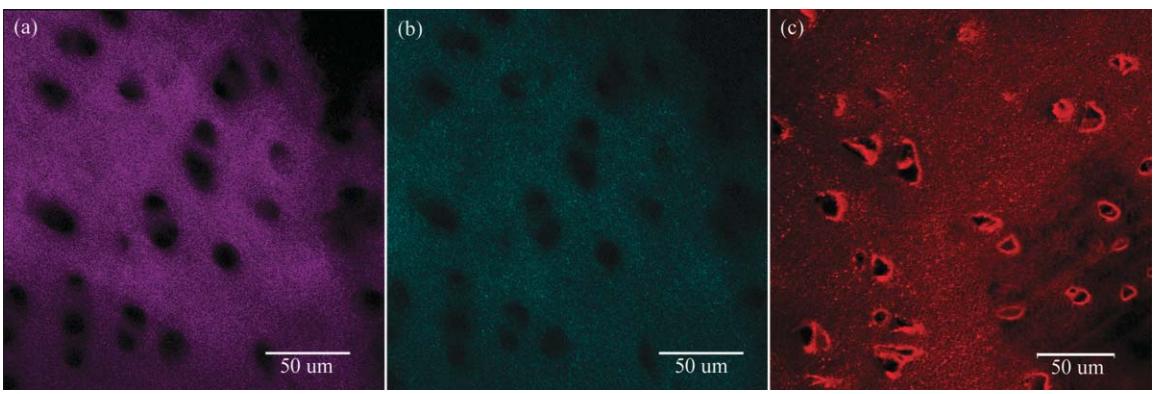

Fig. 4 Collagen in native pig cartilage. The SHG signal of collagen was much stronger in the backward mode (a) than in the forward one (b); (c) immunohistochemical staining of type II collagen using Cy3 detected by CLSM (λ_{exc} = 514 nm, λ_{em} = 555 to 600 nm). Maximum intensity projection, 20× objective, scale = 50 μm.

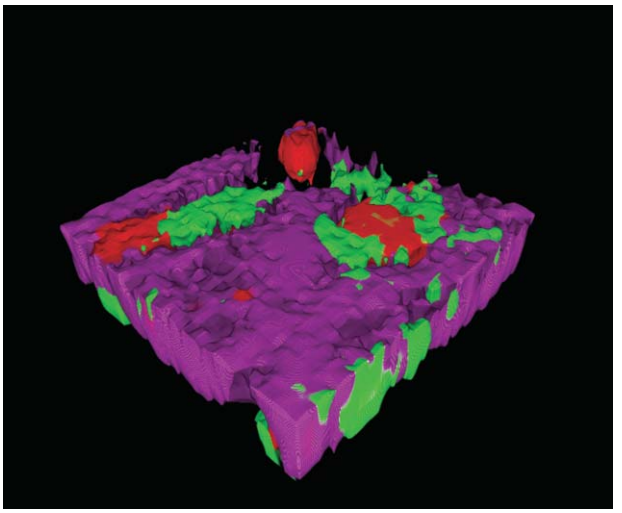

Video 1 A 3-D reconstruction of a PCL scaffold [displayed also in Fig. 2(e)]; collagen detected by SHG imaging in the backward mode (magenta), and by TPE excitation (green), cell nuclei stained by propidium iodide (red). Autofluorescence of the scaffold is also detected. (QuickTime, 10.4 MB).
[URL: http://dx.doi.org/10.1117/1.3509112.1]

images differed in the forward and backward modes. Bianchini and Diaspro[9] and Cox et al.[11] showed that the SHG signal in the forward mode is unable to pass through samples thicker than 500 μm. This finding indicates that the backward SHG detection is more efficient than the forward mode in thick samples, which is in accordance with our results obtained using 100 to 300-μm-thick samples.

Images obtained by employing either of two modes indicate a heterogeneous 3-D collagen distribution and are in agreement with collagen distribution determined by histochemical staining, although in short 5-day cell cultivation on scaffolds, the fluorescent collagen signal was found predominantly in the close vicinity of the cells. This reflects the binding of the antibody to both procollagen and immature collagen (Fig. 2). On the contrary, the strong SHG signal was visible from well organized collagen in the extracellular matrix. This is in agreement with our previous observations in rabbits.[20] Similarly, the sparse SHG signal in gelatine scaffold may be explained by the high amount of immature collagen in the sample.

Aside from collagen, natural and synthetic scaffolds can be visualized by CLSM, TPEM, and SHG imaging.[18,21] Fluorescent amino acids (tryptophan, tyrosine and phenylalanine) in collagen, elastin, and other proteins; advanced glycation end products, flavin adenin dinucleotide; nicotinamide adenine dinucleotide; porphyrin; melanin; lipofuscin, and other natural fluorophores contribute to autofluorescence.[22] The autofluorescence signal depends also on chemical composition of scaffolds; synthetic polyesters such as PCL contain the π-electrons necessary for fluorescence emission.

The type I and II collagen found in the scaffolds seeded with chondrocytes was produced by cells according to their state of differentiation, cell density, medium composition, and biomechanical stimulation.[23,24] The SHG signal was sparsely distributed in the gelatine scaffolds, which was probably caused by a higher amount of immature collagen. A strong SHG signal was observed in a PCL scaffold [Fig. 2(d)]. The 3-D image reconstruction revealed a spatial distribution of mature collagen in the area with a high cell concentration [Figs. 2(e), 3(b2), and 3(c2) and Videos 1, 2, and 3]. The characterization of types of synthesized collagen using SHG in scaffolds will be the subject of future studies.

TPEM and SHG imaging have already been used for visualization of different tissues.[25,26] In our experiments, CLSM, TPEM, and SHG imaging (forward and backward) was used for the visualization of *in vitro* prepared samples. Image analysis, stereological measurements, and 3-D reconstructions enabled us to quantify and visualize cell-collagen-scaffold systems, which had not yet been reported. We demonstrated the just mentioned

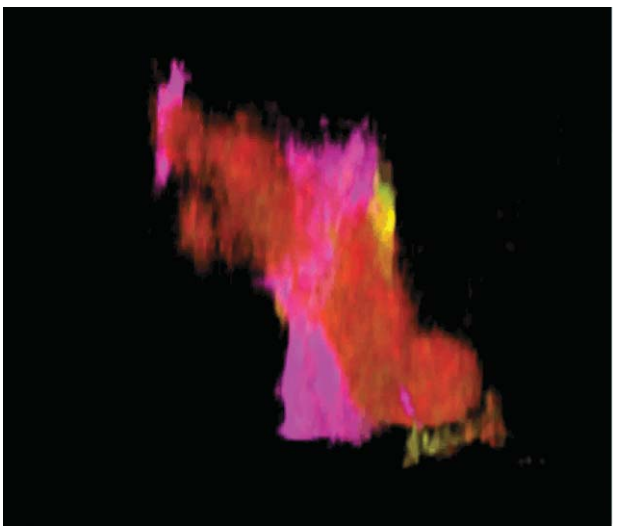

Video 2 A 3-D reconstruction of collagen on a gelatine scaffold in the backward mode (magenta) [displayed also in Fig. 3(b2)]; cell nuclei stained by propidium iodide (red), and autofluorescence of the scaffold (green) are also detected. (QuickTime, 8.7 MB).
[URL: http://dx.doi.org/10.1117/1.3509112.2]

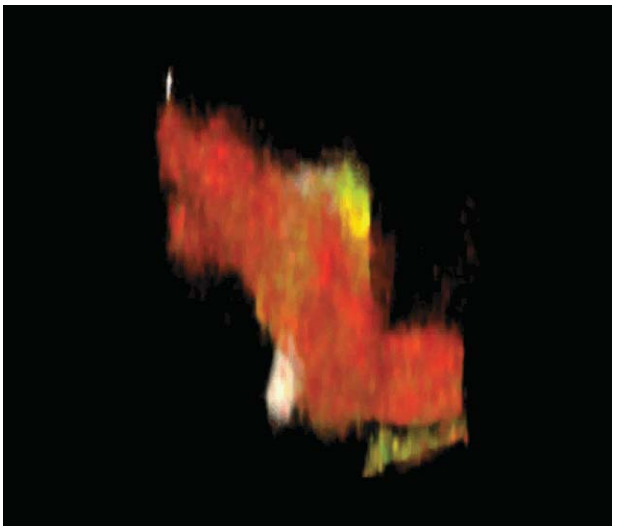

Video 3 A 3-D reconstruction of collagen on a gelatine scaffold in the forward mode (cyan) (displayed also in [Fig. 3(c2)]; cell nuclei stained by propidium iodide (red), and autofluorescence of the scaffold (green) are also detected. (QuickTime, 7.5 MB).
[URL: http://dx.doi.org/10.1117/1.3509112.3]

techniques to be powerful tools for the analysis and visualization of collagen-containing scaffolds, with a broad application in cartilage tissue engineering.

5 Summary

SHG imaging enables us to perform 3-D reconstruction and visualization of cell-collagen-scaffold systems. Collagen volume can thus be reliably determined throughout the scaffold thickness. Moreover, a concurrent application of TPEM makes it possible to correlate scaffold and cell distribution in the samples.

Acknowledgments

The presented study was supported by the Academy of Sciences of the Czech Republic (research projects No. AV0Z50110509, AV0Z50390512, and AV0Z50390703), the Ministry of Education, Youth and Sports of the Czech Republic (research programs LC06063, MSM6840770012, NPV II 2B06130, and 1M0510), the Czech Science Foundation (Nos. GA102/08/0691, GA202/09/1151, and GAP304/10/1307), the EU project BIOSCENT (ID number 214539, and 7E09088), and the Grant Agency of the Academy of Sciences No. IAA500390702.

References

1. W. Denk, J. H. Strickler, and W. W. Webb, "Two-photon laser scanning fluorescence microscopy," *Science* **248**, 73–76 (1990).
2. A. Diaspro, Ed., *Confocal and Two-Photon Microscopy: Foundations, Applications, and Advances*, Willey-Liss, New York (2002).
3. A. Diaspro, G. Chirico, and M. Collini, "Two-photon fluorescence excitation and related techniques in biological microscopy," *Q. Rev. Biophys.* **38**, 97–166 (2005).
4. Y. Imanishi, K. H. Lodowski, and Y. Koutalos, "Two-photon microscopy: shedding light on the chemistry of vision," *Biochemistry* **46**, 9674–9684 (2007).
5. P. J. Campagnola, A. C. Millard, M. Terasaki, P. E. Hoppe, C. J. Malone, and W. A. Mohler, "Three-dimensional high-resolution second-harmonic generation imaging of endogenous structural proteins in biological tissues," *Biophys. J.* **81**, 493–508 (2002).
6. J. A. Palero, "Nonlinear spectral imaging of biological tissues," PhD Thesis, University of Utrecht, The Netherlands (2007).
7. F. Legare, C. Pfeffer, and B. R. Olsen, "The role of backscattering in SHG tissue imaging," *Biophys. J.* **93**, 1312–1320 (2007).
8. R. M. Williams, W. R. Zipfel, and W. W. Webb, "Interpreting second-harmonic generation images of collagen I fibrils," *Biophys. J.* **88**, 1377–1386 (2005).
9. P. Bianchini and A. Diaspro, "Three-dimensional (3D) backward and forward second harmonic generation (shg) microscopy of biological tissues," *J. Biophoton.* **1**, 443–450 (2008).
10. O. Chernyavskiy, L. Vannucci, P. Bianchini, F. Difato, M. Saieh, and L. Kubínová, "Imaging of mouse experimental melanoma in vivo and ex vivo by combination of confocal and nonlinear microscopy," *Microsc. Res. Tech.* **72**, 411–423 (2009).
11. G. Cox, P. Xu, C. Sheppard, and J. Ramshaw, "Characterization of the second harmonic signal from collagen," in *Multiphoton Microscopy in the Biomedical Sciences III*, A. Periasamy, P. T. C. So, Eds., *Proc. SPIE* **4963**, 32–40 (2003).
12. K. G. Brockbank, W. R. MacLellan, J. Xie, S. F. Hamm-Alvarez, Z. Z. Chen, and K. Schenke-Layland, "Quantitative second harmonic generation imaging of cartilage damage," *Cell Tissue Bank* **9**, 299–307 (2008).
13. J. A. Buckwalter and H. J. Mankin, "Articular cartilage: Tissue design and chondrocyte-matrix interactions," *Instr. Course Lect.* **47**, 477–486 (1998).
14. B. Caterson, C. E. Hughes, B. Johnstone, and J. S. Mort. "Immunological markers of cartilage proteoglycan metabolism in animal and human osteoarthritis," in *Articular Cartilage and Osteoarthritis*, K. Kuettner, Ed., pp. 415–428, Raven Press, New York (1992).
15. R. A. Bank, M. Soudry, A. Maroudas, J. Mizrahi, and J. M. TeKoppele, "The increased swelling and instantaneous deformation of osteoarthritic cartilage is highly correlated with collagen degradation," *Arthritis Rheum.* **43**, 2202–2210 (2000).
16. R. Dorotka, U. Windberger, K. Macfelda, U. Bindreiter, C. Toma, and S. Nehrer, "Repair of articular cartilage defects treated by microfracture and a three-dimensional collagen matrix," *Biomaterials* **26**, 3617–3629 (2005).
17. S. Marlovits, P. Zeller, P. Singer, C. Resinger, and V. Vecsei, "Cartilage repair: generations of autologous chondrocyte transplantation," *Eur. J. Radiol.* **57**, 24–31 (2006).
18. Y. Sun, H. Y. Tan, S. J. Lin, H. S. Lee, T. Y. Lin, S. H. Jee, T. H. Young, W. Lo, W. L. Chen, and C. Y. Dong, "Imaging tissue engineering scaffolds using multiphoton microscopy," *Microsc. Res. Tech.* **71**, 140–145 (2008).
19. M. Čapek, P. Brůža, J., Janáček, P. Karen, L. Kubínová, and R. Vagnerová, "Volume reconstruction of large tissue specimens from serial physical sections using confocal microscopy and correction of cutting deformations by elastic registration," *Microsc. Res. Tech.* **72**, 110–119 (2009).
20. E. Filová, F. Jelínek, M. Handl, A. Lytvynets, M. Rampichová, F. Varga, J. Činátl, T. Soukup, T. Trč, and E. Amler "Novel composite hyaluronan/type I collagen/fibrin scaffold enhances repair of osteochondral defect in rabbit knee," *J. Biomed. Mater. Res. B Appl. Biomater.* **87**, 415–424 (2008).
21. Y. W. Wang, Q. Wu, J. Chen, and G. Q. Chen, "Evaluation of three-dimensional scaffolds made of blends of hydroxyapatite and poly(3-hydroxybutyrate-co-3-hydroxyhexanoate) for bone reconstruction," *Biomaterials* **26**, 899–904 (2005).
22. D. Chorvat and A. Chorvatova, "Multi-wavelength fluorescence lifetime spectroscopy," *Laser Phys. Lett.* **6**, 175–193 (2009).
23. S. E. Carver and C. A. Heath, "Influence of intermittent pressure, fluid flow, and mixing on the regenerative properties of articular chondrocytes," *Biotechnol. Bioeng.* **65**, 274–281 (1999).
24. A. Nečas, L. Plánka, R. Srnec, M. Crha, J. Hlučilová, J. Klíma, D. Starý, L. Křen, E. Amler, L. Vojtová, J. Jančář, and P. Gál, "Quality of newly formed cartilaginous tissue in defects of articular surface after transplantation of mesenchymal stem cells in a composite scaffold based on collagen I with chitosan micro- and nanofibres," *Physiol. Res.* **59**, 605–614 (2010).
25. W. L. Chen, Y. Sun, W. Lo, H. Y. Tan, and C. Y. Dong, "Combination of multiphoton and reflective confocal imaging of cornea," *Microsc. Res. Tech.* **71**, 83–85 (2008).
26. A. Zoumi, A. Yeh, and B. J. Tromberg, "Imaging cells and extracellular matrix in vivo by using second-harmonic generation and two-photon excited fluorescence," *Proc. Natl. Acad. Sci. U.S.A.* **99**, 11014–11019 (2002).

Příloha 9

Rampichova, M., Martinova, L., Kostakova, E., Filova,E. et al: A simple drug anchoring microfiber scaffold for chondrocyte seeding and proliferation, JOURNAL OF MATERIALS SCIENCE-MATERIALS IN MEDICINE, Volume: 23 Issue: 2 Pages: 555-563 DOI: 10.1007/s10856-011-4518-x Published: FEB 2012, ISSN: 0957-4530, IF=2,316 (11)

Rampichová M 25%, Martinová L 10%, ***Koštáková E 3%,*** *Filová E 10%, Míčková A 10%, Buzgo M 20%, Michálek J 5%, Přádný M 5%, Nečas A 2%, Lukáš D 5%, Amler E. 5%*

J Mater Sci: Mater Med (2012) 23:555–563
DOI 10.1007/s10856-011-4518-x

A simple drug anchoring microfiber scaffold for chondrocyte seeding and proliferation

Michala Rampichová · Lenka Martinová · Eva Košťáková · Eva Filová · Andrea Míčková · Matěj Buzgo · Jiří Michálek · Martin Přádný · Alois Nečas · David Lukáš · Evžen Amler

Received: 22 February 2011 / Accepted: 6 December 2011 / Published online: 6 January 2012

Abstract The structural properties of microfiber meshes made from poly(2-hydroxyethyl methacrylate) (PHEMA) were found to significantly depend on the chemical composition and subsequent cross-linking and nebulization processes. PHEMA microfibres showed promise as scaffolds for chondrocyte seeding and proliferation. Moreover, the peak liposome adhesion to PHEMA microfiber scaffolds observed in our study resulted in the development of a simple drug anchoring system. Attached foetal bovine serum-loaded liposomes significantly improved both chondrocyte adhesion and proliferation. In conclusion, fibrous scaffolds from PHEMA are promising materials for tissue engineering and, in combination with liposomes, can serve as a simple drug delivery tool.

M. Rampichová · E. Filová · A. Míčková · M. Buzgo · E. Amler
Institute of Experimental Medicine, Academy of Sciences of the Czech Republic, Prague, Czech Republic

M. Rampichová · A. Míčková · M. Buzgo · E. Amler (✉)
Department of Biophysics, 2nd Faculty of Medicine, Charles University in Prague, V Úvalu 84, 150 06 Prague 5, Czech Republic
e-mail: evzen.amler@lfmotol.cuni.cz

L. Martinová · E. Košťáková · D. Lukáš
Department of Nonwoven Textiles, Faculty of Textile Engineering, Technical University of Liberec, Liberec, Czech Republic

J. Michálek · M. Přádný
Institute of Macromolecular Chemistry, Academy of Sciences of the Czech Republic, v. v. i., Prague 6, Czech Republic

J. Michálek · M. Přádný
Center for Cell Therapy and Tissue Repair, 2nd Faculty of Medicine, Charles University in Prague, Prague, Czech Republic

A. Nečas
Department of Surgery and Orthopedics, Small Animal Clinic, Faculty of Veterinary Medicine, University of Veterinary and Pharmaceutical Sciences Brno, Brno, Czech Republic

E. Amler
Faculty of Biomedical Engineering, Czech Technical University, Prague, Czech Republic

1 Introduction

Cartilage lesions are often treated conservatively using various substances such as chondroitin sulfate, D-glucosamine sulfate or hyaluronic acid. Alternatively, standard surgical techniques, such as debridement, penetration of the subchondral bone, osteotomy, or joint distraction, have improved joint functionality [1, 2]. Autographic transplantations from non-weight bearing zones or soft tissue graft implantations into cartilage defects are other plausible alternatives [3, 4]. Modern approaches involve the implantation of three-dimensional biocompatible scaffolds seeded with autologous chondrocytes [5, 6]. Several biopolymers have been reported to be suitable substances for chondrocyte adhesion and proliferation [5, 7]. Among them, macroporous poly(2-hydroxyethyl methacrylate) (PHEMA), in its hydrogel form, was found to be a suitable biomaterial for different applications in tissue engineering, including cartilage [8, 9]. However, scaffolds with native properties suitable for chondrocytes still remain to be developed. Other than biocompatibility, several other key factors are necessary for optimal scaffold design in terms of cell seeding, such as adequate adhesion or porosity to ensure a sufficient supply of nutrients and the creation of a native-like environment. Various synthetic polymers, such as poly(ε-caprolactone) (PCL) [10], poly(lactide acid) (PLA), poly(glycolic acid) (PGA) [11], and poly(vinyl alcohol) (PVA) [12], and natural polymers such as chitosan [13],

collagen, and gelatin [14], have been used in the fabrication of electrospun fibers for tissue engineering applications. Blends of synthetic and natural polymers, such as collagen/chitosan [15] and gelatin/PCL [16], showed promising biomechanical properties as well as biocompatibility.

The structure of the native cartilage extracellular matrix (ECM) is characterized by filaments with diameters on the submicron scale. Typical electrospun polymer fibers were reported to have similar diameters as natural ECM filaments [17]. Thus, nanofibers appear to be an ideal material for scaffold development in regenerative medicine. Such three dimensional structures can properly accommodate chondrocytes due to numerous contacts points with cells. In addition, this structure ensures sufficient cell–cell communication and signal exchange.

Unfortunately, the majority of chemical substances are not suitable for nanofiber fabrication. Thus, the construction of a suitable nanofiber mesh for chondrocyte cultivation is a rather difficult process [18]. In the framework of this study, we prepared fibers from PHEMA and subsequently used them to test chondrocyte seeding in vitro. Furthermore, the unique properties of electrospun fibers, such as their porosity and extremely high surface-to-volume ratio, were studied as well. The aim of this study was to investigate the interaction between liposomes and fiber scaffolds and to develop a novel drug delivery system. Attention was devoted to a system of anchored liposomes containing foetal bovine serum (FBS) and its effect on chondrocyte seeding and proliferation.

2 Materials and methods

2.1 Materials

2-hydroxyethyl methacrylate (HEMA) was purchased from Rohm, Germany. Primary antibodies against type II collagen (clone II-II6B3, DSHB, USA) and a secondary antibody, Cy 3-conjugated Donkey Anti-Mouse IgG (H + L) (Jackson ImmunoResearch), were used. Phospholipids (L-α-phosphatidylserine, Avanti, USA; Asolectin from soybean, Sigma, UK; L-α-phosphatidylcholine, Avanti USA) and fluorescein labeled phospholipids (*N*-(fluorescein-5-thiocarbamoyl)-1,2-dihexadecanoyl-sn-glycero-3-phosphoethanolamine, triethylammonium salt (fluorescein DHPE), Invitrogen, USA) were used for the preparation of liposomes. The fluorescent probe 8-aminonaphthalene-1,3,6-trisulfonic acid, disodium salt (ANTS) and the quencher p-xylene-bis-pyridinium bromide (DPX) (Invitrogen, USA) were used for fluorescent spectroscopy measurements.

2.2 Preparation of PHEMA solution

Soluble PHEMA was prepared by monomer (8.55 g) polymerization in the absence of oxygen and initiated with the oxidation–reduction system, ammonium persulfate (0.05 g)–sodium bisulfite (0.05 g) in aqueous ethanol (66.3% ethanol, 55 g) at 23°C for 1 week. The molecular weight of the polymer ($Mw = 6.9 \times 10^5$ g/mol) was controlled by the initiator amount. After polymerization, PHEMA was precipitated in water then dissolved in 66.3 wt% ethanol/water to achieve a 16 wt% polymer concentration. The conductivity of the electrospinning solution was adjusted to 270 μS/cm by the addition of 0.4 g of saturated NaCl solution/15 ml of polymer solution. Molecular weights were determined by static light scattering using an ALV 6000/E (ALV, Germany). Intrinsic viscosity measurements were performed on an Ostwald viscometer, and its value was determined to be 28.0 at 23°C.

2.3 Electrospinning and nebulization of PHEMA scaffolds

Electrospinning of polymers was carried out on a needleless Nanospider™ technology device as described in detail previously [19–21]. Briefly, polymer solution, mixed 24 h, was electrospun from a rotating drum spinning electrode and produced fibers were collected on a grounded colector. Electrospinning of free liquid surface using NANOSPIDER™ technology was carried out with stainless steel drum, having the length, $L = 200 \pm 0.07$ mm, and radius $r = 20.87 \pm 0.02$ mm. It rotated (5 RPM) in a bath filled with the polymeric solution. The spinning electrode, emitting polymeric PHEMA jets at the voltages 43 kV. The square metallic collector had edge length of 250.9 ± 0.1 mm. The distance between the cleft and the collector was kept at distances of 150–200 mm. Specifications of the high voltage source used were: 300 Watt High Voltage DC Power Supply with regulators; model number PS/ER50N06.0-22; manufactured by Glassman High Voltage, INC.; output parameters 0–50 kV, 6 mA. The temperature during the spinning was 21 ± 2^{o}C and the relative moisture was 73 ± 2%. PHEMA1 scaffolds were nebulized by 5% phosphoric acid and PHEMA2 scaffolds by 10% phosphoric acid. Nebulization is an ultrasound-induced creation of a mist composed of micron droplets containing the cross-linking agent. The interaction of the mist with a uncross-linked fibrous material conserves gently its fibrous morphology as opposed to its immersion into a liquid bath that should destroyed it completely.

2.4 Scanning electron microscopy (SEM) and nanofiber characterization

SEM was performed using a Vega TS 5130 instrument that provides 12–250,000× magnification, and a resolution of 9 nm. A piece of nanofiber sheet was covered by a thin

gold layer of 10–30 nm during dusting in a SCD 030 apparatus. Nanofiber diameters were measured from uniform random sections of the SEM images.

2.5 Preparation of PHEMA1 scaffolds with adhered liposomes

Multilamellar liposomes (MLV) were prepared by mixing 15 mg of asolectin (AS) and 5 mg of phosphatidylserine (PS). For the preparation of fluorescently labeled liposomes, fluorescein DHPE (0.1 mg) was added to the mixture. The blend was then dissolved in chloroform (1 ml) and evaporated under a nitrogen atmosphere. The thin lipid film was then allowed to dry under vacuum overnight to facilitate the removal of the residual solvent. Dried lipid films were then resuspended in phosphate-buffered saline (PBS) (pH 7.4) or in FBS and the mixture was vortexed for 15 min. For fluorescent spectroscopy measurements lipid films were resuspended in a DPX + ANTS system. The final concentration of liposomes achieved in PBS was 15 mg/ml. The MLV suspensions were then passed 15 times through 1-μm-pore-diameter polycarbonate membranes using a Avanti® Mini-extruder (Avanti Polar Lipids Inc., Alabaster, AL) to give the primarily vesicles an approximate diameter of 1 μm.

To achieve adhesion, liposomes were spread on the nanofiber scaffolds at a concentration of 15 mg/ml and incubated overnight. Non-adhered liposomes were removed by washing three times with PBS. Two types of scaffolds with immobilized liposomes were prepared. In the first, FBS was encapsulated in the liposomes as a stimulating factor for cell adhesion and proliferation (PHEMA1/FBS). In the second, liposomes containing only PBS were used as control scaffolds (PHEMA1/PBS).

2.6 Cryo-field emission scanning microscopy

Cryo-field emission scanning microscopy (FESEM) was used for liposome visualization. The sample was rapidly frozen in liquid nitrogen (−210°C). Then the sample was transferred into the cryo-stage of the preparation chamber (ALTO2500) where it was freeze-fractured at −140°C, freeze-etched by raising the sample temperature until sublimation of water started at −95°C for 10 min, and then coated for 30 s with gold at −135°C. After this preparation, the sample was placed on a cold-stage microscope and examined in the frozen state at −135°C. The specimen was observed at 3 and 4 kV using GB-L mode on a Jeol 7401-FE microscope.

2.7 Fluorescent spectroscopy measurements of liposome-nanofiber interactions

Nanofiber layers of PHEMA with a surface area of 2 cm^2 were immersed into a liposome solution for 60 s to evoke liposome adhesion. The nanofibers were then rinsed and washed with TBS (TRIS buffered saline; pH 7.4) solution overnight. Microfibres with adhered liposomes were subsequently dissolved in ethanol to release the DPX + ANTS system. Fluorescence measurements were performed as described in [22] on a FluoroMax-3 JY-Horiba spectrofluorimeter. Excitation and emission wavelengths were 370 and 505 nm, respectively (both with bandwidths of 4 nm). A suspension (1.5 ml) was placed into a 1 × 1 cm quartz cuvette, and the recorded fluorescence intensities were corrected for the background (vesicles without ANTS and DPX, about 2% of total intensity) and for the effect of dilution due to the addition of DPX and Triton X-100.

2.8 Measurements of charge interactions between microfibers and liposomes

Negatively charged and non-charged liposomes were prepared for this experiment. 20 mg of asolectin were mixed with 5 mg of phosphatidylserine (Group PS) to form negatively charged liposomes, or with 5 mg of phosphatidylcholine (Group PC) in the case of non-charged liposomes. Lipid films were prepared as described previously and re-suspended in the DPX + ANTS system. An Avanti® Mini-extruder was used to form 1 μm vesicles. Superfluous fluorophore were wash away using gel filtration (Sephadex G25).

300 μl of liposome suspension (concentration 15 mg/ml) were incubated with PHEMA1 fibres (1 cm^2) for 1 h at room temperature. Then the samples were rinsed with TBS and subsequently 1 ml of fresh TBS was added and incubated with the samples for 1, 2, and 4 h. At each time point, TBS was removed and measured and 1 ml of fresh TBS was added. Finally, after a 17 h incubation, PHEMA samples with adhered liposomes were dissolved in ethanol. The fluorescence of the released fluorophore in solution was measured using a spectrofluorimeter (Synergy 2, Biotec).

2.9 Chondrocyte isolation, culture, and scaffold seeding

For cell isolation and culture, our previously described method was used [6, 24]. Briefly, round patches of scaffolds (6 mm in diameter) were seeded with rabbit chondrocytes at a density of $8 \times 10^4/cm^2$ and cultivated in 96-well plates under static conditions (37°C, 5% CO_2). The medium was exchanged every 3 days.

For testing PHEMA1 scaffolds with liposomes, cells were pre-cultured in serum-free medium for 24 h. Rabbit chondrocytes ($8 \times 10^4/cm^2$) were seeded on scaffolds and incubated in serum-free medium without changing the media for another 72 h.

2.10 MTT test

50 µl of 1 mg/ml [3-(4,5-dimethylthiazol-2-yl)-2,5-diphenyltetrazolium bromide] (MTT) in phosphate-buffered saline, pH 7.4 (PBS), were added to 150 µl of sample medium and incubated for 4 h at 37°C. MTT was reduced, by mitochondrial dehydrogenase of normally metabolizing cells, to purple formazan. Formazan crystals were solubilized with 100 µl of 50% *N,N*-dimethylformamide in 20% sodium dodecyl sulfate (SDS) at pH 4.7. The results were examined by spectrophotometry in an ELISA reader at 570 nm (reference wavelength 690 nm). Tissue culture plastic polystyrene (TCP) was used as a control.

2.11 Confocal and fluorescence microscopy

Cells were fixed in ethanol at −20°C, rinsed in PBS, incubated with propidium iodide (5 µg/ml in PBS) for 10 min, rinsed in PBS, and visualized under a confocal microscope (Leica SP2 AOBS). In live cell staining, cells were incubated in BCECF-AM (1 mM in serum-free medium) for 30 min at 37°C.

For indirect immunofluorescence staining, samples were fixed in 10% formaldehyde for 10 min, washed with PBS and incubated in 3% FBS in PBS/0.1% Triton for 30 min at room temperature. A primary antibody against type II collagen (dilution 1:20; 1-hour incubation at room temperature) was used. After three washes with PBS/0.05% Tween, samples were incubated with the secondary antibody, Cy 3-conjugated Donkey Anti-Mouse IgG (H + L) (dilution 1:300; 45-min incubation at room temperature, light protected). Samples were again washed with PBS/0.05% Tween, once with PBS, then an antifading solution was added (PBS/90% glycerol/2.5% 1,4-diazabicyclo(2,2,2)octane (DABCO). The staining for type II collagen was examined using a Leica SP2 AOBS confocal microscope.

The cell surface density, or the relative area filled by type II collagen, was determined by Ellipse software. The cell surface densities were determined from averaged cell counts in randomly selected squares. The relative area of type II collagen was determined by immunofluorescence staining. Regions of ECM production containing type II collagen were labeled by the fluorescent antibody. Those areas with a fluorescence intensity greater than the assigned standardized intensity were determined, and the relative area of type II collagen was evaluated.

2.12 Cell adhesion

For measurements of cell adhesion, chondrocytes were fixed in methanol (−20°C) for 10 min, rinsed with PBS, and incubated in DiOC6 for 45 min. Stained cells were visualized by confocal microscopy using a Leica SP2 AOBS, and the area of the spread chondrocytes was determined using Ellipse software (ViDiTo, Slovak republic).

2.13 Statistics

Quantitative data are presented as mean/standard deviation (SD). For nanofiber diameters, the average values were determined from ten measurements. For in vitro tests, average values were determined from three independently prepared samples. The results were evaluated statistically using One Way Analysis of Variance (ANOVA) and the Student–Newman–Keuls Method.

3 Results

3.1 Preparation and characterization of microfiber scaffolds from PHEMA

We succeeded in preparing PHEMA fibers; however, they were unstable in an aqueous solution due to their hydrophilicity. Thus, crosslinking to reduce PHEMA microfibers layer instability in water was accomplished during the nebulization process by phosphoric acid. 5 wt% phosphoric acid (sample PHEMA1) and 10 wt% phosphoric acid (sample PHEMA2) were found to be the optimal amounts to form water-stable PHEMA nanofibers. This process resulted in the creation of microfibers stable enough to undergo harsh conditions, such as boiling for 30 min. The final PHEMA1 sample was characterized by SEM as a partially dissipated structure with an average fiber diameter $d = 2.1 \pm 0.6$ µm; PHEMA2 fibers were thicker ($d = 3.6 \pm 1.3$ µm, Fig. 1).

3.2 Interaction of liposomes with the microfibers

The development of functionalized micro- and submicron fibers as well as a comprehensive understanding of their biological effects seem to be major obstacles for their broader application in tissue engineering. We employed PHEMA microfibers as a model for fiber functionalization by liposomes. Functionalization was achieved by proper microfiber incubation with liposomes (see sect. 2). The large surface area and the suitable surface charge of the microfiber mesh resulted in the immobilization of the liposomes, which were prepared from a fluorescent phospholipid mixture (FITC-PC:PL in 1:1,000 molar ratio) and visualized by confocal microscopy (Fig. 2). Clearly, the liposomes adhered very well to the microfibers and remained tightly trapped on them even after intensive rinsing.

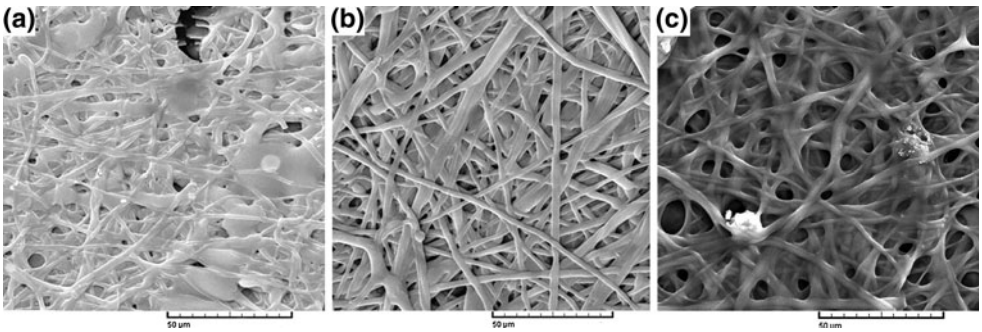

Fig. 1 SEM micrographs of PHEMA microfiber sheets: **a** crosslinked PHEMA1 (5 wt% phosphoric acid), **b** PHEMA2 (10 wt% phosphoric acid) and **c** PHEMA2 after 30-min boiling (5 wt% phosphoric acid, boiled for 30-min and dried)

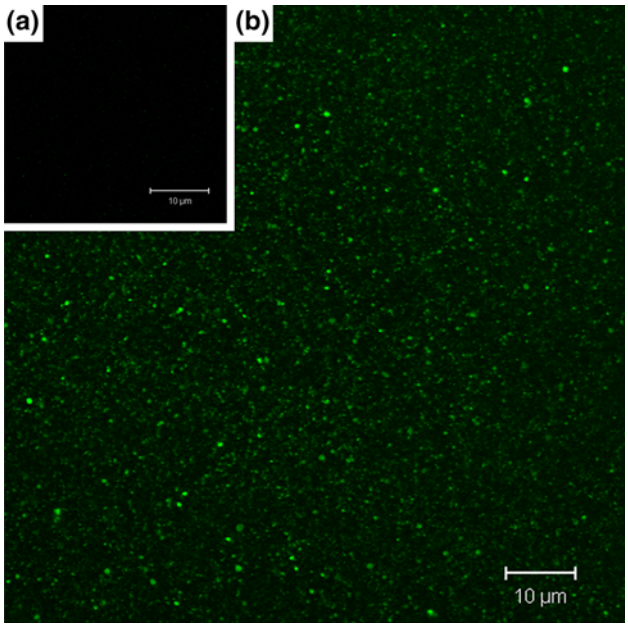

Fig. 2 Liposomes tightly adhered to PHEMA microfibers confocal microscopy of fluorescently labeled (fluorescein DHPE) liposomes adhered to a nanofiber PHEMA scaffold (**b**), control: nanofibers without liposomes (**a**)

The adhesion of the liposomes was confirmed quantitatively by five independent fluorescence measurements of liposomes containing DPX + ANTS. The steady-state fluorescence intensity of ANTS was high ($I = 519 \pm 29$ a.u., background was subtracted) and indicated the presence of an abundant number of adhered liposomes on the microfiber mesh. Interestingly, the liposomes were tightly adhered, and overnight rinsing decreased the steady-state fluorescence intensity to $I = 140 \pm 38$ a.u. (data not shown). Consequently, around 27% of the liposomes still remained tightly bound to the microfibers after overnight washing.

Visualization of the microfibers' interaction with the liposomes was achieved using cryo FESEM (Fig. 3). Clearly, the liposomes were tightly bound on the microfiber surface and penetrated deeply into the fiber mesh.

Charge–charge interactions were confirmed by measuring the release of charged and non-charged liposomes from PHEMA1 fibers. PHEMA is nucleophylic due to the hydroxyl and carbonyl groups in its chains. It was found that negatively charged liposomes (PS) were characterized by a shorter release half-time than non-charged liposomes (PC) (Fig. 4). The faster release of negatively charged liposomes can be explained by repulsion between partially negatively charged functional groups of PHEMA and PS. In contrast, non-charged liposomes (PS) released their contents slower. These results indicate that liposomal interaction with the microfibers was at least partially based on electrostatic interactions.

3.3 Chondrocyte adhesion and proliferation on PHEMA microfiber scaffolds and cartilaginous tissue formation

PHEMA microfibers seem to be promising novel tools for utilization in tissue engineering. However, the fiber structure itself is not sufficient for the preparation of artificial tissue. Besides an adequate fiber diameter, a suitable material must also possess favorable biocompatibility for cell accommodation. Thus, plain (unfunctionalized) microfiber scaffolds were first examined for chondrocyte adhesion. Cells were fluorescently stained and visualized by confocal microscopy. Cell adhesion was estimated from the distribution area measured, as described in Sect. 2. Chondrocytes adhered well to both types of PHEMA microfibers (Table 1).

Chondrocyte metabolic activity and proliferation were determined by a MTT assay. Both microfiber scaffolds prepared from PHEMA displayed strong biocompatibility for chondrocytes. Adhered chondrocytes effectively proliferated on the PHEMA microfibers as determined by the MTT test, 3 and 7 days after scaffold seeding (Fig. 5). In fact, no significant difference in absorbance was found 3 days after seeding between either of the PHEMA scaffolds (absorbance was $A = 0.51$ and 0.42, respectively) and the TCP control ($A = 0.50$). The highest absorbance intensity, 7 days after seeding, was observed on PHEMA2 ($A = 0.77$), higher than on the TCP control ($A = 0.71$). Only a slightly lower intensity was observed on PHEMA1 ($A = 0.66$). However, there was no significant difference among all three samples 7 days after seeding.

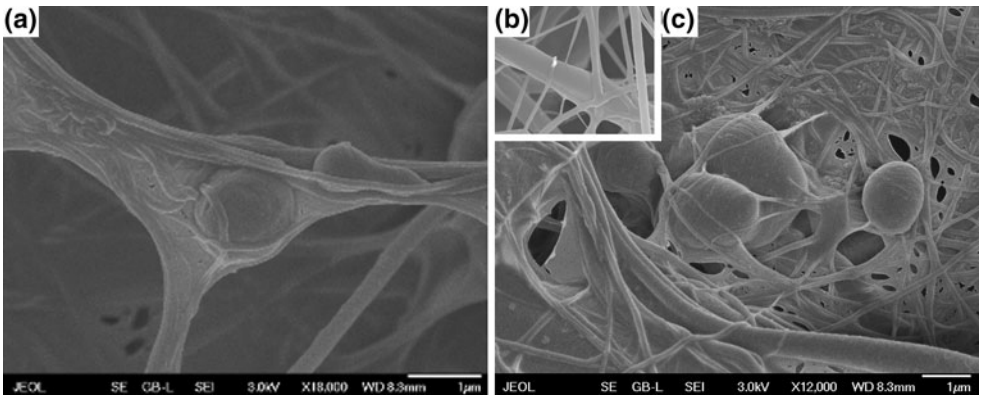

Fig. 3 Detailed visualization of liposome interaction with microfibers FESEM of liposome adhesion on a microfiber PHEMA scaffold: microfibers with adhered liposomes (**a**, **c**) and pure microfibers (**b**)

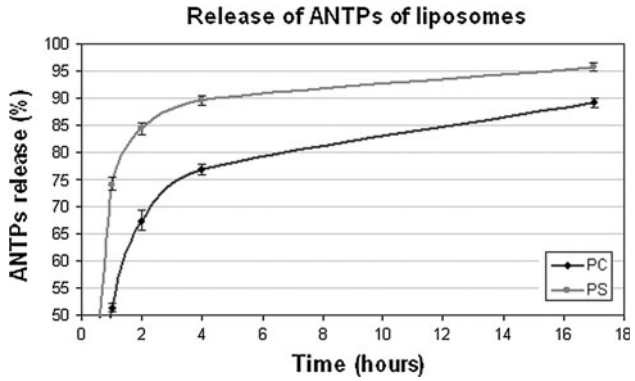

Fig. 4 The fibers' surface charge influenced the adhesion of liposomes temporal release of ANTPS from PC neutral liposomes was significantly higher than from PS negatively charged liposomes

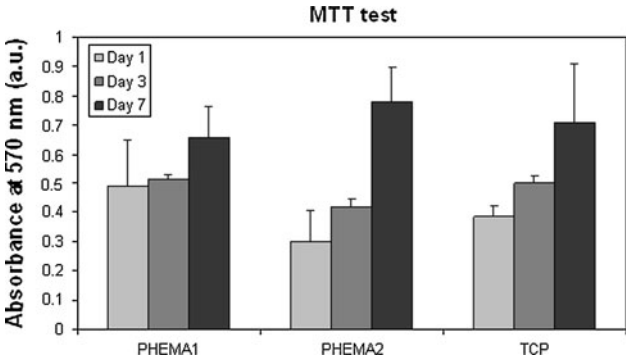

Fig. 5 Chondrocyte adhesion and biocompatibility on PHEMA microfiber scaffolds adhesion and biocompatibility were estimated from the MTT test

Table 1 Liposomes with FBS entrapped in microfibers stimulated chondrocyte adhesion

Scaffold	Cell spreading area (μm^2)
PHEMA1	257 ± 19
PHEMA2	254 ± 25
PHEMA1/PBS	203 ± 63*
PHEMA1/FBS	269 ± 78

Chondrocyte spreading area on nanofiber scaffolds from PHEMA1 and PHEMA2 (cultivated in media with FBS), and on scaffolds with adhered liposomes (PHEMA1/PBS and PHEMA/FBS, cultivated in FBS free media) 24 h after seeding, determined from fluorescence microscopy images

Means ± Standard deviation, * $P < 0.05$

The proliferation and distribution of the cells on the scaffolds was also examined using propidium iodide staining and confocal microscopy. Seven days after seeding, cells were randomly distributed along the PHEMA scaffolds' fibers. They were organized into islands and separated. Their densities significantly increased 14 days after seeding, with an average cell surface density on PHEMA1 scaffolds of 2.2×10^5 cells/cm^2. Comparably, the cell surface density for the PHEMA2 samples was 1.8×10^5/cm^2.

Cartilage formation, originating from chondrocytes seeded on the microfibers, was evaluated by the appearance of characteristic ECM proteins using specific fluorescent staining and confocal microscopy. Type II collagen, as a typical extracellular marker for hyaline cartilage, was detected using a fluorescent type II collagen antibody (Table 2). The relative area filled by type II collagen, 14 days after seeding, covered 47% of the total PHEMA scaffold surface.

3.4 In vitro testing of PHEMA1 scaffolds with adhered liposomes

A microfiber scaffold in combination with liposomes was used as a potential drug delivery system. Stimulating factors were entrapped and immobilized in tightly anchored liposomes on the scaffold in order to positively influence cell adhesion and proliferation. FBS was used as a model

Table 2 Expression of type II collagen 14 days after chondrocyte seeding

Scaffold	Amount of type II collagen (%)
PHEMA1	47 ± 0.9
PHEMA2	47 ± 3.6

Means ± standard deviation

Area of type II collagen produced on fiber scaffolds, 14 days after seeding. Areas were determined from confocal microscopy images processed using Ellipse software

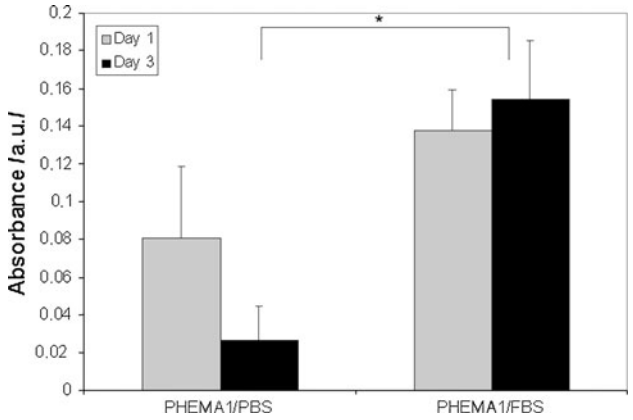

Fig. 6 Chondrocyte adhesion and biocompatibility on PHEMA1 microfiber scaffolds with adhered liposomes adhesion and biocompatibility were estimated from the MTT test. *$P < 0.001$

factor due to its stimulatory effects on cell adhesion and proliferation. Cell adhesion was determined by measuring the spreading area (S) by fluorescent staining 24 h after seeding the scaffold. Exceptionally good cell adhesion was observed on the PHEMA1/FBS scaffolds (S = 269 μm^2). This value was significantly larger than on the PHEMA1/PBS (S = 203 μm^2) and PHEMA1 scaffolds cultivated in a FBS enriched medium (S = 257 μm^2) (Table 1). The medium was not changed during this part of the experiment so as to preserve the release of stimulating factors. For this reason, the MTT assay was performed only 1 and 3 days after scaffold seeding. The results revealed a very good correlation with cell adhesion, and markedly higher cell proliferation was observed on the PHEMA1/FBS sample ($A = 0.15$) 3 days after seeding compared to the control PHEMA1/PBS sample ($A = 0.05$) (Fig. 6).

Improved cell proliferation on the PHEMA1/FBS scaffold was also confirmed by live cell counting (Table 3). In addition, immunofluorescent staining for type II collagen showed typical early maturing chondrogenic ECM production. The relative area of type II collagen was considerably higher on the PHEMA1/FBS (8.2%) scaffolds than on the PHEMA1/PBS scaffolds (1.7%) (Table 4).

Table 3 Liposomes with FBS entrapped in microfibers enhanced chondrocyte viability

Scaffold	Average cell surface density Day 1 (cells/cm^2)	Average cell surface density Day 3 (cells/cm^2)
PHEMA1/PBS	$2.5 \pm 0.9 \times 10^3$	$2.1 \pm 0.7 \times 10^3$
PHEMA1/FBS	$4.4 \pm 1.6 \times 10^{3*}$	$5.2 \pm 3.3 \times 10^{3*}$

Cell surface densities of chondrocyte-seeded scaffolds determined from fluorescence microscopy images, live cell staining

Means ± standard deviation, * $P < 0.05$

Table 4 Enhanced type II collagen expression due to adhered liposomes with FBS

Scaffold	Amount of type II collagen (%)
PHEMA1/PBS	1.7 ± 0.7
PHEMA1/FBS	8.2 ± 2.5*

Area of type II collagen produced on PHEMA1 nanofiber scaffolds with adhered liposomes, 3 days after seeding. (Letters in bars show the extent of statistically significant differences; P is less than 0.05)

Means ± standard deviation, * $P < 0.05$

4 Discussion

4.1 Preparation of electrospun fibers from PHEMA

Synthetic polymer fibers have already been reported to be a suitable material for tissue engineering [17]. In this study, micro- and nanofibers from PHEMA were prepared. In fact, fiber formation from PHEMA was rather expected based on previous results [23]. The problem of the water instability of the PHEMA microfibers was solved by nebulization with phosphoric acid. A lower concentration of phosphoric acid (5%) during the nebulization process, however, resulted in the assembly of microfibers with smaller radii. Consequently, nebulization is an important tool for modulating the fiber mesh structure, and thus a key step in the formation of a solid scaffold. A longer nebulization time lead to a higher concentration of crosslinks and greater stability in an aqueous environment. This presents new opportunities for application in tissue engineering.

4.2 Immobilized liposomes on microfibers as a promising tool for controlled drug delivery

PHEMA microfibers were used for chondrocyte seeding. The favorable adhesion and proliferation of chondrocytes on PHEMA microfibers were demonstrated. In addition, PHEMA microfibers turned out to be a suitable scaffold for liposome adhesion and the preparation of functionalized

systems for cell seeding. Micro- and submicron fibers are characterized by a large surface area and thus, increased adhesion. It was demonstrated, that liposome binding on fibers is influenced by the molecules' charge. Negatively charged liposomes were released faster from the PHEMA fiber surface, which is partially negatively charged. Additional interactions between charged nanofibers and liposomes should be tested.

Liposomes and immunoliposomes have often been used as biocompatible carriers of drugs, peptides, proteins, plasmic DNA, antisense oligonucleotides or ribosomes for pharmaceutical, cosmetic, and biochemical purposes [24–26]. Their membrane is composed of a lipid bilayer, impermeable to ions and large dipoles, such as saccharides and proteins. It enables the protection of encapsulated water-soluble, as well as lipid-soluble, substances from the environment. Based on the properties mentioned above, liposomes can serve as convenient delivery vehicles for a variety of biologically active compounds [27]. Some weak points, however, hinder their broader application, including targeting. Anchoring liposomes to nanofibers could expand their potential usefulness as a tool for drug delivery.

The adhesion of drug-containing liposomes at the same location as chondrocytes led to the localization of the drugs in the vicinity of the cells, as clearly proved by our results using serum-encapsulated liposomes. Liposomes immobilized on the microfiber web, together with chondrocytes, influenced cells in the close proximity. The gradual release of serum to the neighboring cells resulted in improved chondrocyte proliferation (Table 3; Fig. 6). This system, thus, shows promise for the development of a controlled drug delivery system in tissue engineering.

4.3 Perspectives for the use of PHEMA microfibers in tissue engineering

Optimal scaffolds for tissue engineering should resemble native tissues. Thus, fibers with diameters similar to natural extracellular structures should be a promising material for application in regenerative medicine. Nanofibrous composite membranes made of electrospun PLGA–chitosan/PVA were suggested for skin reconstruction [28]. The PVA/chitosan composite membranes also positively mimic the structure of natural extracellular matrices and can be applied as three-dimensional scaffolds for tissue engineering [29]. There are other promising synthetic polymers from which nanofibers can be formed, such as poly(vinyl alcohol) [12], poly(lactic acid) [11], polycaprolactone [10], poly(ethylene glycol) [30], polyacrylamide [31], polyphosphazenes [32] and polyurethane [33]. All of these substances can be potentially used for chondrocyte seeding and other tissue engineering applications.

As follows from our results, high adhesion and drug targeting are important assets of electrospun fibers. Liposome anchoring in the close vicinity of cells can locally strengthen a drug's effects. Such an approach could also locally influence cell growth and proliferation. The preparation of a suitable nanofiber/liposome system could result in innovative applications in cartilage and tissue engineering. Despite of our positive in vitro results, the experiment may not perform well the interaction of this system with native tissue. For this reason further in vivo experiments are planned.

5 Conclusion

Microfibers made from PHEMA proved to be suitable for the construction of artificial cartilages. Both chondrocytes and liposomes substantially adhered to the PHEMA microfibers. Serum-containing liposomes, immobilized on the microfiber mesh, proved able to serve as a cell targeting system, significantly improving chondrocyte proliferation. Consequently, such a system could be useful as a drug delivery tool and could find broader application in tissue engineering.

Acknowledgments The authors would like to acknowledge J. Farberova from the Technical University of Liberec for measurements of fiber diameters and Sam Norris for proof reading of this manuscript. Supported by the Academy of Sciences of the Czech Republic (institutional research plans AV0Z50390703 and AV0Z50390512), the Ministry of Education, Youth and Sports of the Czech Republic (research programs NPV II 2B06130 and 1M0510, research project CARSILA number ME10145), the Grant Agency of the Academy of Sciences Grant No. IAA500390702 and by the Czech Science Foundation Grant No. GA202/09/1151, IGA MZCR, No. NT12156, and the Grant Agency of the Charles University Grant No. 122508.

References

1. Buckwalter JA, Lohmander S. Operative treatment of osteoarthrosis. Current practice and future development. J Bone Joint Surg Am. 1994;76:1405–18.
2. Buckwalter JA, Mankin HJ. Articular cartilage: degeneration and osteoarthritis, repair, regeneration, and transplantation. Instr Course Lect. 1998;47:487–504.
3. Hangody L, Vasarhelyi G, Hangody LR, Sukosd Z, Tibay G, Bartha L, Bodo G. Autologous osteochondral grafting-technique and long-term results. Injury. 2008;39(1):S32–9.
4. Solheim E, Hegna J, Oyen J, Austgulen OK, Harlem T, Strand T. Osteochondral autografting (mosaicplasty) in articular cartilage defects in the knee: results at 5–9 years. Knee. 2009;17(1):84–7.
5. Brittberg M, Sjogren-Jansson E, Lindahl A, Peterson L. Influence of fibrin sealant (Tisseel) on osteochondral defect repair in the rabbit knee. Biomaterials. 1997;18:235–42.
6. Filova E, Jelinek F, Handl M, Lytvynets A, Rampichova M, Varga F, Cinatl J, Soukup T, Trc T, Amler E. Novel composite hyaluronan/type I collagen/fibrin scaffold enhances repair of

osteochondral defect in rabbit knee. J Biomed Mater Res B Appl Biomater. 2008;87:415–24.
7. Benya PD, Shaffer JD. Dedifferentiated chondrocytes reexpress the differentiated collagen phenotype when cultured in agarose gels. Cell. 1982;30:215–24.
8. Kon M, de Visser AC. A poly(HEMA) sponge for restoration of articular cartilage defects. Plast Reconstr Surg. 1981;67:288–94.
9. Pradny M, Lesny P, Fiala J, Vacik J, Slouf M, Michalek J, Sykova E. Macroporous hydrogels based on 2-hydroxyethyl methacrylate. Part 1. Copolymers of 2-hydroxyethyl methacrylate with methacrylic acid. Collection Czechoslov Chem Commun. 2003;68:812–22.
10. Schnell E, Klinkhammer K, Balzer S, Brook G, Klee D, Dalton P, Mey J. Guidance of glial cell migration and axonal growth on electrospun nanofibers of poly-epsilon-caprolactone and a collagen/poly-epsilon-caprolactone blend. Biomaterials. 2007;28: 3012–25.
11. Liang D, Hsiao BS, Chu B. Functional electrospun nanofibrous scaffolds for biomedical applications. Adv Drug Deliv Rev. 2007;59:1392–412.
12. Yang EL, Qin XH, Wang SY. Electrospun crosslinked polyvinyl alcohol membrane. Mater Lett. 2008;62:3555–7.
13. Ren DW, Yi HF, Zhang H, Xie WY, Wang W, Ma XJ. A preliminary study on fabrication of nanoscale fibrous chitosan membranes in situ by biospecific degradation. J Memb Sci. 2006;280:99–107.
14. Li M, Mondrinos MJ, Gandhi MR, Ko FK, Weiss AS, Lelkes PI. Electrospun protein fibers as matrices for tissue engineering. Biomaterials. 2005;26:5999–6008.
15. Chen ZG, Mo XM, Qing FL. Electrospinning of collagen-chitosan complex. Mater Lett. 2007;61:3490–4.
16. Chong EJ, Phan TT, Lim IJ, Zhang YZ, Bay BH, Ramakrishna S, Lim CT. Evaluation of electrospun PCL/gelatin nanofibrous scaffold for wound healing and layered dermal reconstitution. Acta Biomater. 2007;3:321–30.
17. Lannutti J, Reneker D, Ma T, Tomasko D, Farson DF. Electrospinning for tissue engineering scaffolds. Mater Sci Eng C Biomimetic Supramol Sys. 2007;27:504–9.
18. Lukas D, Sarkar A, Martinova L, Vodsedalkova K, Lubasova D, Chaloupek J, Pokorny P, Mikes P, Chvojka J, Komarek M. Physical principles of electrospinning (Electrospinning as a nanoscale technology of the twentyfirstcentury). Text Progr. 2009;41: 59–140.
19. Jirsak O, Sanetrnik F, Lukas D, Kotek V, Martinova L, Chaloupek J. A method of Nanofibres production from a polymer solution using electrostatic spinning and a device for carrying out the method. U.S. Patent No. WO2005024101 2005.
20. Pradny M, Martinova L, Michalek J, Fenclova T, Krumbholcova E. Electrospinning of the hydrophilic poly (2-hydroxyethyl methacrylate) and its copolymers with 2-ethoxyethyl methacrylate. Cent Eur J Chem. 2007;5:779–92.
21. Lukas D, Sarkar A, Pokorny P. Self-organization of jets in electrospinning from free liquid surface: a generalized approach. J Appl Phys. 2008;103:309–16.
22. Fiser R, Konopasek I. Different modes of membrane permeabilization by two RTX toxins: HlyA from *Escherichia coli* and CyaA from *Bordetella pertusis*. Biochim Biophys Acta. 2009; 1788:1249.
23. Horak D, Hlidkova H, Hradil J, Lapcikova M, Slouf M. Superporous poly(2-hydroxyethyl methacrylate) based scaffolds: preparation and characterization. Polymer. 2008;49:2046–54.
24. Ulrich AS. Biophysical aspects of using liposomes as delivery vehicles. Biosci Rep. 2002;22:129–50.
25. Bonanomi MH, Velvart M, Stimpel M, Roos KM, Fehr K, Weder HG. Studies of pharmacokinetics and therapeutic effects of glucocorticoids entrapped in liposomes after intraarticular application in healthy rabbits and in rabbits with antigen-induced arthritis. Rheumatol Int. 1987;7:203–12.
26. Mickova A, Tomankova K, Kolarova H, Bajgar R, Kolar P, Sunka P, Plencner M, Jakubova R, Benes J, Kolacna L, Planka L, Necas A, Amler E. Ultrasonic shock-wave as a control mechanism for liposome drug delivery system for possible use in scaffold implanted to animals with iatrogenic articular cartilage defects. Acta Vet Brno. 2008;77:285–96.
27. Matteucci ML, Thrall DE. The role of liposomes in drug delivery and diagnostic imaging: a review. Vet Radiol Ultrasound. 2000; 41:100–7.
28. Duan B, Yuan XY, Zhu Y, Zhang YY, Li XL, Zhang Y, Yao KD. A nanofibrous composite membrane of PLGA-chitosan/PVA prepared by electrospinning. Eur Polym J. 2006;42:2013–22.
29. Duan B, Wu L, Li X, Yuan X, Li X, Zhang Y, Yao K. Degradation of electrospun PLGA-chitosan/PVA membranes and their cytocompatibility in vitro. J Biomater Sci Polym Ed. 2007;18:95–115.
30. Rhee W, Rosenblatt J, Castro M, Schroeder J, Rao PR, Harner CHF, Berg RA. In vivo stability of poly(ethylene glycol) collagen composites. In: Zalipsky S, Milton Harris J, editors. Poly(ethylene glycol) chemistry and biological applications. Washington: American Chemical Society Series; 1997 p.420–440.
31. Savina IN, Galaev IY, Mattiasson B. Ion-exchange macroporous hydrophilic gel monolith with grafted polymer brushes. J Mol Recognit. 2006;19:313–21.
32. Carampin P, Conconi MT, Lora S, Menti AM, Baiguera S, Bellin S, Grandi C, Parnigotto PP. Electrospun polyphosphazene nanofibers for in vitro rat endothelial cells proliferation. J Biomed Mater Res A. 2007;80:661–8.
33. Zhang C, Zhang N, Wen X. Synthesis and characterization of biocompatible, degradable, light-curable, polyurethane-based elastic hydrogels. J Biomed Mater Res A. 2007;82:637–50.

Příloha 10

Kostakova, E., Gregr, J., Meszaros, L., Chotebor, M., Nagy, Z., K., Pokorny, P., Lukas, D.: Laboratory synthesis of carbon nanostructured materials using natural gas, Materials Letters, 79 (2012) 35–38, 2012, IF=2,307 (11)

Materials Letters 79 (2012) 35–38

Contents lists available at SciVerse ScienceDirect

Materials Letters

journal homepage: www.elsevier.com/locate/matlet

Laboratory synthesis of carbon nanostructured materials using natural gas

Eva Kostakova [a,*], Jan Gregr [a], Laszlo Meszaros [b], Michal Chotebor [a], Zsombor K. Nagy [b], Pavel Pokorny [a], David Lukas [a]

[a] Technical University of Liberec, Czech Republic
[b] Budapest University of Technology and Economics, Hungary

ARTICLE INFO

Article history:
Received 5 December 2011
Accepted 24 March 2012
Available online 31 March 2012

Keywords:
Carbon nanotubes
Carbon nanostructured materials
Chemical vapor deposition
Raman spectroscopy

ABSTRACT

The article describes a simple set-up of chemical vapor deposition (CVD) method for laboratory production of carbon nanostructures including carbon nanotubes. Here we show that natural gas can be utilized as a carbon source for synthesis of carbon nanomaterials on unconventional substrates with integrated catalysts as rocks, metal plates and metal wires by CVD method. Several types of carbon nanomaterial structures not only carbon nanotubes were recognized during these syntheses. Optimal conditions for production of long multiwalled carbon nanotubes were obtained. Diameters of these nanotubes are around hundred nanometers. Raman spectroscopy and scanning electron microscopy were used for the study of produced nanostructures. The available utilization of these carbon nanotubes or nanostructures on the unconventional substrates can be in special active filtration, substrates for catalytic chemical and biochemical reactions, etc.

1. Introduction

The most frequently used synthesis method of carbon nanotubes are [1]: laser ablation; arc discharge method and CVD. The easiest way how to produce carbon nanotubes is the CVD method, which employs mainly gas phase hydrocarbons as a raw carbonaceous material. The synthesis of carbon nanotubes by CVD methods involves the catalytic decomposition of a carbon-containing source on small metallic particles or clusters. Metals generally used for these reactions are transition metals, such as Fe, Co and Ni. It is a "low temperature" process compared to arc-discharge and laser-ablation methods, with the formation of carbon nanotubes typically occurring between 600 °C and 1000 °C.

The technique allows to change several parameters and to study their influence on final product: carbon source, substrate and catalysts; temperature of synthesis; gas flow; atmosphere and duration of synthesis. Hydrocarbons as carbon source for CVD method are used in mixture with hydrogen, because its presence has positive effect on catalyst due to the encapsulation which prevents and slows down its deactivation [2]. The methane [3], ethane [4], acetylene [5], ethanol [6] or liquefied petroleum gas, known as LPG [7], are the most used carbon sources for the CVD type nanotube synthesis. Only a few works dealing with natural gas as a carbon source was published until now [8,9]. An employing of natural gas as a carbon source for the CVD synthesis of carbon nanomaterials with the aid of different substrates is researched in this study.

2. Experimental part

The laboratory set up used for the CVD production of carbon nanostructures is depicted in Fig. 1. A substrate including required metal particles was placed into a quartz tube inside the oven for own CVD process. The quartz tube was then closed and nitrogen started to purge the system inside. When the temperature reached the required value, nitrogen flow was stopped and natural gas was flowed in. After the elapse of required time period, nitrogen was again flowed inside instead of natural gas.

The natural gas has a density 0.693 kg/m^3 and consists of: methane 98.022 mol%; ethane 0.788 mol%; propane 0.247 mol%; iso-butane 0.036 mol%; n-butane 0.038 mol%; iso-pentane 0.006 mol%; n-pentane 0.003 mol%; C_{6+} 0.004 mol%; CO_2 0.066 mol%; and N_2 0.773 mol% [10].

Materials without any chemical treatment were used as substrates with integrated metal particles — as a catalyst: basalt rocks, metal plates and metal wires. Several localities in the Czech Republic were identified after consultation with geologists, where minerals containing iron (Fe) and containing nickel (Ni) can be found. The most appropriate are alkaline olivine basalts from the quarry in Hermanice–Frydlant. Another rock with nickel content, cuprous-nickel ore from Rozany near Sluknov was also applied. Nickel-plated metal as metal catalyst was used. The presence of the transition metals in the surfaces of basalts and metal plate was proven by energy dispersive X-ray spectrometer. All substrates were cut before the experiment to the desired size (10×10×2 mm) by means of diamond saw and polished with a polishing wheel roughness of 500 μm. Company Kanthal (KNTL Ltd.) supplied wires named Nikrothal 80 and Cuprothal 49 that were also applied for the synthesis. Nikrothal 80

* Corresponding author. Tel.: +420 48 535 3230; fax: +420 48 535 3542.
E-mail address: eva.kostakova@tul.cz (E. Kostakova).

0167-577X/$ – see front matter © 2012 Elsevier B.V. All rights reserved.
doi:10.1016/j.matlet.2012.03.101

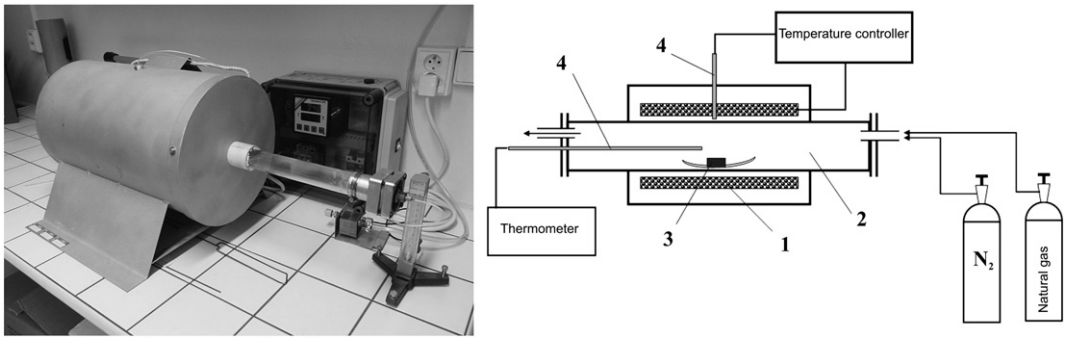

Fig. 1. Photo and scheme of the set up used for CVD synthesis of carbon nanostructures. Cylindrical oven (1) with quartz tube (2), substrate (3), feeding and removing hoses for nitrogen and natural gas, temperature controller and thermometer connected with thermal sensors (4) are the main parts of the CVD set up.

contains 79.15% Ni; 19.5% Cr; 1.35% Si. Cuprothal 49 thermocouple is an alloy consist of 44% Ni; 0.5% Fe; 45.3% Cu; 0.5% Mn, and 0.3% Co.

The influence of different reaction temperatures of 830–1120 °C, the influence of different gas flow rates from 15 to 80 ml/min and the influence of different reaction times from 6.5 to 70 min were tested in the experiments.

Final samples were studied by scanning electron microscopy (Tescan, Vega) and Raman spectroscopy (Horiba JOBIN Yvon — LabRam IR with Olympus BX41).

3. Results and discussion

The scanning electron microscopy showed surface morphological features of produced carbon nanostructures. Carbon nanofibrous structures are shown in Fig. 2. The final nanofibrous structures synthesized on different substrates differ by occurrence density at the surface, thickness and shape (straight or wavy).

Other carbon nanostructures produced during our experimental work obtained with the device described above are introduced in Fig. 3. The

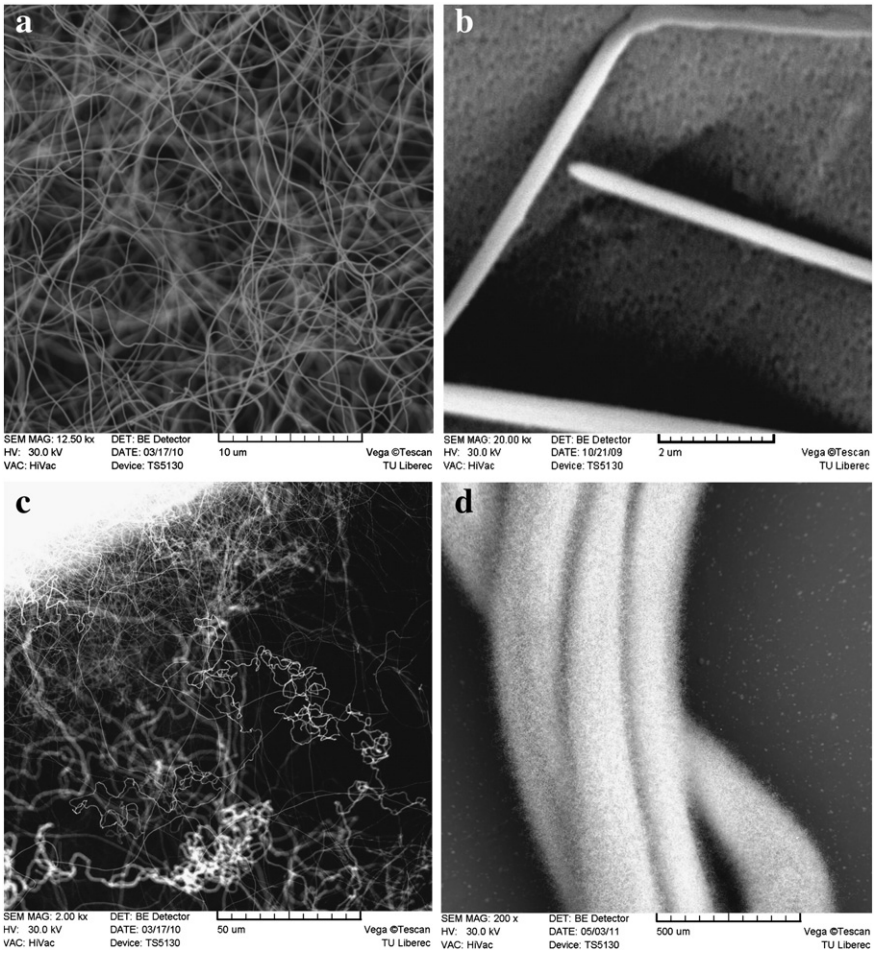

Fig. 2. Carbon nanofibrous products at these substrates (with synthesis conditions — reaction temperature, gas flow and reaction time): a) cuprothal 900 °C; 40 ml/min; 60 min; fiber diameter 121 ± 16 nm b) basalt from Hermanice 800 °C; 40 ml/min; 30 min; fiber diameter 381 ± 30 nm c) and d) Nikrothal 840 °C; 40 ml/min; 30 min fiber diameter 107 ± 13 nm (the same material with different magnification).

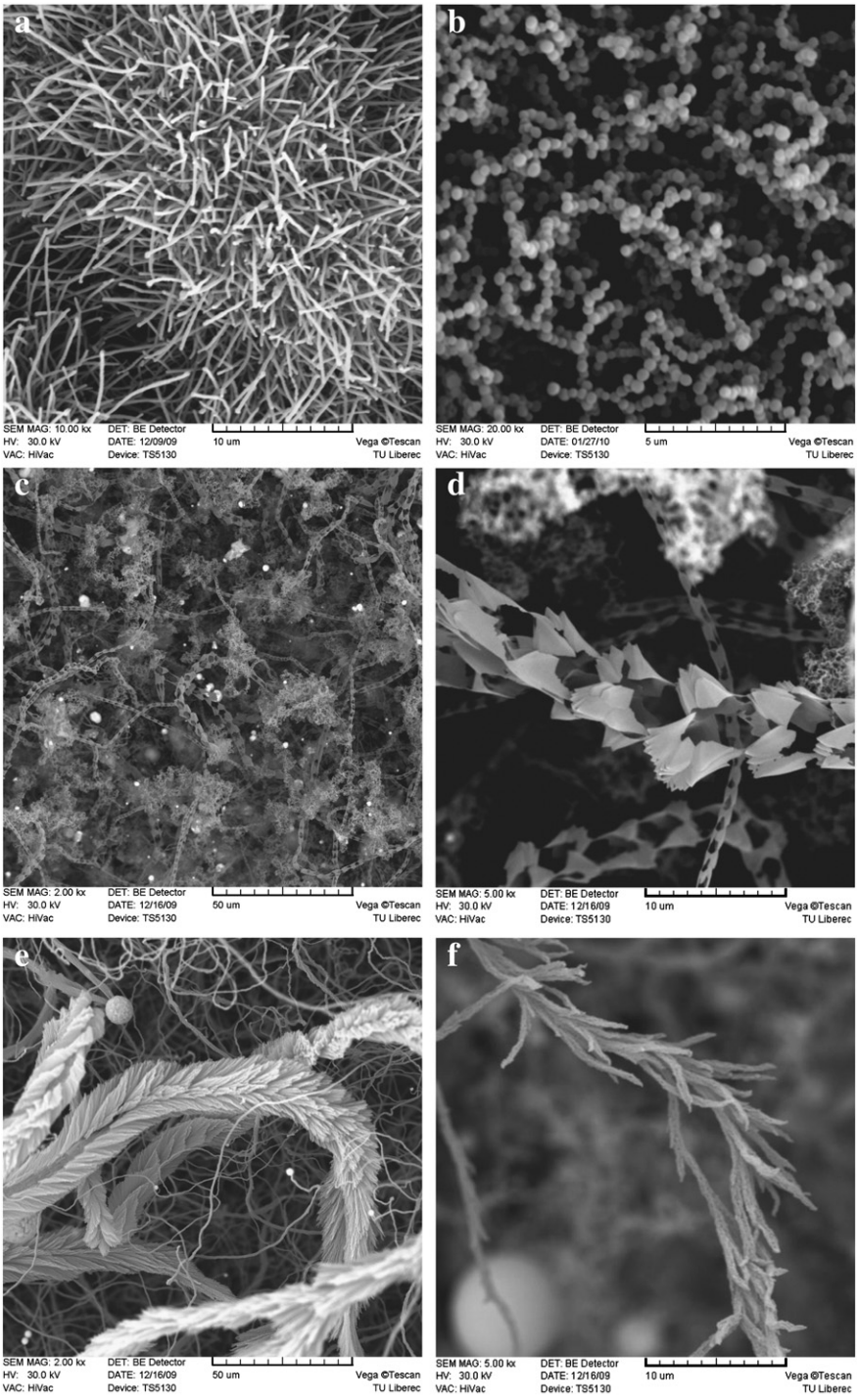

Fig. 3. Examples of next carbon nanostructures as final products of various synthesis conditions: a) nickel plate; 1120 °C; 50 ml/min; 10 min; b) nickel plate; 1120 °C; 45 ml/min; 10 min; c) and d) nickel plate; 1120 °C; 40 ml/min; 10 min; e) cuprous-nickel ore from Rozany; 1120 °C; 40 ml/min; 10 min; f) basalt from Hermanice; 1120 °C; 40 ml/min; 10 min.

structures contain thicker straight fibers (Fig. 3a) (diameter 280 ± 29 nm); connected balls (Fig. 3b) (diameter 360 ± 30 nm); connected carbon multilayered unclosed cones — looking like coiled ginkgo leave (Fig. 3c and d) and structures resembling branches with needles (Fig. 3e and f) were produced at various synthesis conditions.

The Raman spectroscopy was used for the samples where nanofibrous structures were detected on scanning electron microscope images, to prove their tubular nature. The characteristic spectra for carbon nanotubes usually have two peaks. One is around 1350 cm^{-1} (known as the D-band peak) and the last one around 1590 cm^{-1} (known as the G-band peak) [11,12]. The example of Raman spectrum for the sample with carbon nanofibrous structures visible in Fig. 2a is shown in Fig. 4. The spectrum clearly shows the multiwalled carbon nanotube structure of the material.

4. Conclusions

The main experimental achievement of the work is that very simple CVD device in combination with natural gas and the described untreated substrates can finally offer different types of nanostructures including also carbon multiwalled nanotubes with relatively high purity and uniformity. The best results were obtained (the best

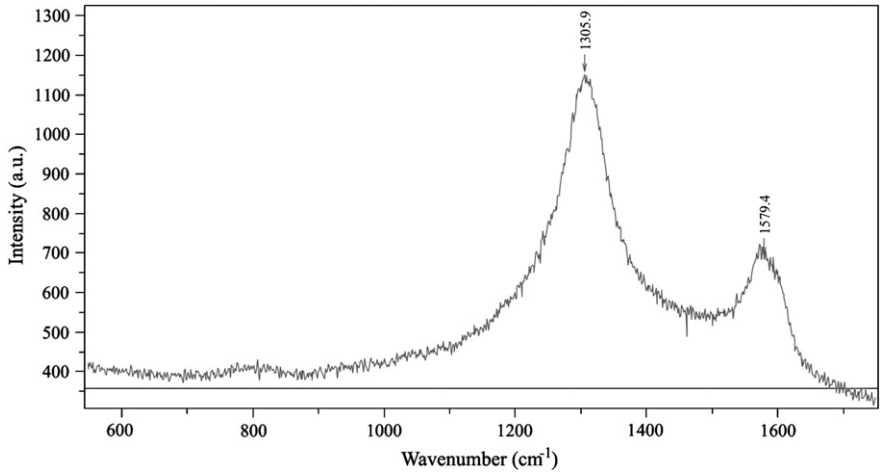

Fig. 4. Raman spectra of the produced nanofibrous product by the presented CVD method (Cuprothal 49; at 900 °C; 40 ml/min; 60 min).

structures of multiwalled carbon nanotubes — thin, long, relatively large amount, without impurities, etc.) at substrates from special wires (Cuprothal and Nikrothal) at synthesis temperature about 900 °C and gas flow 40 ml/min. Duration of synthesis seems to have no important influence on formation of nanostructure on the size rather length in carbon nanotubes case.

Acknowledgment

The support for this research was provided by The Ministry of Interior of the Czech Republic (program BV II/2-VS, grant No. 1656) and by the Czech–Hungarian intergovernmental research support KONTAKT (No. MEB 041008). The authors gratefully acknowledge Kanthal (KNTL Ltd.) for providing the wires.

References

[1] Bhushan B. Springer handbook of nanotechnology. 2nd ed. New York: Springer; 2006.
[2] Zhao N, He C, Juany Z, Li J, Li Y. Fabrication and growth mechanism of carbon nanotubes by catalytic chemical vapor deposition. Mater Lett 2006;60(2):159–63.
[3] Vallés C, Pérez-Mendoza M, Maser WK. Effects of partial and total methane flows on the yield and structural characteristics of MWCNTs produced by CVD. Carbon 2009;47(4):998–1004.
[4] Gulino G, Vieira R, Amadeu R. C_2H_6 as an active carbon source for a large scale synthesis of carbon nanotubes by chemical vapour deposition. Appl Catal Gen 2005;279(1–2):89–97.
[5] Yi W, Yang Q. CVD growth and field electron emission of aligned carbon nanotubes on oxidized Inconel plates without addition of catalyst. Diamond Relat Mater 2010;19:870–4.
[6] Ortega-Cervantez G, Rueda-Morales G, Ortiz-Lopez J. Catalytic CVD production of carbon nanotubes using ethanol. Microelectron J 2005;36(3–6):495–8.
[7] Ndungu P, Godongwana ZG, Petrik LF. Synthesis of carbon nanostructured materials using LPG. Microporous Mesoporous Mater 2008;116(1–3):593–600.
[8] Bonadiman R, Lima DM, de Andrade MJ, Bergmann CP. Production of single and multi-walled carbon nanotubes using natural gas as a precursor compound. J Mater Sci 2006;41:7288–95.
[9] Danafar F, Fakhrul-Razi A, Mohd Salleh MA, Biak DRA. Fluidized bed catalytic chemical vapor deposition synthesis of carbon nanotubes—a review. Chem Eng J 2009;155:37–48.
[10] http://www.rwe-gasnet.cz/cs/kvalita-plynu/gas.
[11] Saito R, Jorio A, Souza Filho AG, Grueneis A, Pimenta MA, Dresselhaus G, et al. Dispersive Raman spectra observed in graphite and single wall carbon nanotubes. Physica B 2002;323:100–6.
[12] Zhang Z, Peng K, Chen Y. Express Polym Lett 2011;5(6):516–25.

Příloha 11

Gombos, Z., Nagy, V., Kostakova, E., Vas, L.,M.: Absorbency behaviour of vertically positioned nonwoven glass fiber mats in case of two different resin viscosities, Macromolecular symposia, Vol. 239, pg.227-231, 2006

Absorbency Behaviour of Vertically Positioned Nonwoven Glass Fiber Mats in Case of Two Different Resin Viscosities

Zoltán Gombos,[*1] *Veronika Nagy,*[1] *Eva Košťáková,*[2] *László Mihály Vas*[1]

Summary: The resin absorbency of vertically positioned chopped strand mat samples was examined as a function of time with a microtensiometer type Krüss K12. With the help of a theoretical model the results of this measurement can be interpreted and evaluated. The samples of different structure (mats bonded with powder or emulsion) were compared and the impact of resin viscosity was studied and conclusions were drawn about the pore and capillary sizes in the mats. The results verified the applicability of the method and revealed the typical pore characteristics of mats and this way estimations can be made on the properties of composites.

Keywords: absorption; glass fiber mat; Lukas–Washburn equation; resins; viscosity

Introduction

Composites are applied in a wider and wider range as engineering materials. They are made up of reinforcing material of high strength (usually in a fibrous form) and the embedding matrix of high toughness (usually resin). The most commonly used and cheapest reinforcement is still glass fiber or glass fiber mat (GFM), which is usually processed with unsaturated polyester resin. The adhesion between the matrix and the reinforcement determines the mechanical properties of composites mostly; hence the resin impregnation of glass fibers is a key factor when producing this kind of composite structures. Hence the absorption properties of the applied product has to be known in order to be able to determine the mechanical properties such as tensile and bending strength, as well as modulus of the final product. On the other hand, porosity and absorbency of fibrous structures has been studied for a long time, mostly in case of textile materials. [1–4] Hence the methods for testing absorbency are already known but have not been applied for studying resin absorbency. [5]

This paper aims to reveal that this method of microtensiometry, basically used for textile testing, can be applied for the fibrous reinforcement of composites. The other objective is to compare the effect of two different resin viscosities.

Theoretical Background

The absorption process in a fibrous structure can be described by the Lukas–Washburn equation, the general formula of which for a monocapillary system is [6,7]:

$$\frac{dh}{dt} = \dot{h} = \frac{b}{h} - a \tag{1}$$

where h is the height of the meniscus (which is in correlation with the absorbed weight of resin), t denotes time and a and b are constants defined in the following expressions:

$$a = \frac{r^2 \rho g}{8\eta} \quad b = \frac{r\gamma \cos\theta}{4\eta} \tag{2}$$

where r is the radius of pore or capillary, g is gravitational acceleration ($g = 9.81$ m/s^2), γ is the surface tension of resin, ρ and η are the density and viscosity of the resin,

[1] Department of Polymer Engineering, Budapest University of Technology and Economics, Műegyetem rkp. 3, H-1111 Budapest, Hungary
Fax: (+36) 1 4631527
E-mail: gombos@pt.bme.hu
[2] Department of Nonwovens, Technical University of Liberec, Hálkova 6, 46117 Liberec, Czech Republic

respectively while θ is the contact angle between the resin and the GFM.

If the mass (m) of the absorbed resin is measured, it is proportional to meniscus height:

$$m = hA\rho \tag{3}$$

where A is the approximate free cross section area of the sample. In our case the absorbed mass was measured as a function of time. Then Eq. (1) can be transformed into the following formula:

$$\frac{dm}{dt} = \dot{m} = \frac{b_m}{m} - a_m \tag{4}$$

$$b_m = bA^2\rho^2 \quad a_m = aA\rho \tag{5}$$

The absorption process in the initial phase can be described by the following simplified Lukas–Washburn equation:

$$\frac{dm}{dt} = \frac{b_m}{m} \tag{6}$$

In case of zero initial condition, the solution of Eq. (6) is as follows:

$$m(t) = \sqrt{2b_m t} = k_{0m}\sqrt{t} \tag{7}$$

where $k_{0m}[g/\sqrt{s}]$ is a coefficient of the dynamics of resin absorption in the initial state of the process and corresponds to the steepness of the curve (see Fig. 1).[8]

This means that the absorbed mass of resin as a function of the square root of time is linear but only in the initial part. Afterwards the curve can be described with the following equation:

$$m(t) = m_\infty\left[1 - e^{-\left(\frac{2a_m \cdot t}{m_\infty}\right)^p}\right]^q \tag{8}$$

In this equation m_∞ is the maximum absorbed mass of resin in equilibrium (see also Fig. 1). Eq. (8) provides a good approximation in the sense of the asymptotic behavior as well if:

$$p \cdot q = \frac{1}{2} \tag{9}$$

while

$$\begin{aligned} m(t) &\sim \sqrt{2\mathrm{b_m}t}, \quad t \to 0 \\ m(t) &\to m_\infty, \quad t \to \infty \end{aligned} \tag{10}$$

The above mentioned equations are only valid in case of one single capillary (monocapillary). However, in reality there are always more capillaries of different sizes, i.e. a multicapillary system should be taken into consideration. In this case the system is stochastic because the radii of capillaries and the quantities of resin in one capillary are stochastic variables. If the solution of Eq. (1) is extended for statistical multicapillary systems where the following formula is obtained for the mean capillary pore size:

$$r_{P,hydr} \approx \left[\frac{k_{0m}2\sqrt{2\eta\gamma\cos\theta}}{m_\infty\rho g\left(1 + \frac{15}{8}V_r^2\right)}\right]^{2/3} \tag{11}$$

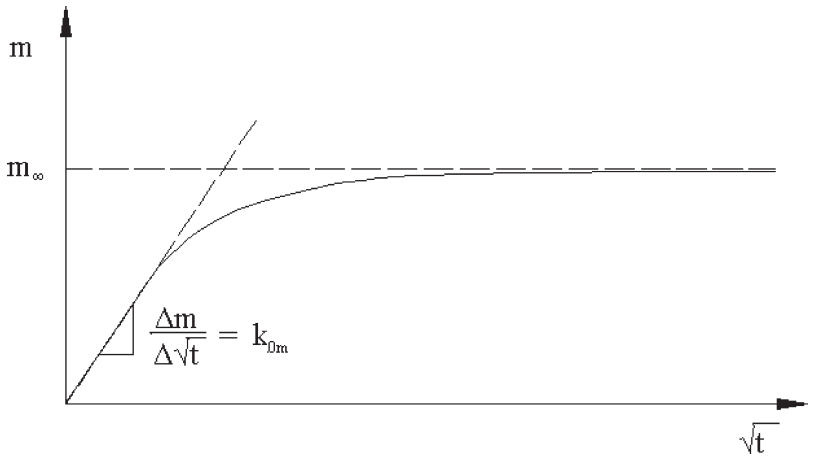

Figure 1.
The absorbed mass of resin as a function of the square root of time.

where $r_{p,hydr}$ is hydraulic pore radius, and V_r is the variation coefficient of the hydraulic pore (capillary) radius.

Based on a statistical fiber mat model [9] the expected value of the geometrical pore radius can be calculated as an upper estimation as follows:

$$r_{P,geo} \leq \frac{1}{2Kl} \tag{12}$$

$$K = \frac{Q_\infty}{q_0 nl} \tag{13}$$

where K is the average number of fiber bundle centers in a designated area, l is the mean length of the fiber bundles, Q_∞ is the mean surface mass of the mat, q_0 is the linear density of fibers, n is the mean number of fibers in the fiber bundle.

Making the mean hydraulic pore radius equal with the mean geometrical one the variation coefficient of pore radius (V_r) can be estimated.

Materials and Method

The GFMs used in the experiments are denoted and classified. The main properties of these GFMs are the same: the nominal fiber diameter is 12 μm, the linear density of the rovings is 30 tex, the length of the chopped roving is around 50 mm, the surface mass of the mat is 450 g/m^2 and the density of glass is 2.6 g/cm^3. The difference among them lies in the bonding agent (powder-P and emulsion-E) and the producer (Johns Manville-1, Scottbader-2, Ahlstrom-3). Two types of unsaturated polyester (UP) resins of different viscosities measured according to standard Brookfield LVF 2/12 at 23 °C at 20 1/s shear rate were used: *VIAPAL VUP 4627 BEMT/56* ($\rho_1 = 1060$ kg/m^3; $\eta_1 = 0.45$ Pas; $\gamma_1 = 0.035$ N/m; $\cos\theta_1 = 0.95$) and *ChS Polyester Lamit109* ($\rho_2 = 1140$ kg/m^3; $\eta_2 = 0.30$ Pas; $\gamma_2 = 0.033$ N/m; $\cos\theta_2 = 0.95$).

A relatively small sample (30 mm × 40 mm) was hung vertically in a micro-tensiometer type Krüss K12. The principle of this measurement is the following (see Fig. 2): the sample of GFM is hung vertically in the microtensiometer, the sensitivity of which is 0.0001 g. A beaker filled with liquid (in this case polyester

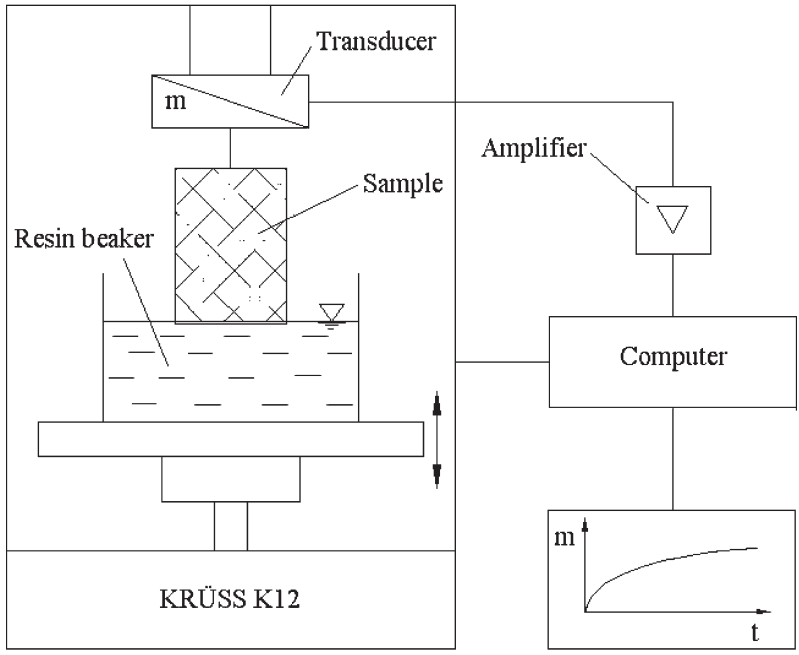

Figure 2.
Schematic arrangement of measurement (device KRÜSS K12).

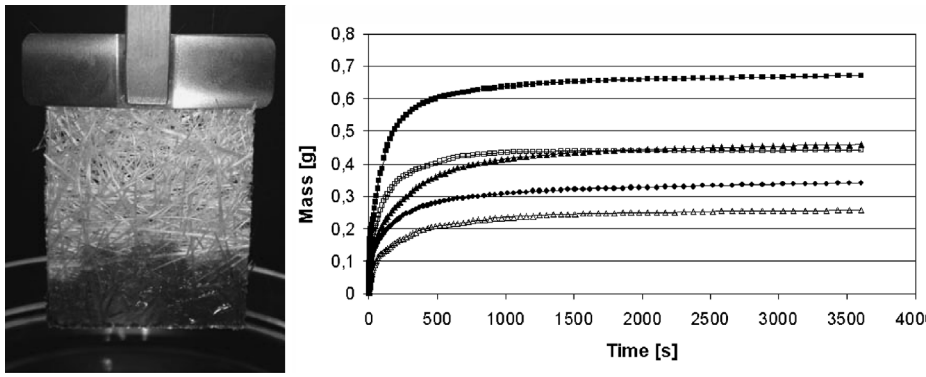

Figure 3.
Lower viscosity case: sample measured (left); and the absorbed resin mass as a function of time (right) ■ = GFM1P, ▲ = GFM2P, ● = GFM3P, □ = GFM1E, △ = GFM2E.

resin) approaches the vertical sample slowly and when the first change of mass is registered, the beaker stops and the measurement of weight increase starts in this position. The schematic arrangement of the measurement is shown in Fig. 2.

Results and Discussion

The samples that were hung in the resin of lower viscosity obviously absorbed more resin, hence the height of absorbed resin was also higher in this case as revealed by Figs. 3 and 4, the images of which were taken after 1 hour of measurement. Figs. 3 and 4 also show the absorbed resin mass as a function of time for both kinds of resin.

The comparison of these two graphs reveals the difference between the two kinds of resin, i.e. the process of absorption in case of the resin of lower viscosity is less dynamic, meaning that the value of k_{0m} is smaller. On the other hand, if the resin has lower viscosity, the GFM sample absorbs higher amount of it, as expected, but the front of flow is not so homogenous in this case.

Variation coefficient of hydraulic pore radius, V_r was of lower value (revealed in Fig. 5 by the steepness of lines) if the resin had lower viscosity. This means that the distribution of capillary radii is more uniform in this case. The value of V_r is obtained

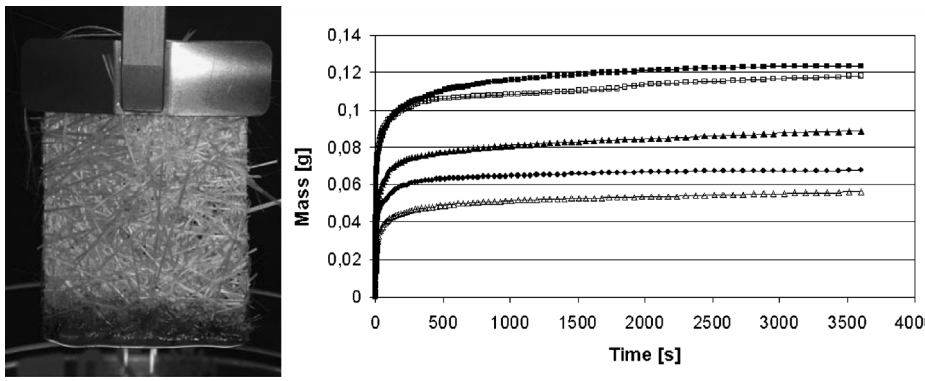

Figure 4.
Higher viscosity case: sample measured (left); and the absorbed resin mass as a function of time (right) ■ = GFM1P, ▲ = GFM2P, ● = GFM3P, □ = GFM1E, △ = GFM2E.

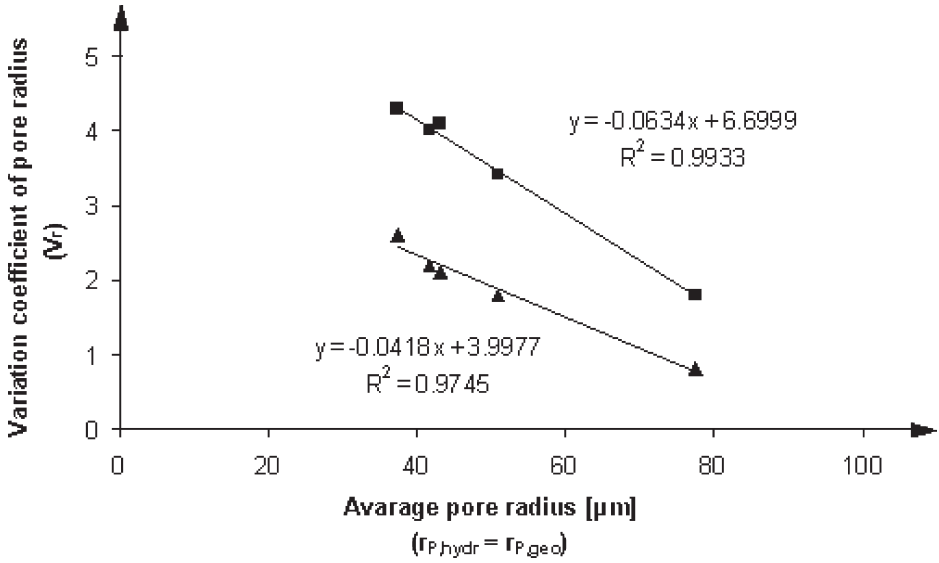

Figure 5.
Variation coefficient of pore radius V_r as a function of the average pore radius in case of $r_{P,hydr} = r_{P,geo}$; condition of the absorption process: T = 23 °C; ■ = unsaturated polyester resin with higher viscosity *VIAPAL VUP 4627 BEMT/56*, ▲ = unsaturated polyester resin with lower viscosity *ChS Polyester Lamit109*.

if the mean geometrical pore size measured and determined on the basis of a statistical fiber mat model were considered to be equal to the hydraulic pore size, and the mat properties [9] are substituted into Eq. (10). It is visible in Fig. 5 that the variation coefficient of pore radius (V_r) decreases with the increase of the average pore radius.

Conclusion

The conclusions that the resin of lower viscosity is absorbed in greater amount than that of higher viscosity but more slowly can be drawn from these measurements. If resin viscosity is lower, the calculated variation coefficient of pore radius (V_r) was also found to be of lower value. Another conclusion is that the variation coefficient (V_r) of differently bonded GFMs versus the mean pore radius relationship can be estimated by a linear trend line for both examined resin viscosities. This process using a microtensiometer turned out to be applicable in examining the interaction of fiber and resin and should be studied with other fiber types due to the simplicity of the method.

Acknowledgements: This paper was supported by Czech-Hungarian intergovernmental TéT application (No. CZ-1/04) and Hungarian Research Fund (OTKA 049069).

[1] V. Nagy, E. Kostakova, L.M. Vas, *Textile Science 5th International Conference TEXSCT03*. **2003**; Liberec CZ Proceedings, p. 164–167.
[2] A. Perwuelz, P. Mondon, C. Cazé, *Text. Res. J.* **2000**; 70 (No.4), p. 333–339.
[3] L. Rebenfeld, B. Miller, *J. Tex. Inst.* **1995**; 86 (No.2), p.241–251.
[4] J. Dutkiewicz, *Autex Research Journal*. **2002**; 2 (No.3), p. 153–165.
[5] H.W. Beckham, W. Carr, S.B. Warner, *National Textile Center*. **1999**; Project No.C97–G31, p. 1–10.
[6] E.W. Washburn, *The Physical Review*, **1921**; 17 (No.3), p.273–283.
[7] V. Nagy, L.M. Vas, *Fibres & Textiles in Eastern Europe*. **2006**, 14 (in press).
[8] S.J. Park, M.H. Kim, J.R. Lee, S. Choi, *J. Colloid Interface Sci.* **2000**; 228, p. 287–291.
[9] Z. Gombos, V. Nagy, L.M. Vas, J. Gaál, *Periodica Polytechnica Mechanical Engineering*. **2005**; 49 (No.2), p. 131–148.

Příloha 12

Molnar, K., Kostakova, E., Meszaros, L.: Electrospinning of PVA/carbon nanotube composite nanofibers: the effect of processing parameters, Material Science Forum, Vol. 589 (2008) pp 221-226

Materials Science Forum Vol. 589 (2008) pp 221-226
online at http://www.scientific.net

Electrospinning of PVA/carbon nanotube composite nanofibers: the effect of processing parameters

Kolos Molnár [1,a], Eva Košťáková[2,b], László Mészáros[1,c]

[1]Department of Polymer Engineering, Budapest University of Technology and Economics, H-1111 Budapest, Muegyetem rkp. 3., HUNGARY

[2]Department of Nonwovens, Faculty of Textile Engineering, Technical University of Liberec, Hálkova 6, Liberec 461 17 CZECH REPUBLIC

[a]kolos2@interware.hu, [b]Eva.Kostakova@seznam.cz, [c]meszaros@pt.bme.hu

Keywords: Electrospinning, PVA, Carbon nanotubes, Nanofibers

Abstract. Poly(vinyl alcohol)/carbon nanotube (CNT) composite nanofibers were processed by both conventional and needleless electrospinning method. The effect of the processing parameters on the possibility of manufacturing was investigated. The results were evaluated by surface tension and conductivity measurements. For the investigation of surface morphology scanning electron microscopy (SEM) was used. It was concluded that surface treatment of carbon nanotubes was necessary for needleless electrospinning. Lower surface tensions were better for this process but the effect of conductivity was not so significant.

Introduction

Nowadays many researchers are dealing with nanomaterials. Carbon nanotubes (CNTs), usually having a diameter between 10 and 50 nm, are widely used in nanocomposites [1]. Electrospinning has been recognized as an efficient technique for manufacturing polymer nanofibers [2]. This procedure uses an electrostatically driven jet of polymer solution or melt for producing electrospun textiles, whose structure is a kind of statistical fibrous network [3,4]. The typical diameter range of the fibers is from 1 nm to a few microns and the average value can be adjusted consistently. Among other parameters the diameter of the fibers depends on the applied voltage, the distance between the two electrodes, the viscosity of precursor and the conductivity of polymeric fluids [5]. The idea was to make composite nonwoven materials so that the matrix is electrospun fibrous textile and the reinforcing materials are carbon nanotubes located inside the fibers. Presently, the most of the electrospinning techniques used for production of nanofibrous materials are based on capillary electrospinning [6-9], although there is a process called needleless electrospinning presented by Yarin [10], which uses a free surface of fluid for electrospinning. A new needleless modification for continuous production of nanofibers has been patented [11,12], Fig. 1. This modified technology is called Nanospider. A polymer solution is supplied into the electric field using a surface of a rotating charged cylindrical electrode. Thus no syringes, capillaries, nozzles or needles are necessary. The main advantages of the technology are: continuous mass production, high production capacity and ease of upkeep [13].

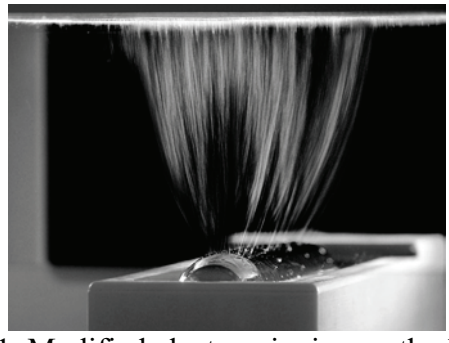

Fig. 1. Modified electrospinning method [13]

In this study nanofibers were produced both with Nanospider technology and a method based on the classical capillary electrospinning process. One of the most frequented questions is how to disperse the nano-sized reinforcing materials in a polymer matrix. After the separation process the stabilization of the composite system is also very important. The electrospinning process seems to be a good method to solve this problem. Generally carbon nanotubes are admixed into the polymer solution destined for electrospinning. Results are composite nanofibers with special properties, for example they have higher tensile strength and conductivity than fibers without CNTs. The composite nanofiber materials can be used as an excellent precursor for the production of carbon nanofibers and subsequently as absorbers of toxic materials because of their huge surface. Electrospun nanostructures can also serve as a basis of controlled drug delivery systems [14,15]. Another potential possibility is to utilize these composite nanofibers as part of special filters used at high temperature or as reinforcement for special transparent composites. The subject of composite nanofibers including carbon nanotubes was already studied by some researchers but usually in case of polymers (as poly(acrilonitrile)) solved in organic solvents. The electrospinning of these solutions is often not environmentally friendly because of its toxic content [16]. Electrospinning of poly(acrylonitrile) nanofibers reinforced by single-wall nanotubes (SWNTs) is a part of Lam's thesis [17]. In this case, composite fibers were subjected to carbonization and also to graphitization. Ge et al. [18] described composite nanofiber materials made from composition of surface-oxidized multiwalled carbon nanotubes (MWNTs) and poly(acrylonitrile), which were successfully developed using the electrospinning method. The present contribution deals with production of composite nanofibers from poly(vinyl alcohol) water solution mixed with different types of carbon nanotubes. Single and multi walled nanotubes, with and without surface treatment with OH and COOH groups were used. The most important parameters of solutions used for electrospinning: conductivity, surface tension and viscosity were measured. These parameters can potentially change the formation and therefore the properties of the emerging fibers. Also distribution of carbon nanotubes in water solution of poly(vinyl alcohol) was studied after the impact of ultrasound and mechanical mixing in a mortar.

Materials and methods

In this study basic poly(vinyl alcohol) (PVA) aqueous solutions were used for electrospinning, in some cases ethanol was added to the solvent. Basic PVA water solution (10 wt%) including crosslinking agents (glyoxal 2.5 wt% and phosphoric acid 2.5 wt% of PVA) was electrospun and subsequently crosslinked at 140°C for 10 minutes. A complete set of samples were made by mixing 0.1 wt% single or multi wall carbon nanotubes into the PVA solution. These samples are described in Table 1. and below.

Marking	Nanotube type	PVA	Distilled Water	Ethanol
-	-	wt%	wt%	wt%
0	-	10	90	-
1	MWNT	10	90	-
2	SWNT-COOH	10	90	-
3	MWNT-COOH	10	90	-
4	MWNT-OH	10	90	-
5	SWNT-OH	10	51.5	38.5
6	MWNT-OH	10	51.5	38.5

Table 1. Prepared solutions and their composition

The basic solution including multi walled carbon nanotubes dispergated in water (MWCNTs) presents the first type of introduced samples. The second sample was the basic PVA solution containing single walled carbon nanotubes (SWCNTs) with COOH surface modification (made by Nanocyl, Belgium in each case). The third and fourth samples were the basic PVA solutions containing multi walled carbon nanotubes (MWCNTs) with either COOH or OH surface modification. In case of last two samples the solvent was a 4:3 proportioned mixture of water and ethanol. Fong et al. [19] demonstrated that ethanol added to aqueous solution of poly(ethylene oxide) decreases the surface tension, thus fibers with more favourable properties can be produced. The fifth sample contained SWCNTs with COOH surface modification and the last (sixth) contained MWCNTs with OH surface modification. All solutions containing carbon nanotubes were mixed for one minute by sonication in order to completely separate the agglomerates of nanotubes inside the solutions. The short time of the treatment was important, otherwise serious damage of nanotubes could occur [20]. Couptiss Ultra Sons HS30 device (Calemard, France) was used with 30 W power and 30 kHz frequency. The suspensions of CNTs and water (and in two cases additional ethanol) were mixed with PVA by magnetic mixer for 5 minutes. Surface tensions of the prepared solutions were measured with Kruss K121 device three times for each sample. The conductivity was measured with a WTW device. The electrospinning was done in two different ways. At first the classical method (electrospinning from droplet) with grounded flat collector was used. The spinneret was a cylindrical bar with a diameter of 4 mm. Samples large enough for SEM analysis were made of only one droplet placed on the top of the bar. The distance between the collector and spinneret was 10 cm and the voltage was 22-30 kV. The other electrospinning process was done with a modified method called Nanospider. The distance between the grounded collector and a charging rotating cylinder in bath of polymer solution was 8 cm, voltage was 45-53 kV and speed of collecting the nonwoven textile was 0.1 m/min. The surface density of these samples is 5 g/m^2. It is estimated that the final amount of nanotubes inside the final composite nanofibrous materials is approximately 1 wt% of PVA. The crosslinking process after electrospinning was the same as in case of the basic solution for all types of composites. The surface morphology was studied by a JEOL 6380LVa type scanning electron microscope (SEM).

Results and discussion

Fig.2. shows sample 3 and 4 after the procession with magnetic mixer. The only difference between the two samples was the surface modification.

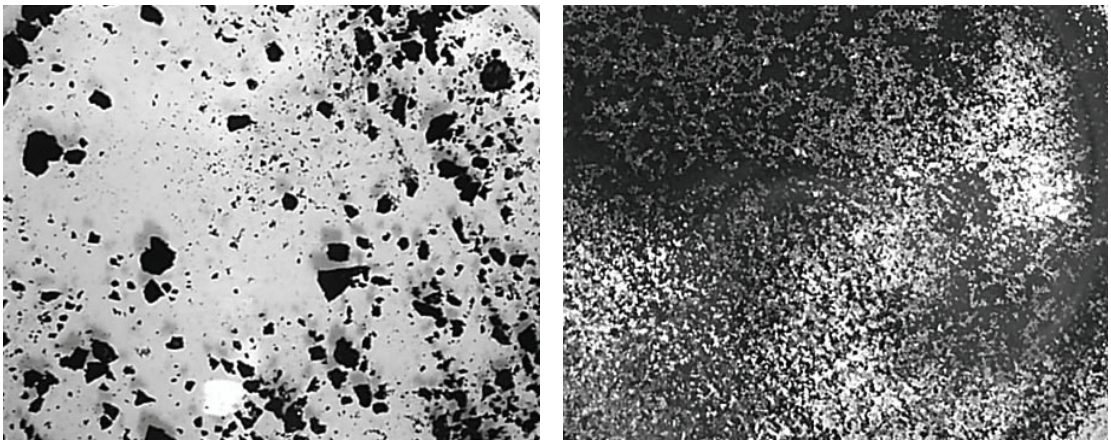

Fig. 2. Sample 3 containing MWCNT with COOH surface modification (left), Sample 4 containing MWCNT with OH surface modification (right)

It shows that CNTs with COOH modification form agglomerates and these remain even after sonication and mixing. Sonication separated the nano-sized reinforcing materials better in the polymer solution in case of MWCNTs+OH surface modification. Thus COOH surface modification of CNTs gave a better solution destined for electrospinning and also these are more processable with Nanospider technology than CNTs with OH surface modification. Nanofibers were successfully produced from every solution with the classical method. In case of Nanospider procession only the samples 2, 4, 6 and the PVA sample gave reasonable materials. The different processing parameters can be the reason of failure in case of samples 1 and 3. Scanning electron microscope images of materials successfully electrospun with Nanospider technology can be seen in Fig. 3. It can be observed that in case ofsamples 3 and 5 the diameters of the nanofibres are similar to those of the pure PVA nanofibers. When ethanol was used the diameters increased.

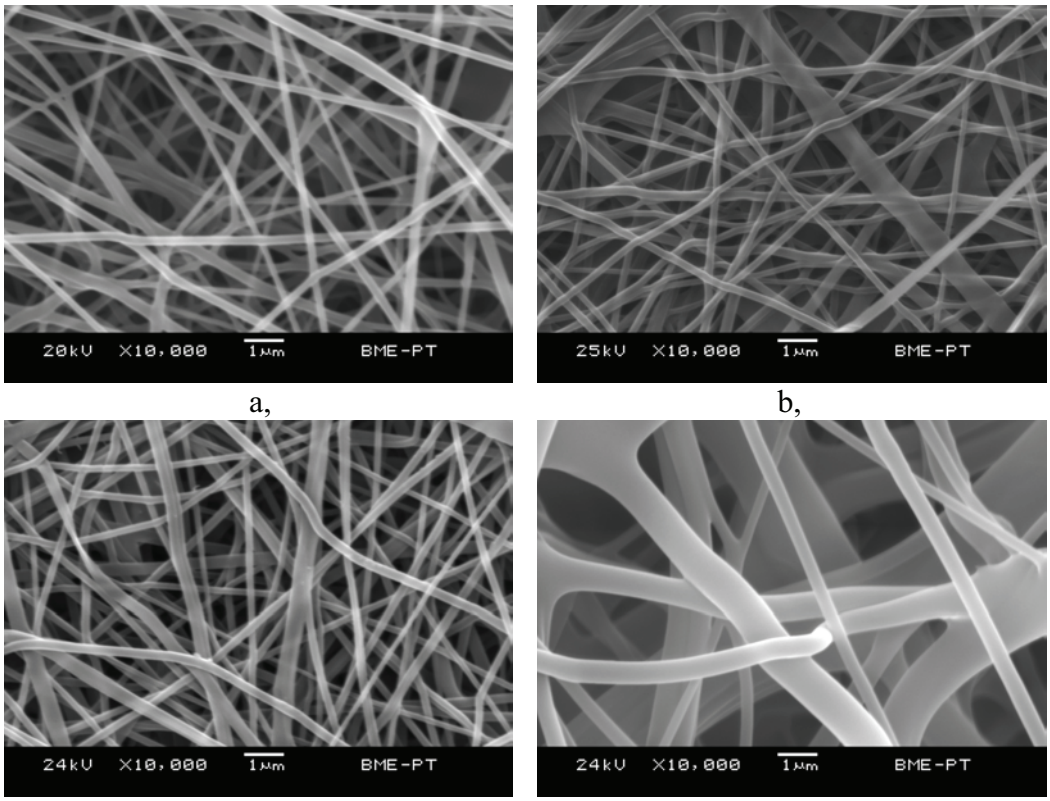

a, b,

c, d,

Fig.3. SEM pictures of samples 1, 2, 4, 5 (a-1, b-2, c-4, d-5)

Measured surface tensions and their deviance are shown in Table 2.

Material		0	1	2	3	4	5	6
Surface tension	[mN/m]	45.90	45.94	43.86	45.24	44.32	41.80	42.62
Deviance	[mN/m]	0.20	0.12	0.27	0.24	0.25	0.23	0.25

Table 2. Surface tensions

Usually lower surface tension causes favourable conditions for producing nanofibers and it is definitely necessary when mixing nanotubes into the solutions. Although in these cases the surface tension changed only in a small extent, but due to nanotubes sample 2 and 4 were suited for processing with Nanospider technology. For additional reduction of the surface tensions suspensions were made by adding ethanol to the aqueous solutions. In case of the last two samples the surface tensions decreased matching our expectations but the conductivity (Table 3.) dropped by one order of magnitude, which made the procession unfeasible. In spite of this sample 6 was adapted to suitably generate nanofibers with Nanospider technology.

Material		0	1	2	3	4	5	6
Conductivity	[mS/cm]	7.57	9.48	4.36	7.71	6.54	0.3	0.3

Table 3. Conductivities

This latter symptom can be explained by the appropriate relationship between the carbon nanotubes and the PVA. On the score of the SEM micrographs it can be seen that the average thickness of the fibers of sample 2 and 4 are approximately the same as in the basic PVA solution (sample 0). In case of the samples containing ethanol solvent (5-6), thicker fibers have started up and those had thickness over 1μm. This phenomenon is explicable with the significant decrease of the conductivity.

Summary

In this study nanofibers were produced by electrospinning from different PVA solutions applying both the classical method and Nanospider technology. Both methods resulted in carbon nanotube reinforced nanofiber composites as a nonwoven. Decreasing the surface tension made the processing more convenient. Mixture of water/ethanol gave worse results than the PVA aqueous solution, because it decreased the conductivity (which is also important for electrospinning) largely. Carbon nanotubes with OH surface modification gave better electrospun results than carbon nanotubes with COOH surface modification, which were unsuitable for Nanospider processing.

Acknowledgement

This research was supported by the Czech-Hungarian intergovernmental research support KONTAKT (No. CZ-4/2007), as well as the Hungarian Research Fund (OTKA NI 62729 and OTKA F 67897) and by the grant of Ministry of Industry and Trade of the Czech Republic, No. MPO – 1M 0553, 1H PK-2/46.

References

[1] J.-H. Du, J. Bai, H.-M. Cheng: Express Polymer Letters Vol. 1 (2007) p. 253
[2] S. Kamel: Express Polymer Letters Vol. 1 (2007) p. 546
[3] O. Jirsak, D. Lukas, R. Charvat: Journal of the Textile Institute Vol. 84 (1993) p. 1
[4] L.M. Vas, K. Balogh: VI. International Textile Conference IMTEX'2000. Lodz, june 5-6, (2000) Proceedings p. 69
[5] J. Zhao, C. Jia, H. Duan, H. Li, E. Xie: Journal of Alloys and Compounds (2007) in press
[6] J.M. Deitzel, J.D. Kleinmeyer, J.K. Hiroven, N.C. Beck Tan: Polymer Vol. 42 (2001) p. 8163
[7] P.D. Dalton, D. Klee, M. Moller. Polymer Vol. 46 (2005) p. 611
[8] A. Varesano, A. Montarsolo, C. Tonin: European Polymer Journal Vol. 43 (2007) p. 2792
[9] W.-E. Teo, R. Gopal, R. Ramaseshan, K. Fujihara, S. Ramakrishna, Polymer Vol. 48 (2007) p. 3400
[10] A.L. Yarin, E. Zussman: Polymer Vol. 45 (2004) p. 2977
[11] O. Jirsak: CZ Patent 2003-2414 (294274)
[12] O. Jirsak. World Patent WO/2005/024101
[13] Information on http://www.elmarco.com
[14] P. Taepaiboon, U. Rungsardthong, P. Supaphol: Eur. J. Pharm. Biopharm. Vol. 67 (2007) p.387
[15] A. Chunder, S. Sarkar, Y. Yu, L. Zhai: Coll. Surf. B: Biointerfaces Vol. 58 (2007) p. 172
[16] I.S. Chronakis: Journal of Materials Processing Technology Vol. 167 (2005) p. 283
[17] H.L. Lam: Electrospinning of single wall carbon nanotube reinforced aligned fibrils and yarns, a thesis, Drexel University, 2004

[18] J.J. Ge, H. Hou, Q. Li, M.J. Graham, A. Greiner, D.H. Reneker, F.W. Harris, S.Z.D. Ceng: J. Am. Chem. Soc., Vol. 126 (2004) p. 15754
[19] H. Fong, I. Chun, D.H. Reneker: Polymer Vol. 40 (1999) p. 4585
[20] K.L. Lu, R.M. Lago, Y.K. Chen, M.L.H. Green, P.J.F. Harris, S.C. Tsang: Carbon Vol. 34 (1996) p. 814

Příloha 13

Kostakova, E., Zemanova, E., Klouda, K.: Fullerene C60 and its derivatives as nanocomposites in polymer nanofibers, 3rd International Conference on NANOCON, Brno, Czech Republic,SEP 21-23, 2011, pg.470-474 (2011)

FULLERENE C60 AND ITS DERIVATIVES AS NANOCOMPOSITES IN POLYMER NANOFIBRES

Eva KOŠŤÁKOVÁ[a], Eva ZEMANOVÁ[b], Karel KLOUDA[b]

[a]*Technical University of Liberec, Studentska 2, 460 01 Liberec, Czech Republic, EU eva.kostakova@tul.cz*

[b]*State Office for Nuclear Safety, Senovazne namesti 9, 110 00 Praha 1, Czech Republic, EU, eva.zemanova@sujb.cz, karel.klouda@sujb.cz*

Abstract

This work describes the application of oxo-derivatives of fullerene C60 and pristine fullerene as a nanocomposite in polymerous nanofibres. In this work we used oxo- fullerene derivative, of which preparation was presented by the authors of the State office for nuclear safety (Prague) on Nanocon 2009 and on Nanocon 2010 [1, 2]; there was presented its application in vivo as a radioprotective agens. With respect to wild spectrum of potential utilization of unique chemical, structural a electron properties of fullerene we investigate its another possible technical application as nanocomposite in polymer nanofibres. The nanocomposite polymer nanofibers were produced by needle-less electrospinning method. Polyvinyl alcohol, polyurethane a polyvinyl butharate were used as polymers. Thermal resistance of obtained nanofibres without and with nanocomposites was tested by simultaneous thermogravimetric analysis and differential thermal analysis (TGA/DTA). The retarding influence of fullerene and its derivative on the course of the thermal decomposition of nanofibres is discussed.

Keywords: Fullerene C60, Derivative of C60, Nanocomposites, Polymer nanofibres, TGA, DTA

INTRODUCTION

Fullerenes C60, molecules composed of 60 carbon atoms in the form of hollow sphere, are very interensting and nowadays all over the world studied nanomaterial [3]. Fullerenes C60 can be also incorporated into other amazing nanomaterial – electrospun nanofibers. The production of such nanocomposite material where the matrix is presented by polymer nanofibers and “reinforcement” is presented by C60 is done by electrospinning technology. The technology uses electrostatic forces for self-organization of polymer solution/melt into a nanofibrous layer as is generally known [4]. Presently, the most of electrospinning techniques used for production of nanofibrous materials is based on capillary electrospinning. On the other hand, the electrospinning from free surface (or almost free surface) of liquid was named as a needleless electrospinning by Yarin [5]. However before that, the needleless modification for continuous production of nanofibers was patented [6, 7] and it is generally known as Nanospider^{TM} technology now.

The materials originated thanks to connection of carbon nanoparticles (fullerenes or nanotubes) and electrospun nanofibers are also in the center of the scientific researches, it is for example described in [4, 8-10]. Althought the most of these publications presents nanofibrous materials electrospun from capillary electrospinners. A preparation of polymer solution with integrated nanoparticles C60 is fundamental for composite nanofibers production by needleless electrospinning. The solution preparation can be enhaced by ultrasound if it is necessary [9].

ELECTROSPUN NANOFIBERS PREPARATION

For the presenting contribution, there were chosen three different polymer materials as a matrix for fullerene and as “blind” samples. These polymers were polyvinyl alcohol (PVA, Slovácké chemické závody, M_w approximately 60 000 g/mol; polymerization degree approximately 1100, 16 wt% water solution), polyurethane (PUR, Larithane LS1086 aliphatic elastomer based on 200g/mol, linear polycarbonated diol,

isophorone diisocyanate and extended isophorone diamine, 30 wt% dimethylformamid solution), polyvinyl buthyral (PVB, Kuraray, Mowital B60T, M_w approximately 60 000 g/mol). Polymer solutions described above were prepared from these polymers with and without C60 and derivative C60 addition. The derivative C60 was prepared using peracetic acid and subsequent hydrolysis (follow only "C60oxi") according to the method that we described in [1, 2]. Electrospun by needleless electrospinning method was used. A distance between a grounded collector and a drop of the solution on the top of a charging metal cylinder was 10 cm. The surface density of all these samples was approximately 2 gm^{-1}. The nanofibrous layers were collected on spun-bond material for subsequent better separation.

Basic PVA water solution (10 wt.%) plus crosslinking agents (glyoxal 2,5 wt.% and phosphoric acid 2,5 wt.% of PVA) were electrospun and subsequently crosslinked at 140°C for 10 minutes. It was the "blind" sample. The basic PVA solution plus addition of water solution of 0,1 wt.% C60oxi was also prepared. Thus the final electropun PVA nanofibers contain 1wt% of C60oxi. Used voltage for electorspinng was 23kV. After electrospinning was the same crosslinking process as for the blind sample. There were used device Couptiss Ultra Sons HS30 with power 30 W and frequency 30 kHz (Calemard, France).

Basic PUR solution used for electrospinning of the blind sample had 10 wt.% in DMF. The basic PUR solution plus addition of 0,1 wt.% of C60 was also prepared. Thus the final electropun PUR nanofibers contain 1wt% of C60. Solutions with C60 mixed one minute by sonication to completely separate agglomerates of nanotubes inside the solutions. Used voltage for electorspinng was 26kV.

Basic PVB solution used for electrospinning of the blind sample had 10 wt.% in acetic acid and ethanol in 1:2 ratio. The basic PVB solution plus addition of 0,1 wt.% C60oxi was also prepared. Thus the final electropun PVB nanofibers contain 1wt% of C60oxi. Solution with C60oxi was mixed one minute by sonication to completely separate agglomerates of nanotubes inside the solutions. Used voltage for electorspinng was 22kV. Examples of produced nanofibrous materials are presented in **Fig 1**.

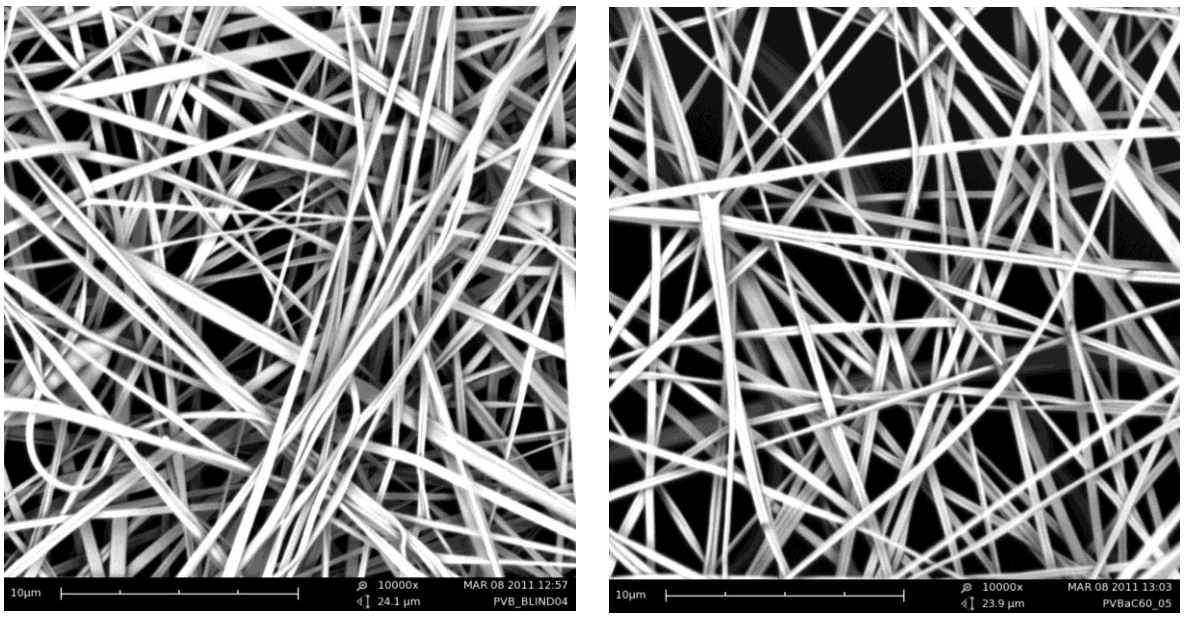

Fig 1. Scanning electron images of PVB electrospun nanofibers; blind sample on the left side and sample with C60oxi on the right side.

MEASURING

A change of thermal stability of the produced nanofibrous materials was assessed at Fire rescue service of Czech republic, by means of TGA and TG-DSC methods. These methods are based on measurements of

weight loss and relaxed-consumed thermal energy depending on used temperature and time. The tests were performed according to accredited methods, apparatus STA 1500 THASS. The used degradation medium was air, used temperature regime went from 25°C to 550°C and sample-heating rate was 10°C/minute.

CONCLUSIONS

The results, which are listed in **Table 1**, showed that the samples with addition of C60oxi have significantly higher thermal resistance. A change of the thermal decomposition of nanofibers is evident from the curves of TGA and TG-DSC (see **Fig 2**) for nanofibers without and with addition of C60oxi. The main exoeffect characterizing thermal decomposition of PVA blind sample is supressed after addition of C60oxi. Also the begiining of thermal decomposition shifted of 90°C. The polymer solution preparation before the electrospinning has an influence on thermal stability of final nanofibers. The result was shown mainly for PUR nanofibers with and without C60.

Table 1: Thermal characteristics of nanofibers based on PVA with and without C60oxi.

Material	The temperature of the sample weight loss start [°C]	Temperature maximum peak of the first exoeffect [°C]	Thermal decomposition of color (the first exoeffect/ total) [mW]
PVA (blind sample)	220	310	70/92
1. PVA - C_{60}oxi (solution without crosslinking agents; fullerenes were mixed firstly only with water)	310	450	50/75
2. PVA - C_{60}oxi (solution withou crosslinking agents)	260	450	54/84
3. PVA - C_{60}oxi (with crosslinking agents)	250	350	13/75

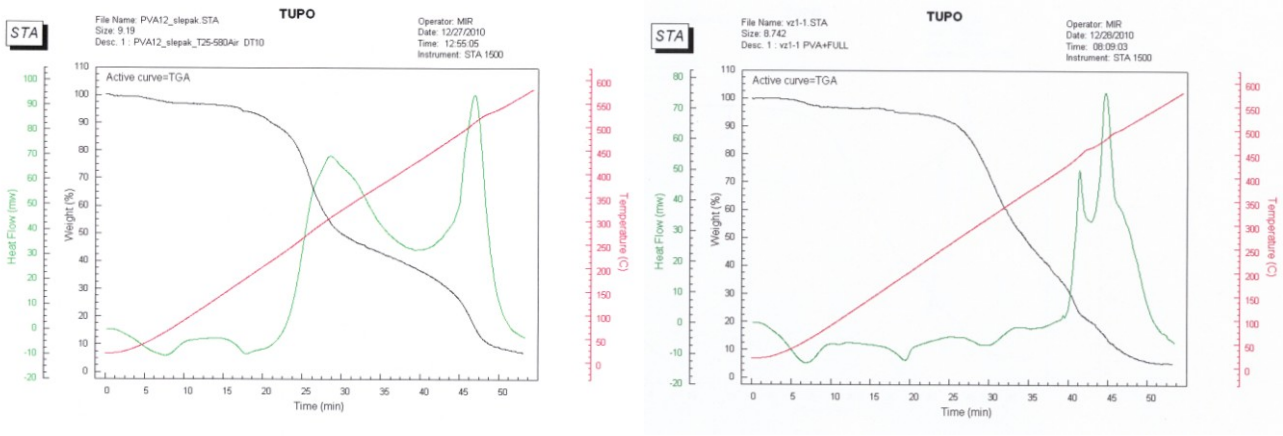

Fig 2. Thermal analysis graphs presenting blind sample of PVA nanofibers on the left side and PVA nanofibers with addition of C60oxi.

For the PVB nanocomposite - nanofibers with addition of C60oxi, thermal decomposition of color (exothermic reaction) was calculated from the TGA and TG-DSC measurements. The exothermic reaction was 20% higher for PVB blind sample in comparison with PVB nanofibers with C60oxi addition. Decomposition temperature is lower in PVB nanofibers blind sample (see **Table 2**).

Table 2: Interpretation of the test results from PVB and PUR nanofibers measurements.

Nanofibers	Temperature of the decomposition beginning [°C]	Δm/Δt [mg/min]	ΔH [kJ/kg]
1. PVB - C_{60}oxi	337	0,15	-2374
2. PVB – blind sample	315	0,07	-2822
3. PUR – blind sample	237	0,17	2625
4. PUR - C_{60} (mixing in polymer solution)	275	0,15	3908
5. PUR - C_{60} (mixing in solvent at first)	288	0,14	-2641

Δm/Δt – average rate of the sample weight loss
ΔH – thermal decomposition of color (ΔH < 0 exothermic reaction, ΔH > 0 endothermic reaction)

The thermal testing of PUR nanofibers confirmed that the resulting effect (thermal resistance) of prepared composite nanofibers also depends on the method (polymer, solvent, nanoparticles, conditions and so on) of solution for electrospinning preparation. As it was mentioned before, dimethylformamid was used as a solvent for PUR for electrospinng. In one case, the fullerenes were incorporated into the final polymer solution (PUR and DMF) by ultrasound enhacement (see Table 2 – sample No. 4). In the second case, the fullerenes are mixed with DMF at first and then PUR is added (see Table 2 – sample No.5). The curves characterizing the decomposition by endoeffect (PUR without C60) and by exoeffect (PUR with C60) are shown in **Fig 3**. In the both cases, when PUR containg nanoparticles C60, the initial temperature of the decomposition increases.

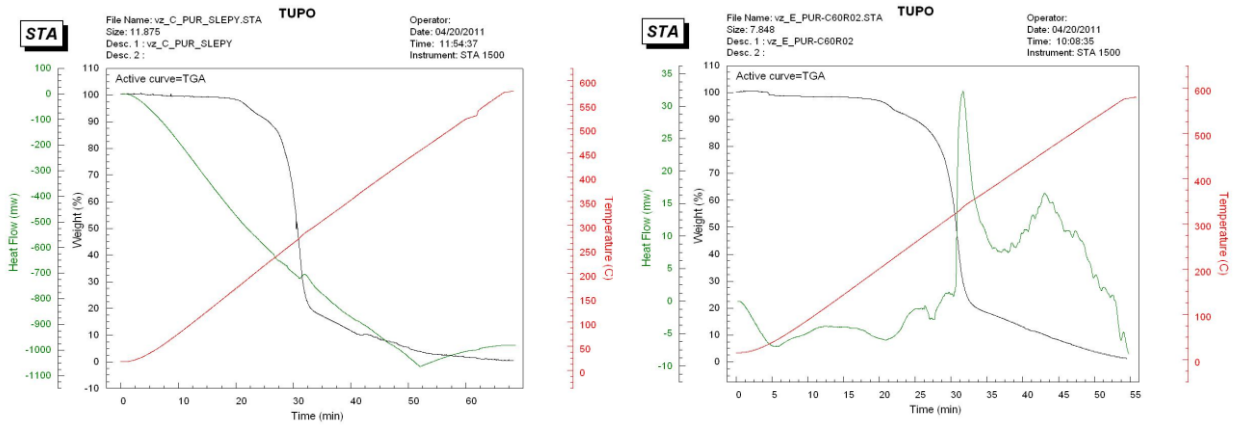

Fig 3. Thermal analysis graphs presenting blind sample of PUR nanofibers on the left side and PUR nanofibers with addition of C60 (mixing in solvent at first).

Several alternatives polymer-fullerene bounds are described in literature [3]. It is depending on the fact whether the fullerene reacts with a functional group of polymer chain additionally, or the fullerene molecule is a part of the polymerization process. A linking of fullerene can be realized at the ends, on the sides, star-like, or between polymer chains. An interaction between functional groups of polymer and fullerenes based on donor-acceptor process can be realized too. Also an exfoliating nanocomposite arrangement of polymer and fullerenes is not excluded here. However the authors of the contribution are not able to precisely defined how is the fullerene C60 and C60oxi bound to the basic polymer of prepared nanofibers. Nevertheless the inhibitory effect of fullerene C60 or its derivative C60oxi was detected during the nanocomposite nanofibers thermo-oxidative degradation. This was probably due to interaction with the radicals generated by

degradation of the polymer and the ability of fullerene to trap this reactive species. The scavenger effect of fullerene was also confirmed in the work [2] with the same fullerene derivative, in role of radioprotector.

ACKNOWLEDGEMENTS

The main support for this research was provided by The Ministry of Interior of the Czech Republic, program BV II/2-VS; grant No. 1656, "Nanomaterials to persons protection against CBRN substances". The authors also thank to Ing. Hana Matheislova and Ing.Otto Dvořák, Ph.D. from Fire rescue service of Czech republic, Písková 42, Praha 4

LITERATURE

[1.] Beranová (Zemanová), E.; Klouda, K.: Conference Proceedings NANOCON 2009, Ostrava, CZ, p. 139-148
[2.] Beranová (Zemanová), E., et al.: Conference Proceedings NANOCON 2010, Ostrava, CZ, p. 251-262
[3.] Martin, N.; Giacalone, F.: Fullerene Polymers, Synthesis, Properties and Application. WILLEY- VCH, 2009
[4.] Huang, Z.,M., Zhang, Y.,M., Kotaki., M., Ramakrishna, S.: Composite Science and Technology, 2003, 63, p. 2223-53
[5.] Yarin, A.,L., Zussman, E.: Polymer, 2004, 45, p. 2977-80
[6.] Jirsak, O., et al. CZ Patent 2003-2414
[7.] Jirsak, O., et al. World Patent WO/2005/024101
[8.] Ko, F., et al. Advance Materials, 2003, 15(14), p. 1161-5
[9.] Ge, J.,J., et al. J Am Chem Soc, 2004, 126, p. 15754-61
[10.] Kostakova, E., Meszaros, L., Gregr,J.: Material Letters, 2009, 63, p. 2419-2422